POSTEARTHQUAKE REPAIR OF PRECAST CONCRETE COLUMN-TO-FOOTING PLASTIC HINGES

by

Dylan Neil Brown

A thesis submitted to the faculty of
The University of Utah
in partial fulfillment of the requirements for the degree of

Master of Science

Department of Civil and Environmental Engineering

The University of Utah

August 2014

The University of Utah Graduate School

STATEMENT OF THESIS APPROVAL

The following faculty members served as the supervisory committee chair and members for the thesis of **Dylan Neil Brown**.

Dates at right indicate the members' approval of the thesis.

Chris P. Pantelides, Chair	**3/19/14** Date Approved
Lawrence D. Reaveley, Member	**3/19/14** Date Approved
Evert C. Lawton, Member	**3/19/14** Date Approved

The thesis has also been approved by **Michael Barber**

Chair of the Department/School/College of Civil and Environmental Engineering

and by David B. Kieda, Dean of The Graduate School.

ABSTRACT

Bridge design is moving towards performance-based design in which acceptable levels of damage following an earthquake are prescribed, allowing the possibility to repair and not replace bridges. A repair technique for precast reinforced concrete bridge column-to-footing assemblies constructed with Grouted Splice Sleeve (GSS) connections has been developed. The repair is implemented and verified through laboratory testing and Strut-and-Tie Models (STM).

The repair utilizes prefabricated carbon fiber-reinforced polymer shells and epoxy anchored headed mild steel rebar to relocate the column plastic hinge. Prior to the repair procedure, two undamaged, as-built, column-to-footing specimens constructed with GSS connections were tested to failure under a quasi-static cyclic lateral load. During testing, both of the as-built specimens experienced longitudinal rebar fracture, with lateral load carrying capacities degrading to 63%–65% of their ultimate load capacities. The as-built column plastic hinge region was subsequently repaired by increasing the column cross-section from a 21 in. octagonal section to a 30 in. diameter circular section, over a column height of 18 in. The repaired specimens were tested following the same cyclic loading protocol as the as-built specimens. The plastic hinge was successfully relocated to the column section above the repair, and the failure mode was longitudinal rebar fracture in the relocated plastic hinge region. The repaired assemblies had an increase in the ultimate lateral load capacities of 28%–30%, while being capable of maintaining the as-built lateral displacement capacity.

To aid in the design of future as-built and repaired assemblies, a conventional STM and a nonlinear STM were developed. Generic modeling parameters were developed, which can be used with varying reinforcement layouts and element geometries. Results from the STM models match the as-built and repaired test results, predicting the ultimate lateral load capacities and nonlinear force-displacement response envelopes.

To my parents.

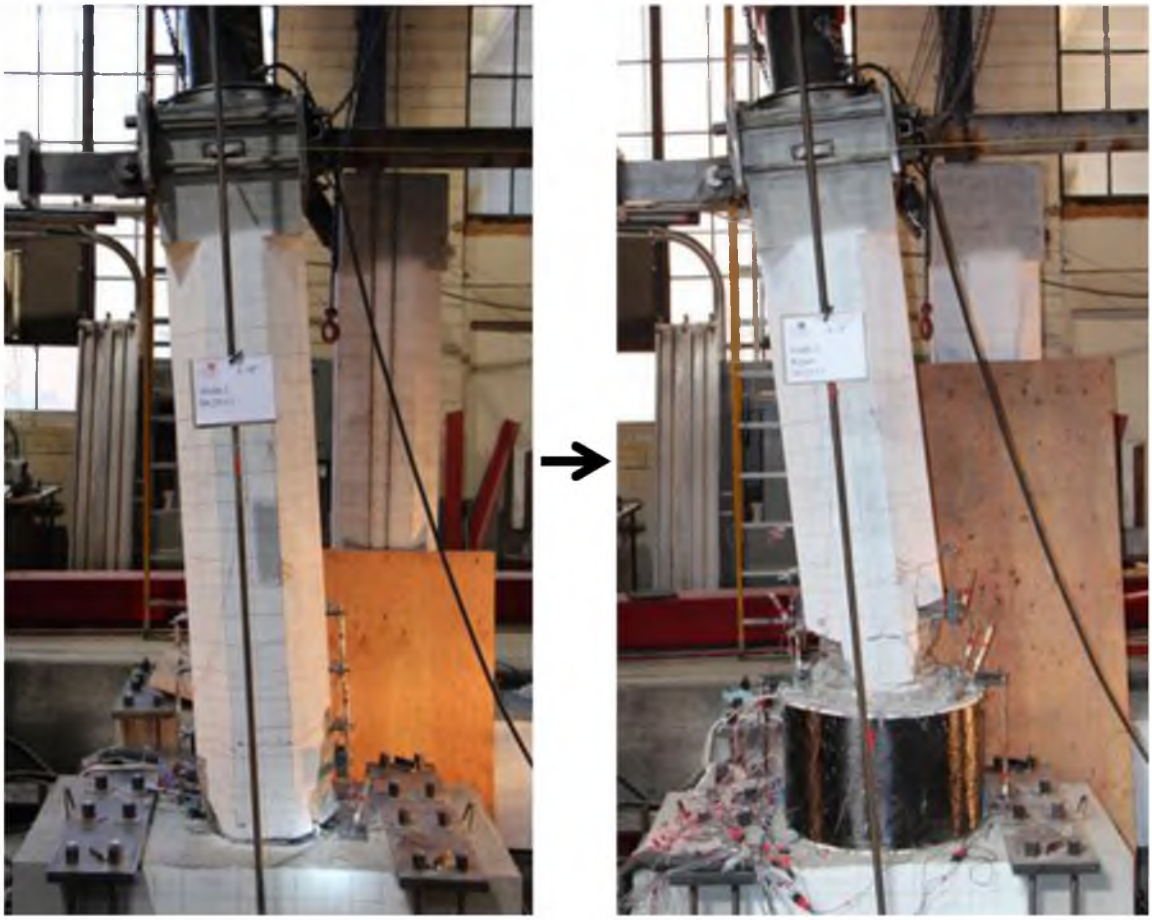

TABLE OF CONTENTS

ACKNOWLEDGEMENTS

I would like to thank the members of my supervisory committee, Dr. Chris Pantelides, Dr. Lawrence D. Reaveley, and Dr. Evert Lawton, for their support in this research. Special thanks to my advisor and chairman of the committee, Dr. Chris Pantelides, for the guidance, mentorship, and countless hours that he has dedicated to this project. I would like to acknowledge and thank the other graduate students working on this project, M.J. Ameli and Joel Parks. Thanks to Mark Bryant, the University of Utah Structures lab manager, for all of the assistance in the laboratory.

Additionally I would like to thank the Mountain Plains Consortium, the Utah Department of Transportation, Texas Department of Transportation, New York Department of Transportation, NMB Splice Sleeve, Headed Reinforcement Corp., Sika Corporation, and Hanson Structural Precast for their contributions to this research.

CHAPTER 1

INTRODUCTION

Bridge design philosophy is shifting beyond simply providing structures that will not collapse during a large earthquake and moving towards performance based design in which acceptable damage states after an earthquake are being prescribed. An example of this shift is illustrated by CALTRANS limiting the allowable displacement ductility to a value between four and five (*1*) for bridge columns. Limiting the amount of displacement ductility controls the amount of permanent damage the bridge experiences from the design earthquake and allows for potentially repairing the damaged structure. It is not possible to design bridges that will remain undamaged during an earthquake due to the high cost of materials, uncertainty in loading, and design time necessary to build such a structure. Therefore, repair procedures that can rehabilitate a bridge after an earthquake are necessary to avoid the cost, construction time, and interruption to emergency services and the general public that bridge replacement causes.

Accelerated Bridge Construction (ABC) is gaining popularity and is used nationwide due to decreased user interruption and increased safety of the construction personnel. Grouted Splice Sleeves (GSS) are gaining attention as a method for connecting precast concrete bridge elements using ABC standards. The use of GSS connections for bridge elements in areas of high seismicity is currently being studied (*2*–*4*). Recent projects, including the construction of the FrontRunner light rail train bridges in Salt Lake City, show the promise for GSS becoming a popular precast concrete connection option in areas of high seismicity. The expected increase in use of GSS connections poses the need for a postearthquake repair technique, which is the focus of this study.

Since current code directed capacity-based bridge design directs the damage of bridge assemblies into the columns, thus protecting the footings and pier caps, the repair has been developed for column plastic hinges. The repair method developed in this project uses Carbon Fiber-Reinforced Polymer (CFRP) shells, headed mild steel rebar, and nonshrink or expansive concrete to strengthen the column plastic hinge region, relocating subsequent damage above the repaired section. This plastic hinge relocation is achieved by increasing the column cross-section. On the half-scale specimens tested in the current study the column was increased from a 21 in. octagonal section to a 30 in. diameter circular section over a column height of 18 in. The repair can be implemented rapidly and uses standard construction techniques and a small amount of readily available materials. The purpose of the repair is to restore the diminished load and displacement capacities of an earthquake damaged column, alleviating the need for bridge replacement.

Two precast concrete bridge column-to-footing assemblies connected using GSS have been tested to failure under quasi-static cyclic lateral loads and a constant axial load, simulating earthquake loading. These assemblies were then repaired using the repair method developed in this study and retested cyclically. The results of the tests for the repaired specimens were then evaluated and compared to the performance of their undamaged precast counterparts.

To aid in the design of both the undamaged and repaired specimens, conventional and nonlinear Strut-and-Tie Models (STM) were developed using generic modeling parameters. The conventional model uses the STM procedures outlined in ACI 318 (*5*) to predict the ultimate load capacity of the assembly being modeled. The nonlinear STM expands upon the conventional STM by using nonlinear material properties, which incorporate allowable strengths reflecting the effects of cyclic degradation, to predict the nonlinear force-displacement response envelope of an assembly that is subjected to lateral load reversals.

1.1 Literature review

The literature review for this research is separated into three parts: the cyclic performance of GSS connections, bridge column retrofit and repair, and STM analytical findings.

1.1.1 Cyclic performance of GSS connections

GSS have been used for bridge column connections in nonseismic regions in the past. Recently, research programs at the University of Utah (*2*), University of Nevada at Reno (*3*), and University of Bergamo (*4*) have begun to investigate the applicability of GSS connections is seismic regions. The findings from these research programs are showing acceptable levels of cyclic performance for the GSS connections. However, the precast specimens do not match the performance of their monolithic counterparts in terms of displacement ductility and energy dissipation. The specimens that are referred to as the "as-built" specimens in this study are the precast concrete column-to-footing GSS specimens being studied at the University of Utah (*2*).

1.1.2 Bridge column retrofit and repair

Extensive research has been conducted on retrofit and repair techniques for bridge columns utilizing CFRP composites (*6, 7*), steel *(8),* and concrete jacketing *(9)*. The objective of these studies was to increase the flexural performance of the column plastic hinge region through jacketing. Recently, a precast concrete specimen connected using GSS was repaired after being tested cyclically (*4*). The repair consisted of a grout jacket made from high-strength shrinkage-compensating grout. The exact details of the retrofit are not known, but the results were unsatisfactory in terms of displacement ductility and energy dissipation capacity.

Little research has been conducted that investigates plastic hinge relocation as a method to control the location of damage or to restore diminished load and displacement capacities of earthquake-damaged bridge columns. Hose et al. *(10)* studied the effectiveness of strengthening likely plastic hinge regions to force damage away from joint regions. The plastic hinge regions were successfully relocated by increasing the longitudinal and transverse reinforcement ratios in the traditional plastic hinge regions. Lehman et al. studied multiple concrete jacketing techniques, including techniques to relocate the original plastic hinge, on columns of varying damage states *(9)*. One repair, performed on a column with fractured longitudinal rebar, increased the original column cross-section from a 24 in. to 30 in. diameter cross-section over a column length of 22 in. The increased cross-section was reinforced with double headed rebar in

the longitudinal direction and a spiral at a 1.5 in. pitch in the transverse direction. The intent of the repair was to relocate the plastic hinge region to the top of the repaired section. The repair was successful but did not restore the diminished displacement capacity of the specimen. Recently, Rutledge et al. have used CFRP oriented in the longitudinal and transverse directions to perform plastic hinge relocation on earthquake-damaged monolithic column-to-footing specimens *(11)*. The damage state of the specimens prior to repair was severe, including longitudinal rebar that had buckled or fractured. Three tests were performed on the repaired specimens; plastic hinge relocation was achieved for specimens which had buckled rebar. However, the repair proved incapable of restoring the diminished load and displacement capacities if the longitudinal rebar had fractured prior to the repair.

1.1.3 Strut-and-tie models

Strut-and-Tie Modeling (STM) is an accepted and well documented approach for analysis of reinforced concrete elements with disturbed-regions (D-regions). National bridge and building codes *(5, 12*) have adopted STMs as an applicable analysis procedure for D-regions. The STM design method prescribed in ACI 318 (*5*) is referred to as the conventional STM method within this study. The use of conventional STMs to design members that utilize CFRP has recently been investigated for shear transfer across precast concrete joints *(13)* and deep beams strengthened with CFRP *(14)*. Additionally, the development of headed rebar has been modeled for exterior beam-column joints using a conventional STM *(15)*.

Recently, To et al. (*16–18*) have added modeling parameters that expanded upon the conventional STM to predict the force-displacement response envelopes of a specimen, referred to as nonlinear STMs. The modeling parameters that are needed to shift from the conventional STM to the nonlinear STM are the material force-displacement properties and the STM member areas. To et al. *(16)* describe methods to determine both of these parameters, including the effect that cyclic degradation plays on the material properties. The nonlinear STM has been further expanded to predict the hysteretic response and failure mode of structural systems using nonlinear STMs *(19, 20)*.

1.2 Overview of tests

The focus of this study is the development of a repair procedure for earthquake-damaged modern bridge column-to-footing specimens connected using GSS couplers. In order to design and test the repaired specimen, a damaged specimen must first be created, and the damage state must be assessed. Two tests were performed on undamaged precast column-to-footing specimens connected using GSS, referred to as the as-built specimens. After testing and assessing the performance of the as-built specimens, a repair procedure was developed and implemented for both damaged specimens. The repaired assemblies were then retested following the same procedures as the as-built specimens. After the completion of the repair for the as-built specimens, the assemblies are referred to as the repaired specimens.

The column-to-footing specimens were tested in single curvature, replicating an idealized subsection of a multicolumn bridge subassembly that is subjected to double curvature. The bridge subsection that is being tested is the column-to-footing portion of the bridge subassembly from the point of inflection down, as shown in Figure 1.1. The specimens were designed to be half-scale of typical bridge elements in Utah. The soil-structure interaction at the footing-soil interface was neglected and the footing was secured to a rigid strong floor. All of the as-built and repaired specimens were tested laterally with a constant axial load of 6% of the column's 28-day concrete strength axial load capacity, representing typical axial loading of bridge structures. The lateral load was applied following a displacement controlled quasi-static cyclic loading protocol, which remained the same for all tests.

1.2.1 As-built tests

Two precast column-to-footing as-built specimens were constructed, instrumented, and tested in the University of Utah Structures Laboratory. The columns were 8.5 ft. tall and had a 21 in. wide octagonal cross-section. The footings were 6 ft. long, 3 ft. wide, and 2 ft. deep. Both as-built specimens were precast as two separate pieces, a column and a footing, and later connected using GSS couplers. The first as-built specimen to be tested, NMB-2, was built with the GSS located in the footing, and the second as-built specimen to be tested, NMB-3, was built

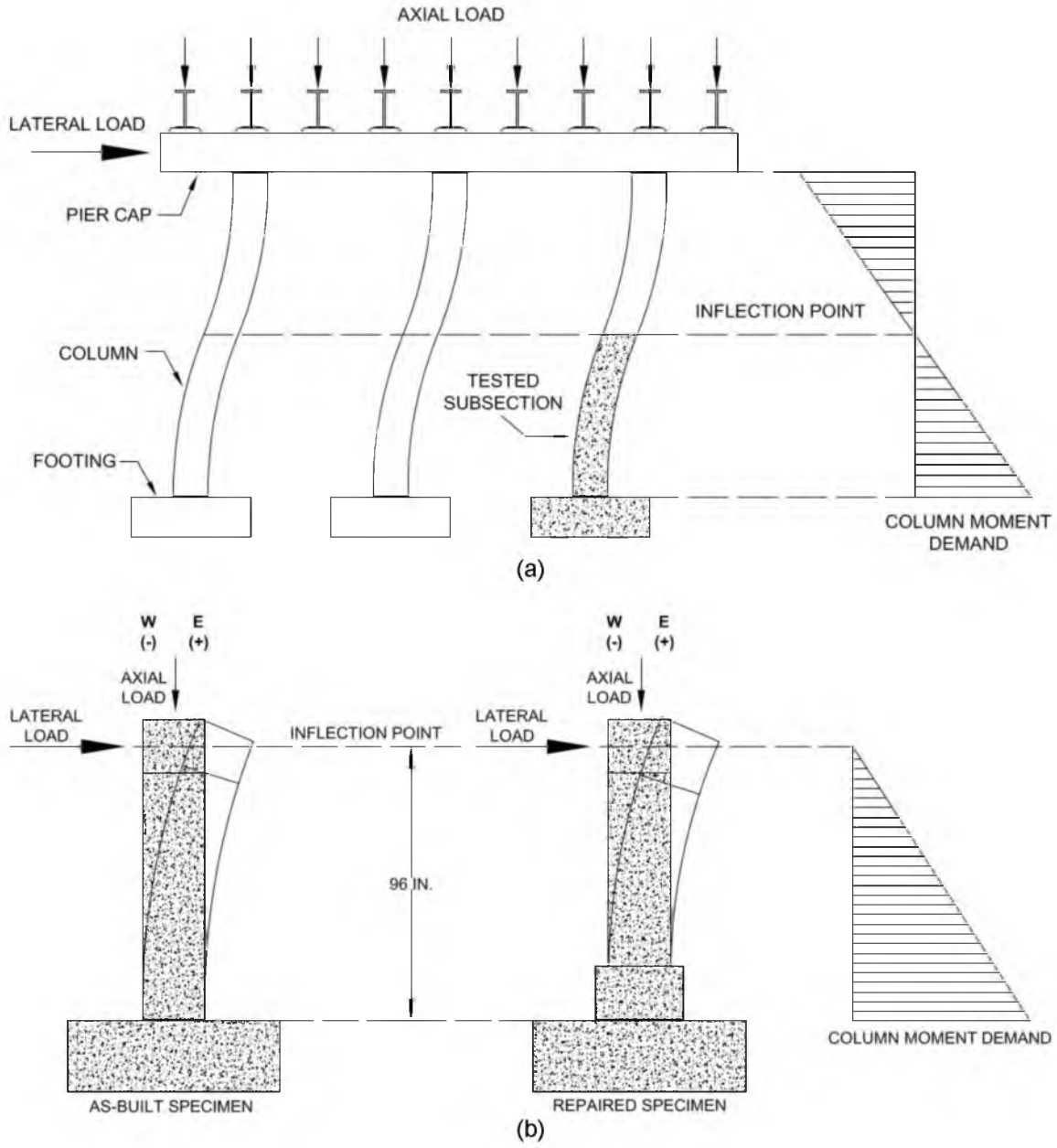

Figure 1.1 – Test explanation: (a) Idealized bridge subassembly subjected double curvature, (b) Tested subsection of bridge subassembly

with the GSS located in the column. The footing bars in NMB-3, which were left extending out of the concrete to grout with the GSS, were debonded for 8 in. below the footing concrete surface. The column and footing of both specimens were designed adhering to current seismic bridge design standards *(21)*.

1.2.2 Repaired tests

After testing the as-built specimens, they were evaluated in terms of their damage state, and a repair procedure was developed to restore their diminished performance. Both as-built specimens experienced flexural failure, with plastic hinging occurring in the column and footing at the column-footing interface. Longitudinal rebar fracture occurred in the plastic hinge region of both as-built specimens. The repair designed for NMB-2 and NMB-3 was identical due to their similarities in reinforcement, geometry, and damage states prior to repair. The plastic hinge region from the as-built test was repaired by increasing the column cross-section from a 21-in. octagonal section to a 30-in. diameter circular section over an 18 in. length. The 30-in. diameter circular cross-section was constructed using prefabricated CFRP shells. Headed mild steel bars were epoxy-anchored into the footing within the CFRP shell, and nonshrink or expansive concrete was used to fill the void between the original column and CFRP shell. The repair was designed to relocate the plastic hinge to the column section adjacent to the repaired section, which remained relatively undamaged during the as-built test.

After the repair procedure was complete for NMB-2 and NMB-3, they were renamed NMB-2 Repair and NMB-3 Repair, respectively. Both NMB-2 Repair and NMB-3 Repair were tested with the same axial load and lateral loading protocol as their as-built counterpart. The load, displacement, and instrumentation results were then analyzed and compared with the as-built results to determine the effectiveness of the repair.

1.3 Overview of strut-and-tie modeling

Strut-and-Tie Models (STM) were developed for the as-built and repaired specimens. STM are commonly used models to design reinforce concrete elements within D-regions of

structures. The purpose of the models was to develop STM procedures that could be used by designers with varying needs. To accomplish this, generic modeling parameters were developed that could be implemented on different reinforcement layouts and element geometries. Two types of STM were developed for the as-built and repaired specimens: a conventional STM and a nonlinear STM. The specimens modeled were NMB-2, NMB-2 Repair, LEN-2, and LEN-2 Repair. LEN-2 is a precast column-to-pier cap specimen connected using a different type of GSS than NMB-2. LEN-2 Repair is the repair of LEN-2 after the as-built test. LEN-2 Repair was repaired following the same procedure as NMB-2 Repair and NMB-3 Repair.

1.3.1 Conventional STM

The conventional STM method was developed following the modeling procedures outlined in ACI 318 (*5*). The model provides the designer with an estimate of the ultimate lateral load carrying capacity of the assembly. However, the STM procedure within ACI 318 is not intended to be used to analyze elements within a lateral-force resisting system. In addition, the parameters needed to predict the displacement response are generally neglected, leaving only a prediction of the force response.

1.3.2 Nonlinear STM

The nonlinear STM has been developed to provide the designer with an estimate of the force-displacement response envelope of the assembly being modeled. From the nonlinear STM response envelope the ultimate load and displacement can be predicted as well as the yield displacement, displacement ductility, and stiffness. Modeling recommendations given by To et al. (*15–17*) have been adopted in this study.

To obtain displacements from an STM model, the member areas and material properties must be known. To accurately predict the response of a specimen which is undergoing cyclic load reversals, material properties that account for the cyclic degradation of the materials must be used. Also, nonlinear steel reinforcement and CFRP confined concrete models have been used

to accurately obtain displacements from the model. Member areas that represent the state of stress at first yield have been adopted.

CHAPTER 2

EXPERIMENTAL SETUP AND RESULTS FOR AS-BUILT SPECIMENS

The specimens referred to as "as-built" are the precast concrete column-to-footing specimens prior to the repair. After cyclically testing the as-built specimens, they were repaired and retested. The details of two as-built specimens will be discussed in this section, NMB-2 and NMB-3 (*2*).

2.1 As-built specimen details

Both NMB-2 and NMB-3 are precast reinforced concrete specimens. The specimens were precast as two separate elements, a column and a footing, and later attached using Grouted Splice Sleeve (GSS) connections. The GSS connections used were NMB splice sleeves, size 8U-X, as shown in Figure 2.1. NMB-2 had the GSS connectors precast into the footing, and NMB-3 had the GSS connectors precast into the column, as seen in Figure 2.2. The GSS connectors are precast into an element with rebar from the connecting element extending into the sleeve. Special care is taken to ensure that the sleeve remains void of concrete during casting. Upon assembly, rebar protruding from the concrete of the element without the GSS connectors are inserted into the sleeves. The bars that extend from the element cast without the GSS are referred to as field dowels. Both the field dowels and the bars cast into the GSS are grouted with a high strength nonshrink grout to complete the connection. This type of GSS connection uses grout to secure the rebar at both ends of the connection.

The reinforcing details of both the column and footing adhere to current bridge design specifications *(12, 21)*. The longitudinal and transverse reinforcement ratios in the column are

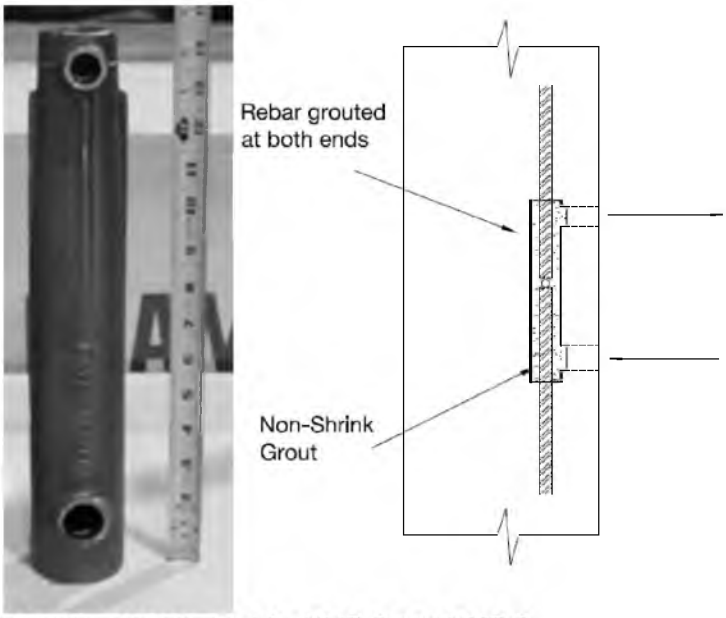

Figure 2.1 - Grouted splice sleeve used for NMB-2 and NMB-3

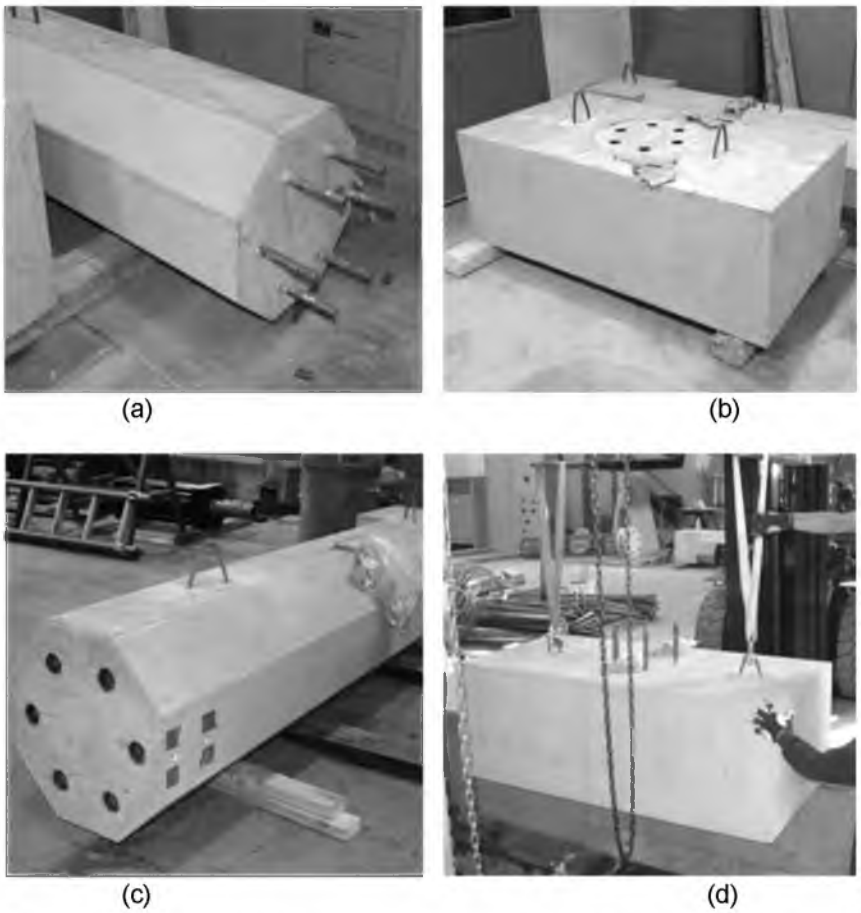

Figure 2.2 – Precast columns and footings prior to grouting: (a) NMB-2 column, (b) NMB-2 footing, (c) NMB-3 column, (d) NMB-3 footing

1.3% and 1.9%, respectively, conforming to both AASHTO and CALTRANS requirements (*1*). The column cross-section is nonprismatic with a 21-in. square top section extending 18 in. from the top of the column, changing to a 21-in. octagonal section for the rest of the column length. The square top was designed to easily connect with the lateral load application system. The octagonal column cross-section was used over the length being tested to match the current bridge geometry used by the Utah Department of Transportation. The octagonal cross-section is 7 ft. long and includes the probable plastic hinge region at the column-footing interface. The footing is 6 ft. long in the direction of the lateral load application, 3 ft. wide and 2 ft. deep. The sizes of the elements were designed to be approximately half-scale of typical bridge dimensions.

The reinforcement details for NMB-2 are shown in Figure 2.3. The column reinforcement consists of six no.8 longitudinal steel bars and a no.4 spiral at a pitch of 2.5 in. The NMB-2 footing reinforcement consists of 18 no.8 longitudinal steel bars, a no.4 joint spiral, and two overlapping no.4 stirrups spaced at 2.5 in. on center.

The reinforcement details for NMB-3 are shown in Figure 2.4. The column reinforcement consists of six no.8 longitudinal bars and two no.4 spirals at a pitch of 2.5 in. The additional spiral used in the column of NMB-3 is provided for shear reinforcement around the GSS connections. Two different spirals were required since the perimeter around the GSS is larger than the perimeter of the longitudinal reinforcement. The NMB-3 footing reinforcement consists of 18 no.8 longitudinal bars and two overlapping no.4 closed stirrups at 2.5 in. on center. The six no.8 field dowel bars were debonded in the footing just below the concrete surface for a length of 8 in., corresponding to 8 bar diameters. The debonding was implemented to postpone the longitudinal rebar from fracturing by increasing the strain capacity of the bars by distributing the plasticity over a greater length. Debonding was achieved by wrapping the bars with three layers of adhesive tape over the length in which debonding was desired.

Both the NMB-2 and NMB-3 rebar cages prior to concrete casting are shown in Figure 2.5. The all thread rods that are tack welded onto the longitudinal rebar of the column are used to connect instrumentation.

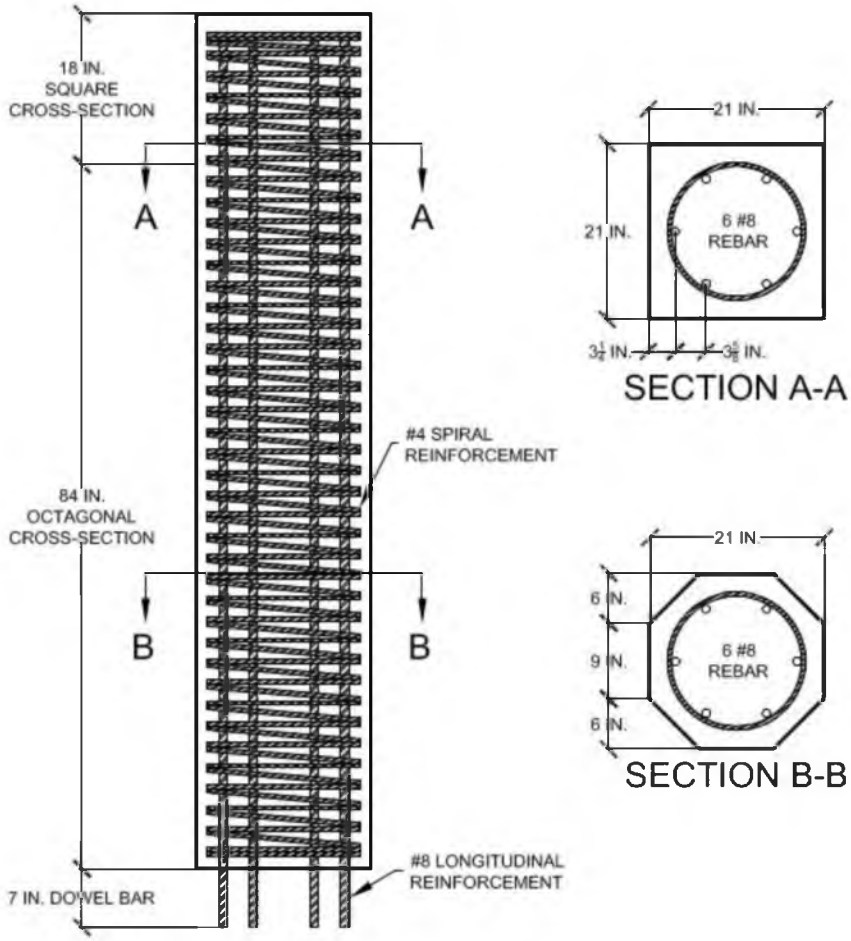

Figure 2.3 - NMB-2 reinforcement details

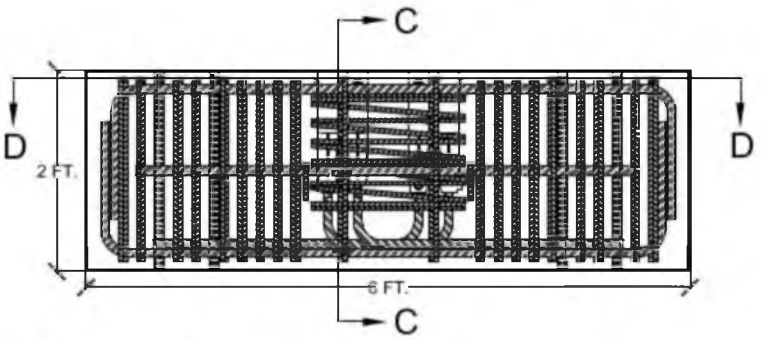

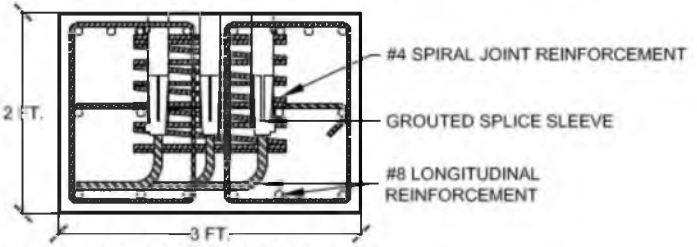

SECTION C-C

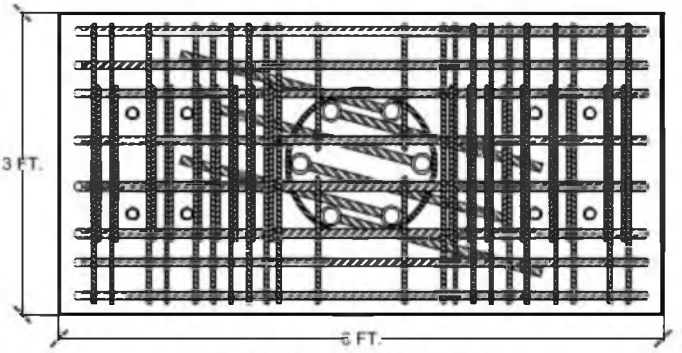

SECTION D-D

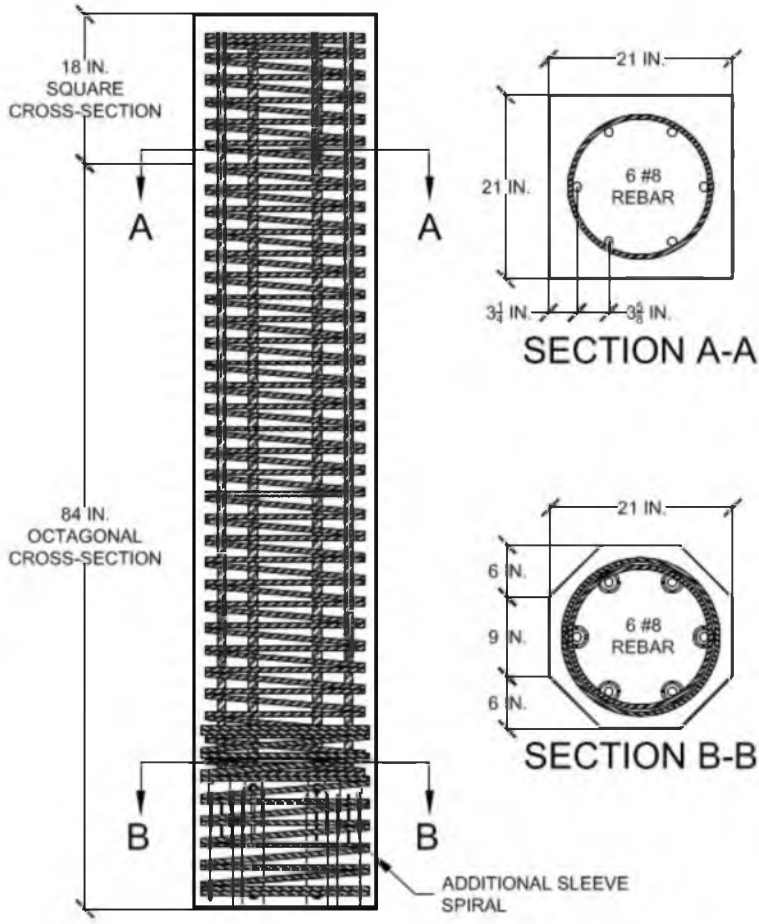

Figure 2.4 - NMB-3 reinforcement details

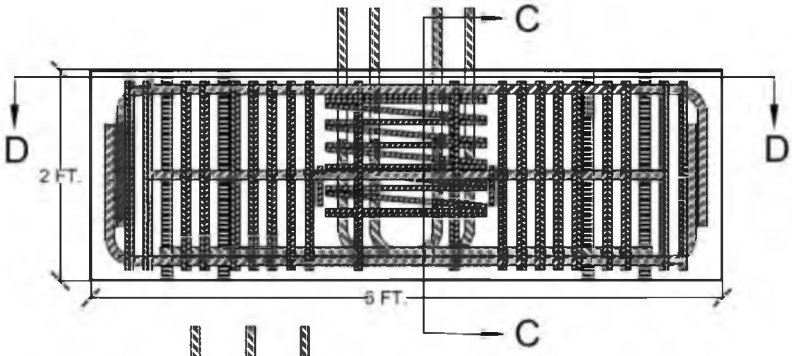

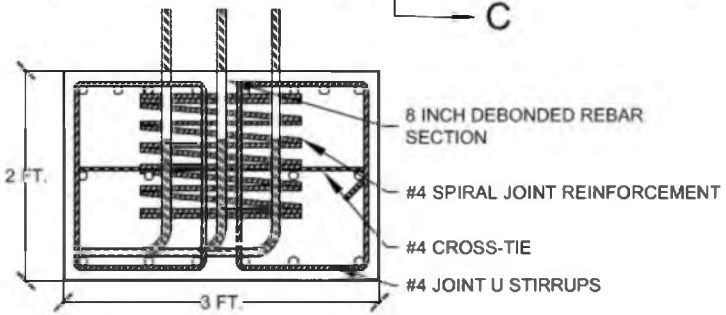

SECTION C-C

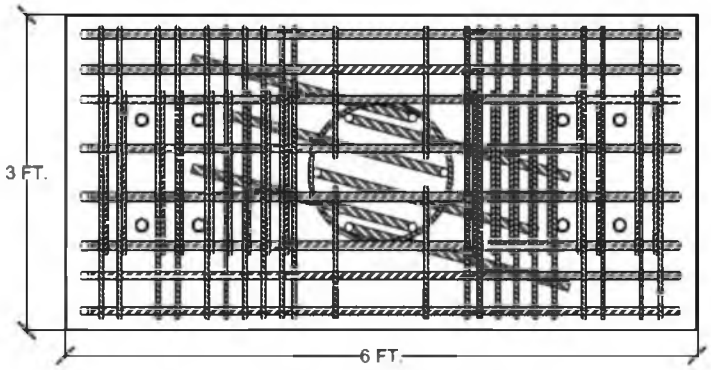

SECTION D-D

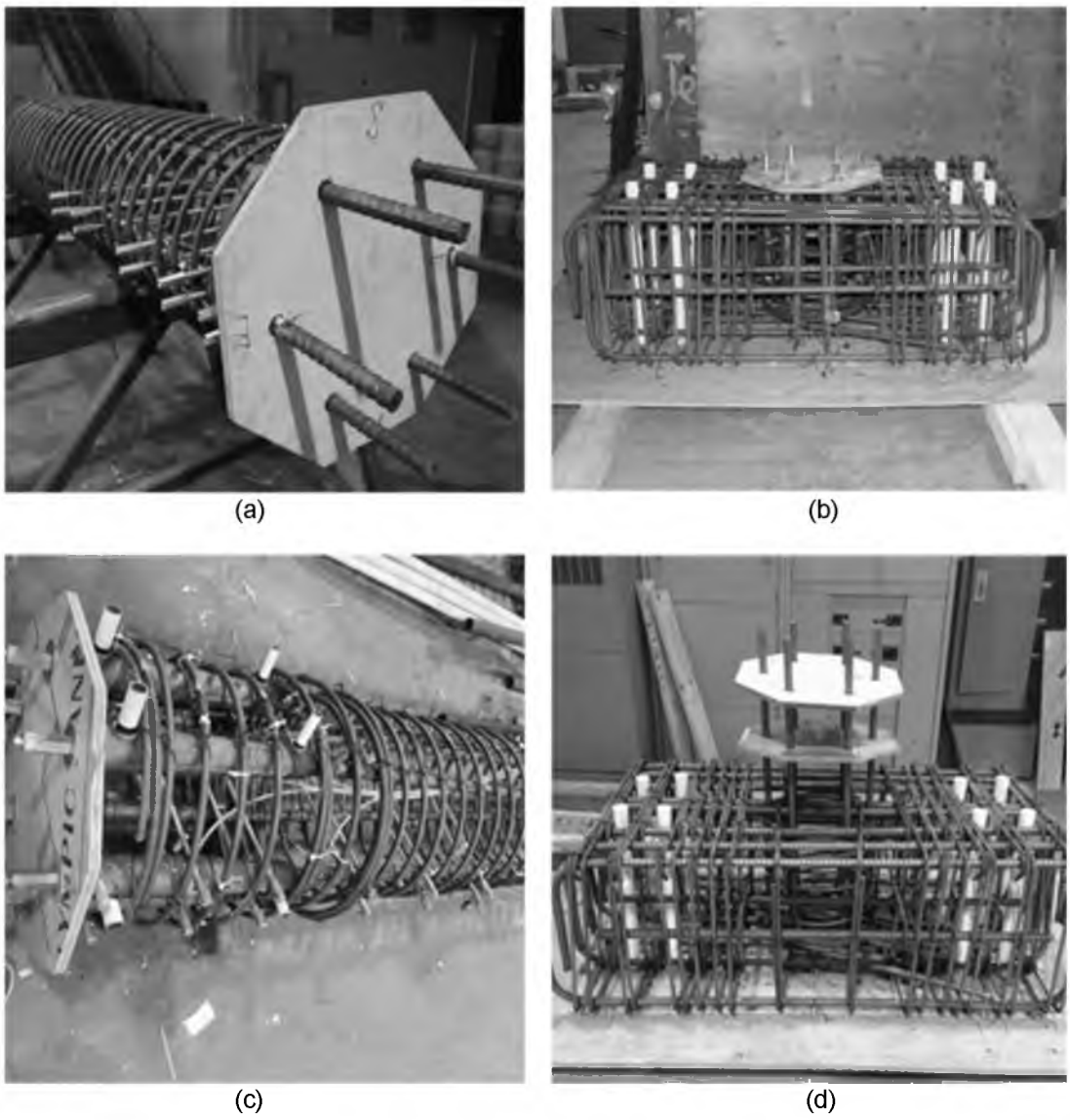

Figure 2.5 - Rebar cages: (a) NMB-2 column, (b) NMB-2 footing, (c) NMB-3 column, (d) NMB-3 footing

2.2 Test assembly

All of the as-built and repair tests were conducted in the University of Utah Structures Laboratory. The primary test components are the loading frame, the lateral load system and the axial load assembly which remained the same for all of the as-built and repair tests. The lateral load system relies on the loading frame to provide the necessary reaction to displace the specimen, while the axial load assembly is self-contained. These three experimental components create the boundary conditions for the tests and will be discussed in this section.

2.2.1 Loading frame details

The loading frame, also referred to as the structures bay, consists of steel W sections anchored into a strong floor, as shown in Figure 2.6. The lateral load system relies on the structures bay to provide an equivalent lateral reaction to balance the load needed to displace the test specimen. Since the loading protocol is displacement controlled, the deflection of the structures bay when providing the reaction to the lateral load system is critical. The structures bay was modified to minimize lateral deflection by increasing the stiffness of the girder used to attach the lateral actuator. The increase in stiffness was achieved by welding web stiffeners onto the girder on either side of the actuator, welding a steel W section on its side to the back of the girder, and by welding steel HSS tubing from the additional W section to another member of the structures bay, shown in Figure 2.6.

Another function of the loading frame is to provide the necessary reactions for the test specimens. These reactions were achieved by anchoring the specimens to the strong floor with high strength, 150 ksi, threaded steel rods. Each end of the footing was connected with eight high strength rods, four of which ran through PVC pipes embedded into the concrete and four of which were outside the concrete. These rods were then tensioned prior to testing to prevent the specimens from rocking or slipping on the strong floor.

2.2.2 Lateral load application system

The lateral load is applied to the test specimens 96 in. above the top of the footing. This point represents the theoretical inflection point of a bridge column that is subjected to double curvature. Double curvature is present in bridges between the pier cap and footing when subjected to earthquake loading. The lateral load system consists of an actuator, load cell, and spherical bearing connection, as shown in Figure 2.7. The actuator has a capacity of 120 kips and is servo-controlled. A pin connection secures the actuator to the stiffened loading frame girder. The actuator piston is threaded into a 200 kip load cell. This load cell then threads into a machined splice that attaches the test specimen to the load cell through a spherical bearing.

Figure 2.6 – Loading frame: (a) Entire frame, (b) Web stiffeners added on either side of lateral actuator, (c) Stiffened girder

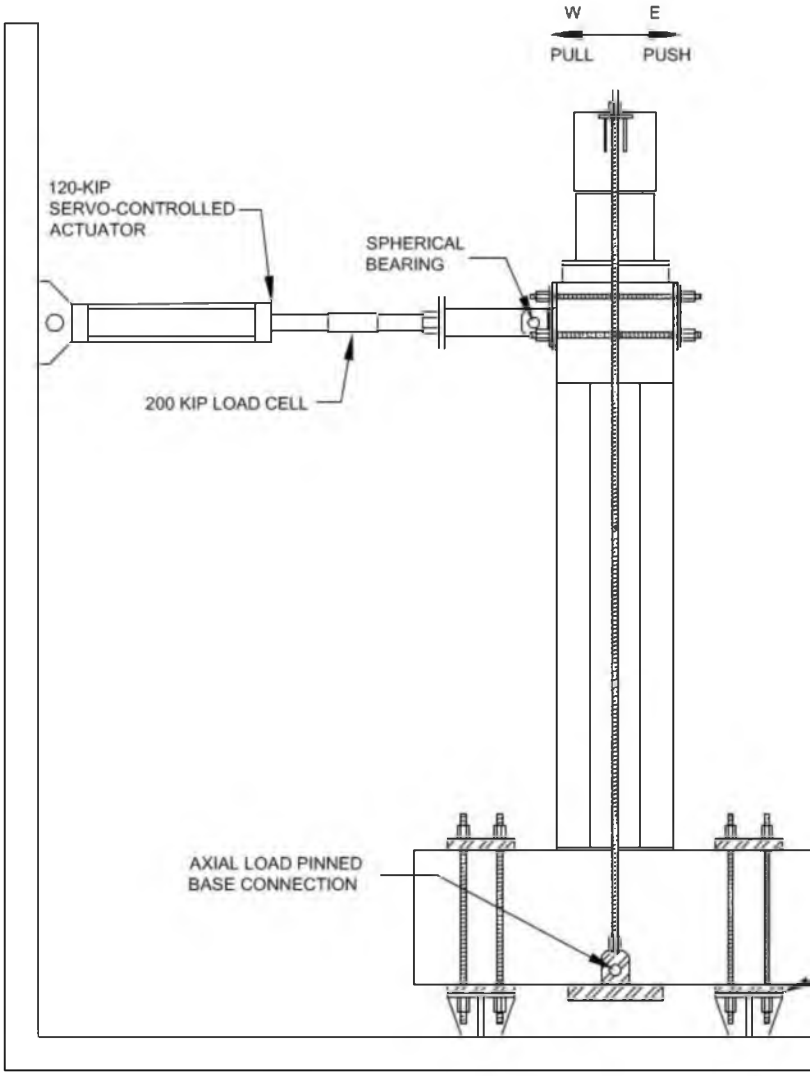

Figure 2.7 – Test assembly details

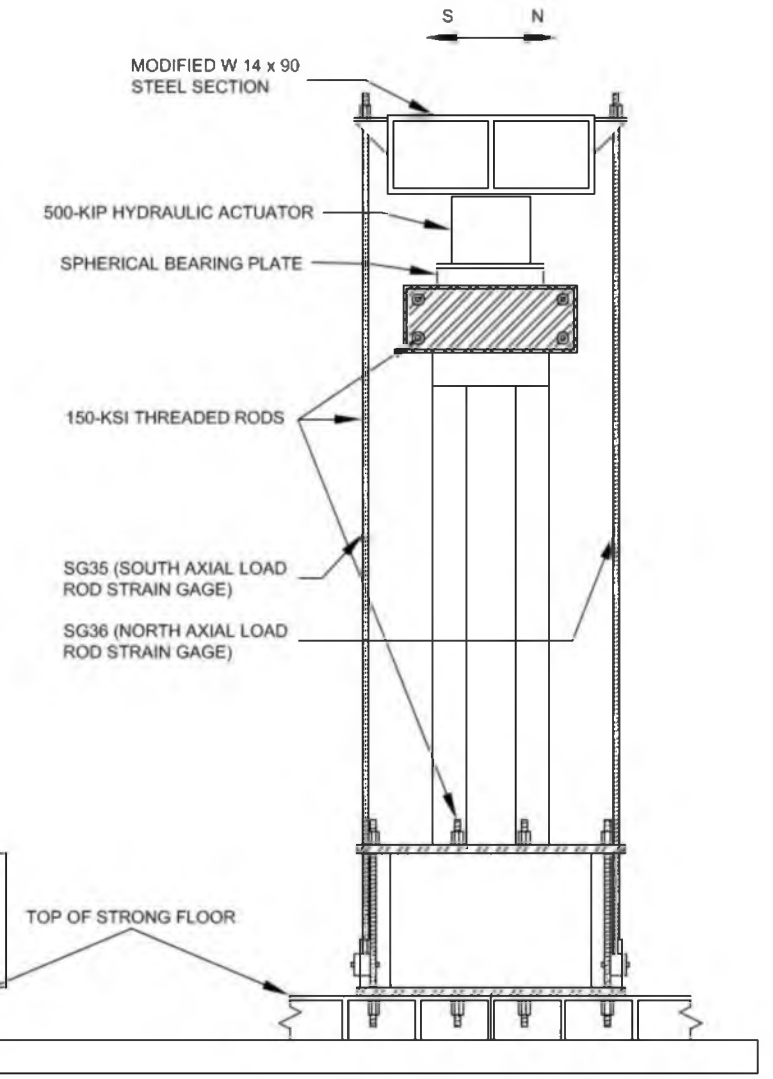
S
N
MODIFIED W 14 x 90
STEEL SECTION
500-KIP HYDRAULIC ACTUATOR
SPHERICAL BEARING PLATE
150-KSI THREADED RODS
SG35 (SOUTH AXIAL LOAD
ROD STRAIN GAGE)
SG36 (NORTH AXIAL LOAD
ROD STRAIN GAGE)
TOP OF STRONG FLOOR

2.2.3 Axial load assembly

The axial load apparatus does not rely on the loading frame. The axial load is self-contained within the specimen, where the reactions are provided from the top of the column and the bottom of the footing, shown in Figure 2.7. The 500 kip hydraulic axial actuator is located on top of the column and rests on a spherical bearing plate, which allows biaxial rotation. At the base of the footing there is a 10-in. wide by 3-in. thick plate that is pulled against the bottom of the footing by the axial load rods, which are tensioned by the actuator. The axial load rods, which connect the W-section on top of the axial actuator to the base plate, are pinned at the base plate to allow rotation of the rods while the assembly is displaced. It should be noted that NMB-2 Repair had the axial load apparatus as detailed in Figure 2.7 while NMB-3 Repair had additional pin connections where the high strength rods connect to the W-section. To achieve a constant axial load, curvature within the high-strength rods should be avoided, and is the reason for the additional pin connection.

2.3 Loading protocol

The applied loading during testing consisted of the axial and lateral loads. Both of these loading components have unique loading protocols. The loading protocol described in this section was used for all of the as-built and repair tests.

2.3.1 Axial load

The axial load applied during testing was designed to remain constant at 6% of the axial load capacity of the column. Typically bridge structures are subjected to small amounts of axial load in comparison to the column sizes that are provided; 6% of the gross column capacity is a reasonable estimate of typical bridge axial loading. The axial load applied during testing, P_{axial}, was calculated from eq. 2.1:

$$P_{axial} = 0.06 * A_g * f_c' \quad (2.1)$$

where A_g is the gross cross-sectional area of the octagonal column cross-section and f_c' is the 28-day cylinder compressive strength of the concrete. From eq. 2.1 the target axial load was determined, and the corresponding strain in the axial load rods needed to achieve P_{axial} was determined. There was slight deviation in the applied axial load and P_{axial} due to uneven straining of the axial load rods and the incremental increase in strain from the actuator. During testing it was observed that there was fluctuation in the axial load as the specimen was deflected in either direction. This variation in axial load was captured by the strain gauges located on the axial load rods. The variation in axial load was always an increase as the specimen was displaced. Since there was no load cell monitoring the axial load, the exact variation in axial load is not known; however, from the axial load rod strain gage data it appears that this variation is small.

2.3.2 Lateral load

All of the tests were conducted with a displacement controlled reversed quasi-static cyclic lateral loading protocol. The applied lateral loading displacement history used was the same for all tests so that the hysteretic behavior could be easily compared. The applied lateral displacement history can is shown in Figure 2.8. The first peak displacement used corresponds to half of the predicted yield displacement of the as-built specimens. Each subsequent peak displacement is an integer multiplier of the predicted yield displacement. Each peak displacement was carried out for two cycles where each cycle consisted of the peak displacement in both the positive and negative direction. The positive displacement, a displacement to the east, is applied before the negative displacement, a displacement to the west, during each cycle. A 5-minute pause was programed into the loading protocol between each displacement step to allow inspection of the test specimens. This applied lateral loading protocol follows the recommendations of ACI Committee 374 *(22)*.

2.4 As-built specimen test results

The as-built specimen tests were part of a separate research project, conducted at the University of Utah, which is looking into the seismic performance and applicability of GSS

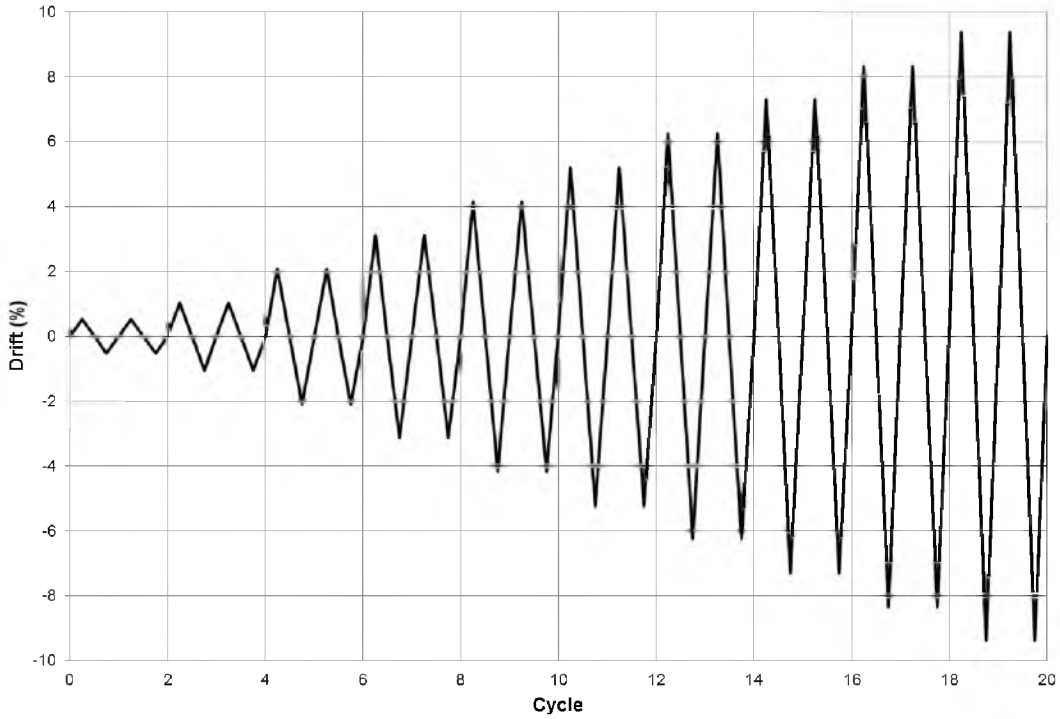

Figure 2.8 - Applied lateral displacement history

connections for bridges in seismic regions (*2*). However, to understand the results of the repaired specimens it is crucial to know both the performance and the final damage state of the as-built specimens.

2.4.1 NMB-2 results

On March 8th, 2013 NMB-2 was tested and brought to failure in the University of Utah Structures Laboratory. NMB-2 was a precast concrete column-to-footing assembly that had GSS located in the footing. Details pertaining to NMB-2 can be found in Section 2.1. The hysteretic response of the specimen is shown in Figure 2.9, and the damage state during the final displacement step, of 7 in., and after testing is shown in Figure 2.10. It can be seen from the hysteresis that the ultimate load achieved during testing was 38.8 kips. The failure mode of the specimen was crushing of the column concrete followed by longitudinal rebar facture. The east extreme longitudinal bar fractured during the first cycle of the 7-in. displacement step, approximately 3 in. above the top of the footing. The lateral load capacity in the west direction of testing was severely diminished when the east longitudinal rebar fractured. The lateral load

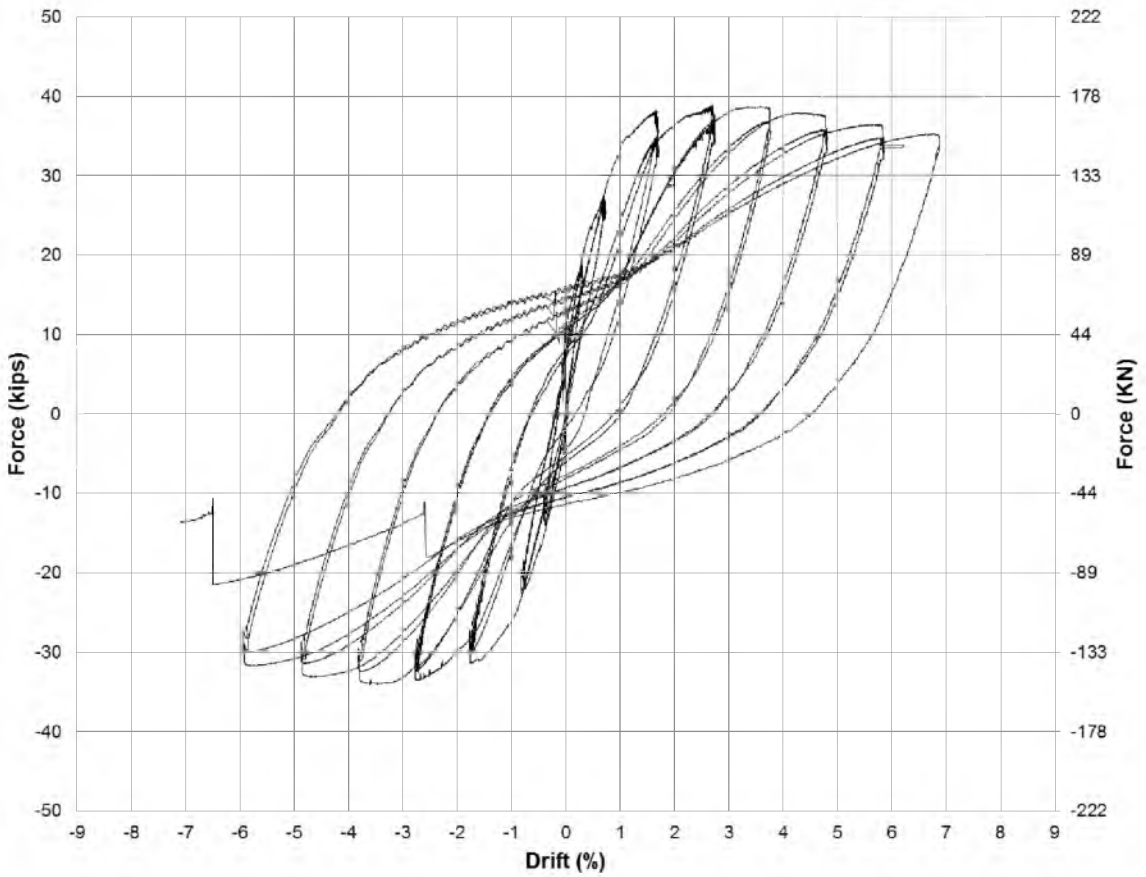

Figure 2.9 – NMB-2 hysteresis curve

capacity in the west direction, after the longitudinal rebar fractured, dropped to 65% of the ultimate lateral load capacity in that direction. The 7-in. displacement step was never completed due to a weld failing that secured the south axial load rod to the base plate of the axial load assembly.

A plastic hinge is evident at the column-footing interface of NMB-2, with spalling extending up the column 8 in.–12 in. on the west and east extreme column faces. Structural cracking of the column occurred at three levels located approximately 6 in., 10 in., and 14 in. above the footing. The maximum crack width at the 6 in., 10 in., and 14 in. levels during the pause between cycles was 0.050 in., 0.025 in., and 0.030 in., respectively. Cracking extended up the column higher than 14 in. but remained hairline in width throughout testing.

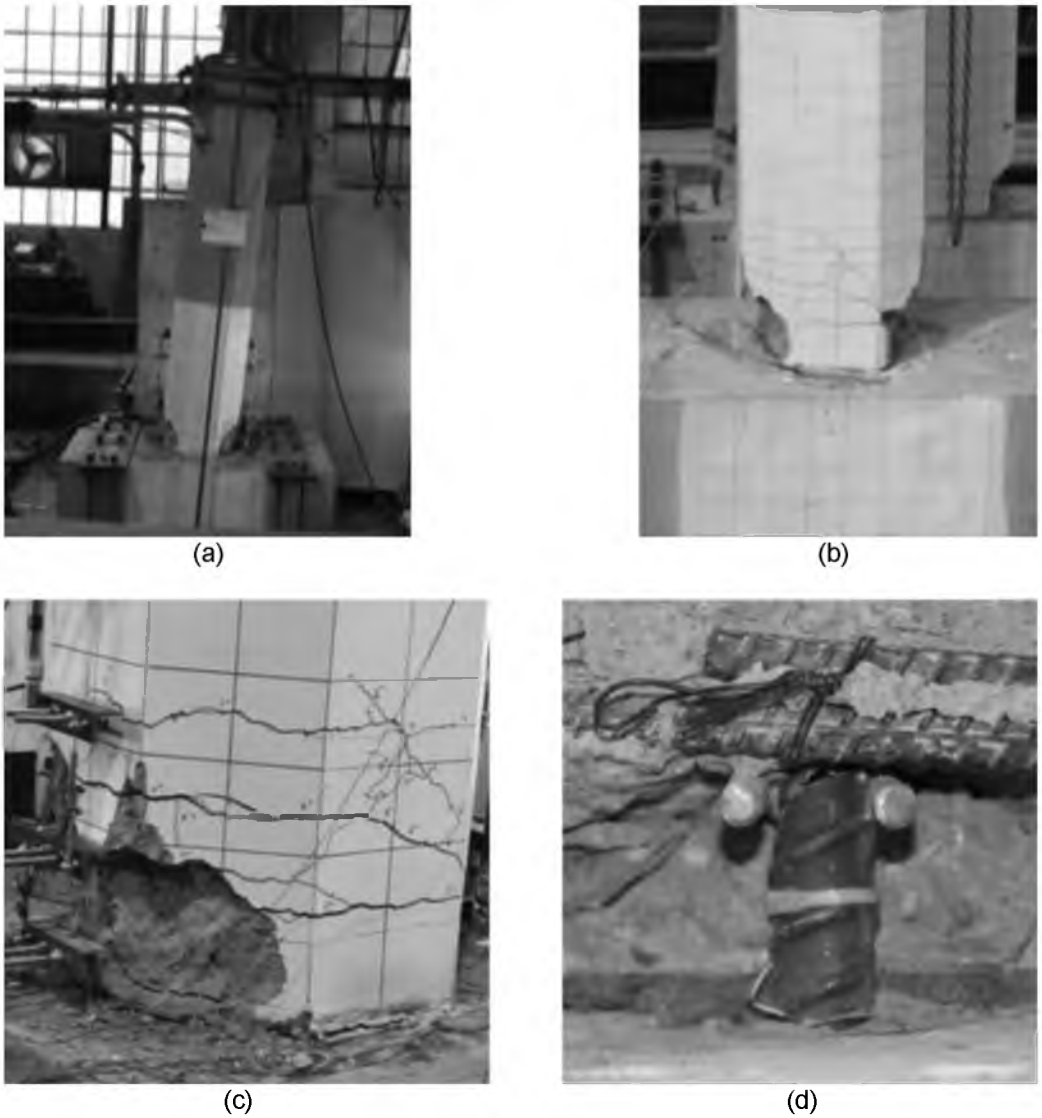

Figure 2.10 – NMB-2 damage state at final displacement step and after testing: (a) Ultimate displacement of 7 in., (b) Final column and footing cracking after testing, (c) Plastic hinge region, (d) Fractured east longitudinal rebar

2.4.2 NMB-3 results

On August 29th, 2013, NMB-3 was tested and brought to failure in the University of Utah Structures Laboratory. NMB-3 had GSS located in the column and had a debonded rebar in the footing. Details pertaining to NMB-3 can be found in Section 2.1. The hysteretic response of the specimen is shown in Figure 2.11. It can be seen from the hysteresis that the ultimate load achieved during testing was 42.0 kips. After the ultimate lateral load was achieved, during the 5-in. displacement step, the east extreme longitudinal rebar fractured during the 8-in. displacement

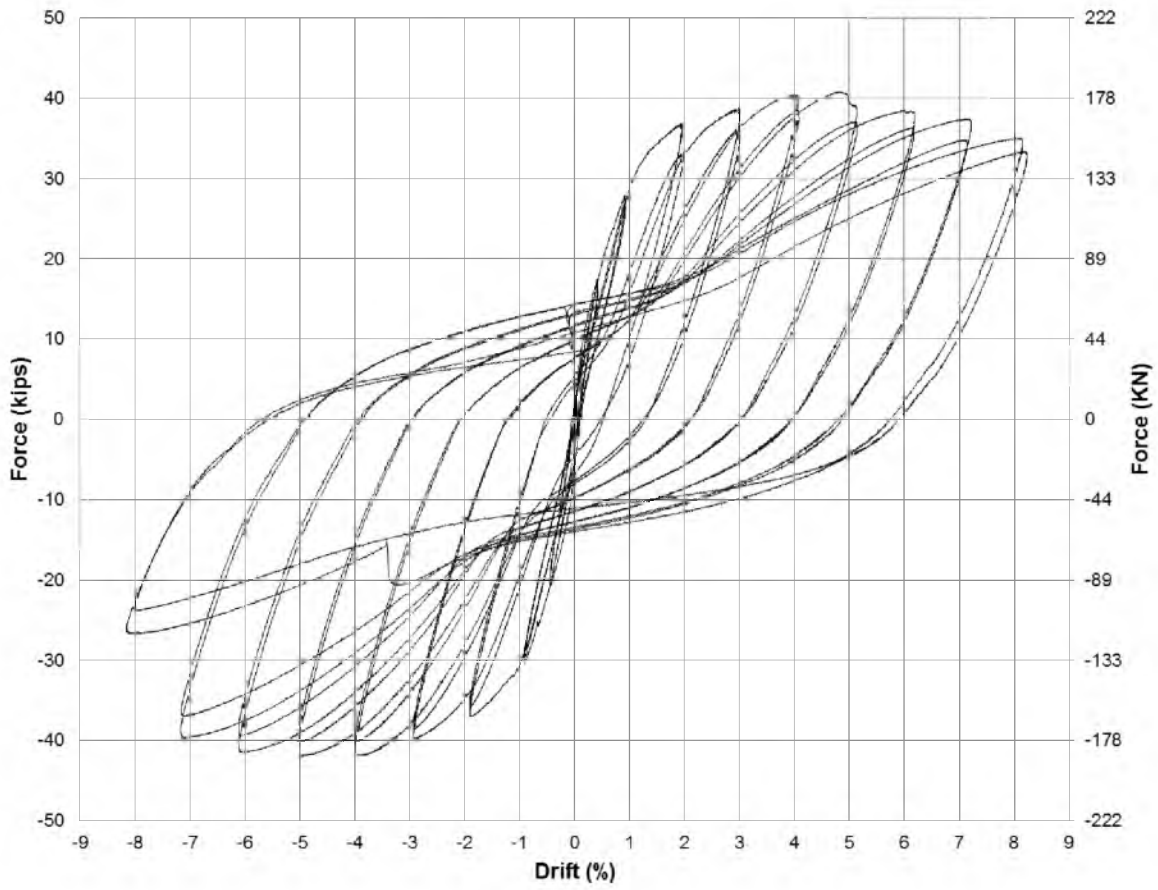

Figure 2.11 - NMB-3 hysteresis curve

step. The east extreme longitudinal rebar ruptured at the column-footing interface during the first cycle of the 8-in. displacement step. The lateral load capacity of the specimen when tested to the west was severely diminished after the longitudinal rebar fractured. The lateral load capacity in the west direction after the fracture dropped to 63% of the ultimate lateral load capacity. The damage state of NMB-3 during the final displacement step and after testing can be seen in Figure 2.12. A plastic hinge was evident at the column-footing interface with spalling extending up the column 12–16 in. on the west and east extreme column faces. However, there was noticeably less damage at the column-to-footing interface than during the NMB-2 test, indicating that the plasticity was forced into the footing due to the debonded bars. Structural cracking of the column occurred at two levels located approximately 14 in. and 23 in. above the footing. The maximum crack widths, measured during the pause between displacement steps, were 0.020 in. and 0.007 in. for the 14 in. and 23 in. crack levels, respectively.

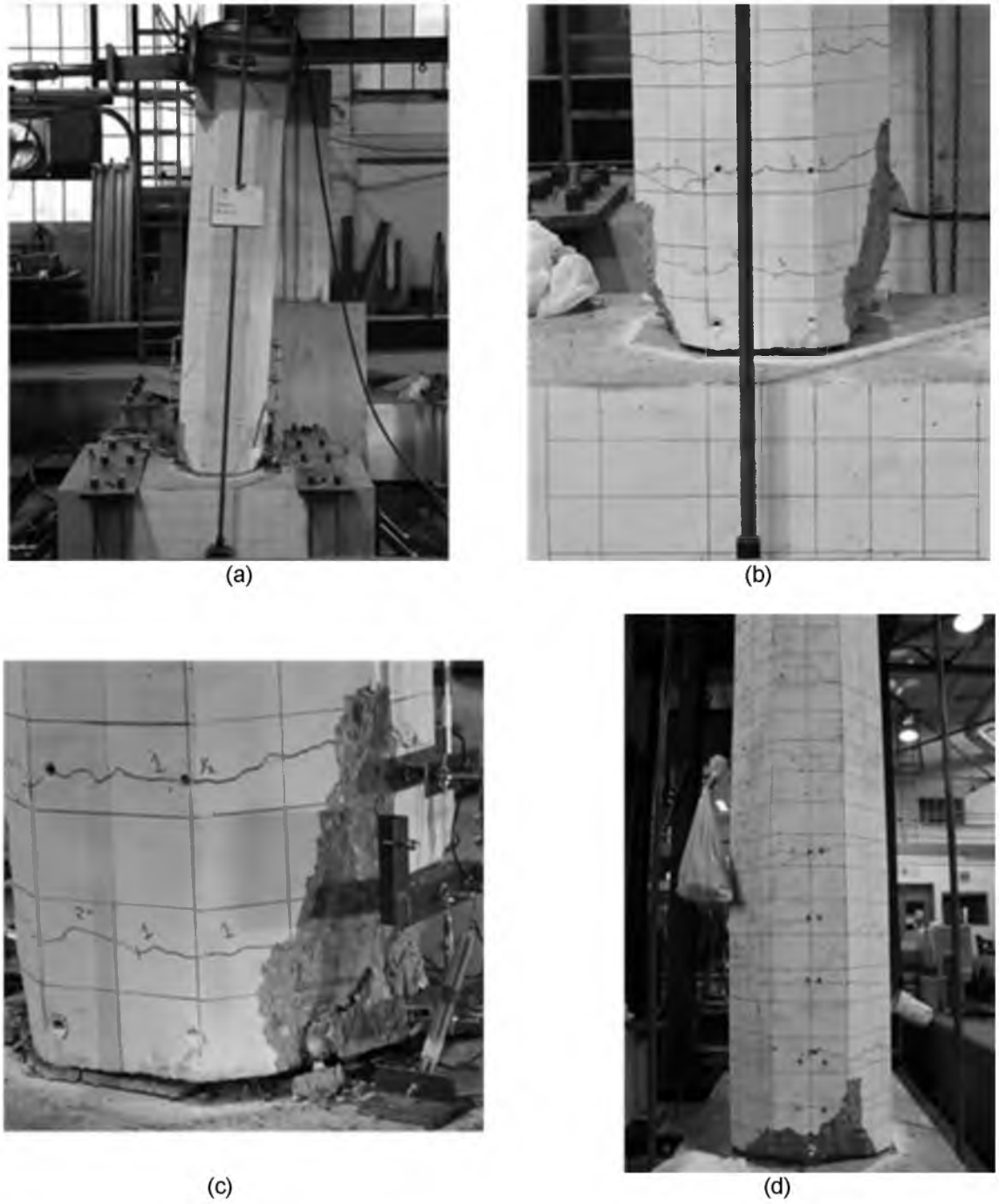

Figure 2.12 – NMB-3 damage state at final displacement step and after testing: (a) Ultimate displacement of 7 in., (b) Plastic hinge region after testing, (c) Gapping between the column and footing, characteristic of the rocking behavior, (d) Seven levels of concrete cracking

During testing, the specimen demonstrated rocking behavior in the joint region. The rocking is thought to be due to the GSS being located in the plastic hinge region of the column, which increased the stiffness of the region and forced the plasticity of the specimen into the footing where the debonded rebar were located. This characteristic led to smaller crack widths in the plastic hinge region. More layers of cracking were observed in NMB-3 than in NMB-2, but only two of the seven layers were larger that hairline.

CHAPTER 3

DESIGN, IMPLEMENTATION, AND EVALUATION METHODS FOR REPAIRED SPECIMENS

After testing NMB-2 and NMB-3, a repair strategy was developed to restore the diminished load capacity of the specimens. The same repair procedure was employed on both NMB-2 and NMB-3. Once repaired, NMB-2 and NMB-3 were renamed NMB-2 Repair and NMB-3 Repair respectively. Both NMB-2 and NMB-3 experienced longitudinal rebar fracture of the east extreme bar. The damage state of both NMB-2 and NMB-3 at the time of repair is described in Chapter 2. The process of repair consists of two parts, the design and the implementation. Both processes are critical to the success of the repair. This chapter outlines the design and construction of the repair as well as the instrumentation and performance evaluation criteria used to evaluate the repaired specimens.

3.1 Repair design

The objective of the repair is to reestablish the load and displacement capacity of a column-to-footing assembly by relocating the plastic hinge region from the column-footing interface to the column-repair interface. To achieve a successful repair, the original plastic hinge region must be strengthened sufficiently to withstand additional shear and moment demand that the plastic hinge relocation will produce. The bending moment that causes plastic hinge formation, M_{PH}, must be reached at the desired plastic hinge location, and a bending moment referred to as, M_{joint}, must be resisted at the column-footing interface. M_{PH} can be determined from a sectional analysis or from test results. From eq. 3.1 it can be seen that M_{Joint} is

proportional to the height of the repair, H_{repair}, and the height of the column from the point of inflection to the column-footing interface, H_{col}.

$$M_{joint} = \frac{M_{PH}}{(1 - \frac{H_{repair}}{H_{col}})} \quad (3.1)$$

Therefore, using the minimum possible repair height is advantageous for limiting the moment demand at the column-footing interface and for decreasing the rotational demand on the column for a given displacement. On the other hand, the height of the repair must be long enough to relocate the new plastic hinge to a minimally damaged cross-section. The ultimate moment demand and required moment capacity for an as-built and repair specimen is shown in Figure 3.1.

From M_{joint}, the shear that must be resisted in order to achieve plastic hinge relocation, V_{PHR}, can be found from eq. 3.2:

$$V_{PHR} = \frac{M_{joint}}{H_{col}} \quad (3.2)$$

Similar to moment demand, the shear demand is directly related to the height of the repair. This relationship can be seen by substituting eq. 3.2 into eq. 3.1, yielding eq. 3.3:

$$V_{PHR} = \frac{M_{PH}}{H_{col} - H_{repair}} \quad (3.3)$$

From both eq. 3.1 and 3.3 it can be seen that the repair height should be kept to a minimum to reduce the moment demand on the repair and the shear demand on the column. The shear capacity of the repaired cross-section will be much higher than the shear capacity of the as-built column. Since the shear demand is constant along the height of the column, it is likely that the shear capacity will be controlled by the as-built column shear capacity. Unless

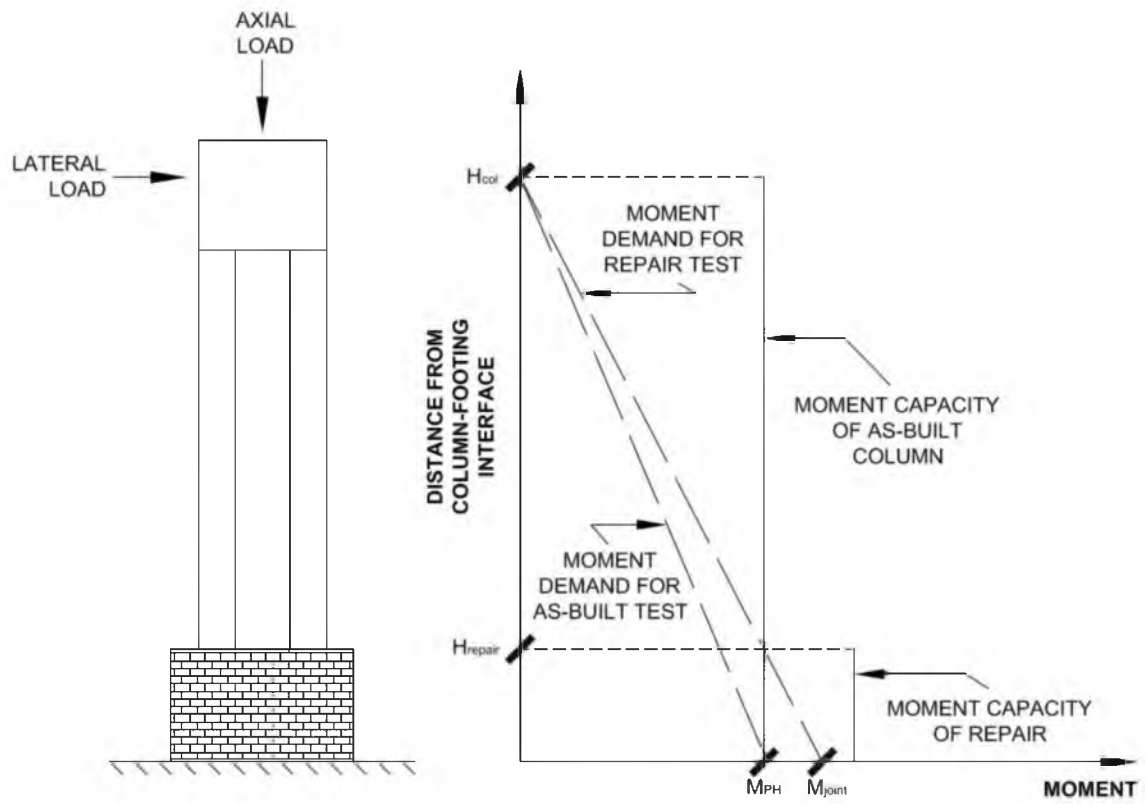

Figure 3.1 – Graphical representation of design loads for simplified design procedure

further research validates the use of external shear reinforcement above the repair, the shear capacity of the as-built column must be greater than V_{PHR}.

The height of the repair was designed to cover the plastic hinge length of the as-built specimen and to cover all of the structural cracking, larger than 0.1 in., while remaining as short as possible. This led to a nominal repair height of 18 in. The 18 in. nominal repair height, ranged from 19 in.–20 in. when the construction process was completed. This increase in height was due to the 0.5 in. gap that was intentionally left between the CFRP wrap and footing. This gap is provided to decrease the risk of the wrap bearing on the footing concrete. Also, additional height was produced from inaccuracies associated with the wet layup process for CFRP.

Once the height of the repair is determined, the loading associated with plastic hinge relocation, in terms of shear and moment, are established. The shear strength of the as-built column must be checked to make sure it can resist V_{PHR}. Additionally, since the repair is

developed for specimens with fractured or highly damaged longitudinal rebar, the tension transfer between the column and footing must be reestablished through the repair cross-section.

To achieve these design criteria, a repair was developed that increased the original plastic hinge region from a 21-in. octagonal cross-section to an additionally reinforced 30-in. diameter circular cross-section. Additional flexural reinforcement was provided in the form of headed rebar. The headed bars were designed to increase the flexural strength of the repair and reestablish the tension transfer between the column and footing. Additional shear reinforcement was provided in the form of a unidirectional CFRP wrap. The CFRP wrap was designed to provide shear strength and confinement to the repaired cross-section. The confinement that the CFRP provides increases the capacity of the repair significantly by increasing the compressive strength and strain capacity of the concrete within the repair.

The repair details are shown in Figure 3.2. There are three components for the repair that must be designed: the headed rebar, the CFRP wrap, and the nonshrink/expansive concrete. As usual with design, the different repair components are reliant upon one another, making the design process iterative.

3.1.1 Headed rebar design

The headed steel bars are designed to increase the moment capacity of the repaired cross-section to a value larger than M_{joint}. The contribution of the as-built longitudinal rebar can be conservatively ignored when determining the repaired cross-section moment capacity. This assumption should be made when longitudinal bars have fractured in the as-built column prior to repair. The moment capacity provided by the headed rebar is controlled by the area of steel that is provided and the moment arm of the steel.

Placement of the headed rebar fixes the moment arm of each rebar and should be determined from several design criteria. First, a clear spacing of 2 in. between the as-built column and the center of the headed rebar should be maintained to allow space for drilling into the footing. Space should also be provided between the headed rebar and the CFRP wrap to

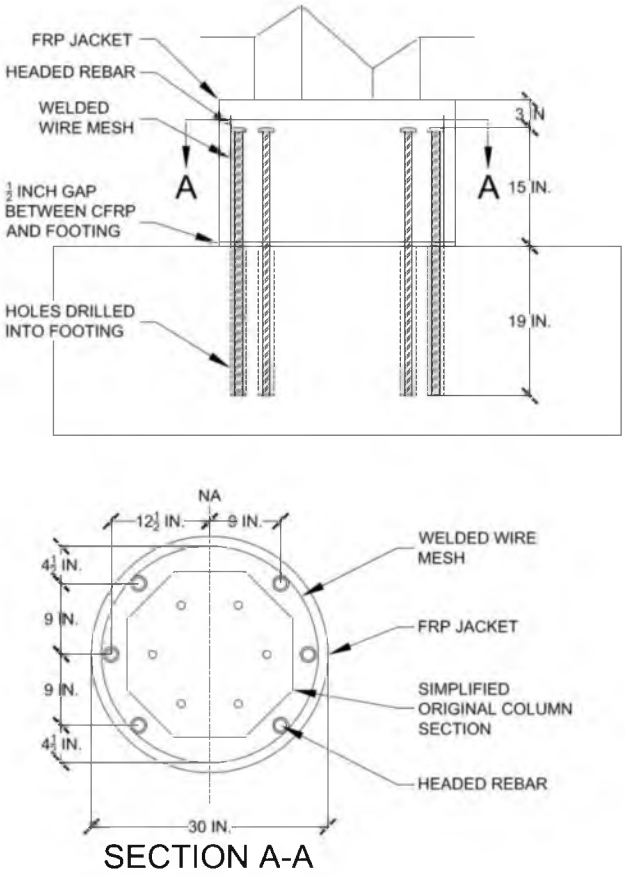

Figure 3.2 – Repair design details

allow proper bonding of the CFRP to the concrete and development of the headed rebar. Caution should be taken when the clear spacing between headed rebar is small due to the group effects that this creates. The headed rebar placement must minimize conflict with the longitudinal reinforcement in the footing, which can be achieved by using a metal rebar detector to find the longitudinal bars in the footing. Additionally, the smallest diameter possible for the CFRP wrap should be selected to facilitate an economical design and to minimize interference with surrounding objects when the repair is installed in the field. From these design criteria the placement of the headed rebar and the diameter of the CFRP jacket can be designed iteratively. In practice, the headed rebar should be distributed around the repair evenly since the direction of lateral loading is not known.

With an estimate of the number of headed bars and placement, the minimum amount of the headed bar area can be determined from eq. 3.4:

$$M_n = A_s * f_y * \left(d - \frac{A_s * f_y}{0.85 * f_c' * b_w}\right) > M_{joint} \quad (3.4)$$

where M_n is the nominal flexural capacity of the repaired section, neglecting compression steel and assuming zero axial load. Since the repair is built with the dead load applied to the bridge and the axial load transfer between the as-built column and the repair is not known, neglecting the axial load contribution to the moment strength of the repaired cross-section is appropriate: A_s is equal to the cross-sectional area of the headed rebar in tension, f_y is the nominal yield strength of the headed rebar, d is the distance from the centroid of the headed rebar to the natural axis, f_c' is the nominal compressive strength of the repair concrete, and b_w is the effective width of the repair. An appropriate margin of safety should be maintained between the flexural capacity of the section and the demand. These design equations lead to six no.8 grade 60 headed bars placed as shown in Figure 3.2, with three headed bars on each side of the repair.

The length of epoxy anchorage into the footing and the amount of embedment into the repair concrete must also be designed to provide proper development length. Since the repair procedure is for bridge columns that are exposed to corrosive environments a clear cover of 3 in. was provided between the top of the headed bars and the top of the repair concrete (*5*). This cover requirement left a development length of 15 in. for the headed rebar in the repair concrete. The required development length is determined from eq. 3.5 (*5*):

$$l_{dt} = \left(\frac{0.016 * \psi_e * f_y}{\sqrt{f_c'}}\right) * d_b > 8 * d_b \text{or } 6 \text{ in.} \quad (3.5)$$

where l_{dt} is the required development length for the headed rebar, ψ_e is equal to 1.0 for nonepoxy coated rebar, and d_b is the diameter of the headed rebar. For the no.8 rebar specified and a conservative f_c' of 4000 psi, the required development length is 12.0 in., which is less than the 15 in. provided. Therefore the design is adequate.

Similar to the development length of the rebar in the repair concrete, the headed rebar must develop in the epoxy anchorage within the footing. The required development length for the epoxy anchorage, l_d, is determined from eq. 3.6:

$$l_d = \frac{A_b * f_y}{d_b * \pi * \tau} \tag{3.6}$$

where A_b is the cross-sectional area of one headed bar and τ is equal to the specified bond strength of the epoxy used. The epoxy used for the repair was Hilti HIT-RE 500-SD epoxy which has a bond strength of 1400 psi *(23)*. Using no.8 headed rebar, the required development length is 12.2 in., which is less than the 19 in. provided. Therefore the design is sufficient.

3.1.2 Nonshrink/expansive concrete mix design

The concrete that filled the void between the as-built column and the CFRP wrap, referred to as repair concrete, was designed differently for NMB-2 Repair and NMB-3 Repair. This was the main design difference between the two repairs. The two different mix designs used for the repair concrete in NMB-2 Repair and NMB-3 Repair are shown in Table 3.1. The repair concrete that was used for NMB-2 Repair was designed as nonshrink concrete, whereas the repair concrete for NMB-3 Repair was designed as expansive concrete. The time dependent expansion results of the repair concrete for NMB-2 Repair and NMB-3 Repair can be found in Section 4.1. The amount of expansion is controlled by the ratio of Komponent cement to Portland Concrete Cement (PCC). Komponent is intended to produce nonshrink concrete when proportioned at 15% of the cementitious materials. The repair concrete in NMB-2 Repair and NMB-3 Repair had

Table 3.1 – Repair concrete mix design

	Cementitious materials			Water		Aggregates (lb/yd @ SSD)		Additives (oz/yd)	
	Komponent (lb/yd)	PCC (lb/yd)	Percent Komponent (%)	Cold water (lb/yd)	Water to cement ratio (%)	Point 3/4 in.	Point sand	Daravair (air entrainer)	Glenium 30-30 (super plastisizer)
NMB-2 Repair	92	599	13	280	41	1600	1060	6.5	49
NMB-3 Repair	262	370	41	280	44	1600	1060	6.5	49

Komponent percentages of 13% and 41% respectively. Previous research has shown that pre-tensioning CFRP wraps significantly increases the load bearing capacity of the specimen *(24, 25)*. However, caution should be taken to not overstrain the jacket when using expansive cementitious materials to provide active pressure *(26)*.

3.1.3 CFRP wrap design

The purpose of the CFRP jacket is to provide confinement and shear strength to the original plastic hinge region. Proper confinement increases both the strain capacity of the confined concrete and its compressive strength. Research has shown that a minimum jacket thickness and associated confinement are required to prevent strain softening of CFRP confined concrete *(27)*. Therefore, a jacket thickness was provided to ensure strain hardening of the concrete within the jacket. The jacket was also designed to withstand all of the shear demand, V_{PH}, over the length of the repair. Although the as-built column has sufficient shear capacity to resist V_{PH}, the original plastic hinge region needs shear strengthening due to concrete crushing and the spiral yielding during the initial test.

From previous research, the CFRP jacket thickness, $t_{j,\,sh}$, required to ensure strain hardening behavior of the confined concrete and provide proper confinement is determined by eq. 3.7 *(27)*:

$$t_{j,sh} = \left(\frac{f_{co}}{E_f}\right) * \left(\frac{H_c * \lambda_{SH}}{4 * C_{sh}}\right) \tag{3.7}$$

where f_{co} is the unconfined concrete compressive strength; E_f is the CFRP modulus of elasticity; H_c is the diameter of the CFRP jacket; λ_{SH} is a factor accounting for the aspect ratio of the CFRP section and is equal to 12 for circular cross-sections; and C_{sh} is the jacket confinement ratio coefficient, which is equal to 1.0 for circular cross-sections.

The CFRP jacket thickness required for shear strengthening of circular column sections in plastic hinge regions, $t_{j,\,v}$, was determined from eq. 3.8 (*6*):

$$t_{j,v} = \frac{\frac{V_{PH}}{\phi_v} - (V_c + V_s + V_p)}{\frac{\pi}{2} * 0.004 * E_f * H_c} \quad (3.8)$$

where V_{PH} is the column shear demand; Φ_v is the shear capacity reduction factor, which was taken as 0.85 (*6*); and $V_{c,}$, V_s, and V_p are the shear capacity contribution of the concrete, shear reinforcement, and axial load respectively. Due to the damage state of the original plastic hinge region, $V_{c,}$, V_s, and V_p can all conservatively be taken as zero.

An additive approach to find the total jacket thickness needed for the repair, $t_{j,\,total}$, is adopted by using eq. 3.9:

$$t_{j,\text{total}} = (t_{j,sh} + t_{j,v} + t_{j,shell}) \quad (3.9)$$

where $t_{j,\,shell}$ is an additional term for the CFRP shell required as formwork for the repair concrete. For NMB-2 Repair and NMB-3 Repair, two layers of CFRP were provided to prevent strain softening and provide confinement, one layer was provided for shear strength, and one layer was provided as a shell for the repair concrete. The shell layer was used as a construction aid to maintain the circular cross-sectional shape. Each CFRP layer has a nominal thickness of 0.04 in.

3.2 Repair procedure

The first step in the repair procedure was creating the CFRP wrap. The CFRP wrap was created from unidirectional SikaWrap Hex 103C fibers oriented in the hoop direction and Sikadur Hex 300 Epoxy. The impregnation process was done by hand using a paint roller and abrasive metal roller. Once saturated, the excess resin was scraped off of the CFRP using a rubber tool.

To create the prefabricated CFRP shells, used as stay-in-place formwork for the repair concrete, a single layer of 18-in. wide CFRP was wrapped and cured around a 30-in. diameter circular sonotube. After the CFRP shells had cured, they were cut into two half cylinders and brought around the column. Although it would have been possible to bring the cylindrical shell over the top of the column as one piece, the shell was cut in two to simulate the way this

procedure would be executed in the field. Once the shell was around the column, it was spliced with a 12-in. long piece of CFRP for the height of the repaired column. The 12-in. splice length was determined to provide proper development of the fibers on either side of the splice. Once the splice was laid up, three additional 100-in. long layers of CFRP composite were wrapped around the shell. The length of 100 in. was used to provide an overlap of over 5 in. for each layer. Special care was taken to alternate the locations of the CFRP shell splice and for each additional layer. The sonotube was left inside the CFRP shell to provide rigidity while the additional layers of CFRP were applied; it was removed once all CFRP layers had cured. Figure 3.3 shows the steps involved in preparing the CFRP shell.

While the CFRP shells were curing, the holes for the postinstalled headed bars were core-drilled into the footing by Penhall Company. The holes were 1.25 in. in diameter, which provided a radial clearance of 0.125 in. between the headed rebar and the hole. Upon completion of drilling, the holes were prepared for the epoxy by cleaning and drying them. Subsequently, Hility HIT-RE 500-SD epoxy was injected into the hole using a Hilti dispenser to avoid the formation of air voids. The headed bars were inserted into the holes, and excess epoxy was forced out of the top of the hole, indicating that a proper amount of epoxy was used. Figure 3.4 shows the steps involved in preparing the headed rebar.

Once the CFRP shell and epoxy for the headed rebar had fully cured, nonshrink/ expansive concrete was added to the space between the column and CFRP shell. The concrete was vibrated to minimize the amount of air voids left within the repair concrete. A 0.5-in. tall cylindrical piece of sonotube was secured under the CFRP shell to maintain the 0.5-in. gap between the CFRP shell and the footing. The piece of sonotube also ensured that the CFRP shell remained centered around the column. Wooden formwork was placed on the top of the CFRP shell to enclose the concrete within the repair. Weights were then placed on top of the formwork to keep the concrete from expanding vertically. The repair concrete was cured for at least 28 days before testing. Figure 3.5 shows the steps involved in casting the concrete for the repair process.

Figure 3.3 – CFRP preparation: (a) Saturation, (b) Making of prefabricated shells, (c) Prefabricated shells split into two, (d) Wet layup

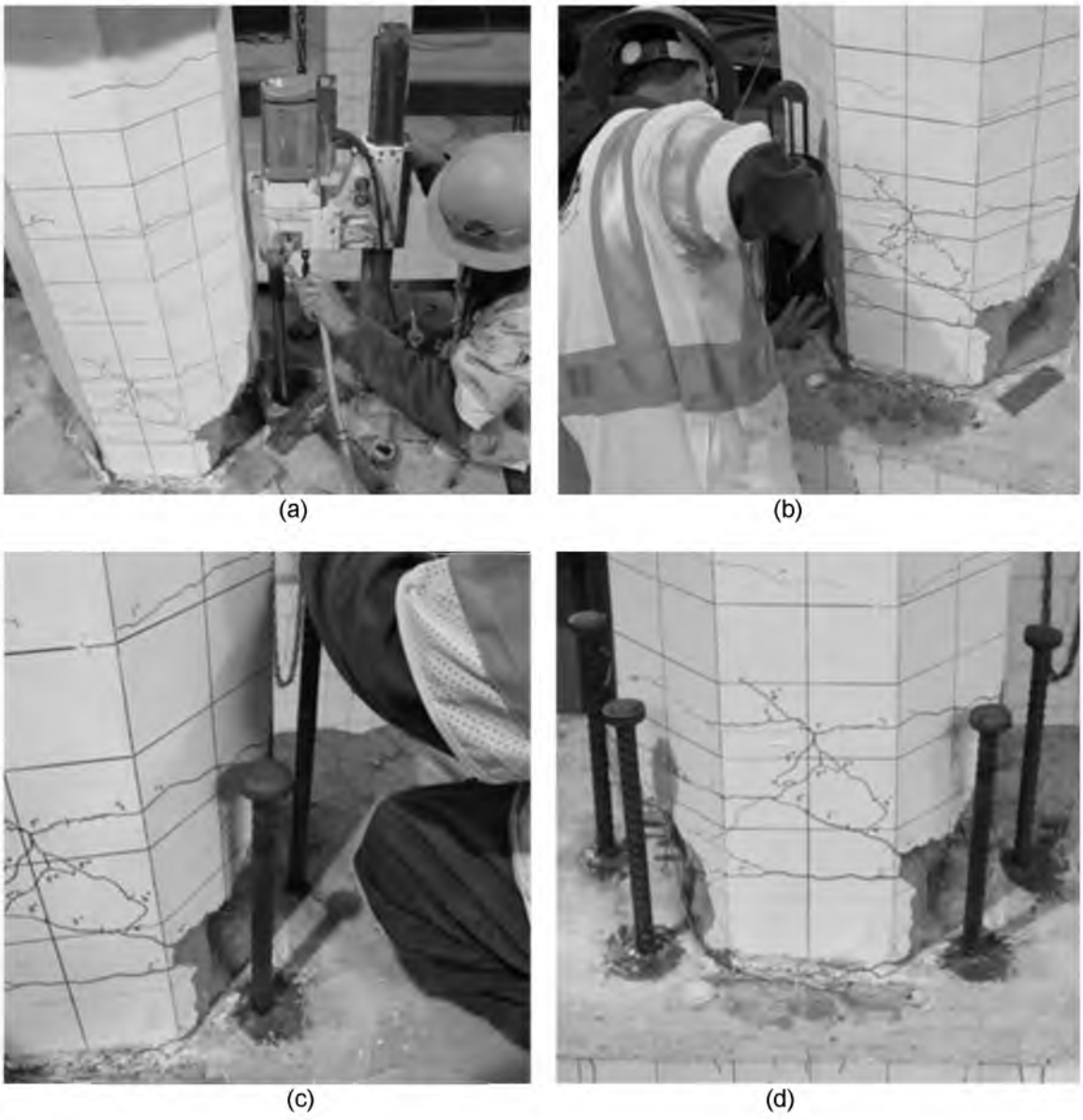

Figure 3.4 – Headed rebar installation: (a) Core drilling, (b) Epoxy injection, (c) Inserting headed rebar, (d) After installation

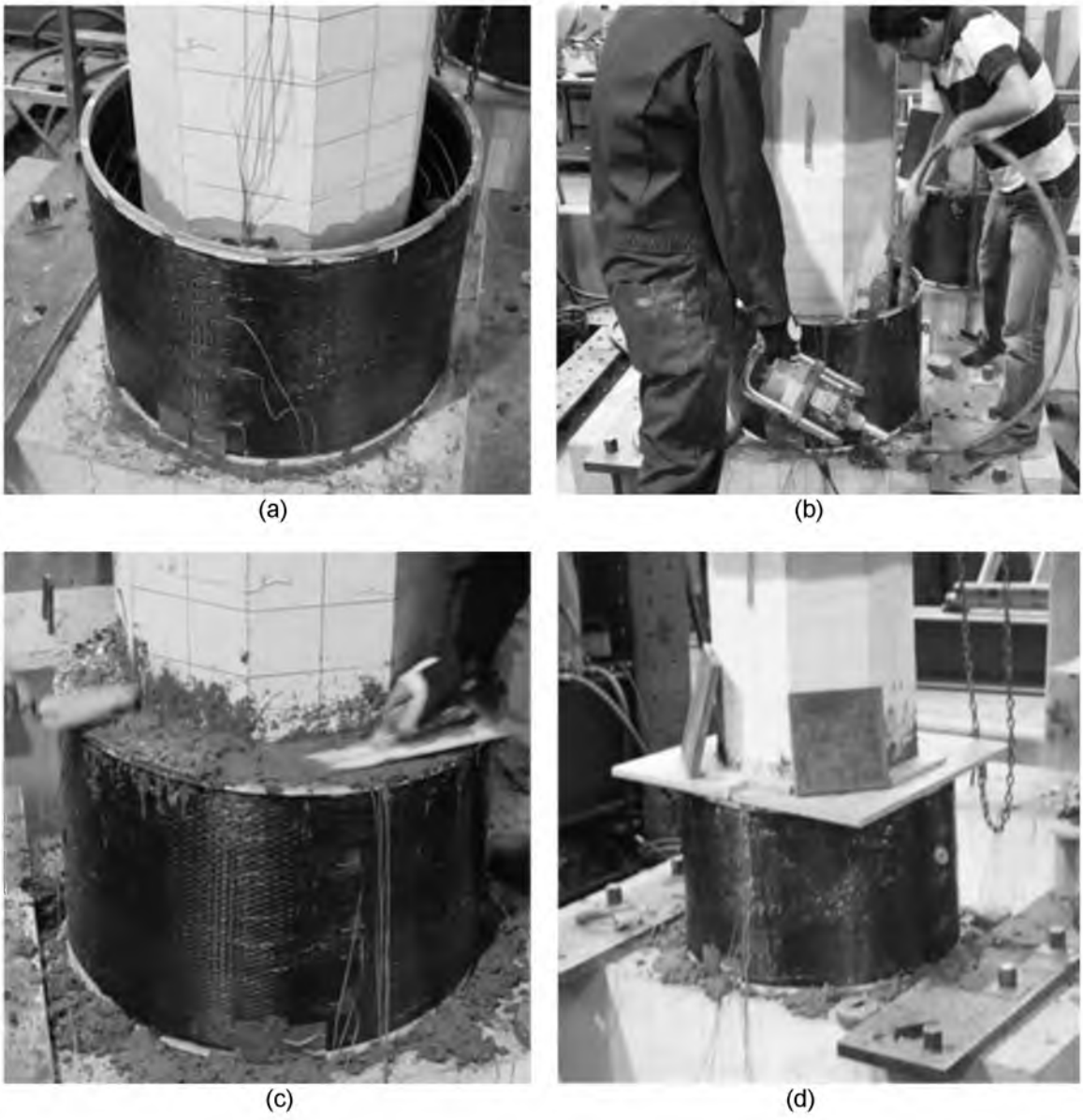

Figure 3.5 – Repair concrete casting: (a) Before casting, (b) Vibrating concrete during casting, (c) Finishing concrete after casting, (d) Wooden formwork and weights in place after casting

3.3 Instrumentation

The instrumentation utilized during testing consisted of a load cell, strain gauges, Linear Variable Differential Transformers (LVDTs), and string potentiometers (string pots). Although the servo-controlled actuator recorded both load and position, only the load values were used in data analysis. The displacement values obtained from the actuator included the movement within the lateral load system and therefore have a small level of inaccuracy. Accurate displacement readings were obtained from the string potentiometers.

3.3.1 Strain gauges

Strain gauges were used to measure the strain in the reinforcing steel, CFRP jacket, and axial load rods during testing. All of the strain gauges that were not damaged in the as-built tests were connected during the repaired assembly tests. Many of the strain gauges from the as-built tests were damaged during testing and provided inaccurate readings during the repaired assembly tests. During the repair process, strain gauges were placed on the headed rebar as well as the CFRP jacket.

The strain gauges used during the NMB-2 Repair test were all MEM strain gauges that record strains until the yield point. The bond between the strain gauge and steel is lost past yield for the MEM strain gauges, and the readings are lost. During the NMB-3 Repair test both MEM and TML strain gauges were used. The TML strain gauges are designed for high strain readings and can read up to five times the yield strain of the steel bars.

Figure 3.6 shows the strain gauge sections that were present for the NMB-2 Repair and NMB-3 Repair test. NMB-3 Repair had more strain gauges on both the wrap and headed rebar. Due to geometrical conflicts the exact locations of strain gauges did not always fall onto the designated section. This variation in placement is recorded in the naming scheme that has been adopted, which gives the strain gauge number entered into the data acquisition system followed by the height above the column footing interface in parentheses. The strain gauge schedules can be seen in Figures 3.7 and 3.8 for NMB-2 Repair and NMB-3 Repair, respectively.

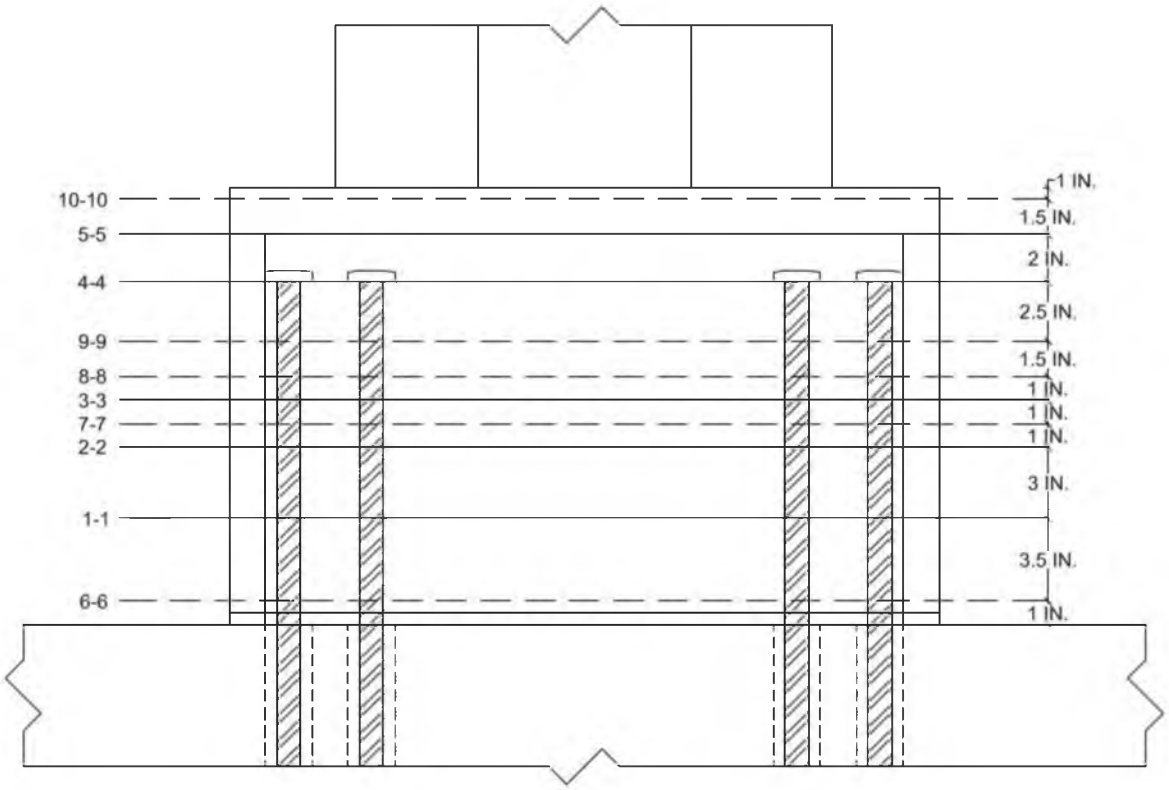

Figure 3.6 - Strain gauge sections for NMB-2 Repair and NMB-3 Repair

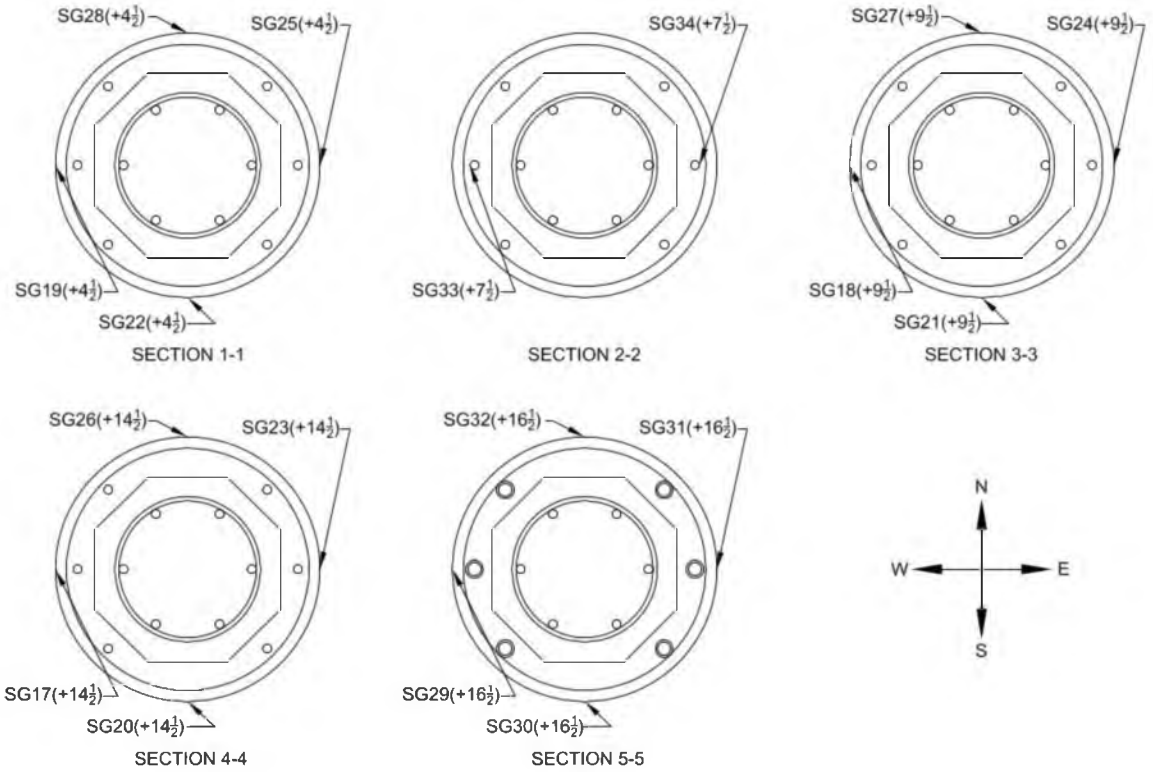

Figure 3.7 - Strain gauge locations for NMB-2 Repair

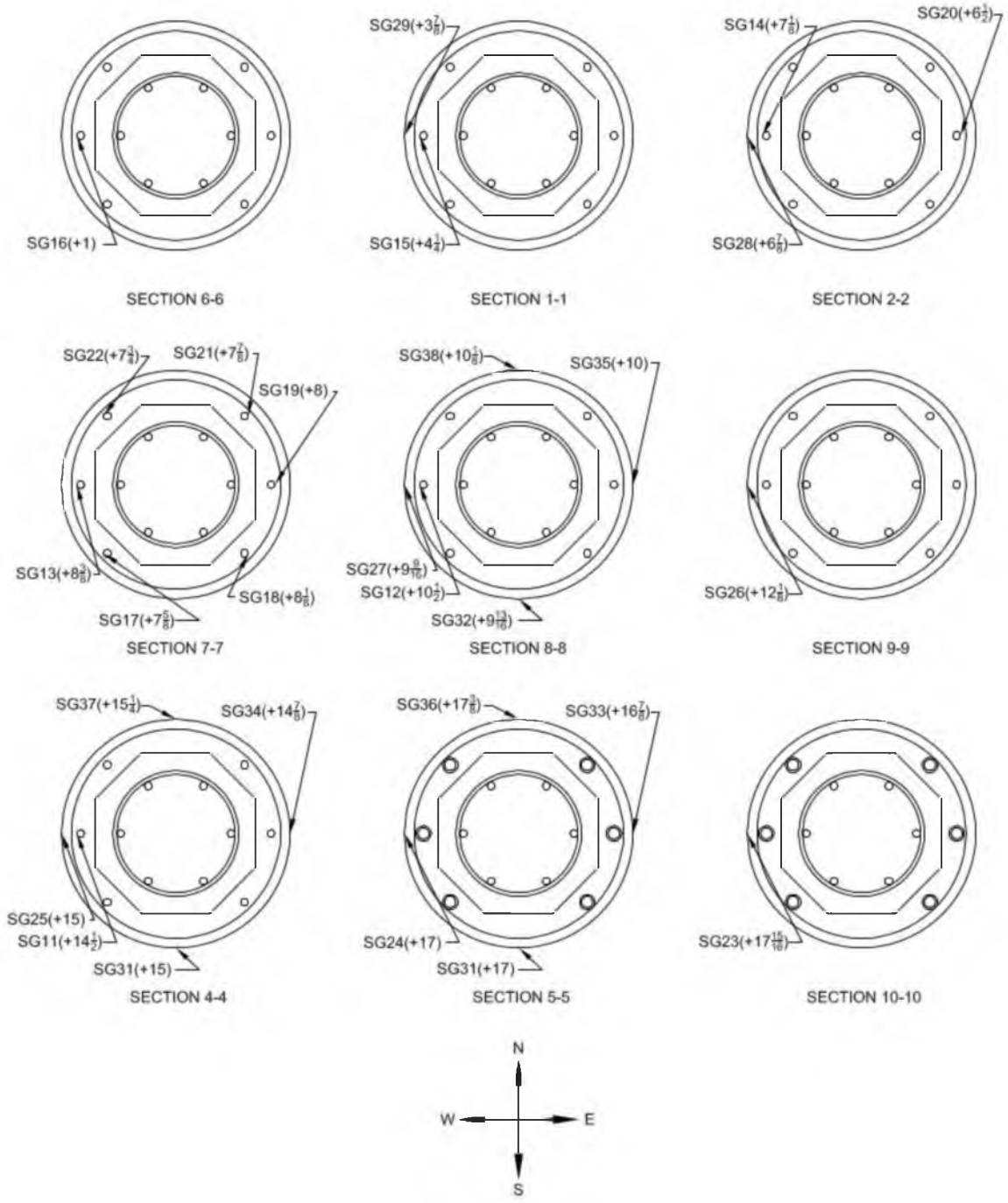

Figure 3.8 - Strain gauge locations for NMB-3 Repair

3.3.2 Linear variable differential transformers

Linear variable differential transformers (LVDTs) were mounted to NMB-2 Repair and NMB-3 Repair to measure displacements at critical locations. The LVDTs were attached to the west and east faces of the columns to obtain strain and curvature measurements. All-thread rods were tack welded onto the as-built longitudinal rebar with couplers at either end to provide attachment points for the LVDTs. An LVDT was placed on the west side of the footing to measure the lateral displacement, or slip, of the footing during testing. Also, an LVDT was placed under the footing east of the neutral axis to obtain deflection readings for the base of the footing. Figures 3.9 and 3.10 show the LVDT layout during the NMB-2 Repair and NMB-3 Repair tests. It should be noted that LVDTs no. 5 to no. 8 were not used during NMB-2 Repair test because the hardware was not installed prior to casting.

The average curvature for an LVDT cell, Φ, was found following eq. 3.10:

$$\phi = \frac{A - B}{W * h} \tag{3.10}$$

where A and B are the LVDT readings on the tension and compression faces of a cell, respectively. Extension is taken as a positive LVDT reading. W is the horizontal distance between the LVDTs that recorded A and B, and h is the cell height. There were two LVDT cells recording curvature during the NMB-2 Repair test and four LVDT cells recording curvature during the NMB-3 Repair test. The two LVDTs that make up each cell are no. 1 and no. 2, no. 3 and no. 4, no. 5 and no. 6, and no. 7 and no. 8.

3.3.3 String potentiometers

String potentiometers (string pots) were used to measure the lateral displacement of the column. The string pots were connected to the column was at the level of the actuator. The distance between the string pot and the connection to the specimen was large in comparison to the vertical deflections being induced on the specimens from the lateral displacement. Therefore, the small angle approximation was made in all of the string pot readings, and the recorded displacements were taken as the true lateral displacements. The string pots were mounted to

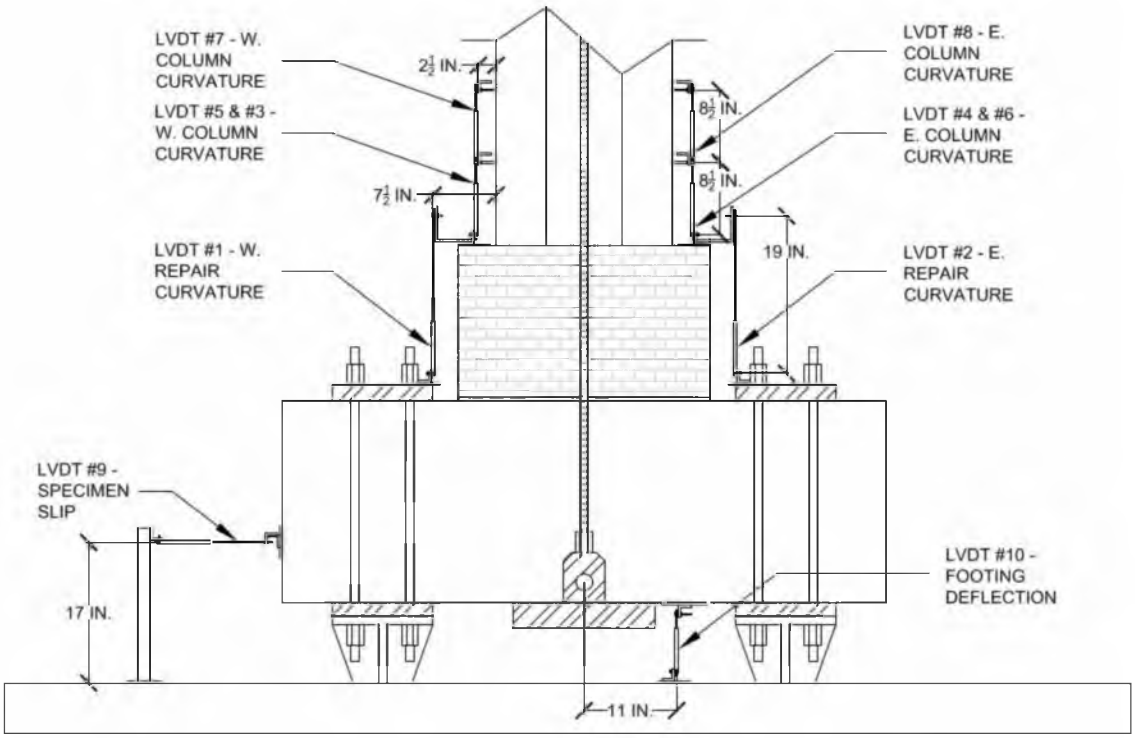

Figure 3.9 – Typical LVDT layout looking north with approximate dimessions

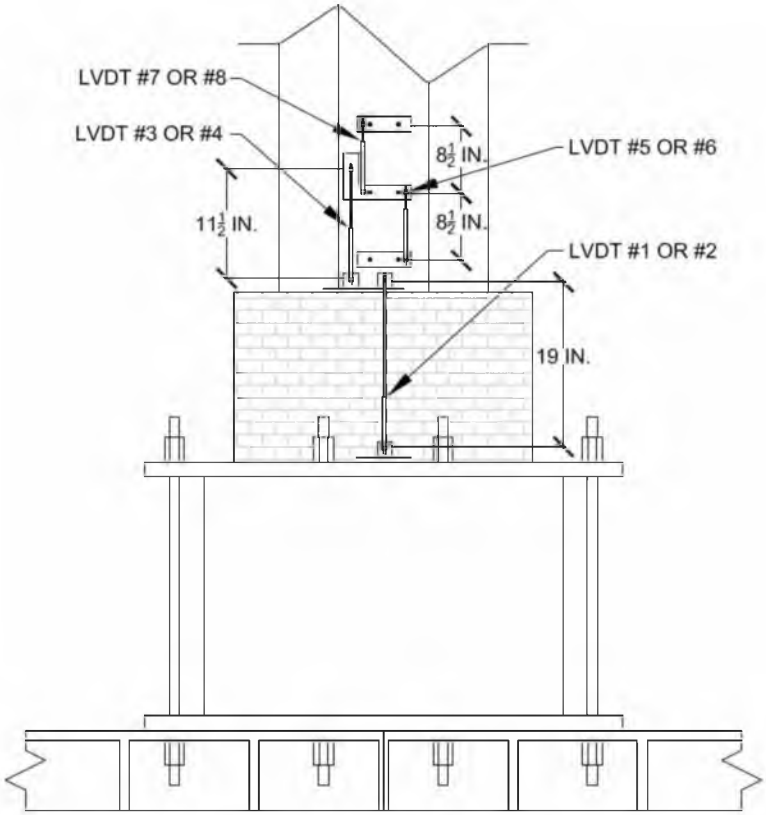

Figure 3.10 – Typical LVDT layout of east or west column face with approximate dimessions

steel fixtures that were not in contact with the loading frame. This ensured that there were no unwanted deflections being recorded during testing. The side of the string pots that attached directly to the column were in direct contact with the concrete. The string pots were connected to the north and south column faces and were parallel to the west and east plane, as shown in Figure 3.11. This configuration provided two measurements to use when determining the true column displacement and could also detect any twisting of the column about a vertical axis. If equal values were recorded by both string pots, the column was not twisting, and the recorded values were averaged to find the displacement of the column.

3.4 Performance evaluation criteria

The performance evaluation criteria used to compare and measure the success of the tests were load capacity, displacement capacity, displacement ductility, energy dissipation, and

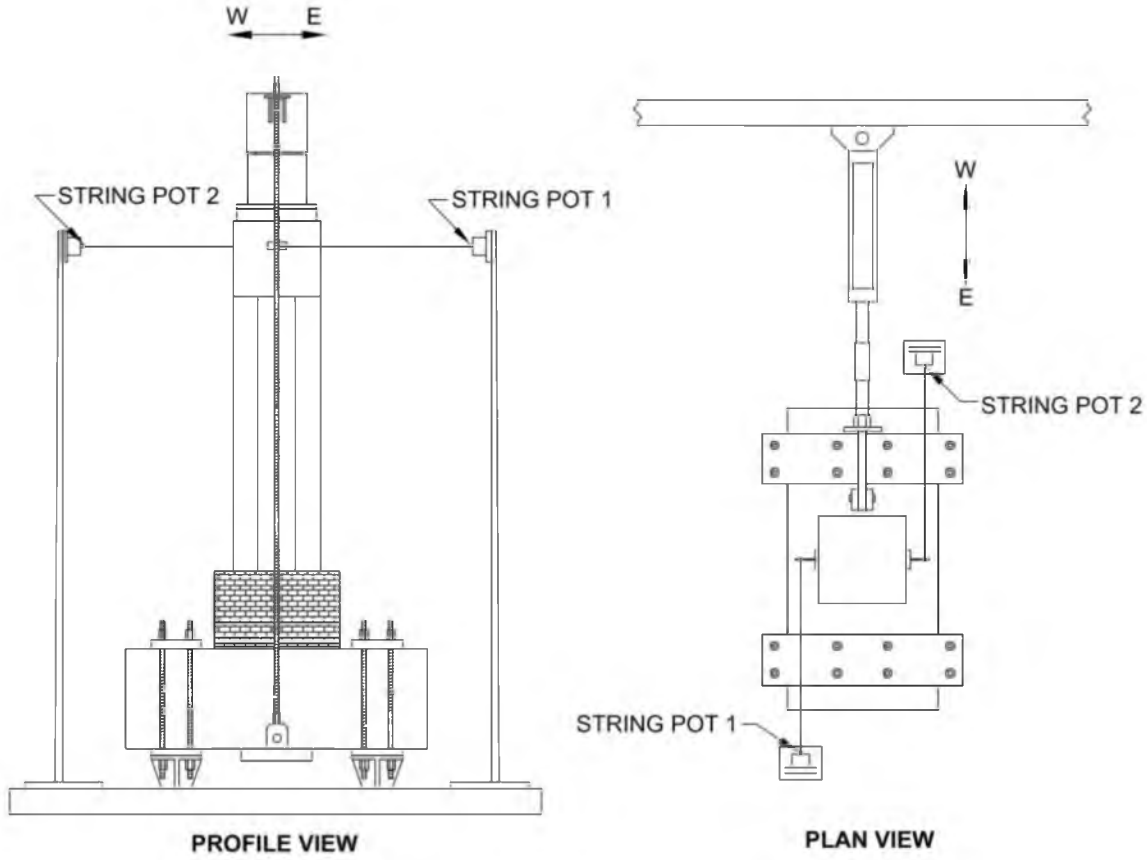

Figure 3.11 – String pot layout

hysteretic stiffness. Different methods exist for obtaining these specific performance evaluation criteria. To provide continuity between test results, standardized methods for obtaining the listed performance evaluation criteria have been adopted for both the as-built and repaired specimens. The exact procedure followed for each of the performance evaluation criteria will be described within this section.

3.4.1 Lateral load capacity

The lateral load capacity of each specimen is defined as the maximum load recorded during testing. Three values of lateral load capacity exist for a test: one for the east direction of testing and one for the west direction of testing and an average value from both directions of testing. The 120-kip load cell attached to the piston of the lateral actuator recorded the force values induced on the specimen.

3.4.2 Displacement capacity

The displacement capacity of each specimen is defined as the average failure displacement value reached in the east and west directions. The failure displacement is also referred to as the ultimate displacement. Failure is defined as the point at which the specimen's lateral load carrying capacity has dropped to 80% of the maximum lateral load capacity in a given direction. If failure occurs between two displacement steps, linear interpolation of the specimen's envelope curve is used to find the ultimate displacement.

The envelope curve is obtained from the specimen's hysteretic curves. For each displacement step, the points at which the specimen reaches the highest load, in both directions of testing, are taken as points on the envelope curve. The envelope curve is then constructed by connecting each deformation step point linearly. If failure did not occur for a specimen in a certain direction of testing, the ultimate displacement is defined as the maximum displacement achieved in that direction. String pots attached to the north and south faces of the column recorded the displacement values for the specimens.

The displacement of a specimen is often shown as drift within this document. The drift is often listed as a percent and is defined as the lateral deflection divided by the distance between the top of the footing and the lateral load application. The distance between the top of the footing and the point of lateral load application was used as the denominator when calculating drift for both the as-built and repaired specimens.

3.4.3 Displacement ductility

The displacement ductility of a specimen, μ_Δ, is defined by eq. 3.11:

$$\mu_\Delta = \frac{\Delta_u}{\Delta_y} \tag{3.11}$$

where Δ_u is equal to the ultimate displacement, as defined in section 3.4.2, and Δ_y is equal to the yield displacement. Both Δ_u and Δ_y are obtained from the specimen's envelope curve.

Once the envelope curve is constructed, an idealized bilinear, elasto-plastic curve is fit to the envelope to get the value of Δ_y. Δ_y is defined as the displacement at which the elasto-plastic curve changes from elastic to plastic. The equal energy rule was used when constructing the elasto-plastic curve, which states that the energy of the envelope and elasto-plastic curve must be equal. Since the envelope and elasto-plastic curves are developed in force-displacement space, the energy of each curve is simply the area underneath the curve. When following the equal energy rule there are an infinite number of elasto-plastic curves that could be constructed from an envelope. To ensure that there was only one possible bilinear curve that could be developed for any given envelope, an additional modeling parameter was adopted to ensure consistency between tests. The intersection of the elasto-plastic curve and the envelope curve was set to 0.70 Δ_y *(22)*. With this additional modeling parameter there is only one possible elasto-plastic curve for any given envelope.

Once the elasto-plastic curve is developed, Δ_u and Δ_y are defined, and the displacement ductility can be calculated following eq. 3.12. For each test there are three different displacement

ductility values. There is displacement ductility for each direction of testing, and there is an average displacement ductility value from both directions of testing. The average displacement ductility is found from an average envelope curve. The average envelope curve is constructed by averaging the absolute value of the envelope cures in both directions of testing for each displacement step. From the average envelope curve, an elasto-plastic curve is developed following the procedures described in this section, and the average envelope displacement ductility can be calculated.

3.4.4 Energy dissipation

Energy dissipation capacity of a structural system is paramount to the seismic performance of the system. The energy dissipation of a cycle is calculated from the area within the hysteretic loop that is created during the cycle. For each displacement step, two cycles are carried out, creating two hysteretic loops. The area of both loops was added to produce the energy dissipation at the given displacement step. The results in this study are shown as the total energy dissipated by the system at the conclusion of a certain displacement step, referred to as the cumulative energy dissipation capacity.

The data acquisition system used during the tests collected 10 data points per second. Each data point was connected linearly to calculate the energy dissipation. Numerical integration and the rectangle rule were used to find the area within each loop. Due to the small time step used and the slow displacement rate, these approximations provide sufficiently accurate energy dissipation results.

3.4.5 Hysteretic stiffness

Hysteretic stiffness is calculated for each displacement step. These values can then be looked at to see the stiffness degradation characteristics of the test and also to compare the hysteretic stiffness characteristics between tests. Every hysteretic stiffness value is calculated by averaging four stiffness results from the displacement step. The four stiffness values come from both directions of testing for both cycles. The slope of the line connecting the origin to the point

of maximum displacement, for a given direction and cycle, is defined as one stiffness value. The displacement, or drift, that the hysteretic stiffness is plotted with is the average of the absolute value of the four displacements that the stiffness values for the displacement step were calculated from.

To help visualize the stiffness degradation characteristics of each test versus one another, the hysteretic stiffness results have been plotted normalized to the initial stiffness. This means that each hysteretic stiffness value is divided by the hysteretic stiffness during the first displacement step. Therefore the first displacement step, 0.5 in., will have a normalized stiffness value of 1. This normalization helps get rid of the different stiffness values due to concrete strength and column length and provides a comparison between all of the tests.

CHAPTER 4

EXPERIMENTAL RESULTS OF REPAIRED SPECIMENS

The results of the NMB-2 Repair and NMB-3 Repair tests are discussed in this chapter. Performance evaluation criteria are presented and compared for each test.

4.1 Material properties

The material properties of NMB-2, NMB-2 Repair, NMB-3, and NMB-3 Repair are discussed in this section. Eight different materials work simultaneously during the repair tests, each influencing results. These materials include three different types of steel reinforcement, the CFRP jacket, two types of concrete, high-strength nonshrink grout used for the GSS connections, and epoxy, which anchors the headed rebar. The pertinent material properties for all four tests are summarized in Table 4.1. The results were obtained for tests carried out at the University of Utah Structures Laboratory unless noted otherwise.

The concrete properties vary in strength and behavior significantly between tests. The column and footing concrete strength during the NMB-2 test is 58% of the strength of the column and footing concrete during the NMB-3 Repair test. Also, the repair concrete used for NMB-3 Repair created nearly 15 times the amount of pre-tensioning in the CFRP jacket as the repair concrete used with NMB-2 Repair. These variations in material properties highly influence the test results and must be kept in mind when comparing the test results.

Table 4.1 – Material properties

Specimen	#8 Longitudinal steel (ksi)		#4 Transverse steel (ksi)		#8 Headed rebar (ksi)		CFRP jacket			Compressive strength (ksi)					
										Column and footing concrete		Repair concrete		GSS grout	
	Yield strength	Ultimate strength	Yield strength	Ultimate strength	Yield strength	Ultimate strength	Tensile strength	Tensile modulus	Layer thickness	28-Day	Day of test	28-Day	Day of test	28-Day	Day of test
NMB-2	68	93	63	103	-	-	-	-	-	3.94	5.45	-	-	11.1	13.5
NMB-2 Repair	68	93	63	103	62	86	101 ksi	8990 ksi	0.047 in.	3.94	6.43	6.36	7.51	11.1	15.2
NMB-3	68	93	63	103	-	-	-	-	-	6.74	8.42	-	-	15.6	14.6
NMB-3 Repair	68	93	63	103	62	86	101 ksi	8990 ksi	0.047 in.	6.74	9.33	Expansive		15.6	16.9

4.1.1 Steel

Three different batches of grade 60 steel reinforcing rebar are present in the as-built and repair tests. These include the no.8 longitudinal rebar, no.4 transverse reinforcement, and the headed rebar. The no.8 longitudinal and no.4 transverse rebar make up the reinforcement present in both the column and footing. The no.8 headed bars were post installed after the as-built tests and are present during the repair tests. All of the tensile properties for the reinforcing bars were obtained using the standards outlined in ASTM A370-09a *(28)* and are listed in Table 4.1.

4.1.2 CFRP

The Carbon Fiber Reinforced Polymer (CFRP) jacket used for the repair consists of a carbon fiber fabric and epoxy resin matrix. The carbon fiber fabric that was used is SikaWrap Hex 103C. This fabric is unidirectional and all of the fibers were oriented in the hoop direction. The binding matrix that was used is Sikadur Hex 300 Epoxy. The CFRP tensile properties were obtained following ASTM D3039 *(29)*. The CFRP coupon preparation and testing was performed in the Mechanical Engineering Department laboratories at the University of Utah. Selected results are shown in Table 4.1.

4.1.3 Column/footing concrete and GSS grout

The concrete properties for all tests were obtained from compression tests on 4-in. diameter, 8-in. tall concrete cylinders. These cylinders were tested in accordance to ASTM C39 *(30)*. The high strength nonshrink grout used in the GSS connections was tested using 2-in. tall, 2-in. wide, and 2-in. long grout cubes following ASTM C109 *(31)*. The results from these tests are shown in Table 4.1.

4.1.4 Nonshrink/expansive concrete

The nonshrink/expansive concrete, also referred to as the repair concrete, was designed differently for NMB-2 Repair and NMB-3 Repair. The repair concrete used for NMB-2 Repair was

designed as nonshrink, and the repair concrete used for NMB-3 Repair was designed to be expansive. Komponent cement was added to the repair concrete and proportioned at 13% and 41% of the cementitious materials for NMB-2 Repair and NMB-3 Repair, respectively. When proportioned at 15%, Komponent is designed to be a type K, shrinkage-compensating concrete *(32)*. The mix designs for both NMB-2 Repair and NMB-3 Repair can be found in Table 3.1.

The repair concrete from NMB-2 Repair and NMB-3 Repair was sampled in 4-in. diameter by 8-in. tall cylinders. These cylinders were tested following ASTM C39 for NMB-2 Repair, and the results from these tests can be found in Table 4.1. The repair concrete for NMB-3 Repair was too expansive to test. The cylinders were cracked from the expansion prior to testing and achieved extremely low compressive strength results. In the future, confinement needs to be provided for cylinders sampled with expansive concrete. Tests were conducted on the repair concrete used for NMB-3 Repair with a concrete hammer prior to testing. These test results showed that the compressive strength of the repair concrete, at the column-repair interface, was similar to the compressive strength of the column and footing concrete.

The pre-tensioning in the CFRP wrap as a function of time, up to 1 day prior to testing, for NMB-2 Repair and NMB-3 Repair is shown in Figure 4.1. The pre-tensioning that the NMB-3 Repair CFRP jacket experienced at different heights above the footing can be found in Figure 4.2. Both Figure 4.1 and 4.2 are plots of CFRP jacket hoop strain versus time. The strain plotted in Figure 4.1 is the average jacket strain from 12 strain gauges that were located at three levels approximately 10 in., 15 in., and 18 in. above the top of the footing on the north, east, south, and west sides of the CFRP shell. The strain plotted in Figure 4.2 is the average value of the four strain gauges located at heights of approximately 10 in., 15 in., and 18 in. above the footing. The exact locations of these strain gauges can be found in Figures 3.7 and 3.8.

From this data, an average pre-tensioning value of the CFRP jacket 1 day prior to testing was determined. The average pre-tensioning prior to testing is 105 microstrain for NMB-2 Repair and 1535 microstrain for NMB-3 Repair. These pre-tensioning values account for 1% of the strain capacity of the CFRP jacket for NMB-2 Repair and 14% of the strain capacity of the CFRP jacket for NMB-3 Repair. Prior to testing, the data acquisition system was zeroed, and

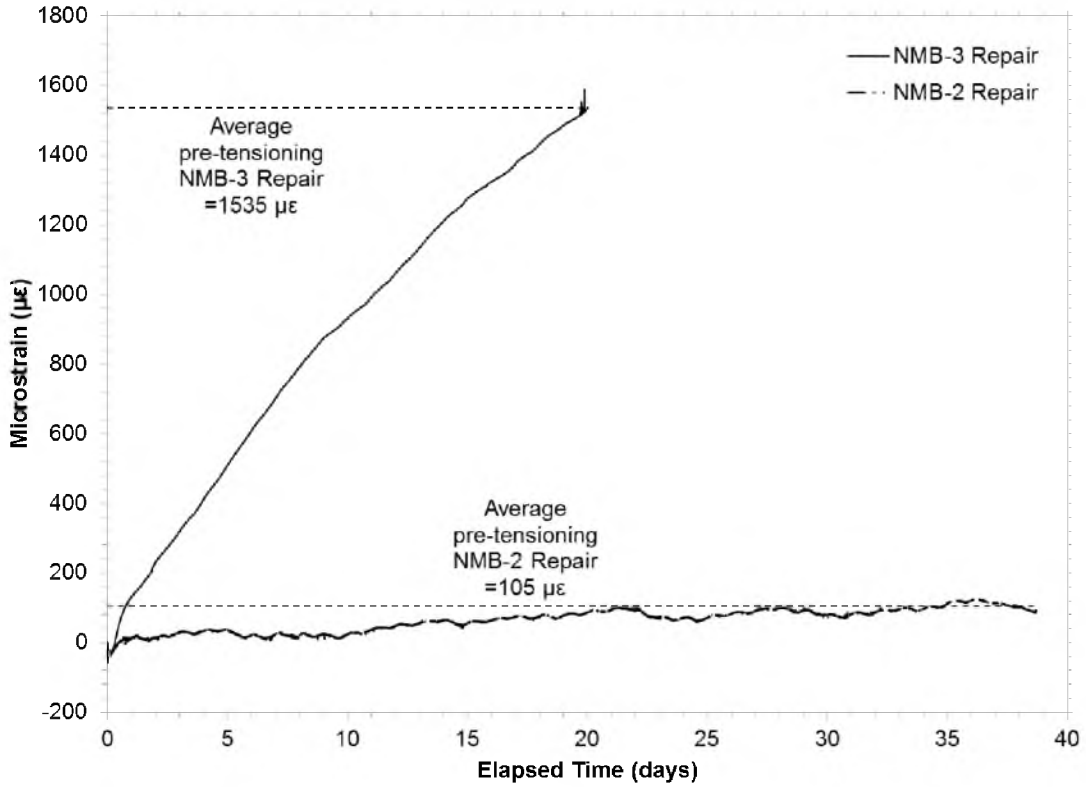

Figure 4.1 – CFRP pre-tensioning for NMB-2 Repair and NMB-3 Repair prior to testing

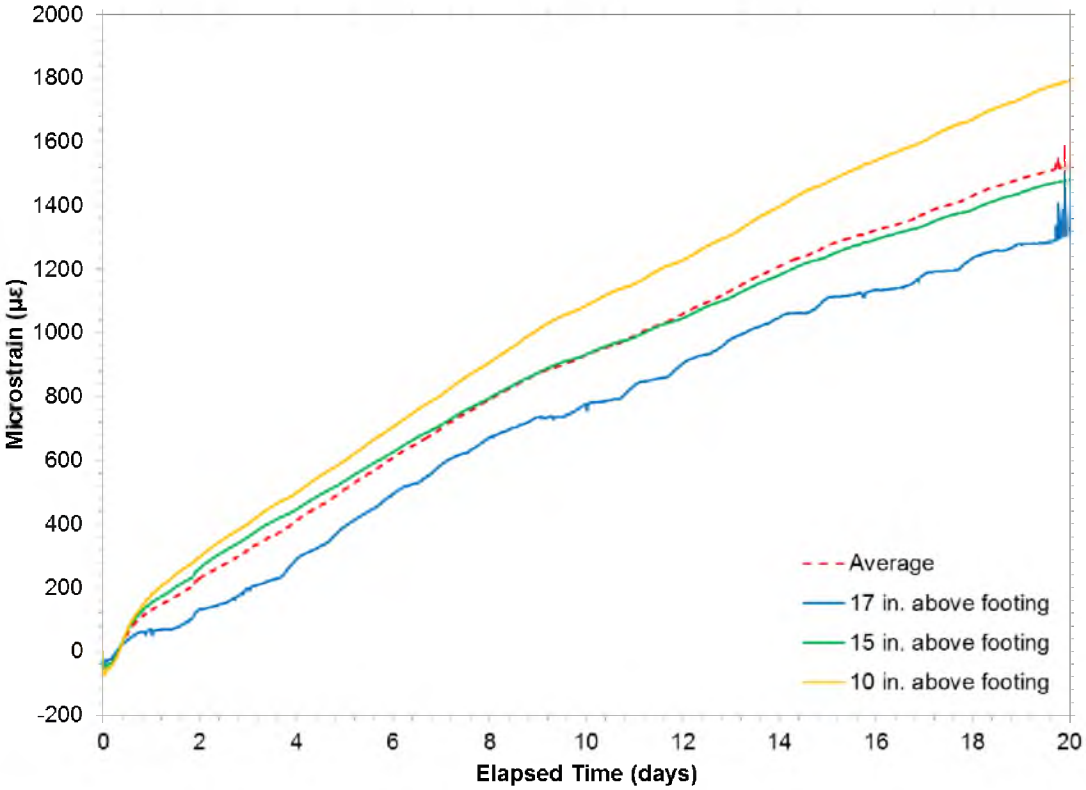

Figure 4.2 – CFRP pre-tensioning by height for NMB-3 Repair prior to testing

additional instrumentation was armed to the system. One day after the strain gages were disconnected, the specimens were tested. After testing, the average pre-tensioning, from Figure 4.1, was added to all of the wrap strain gauge values obtained during testing. It should be noted that the repair concrete within NMB-3 Repair had not reached a plateau in pre-tensioning prior to testing. It is not known how much more pre-tensioning would have occurred if the concrete were allowed to cure for a longer time. Previous research has explained the difficulties of using expansive concrete in CFRP jackets due to the time-dependent expansion properties *(26)*.

Figure 4.2 shows that there is an uneven vertical distribution of pre-tensioning from the concrete used for NMB-3 Repair. It is clear from this plot that more expansion occurs in the lower portions of the jacket. At the time of testing there was 27% more pre-tensioning in the jacket at 10 in. above the footing than at 17 in. above the footing. This uneven vertical distribution of strain is likely due to the restraints that were provided at the top and bottom of the repair. The footing was at the bottom of the repair, which does not allow any vertical expansion, while a form was placed on top with weights, which could have allowed some vertical expansion.

4.1.5 Epoxy

The epoxy used to anchor the headed rebar for the repair is Hilti HIT-RE 500-SD epoxy. This epoxy has a design bond strength of 1400 psi for core drilled holes in concrete with compressive strengths of 4500 psi–6000 psi *(23)*.

4.2 NMB-2 Repair test results

NMB-2 Repair was tested on May 29th, 2013, in the University of Utah Structures Laboratory. The results of the NMB-2 Repair test will be examined within this section. To understand the results of the NMB-2 Repair test, the damage state prior to repair, at the conclusion of the NMB-2 test, must first be understood and can be found in Section 2.4.1.

The objectives in repairing NMB-2 were to restore the diminished load and displacement capacities through plastic hinge relocation. Plastic hinge relocation was achieved and is shown in Figure 4.3. The hysteretic response and envelope of NMB-2 Repair during testing is shown in

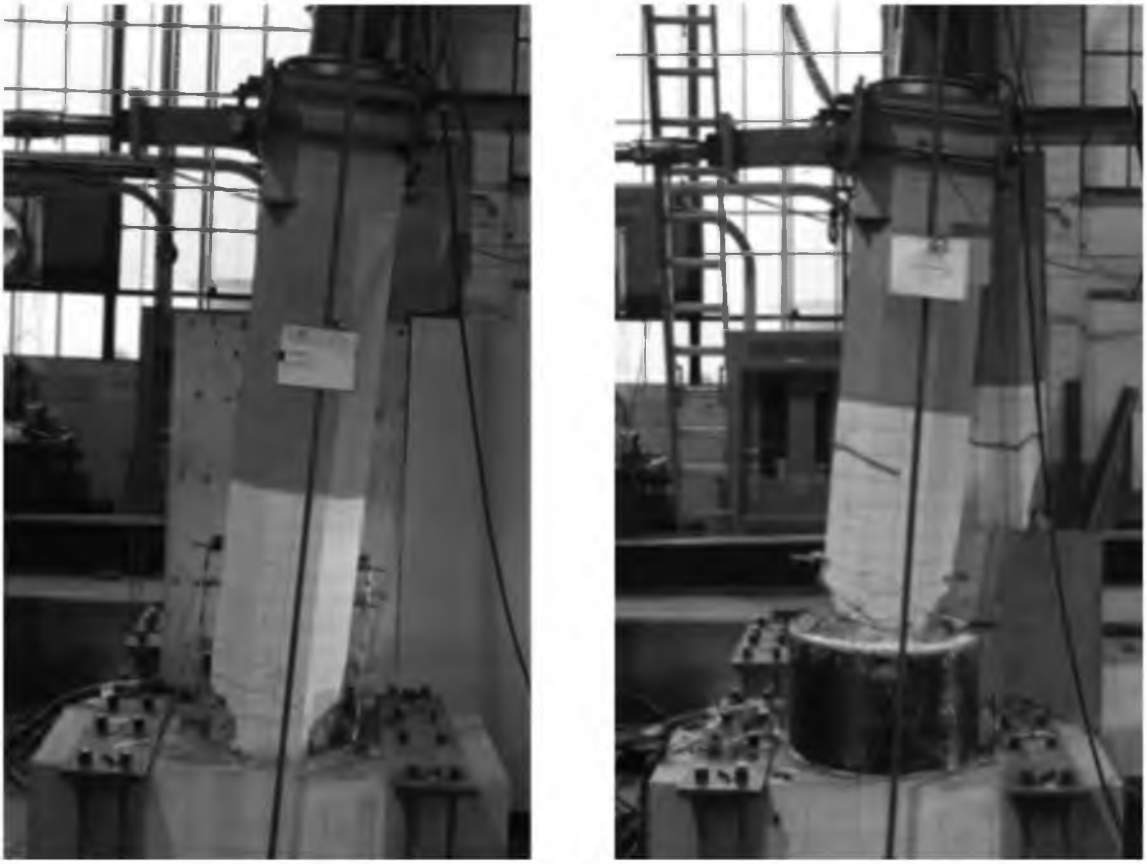

(a) (b)

Figure 4.3 – Specimens displaced to the east at the maximum displacement step: (a) NMB-2, (b) NMB-2 Repair

Figures 4.4 and 4.5, respectively. From these Figures it can be seen that both the load and displacement capacities of NMB-2 were restored. The ultimate drift achieved was 6.96%, and the ultimate load was approximately 45.56 kips. The displacement ductility that NMB-2 Repair achieved was 7.52 when displaced to the east and 4.15 when displaced to the west. The displacement ductility when displaced to the west is approximately 55% of the displacement ductility when displaced to the east. The loading protocol displaces the specimen to the east before the west for each cycle, degrading the stiffness of the specimen, which causes this difference in displacement ductility. The average ductility, calculated from an averaged envelope response curve of NMB-2 Repair, is 5.95.

NMB-2 Repair reached an ultimate lateral load during the 4-in. to 5-in. displacement step and experienced longitudinal rebar facture of both the west and east extreme bars during the 7-in.

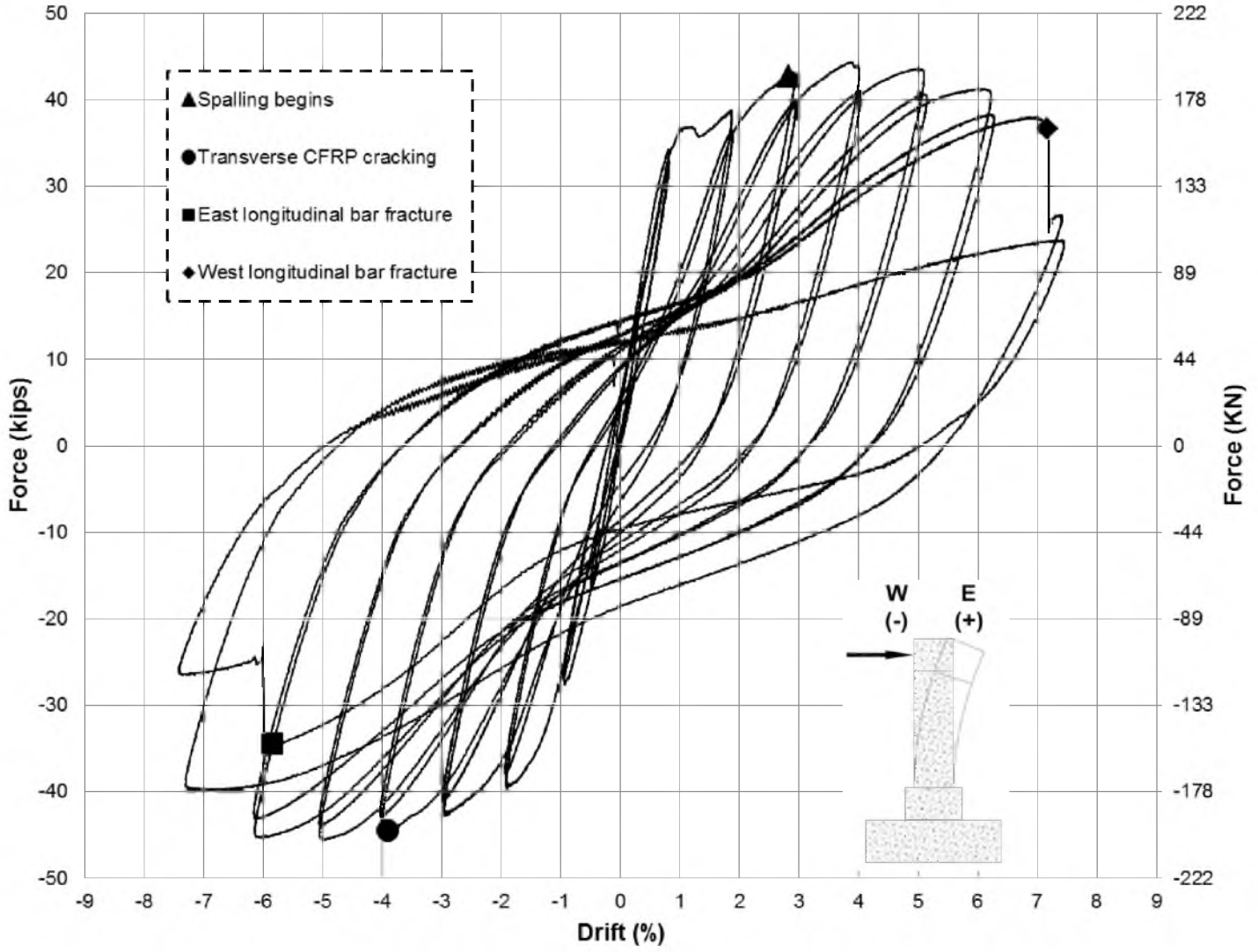

Figure 4.4 – NMB-2 Repair hysteresis curve

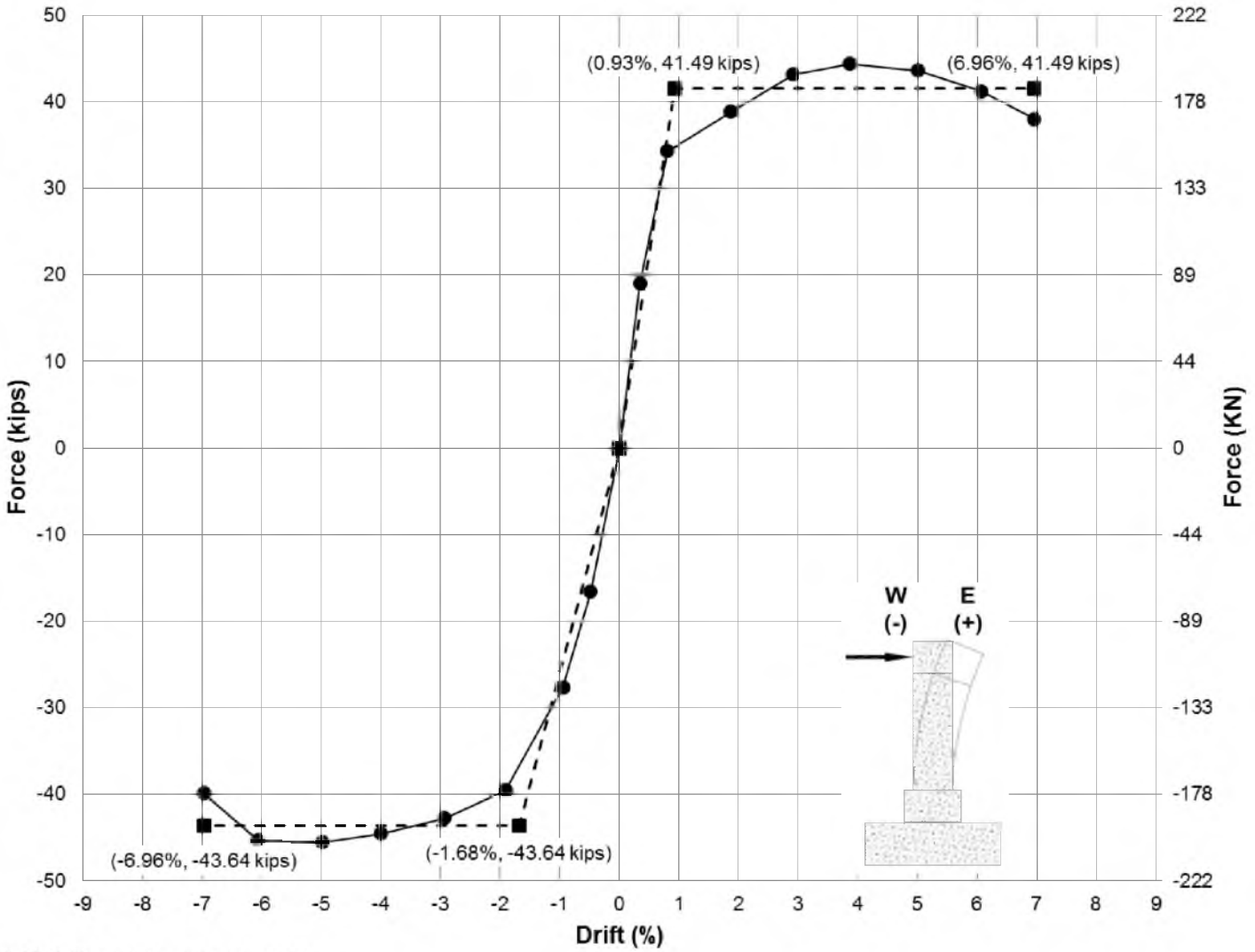

Figure 4.5 – NMB-2 Repair backbone curve

displacement step. The fracture locations for the west and east longitudinal bars were 3 in. and 4.5 in. above the top of the repair, respectively. Both bars fractured during the 7-in. displacement step. The west rebar fractured in tension during the first cycle and the east rebar fractured in tension during the second cycle. The east longitudinal rebar fractured in both the NMB-2 test and the NMB-2 Repair test. The fracture location of the east longitudinal rebar during the NMB-2 Repair test was 21.5 in. above the fracture location during the NMB-2 test. The distance between the two fracture locations corresponds to 51% of the design development length for a no.8 bar (*5*). This small development length shows that the CFRP jacket imposed significant confining forces on the longitudinal reinforcement.

Transverse CFRP cracking was observed during the testing of NMB-2 Repair, as shown in Figure 4.6. The crack began during the 4-in. displacement step and grew during each subsequent displacement step. At completion of the test, the crack extended halfway around the circumference of the CFRP jacket. The hysteretic response of the specimen remained seemingly unaffected by the transverse CFRP crack. The crack was located 3 in.–4 in. below the top of the repair, corresponding to the height of the top of the headed rebar.

The reason that the transverse CFRP crack began is thought to be due to a few reasons. First, the east side of the repair was responsible for transferring more tension to the footing than the west side of the repair since the east extreme longitudinal rebar fractured during the NMB-2 test. This led to larger crack widths on the east column face compared to the west. The maximum crack width on the east column face was 0.1 in., whereas the maximum crack width on the west column face was only 0.025 in. Second, the headed bars terminated approximately 3 in. below the top of the repaired concrete. The headed rebar provides the tension transfer between the repair and the footing perpendicular to the CFRP fiber orientation. Due to the termination location of the headed rebar, the CFRP wrap experienced tension transverse to its fiber orientation above the headed rebar, which caused cracking.

The onset of transverse CFRP cracking can be seen from the curvature profile, shown in Figure 4.7, which shows the maximum and minimum curvatures during the 0.5 in. to 4-in. displacement steps. There are two curvature values plotted for each displacement step in the

Figure 4.6 – Transverse CFRP crack located just above white line

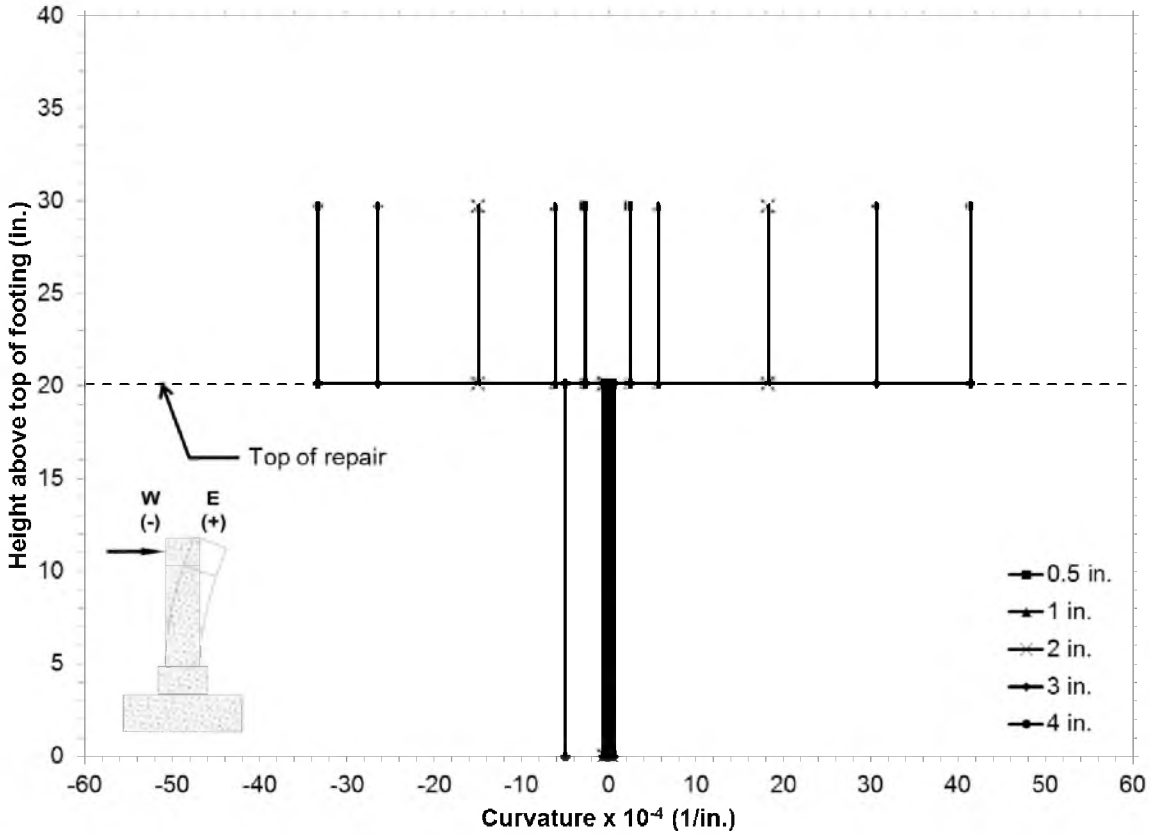

Figure 4.7 – NMB-2 Repair curvature profile up to 4-in. displacement step

east and west directions. The first value is an average curvature value from the top of the footing to the top of the repair. The second value is an average curvature value from the top of the repair to 9.56 in. up the column. From this plot it can be seen that the curvature of the wrapped section is very small when compared to the column, indicating the plastic hinge formation in the column. Also, the onset of the CFRP crack can be seen by the increase in the repair curvature when displaced to the west during the 4-in. displacement step.

Other notable events pertaining to the damage state of NMB-2 Repair during testing will be explained chronologically. During the 0.5-in. displacement step the damage observed was the opening of a crack obtained during the NMB-2 test. The crack only opened at the extreme displacements and was located 1 in. above the top of the repair. Once the specimen was at rest the crack was measured to be hairline.

The 1-in. displacement step marked the onset of radial cracking in the repair concrete. The radial cracks originated from six of the eight column corners and were measured to be a maximum of 0.005 in., as shown in Figure 4.8(a).

The 2-in. displacement round started with an audible event occurring during the first displacement to the east. The event can be seen in the hysteresis as a plateau beginning at approximately 1% drift and continuing through the completion of the cycle. The noise that was heard was due to relaxation of the tie-down rods that anchor the specimen to the strong floor. The imbalance in tension of these rods due to the residual displacement from the original test was relieved as one of the rods shifted. The event resulted in the tie-down rods balancing the reaction forces on either side of the specimen, subsequently making the hysteretic behavior of the test symmetrical from that point forth. New cracking occurred during this round with a 0.06-in. crack opening up 2 in. above the top of the repair on the east column face, as shown in Figure 4.8(b). Also, a 0.025 in. crack originating 3 in. above the repair on the west face was created during the 2-in. displacement step. These cracks continued to grow throughout the test and are the beginning of the plastic hinge formation.

Spalling began during the 3-in. displacement step at the east and west corners of the column. Gapping was observed between the column and the repair concrete and continued to

grow throughout testing, shown in Figure 4.8(c).

During the first cycle of the 4-in. displacement step the transverse CFRP crack, discussed previously, originated on the east side of the repair when the column was displaced to the west. During this displacement step, shear x-cracking began on both the north and south faces, as shown in Figure 4.8(d). The x-cracks were measured to have a maximum width of 0.013 in. Spalling of the cover concrete above the repair continued during this displacement step.

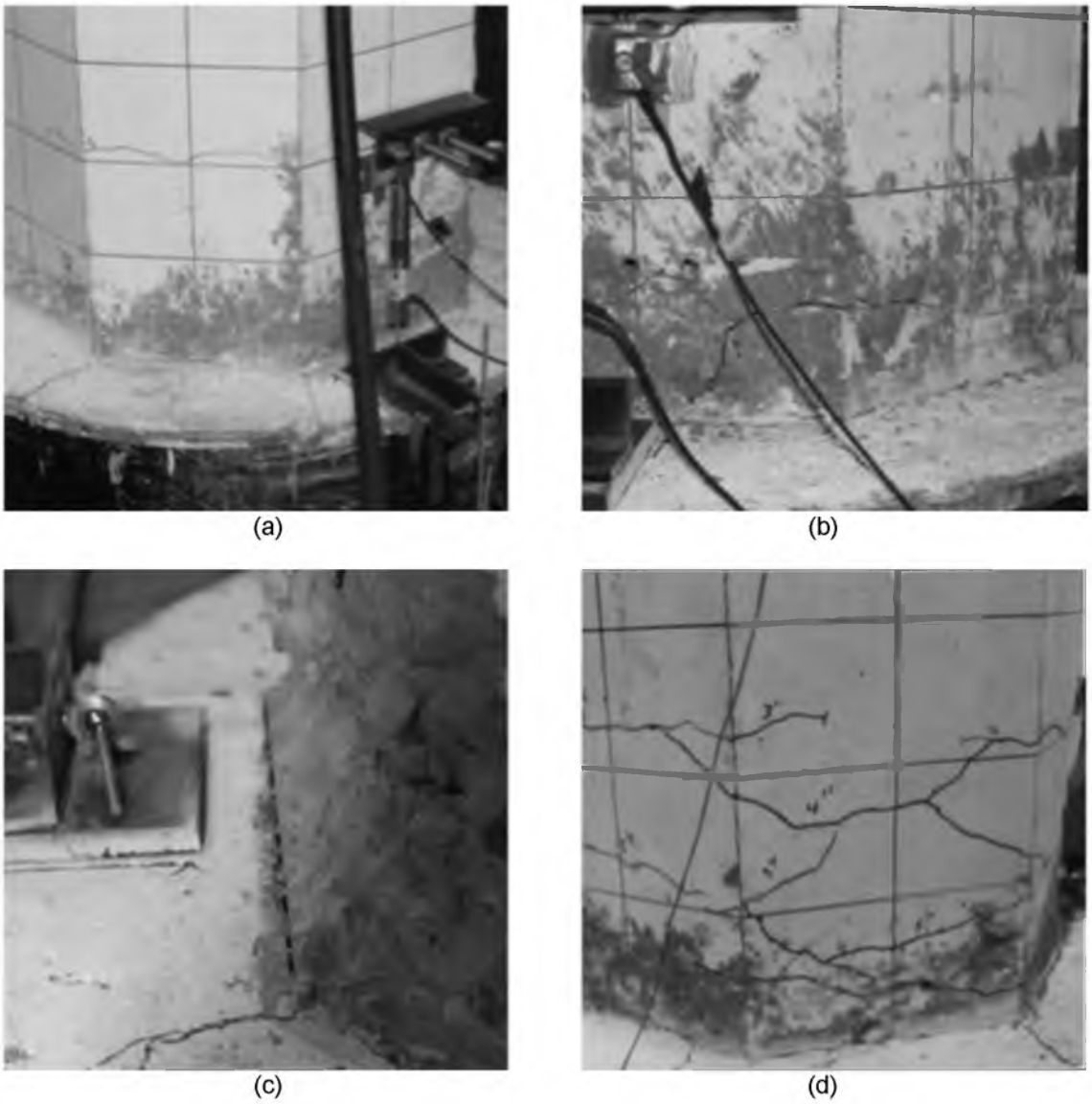

Figure 4.8 – NMB-2 Repair test pictures through the 6-in. displacement step: (a) Radial cracks after 1-in. displacement step, (b) First cracking occurring during 2-in. displacement step, (c) Gapping between repair-column interface during the 6-in. displacement step, (d) Shear x-cracking after the 4-in. displacement step

During the 5-in. displacement step a new flexural crack was observed 10 in. above the top of the repair. When the crack was measured at rest it was hairline. The radial cracks grew considerably during this displacement step from 0.005 in. to 0.025 in. The largest radial cracks were located on the west side of the repair. Spalling continued during this displacement step and the shear x-cracks grew in length, as shown in Figure 4.9(a).

No new cracking was observed during the 6-in. displacement step. The cracks located approximately 10 in. above the top of the repair increased in width from hairline to 0.1 in. and

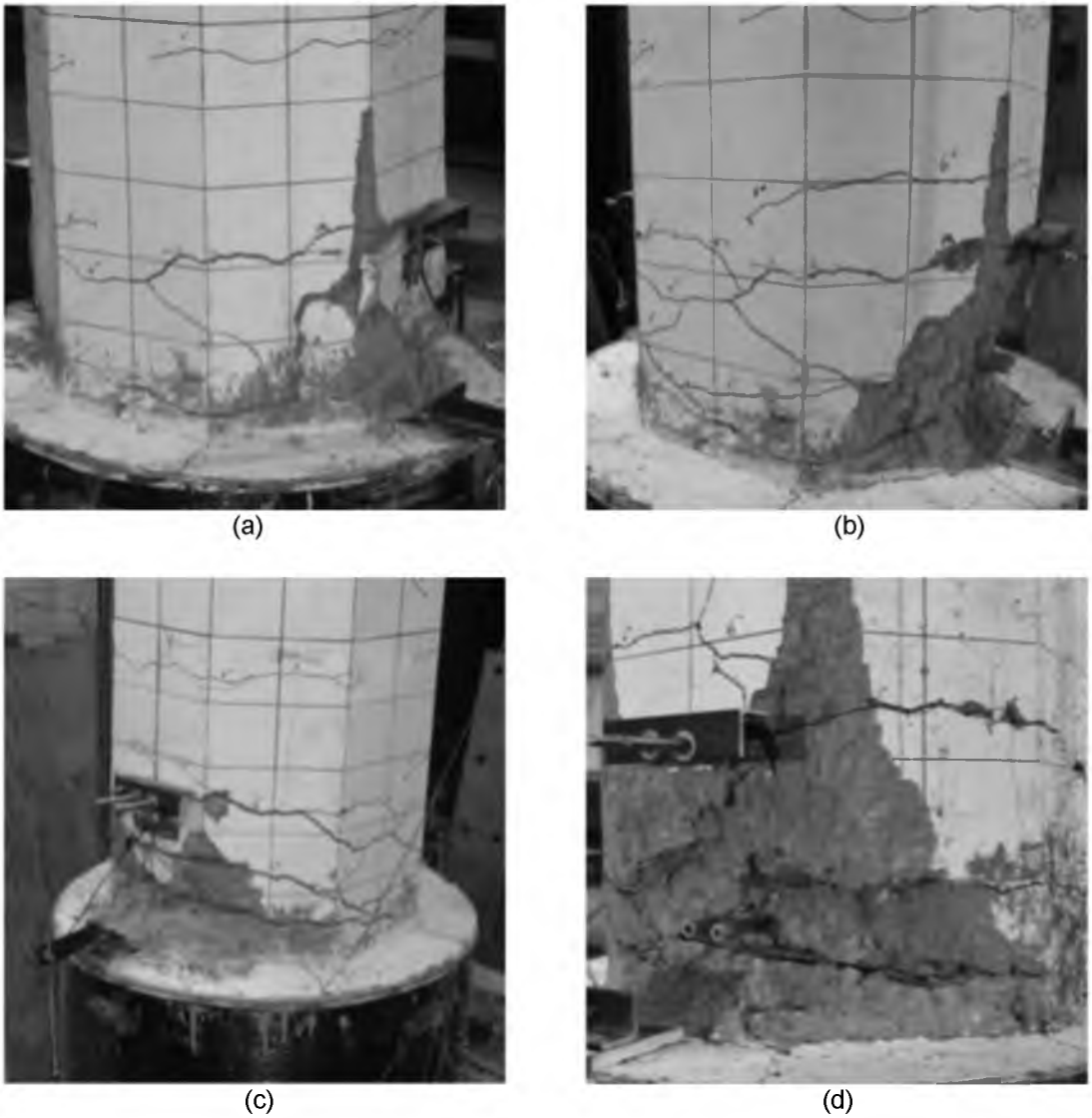

Figure 4.9 – NMB-2 Repair test pictures through final damage state: (a) Major spalling during 5-in. displacement step, (b) Damage level after 6-in. displacement step, (c) Damage state during 7-in. displacement step, (d) Final damage state

0.025 in. on the east and west column faces, respectively. The damage state at the end of the 6-in. displacement step is shown in Figure 4.9(b).

During the 7-in. displacement step both the west and east extreme longitudinal rebar fractured. The west longitudinal rebar fractured during the first cycle, and the east longitudinal rebar fractured during the second cycle, both in tension. In addition to rebar fracture, the shear x-cracking grew on the north and south faces, measuring 0.06 in. at pause. NMB-2 Repair at maximum displacement is shown in Figure 4.9(c). The final damage state of NMB-2 Repair is shown in Figure 4.9(d).

4.3 NMB-3 Repair test results

NMB-3 Repair was tested on October 15th, 2013, in the University of Utah Structures Laboratory. The results of the NMB-3 Repair test will be examined within this section. The damage state at the completion of the NMB-3 test is critical to understanding the performance of NMB-3 Repair and can be found in Section 2.4.2.

The objectives in repairing NMB-3 Repair were to restore the diminished load and displacement capacity of NMB-3 through plastic hinge relocation. The hysteretic performance of NMB-3 Repair is shown in Figure 4.10, and response envelope is shown in Figure 4.11. Plastic hinge relocation was achieved and is shown in Figure 4.12. The load capacity of NMB-3 Repair was improved by 30% when compared to NMB-3. It can be seen from the envelope that the ultimate drift achieved was 4.60% in the east direction and 5.89% in the west direction. A 20% drop in lateral load carrying capacity was reached in both directions between the 5-in. and 6-in. displacement steps; testing continued through the 8-in. displacement step. The damage state of NMB-3 Repair at displacement steps prior to the 6-in. displacement step can be seen in Figure 4.13. The displacement ductility in the east and west directions was 3.86 and 3.88, respectively. This is over a 40% decrease in displacement ductility from NMB-3. The failure mode of the specimen was longitudinal bar fracture of west extreme longitudinal rebar 10.25 in. above the top of the repair. The fracture occurred during the first cycle of the 5-in. displacement step in the east direction. The damage state of NMB-3 Repair after testing is shown in Figure 4.14.

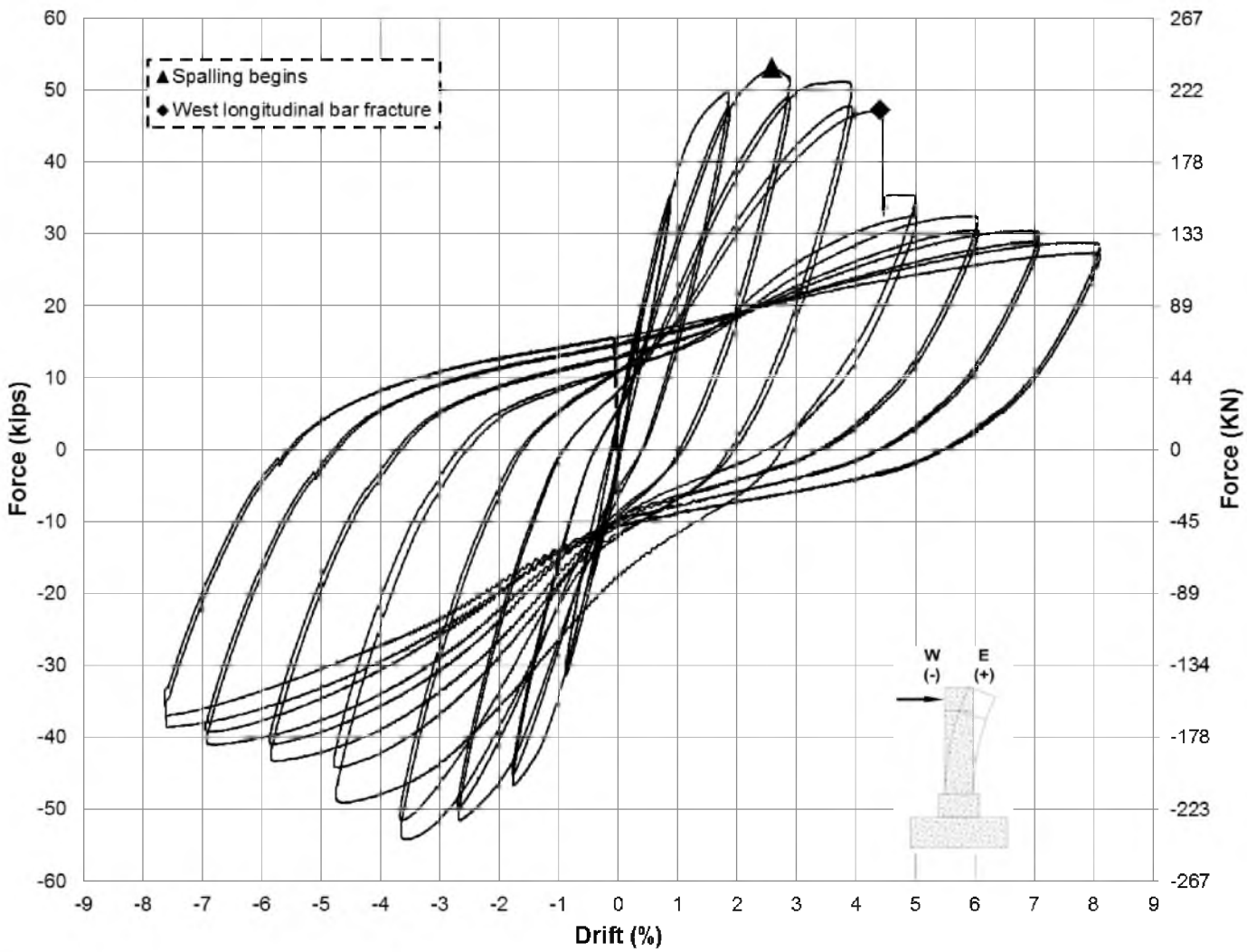

Figure 4.10 – NMB-3 Repair hysteresis curve

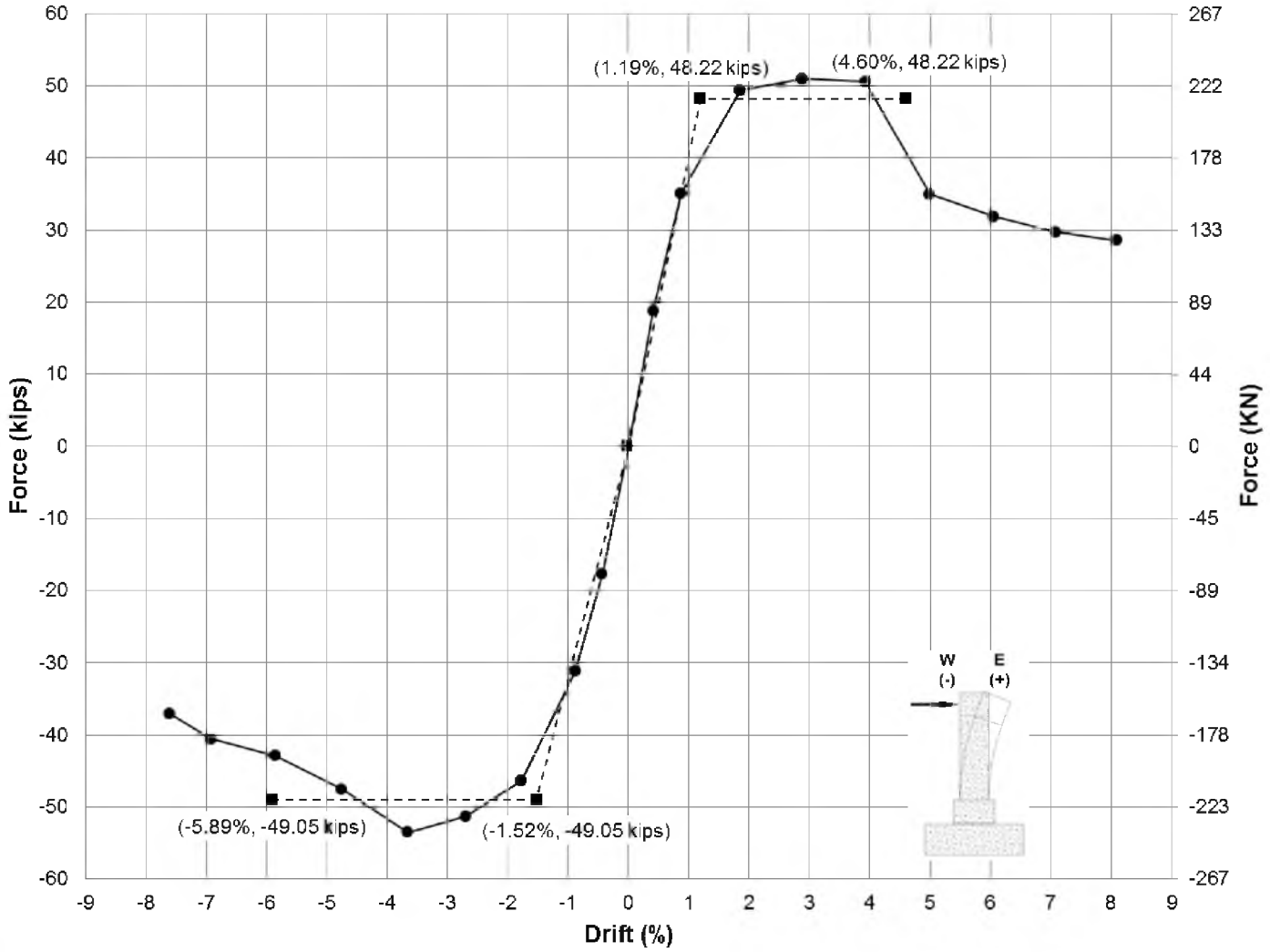

Figure 4.11 – NMB-3 Repair envelope curve

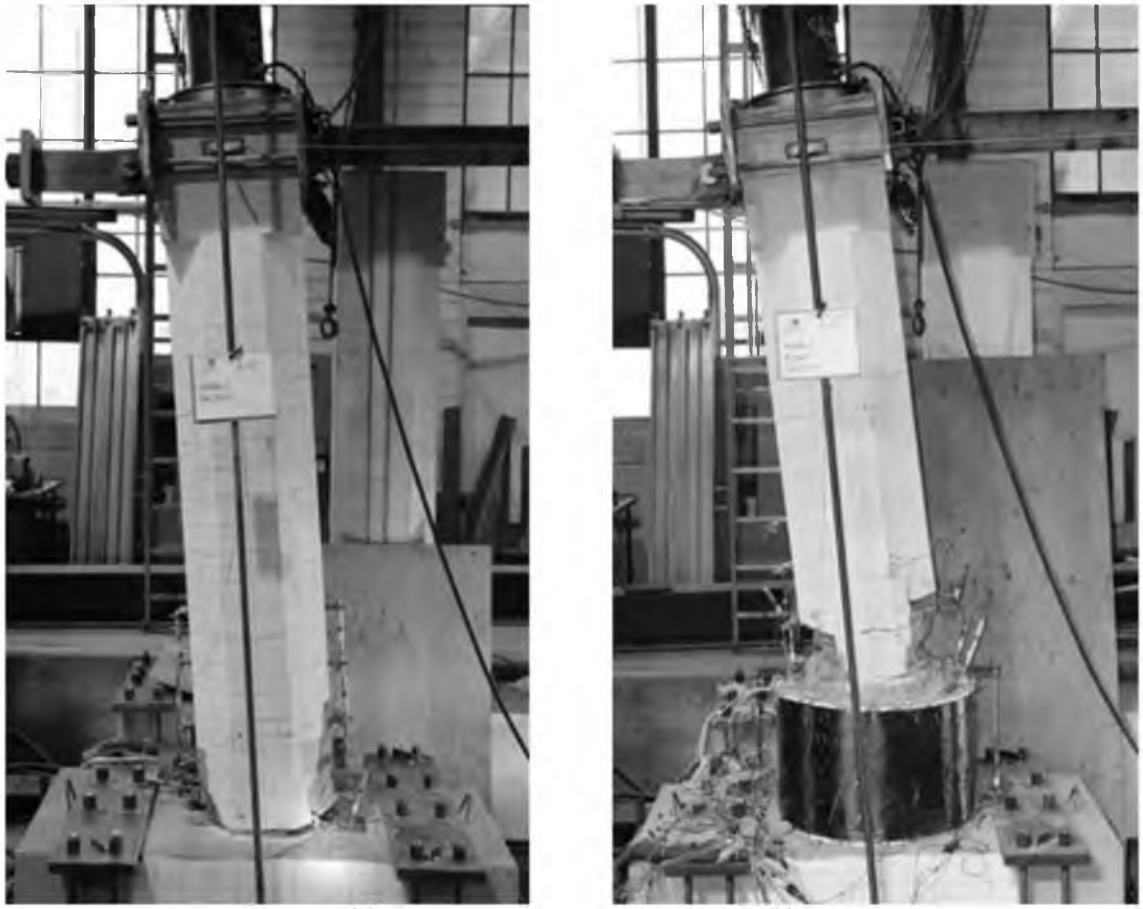

Figure 4.12 – Specimens displaced to the west at the maximum displacement step: (a) NMB-3, (b) NMB-3 Repair

The west longitudinal rebar fracture during the NMB-3 Repair test is believed to be premature. The type of fracture and the location seem to indicate that the rebar was embrittled from welding the all thread rods to the longitudinal rebar. The location of the fracture was in-between two all thread rods. Both of these rods had been tack welded onto the west longitudinal rebar to create a connection to attach LVDTs to during testing. The rebar cage prior to casting and the LVDT rods are shown in Figure 2.5 (c). Typical tack welds were used to secure the LVDT rods, shown in Figure 4.15. The fractured bar is shown in Figure 4.14. The fracture location was 10.5 in. above the top of the repair, corresponding to 30 in. above the top of the footing. This fracture location is higher than a typical longitudinal rebar flexural fracture. In the NMB-2, NMB-2 Repair, and NMB-3 tests, the rebar fractured within 0 in. to 4.5 in. from the

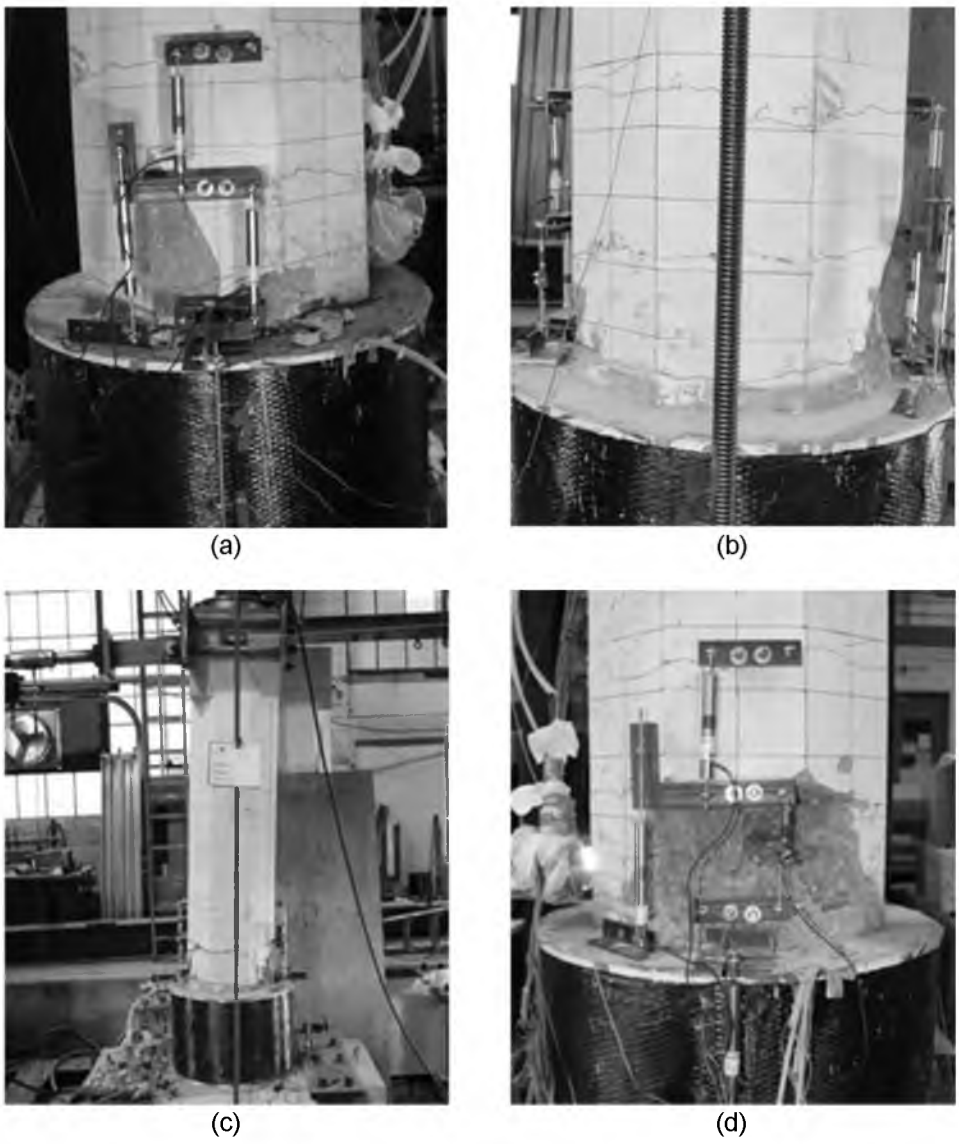

Figure 4.13 – NMB-3 Repair test pictures through 5-in. displacement: (a) Spalling on east face after 3-in. displacement step, (b) Onset of minor shear x-cracking after 4-in. displacement step, (c) The displacement in which fracture occurred, 5-in. displacement step, (d) Damage on west side after 5-in. displacement step

column interface. This interface is the column-footing interface for NMB-2 and NMB-3 and the column-repair interface in the case of NMB-2 Repair. The fracture location observed for NMB-2, NMB-2 Repair, and NMB-3 is typical for flexural behavior because the maximum moment demand on the column occurs at the interface.

The failure surface on the top of the west longitudinal rebar is nearly perfectly smooth and flat, indicating a brittle failure, as shown in Figure 4.14(d). This type of failure surface is

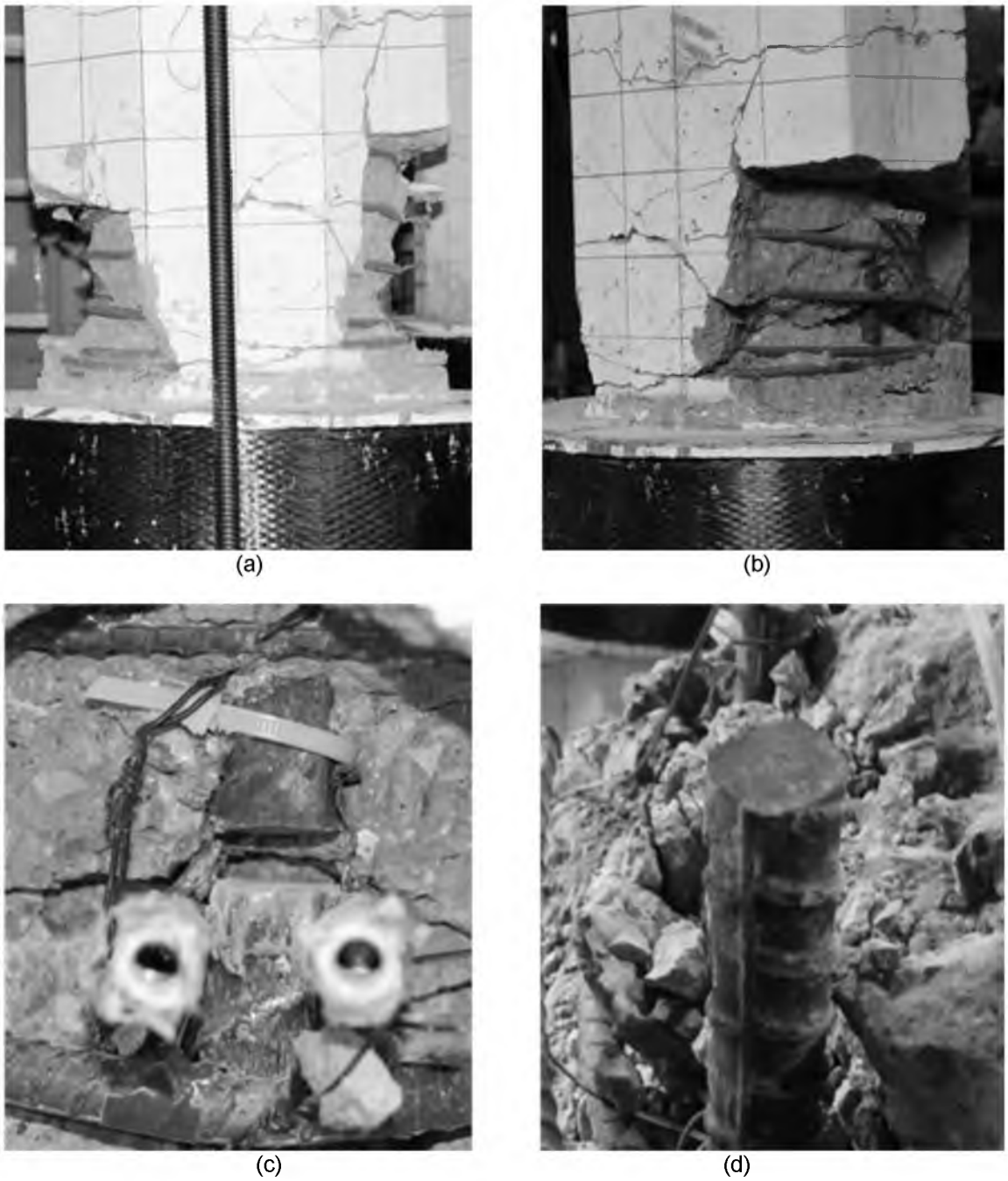

Figure 4.14 – NMB-3 Repair at the completion of testing: (a) Plastic hinge region, (b) East side of plastic hinge region, (c) West longitudinal rebar fracture at completion of test, (d) West longitudinal rebar fracture after removing the concrete

Figure 4.15 – Typical tack weld used to connect LVDT rods to the column longitudinal rebar

characteristic of high strength, brittle metals and does not match the type of failure surface seen in any of the previous tests. The welding is thought to have created an imperfection in the longitudinal rebar, which was verified during testing.

The other factors contributing to the premature failure of NMB-3 Repair include the high strength concrete on the day of testing, which was 9.33 ksi. The concrete strength during the NMB-3 Repair test is 45% stronger than the concrete strength during the NMB-2 Repair test. The high strength concrete increased the stiffness of the NMB-3 Repair specimen significantly when compared to the other specimens and increased the demand on the longitudinal rebar.

The location of the GSS in NMB-2 and NMB-3 were different, causing the loading history of the longitudinal rebar to differ. NMB-2 had the GSS located in the footing which caused the deflection of the column to behave in a monolithic fashion. NMB-3 had the GSS located in the column, which caused the column to deflect in a rocking manner, concentrating the plastisity within the footing. Curvature profiles illustrate these differences in deflection characteristics between the as-built NMB-2 and NMB-3 specimens, which are shown in Figure 4.16. The curvature profiles for the 2-in., 4-in. and 6-in. displacement steps are shown in Figure 4.16. NMB-3 experienced more curvature at heights above the future repair than NMB-2. This indicates that

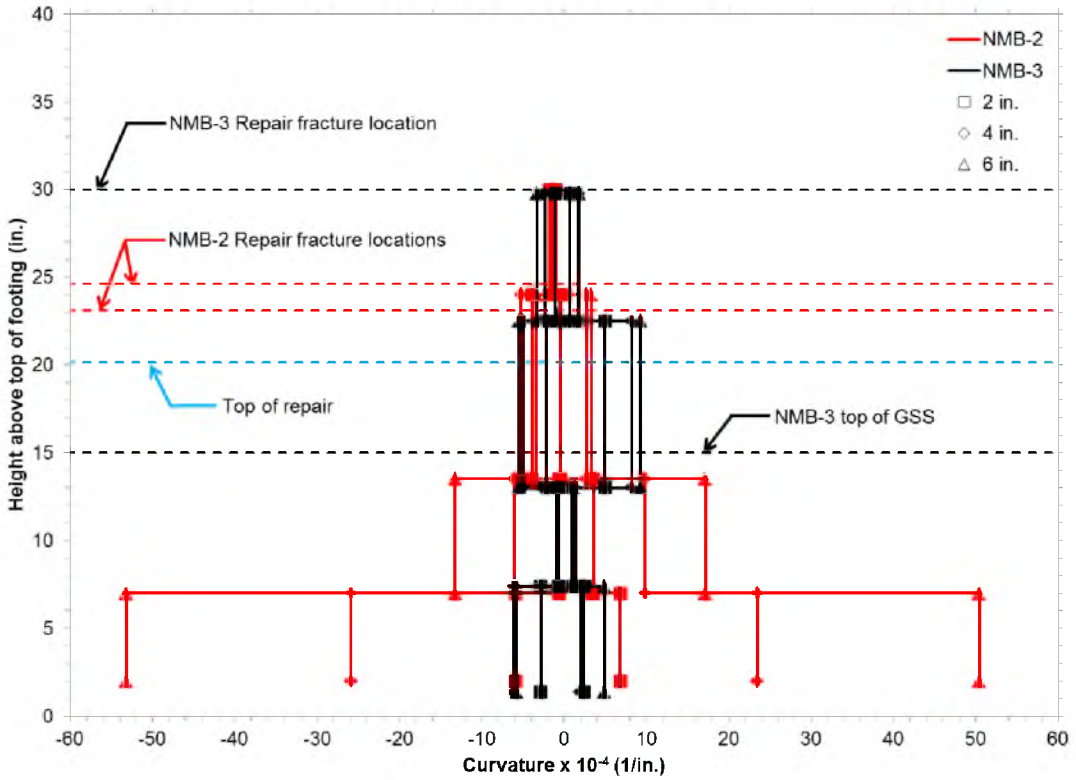

Figure 4.16 – Curvature profiles of NMB-2 and NMB-3

higher strains were present in the longitudinal rebar at the critical height for the repair. This difference in loading history is not thought to be the cause of the higher fracture location in NMB-3 Repair for a few reasons. Although NMB-3 did experience larger curvature than NMB-2 during the as-built test at the location of the NMB-3 Repair fracture, NMB-3 also experienced larger curvature at the typical fracture location, which is the top of the repair. From the NMB-3 Repair curvature profile, shown in Figure 4.17, it can be seen that the curvature just above the repair-column interface was likely much larger than at the location of fracture. From all of these factors it is concluded that the most likely cause of the premature longitudinal rebar fracture during the NMB-3 Repair test was embrittlement of the longitudinal rebar due to welding of the LVDT connection rods to the rebar.

Other notable features of the damage states of the NMB-3 Repair experienced during testing will be explained chronologically. During the 0.5-in. displacement step no damage was observed. The 1-in. displacement step created two new levels of hairline cracks at 8 in. and 18 in. above the top of the repair and opened up the crack obtained during NMB-3 test at 2 in. to 4 in.

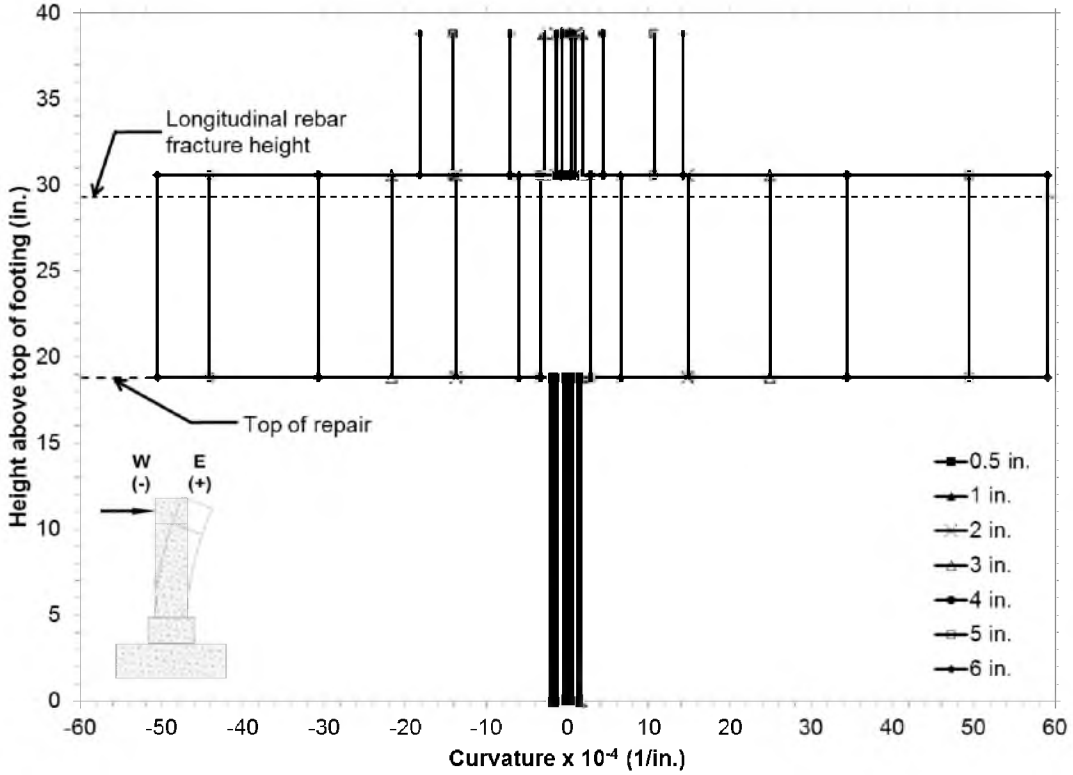

Figure 4.17 – NMB-3 Repair curvature profile

above the repair. All cracks were measured as hairline when no displacement was applied.

The 2-in. displacement step extended existing cracks and developed the first measurable cracks. The crack located at 2 in. to 4 in. above the repair was measured to be 0.009 in. and 0.007 in. wide on the west and east column faces, respectively. This measureable crack indicated the beginning of the plastic hinging formation.

Spalling began during the 3-in. displacement step, extending as much as 12 in. up the column on the east face, as shown in Figure 4.13(d). Cracking continued to grow at levels of 2 in. to 4 in., 8 in. to 9 in., and 18 in. above the top of the repair with maximum crack widths of 0.025 in., 0.009 in., and 0.005 in., respectively.

During the 4-in. displacement step, shear x-cracking began on both the north and south column faces, shown in Figure 4.13(b). The x-cracks were located 8 in. to 16 in. above the top of the repair. Spalling of the cover concrete above the repair significantly extended during this round. Cracking continued to grow at the levels of 2 in. to 4 in., 8 in. to 9 in., and 18 in. above the top of the repair with maximum crack widths of 0.03 in., 0.02 in., and 0.009 in., respectively.

During the first cycle of the 5-in. displacement step, the extreme west longitudinal rebar fractured in tension. The specimen at the time of fracture is shown in Figure 4.13 (c). The fracture was very loud and expanded the spalling on the west face, shown in Figure 4.13(d). Cracking continued to grow at levels of 2 in. to 4 in., 8 in. to 9 in., and 18 in. above the top of the repair with maximum crack widths of 0.04 in., 0.01 in., and 0.007 in., respectively.

A decrease in load of 46% in the east direction and 12% in the west direction occurred during the 6-in. displacement step. The cracks located at 2 in. to 4 in. and 8 in. to 9 in. above the repair could not be measured due to the amount of spalling that had occurred. The spalling had exposed longitudinal bars on both the east and west faces. The crack located 18 in. above the repair closed and was measured as hairline at pause.

No new cracking or spalling occurred during the 7 in. and 8-in. displacement steps. All of the additional damage from these cycles was through rebar straining or damage within the confined concrete core, which could not be seen. The plastic hinge region at the end of testing is shown in Figure 4.14.

4.4 CFRP wrap performance

The performance of the CFRP jacket used during the NMB-2 Repair and NMB-3 Repair tests is studied in this section. The four layers of unidirectional CFRP composite provided sufficient shear strength and confinement to the repaired cross-section, facilitating relocation of the plastic hinge region to the top of the repair for both tests. The CFRP jacket results are highly affected by the repair concrete properties, detailed in Section 4.1.4. The NMB-2 Repair specimen had repair concrete, which behaved similarly to nonshrink concrete, pre-tensioning the jacket to a strain of 0.01% prior to testing. The NMB-3 Repair specimen had repair concrete, which was expansive, pre-tensioning the jacket to a strain of 0.15% prior to testing. The strain results from testing will be compared to the effective strain capacities of the CFRP jackets. The effective strain capacity for both repairs was taken as 57% of the ultimate strain capacity recorded from tensile coupon tests *(33)*. The CFRP strain efficiency factor accounts for strain concentrations, and the multiaxial state of stress acting on the jacket when the CFRP wrapped member is subjected to

compression and bending.

4.4.1 NMB-2 Repair

The concrete that filled the NMB-2 Repair specimen's CFRP jacket was nonshrink concrete that pre-tensioned the jacket to 105 microstrain. This is a very small amount of pre-tensioning, accounting for less than 2% of the jackets effective strain capacity. Transverse CFRP cracking onset during testing at the 4-in. displacement step and grew throughout the subsequent displacement steps, as shown in Figure 4.6. Although this characteristic is of concern, the transverse cracking did not adversely affect the results of the repair. Additional precautions to prevent transverse cracking in future applications of the repair are discussed in Chapter 6.

Figure 4.18 shows the uneven vertical distribution of strain throughout the CFRP jacket during the NMB-2 Repair test. Four different levels of strain gauges, placed at different heights above the top of the footing, are averaged together on all four sides of the CFRP jacket giving an average top band, top, middle, and bottom strain value. The top band, top, middle, and bottom levels of strain gauges are located 16.5 in.,14.5 in.,9.5 in., and 4.5 in. above the top of the footing respectively. From Figure 4.18 it can be seen that the maximum strain reached in the bottom, middle, and top levels is 15%, 38%, and 78% of the maximum strain reached in the top band level.

Figure 4.18 shows a plateau in the strain that the wrap develops, which begins with the 4-in. displacement step. The maximum lateral load was reached during the 4-in. displacement step. The peak strains for each displacement step follow the shape of the response envelope from testing, implying that the jacket strain level is controlled by load rather than displacement. The maximum strain recorded in the jacket was on the east side of the wrap at the level of the top band as 3200 microstrain. The effective strain capacity of the CFRP jacket is 6440 microstrain, meaning that the jacket reached a maximum of 50% of its effective strain capacity during testing.

Uneven straining of the jacket, when displaced east and west, is shown in Figure 4.18. The second displacement in each cycle, corresponding to a displacement in the east direction, experiences more strain than in the first displacement. This uneven directional straining is

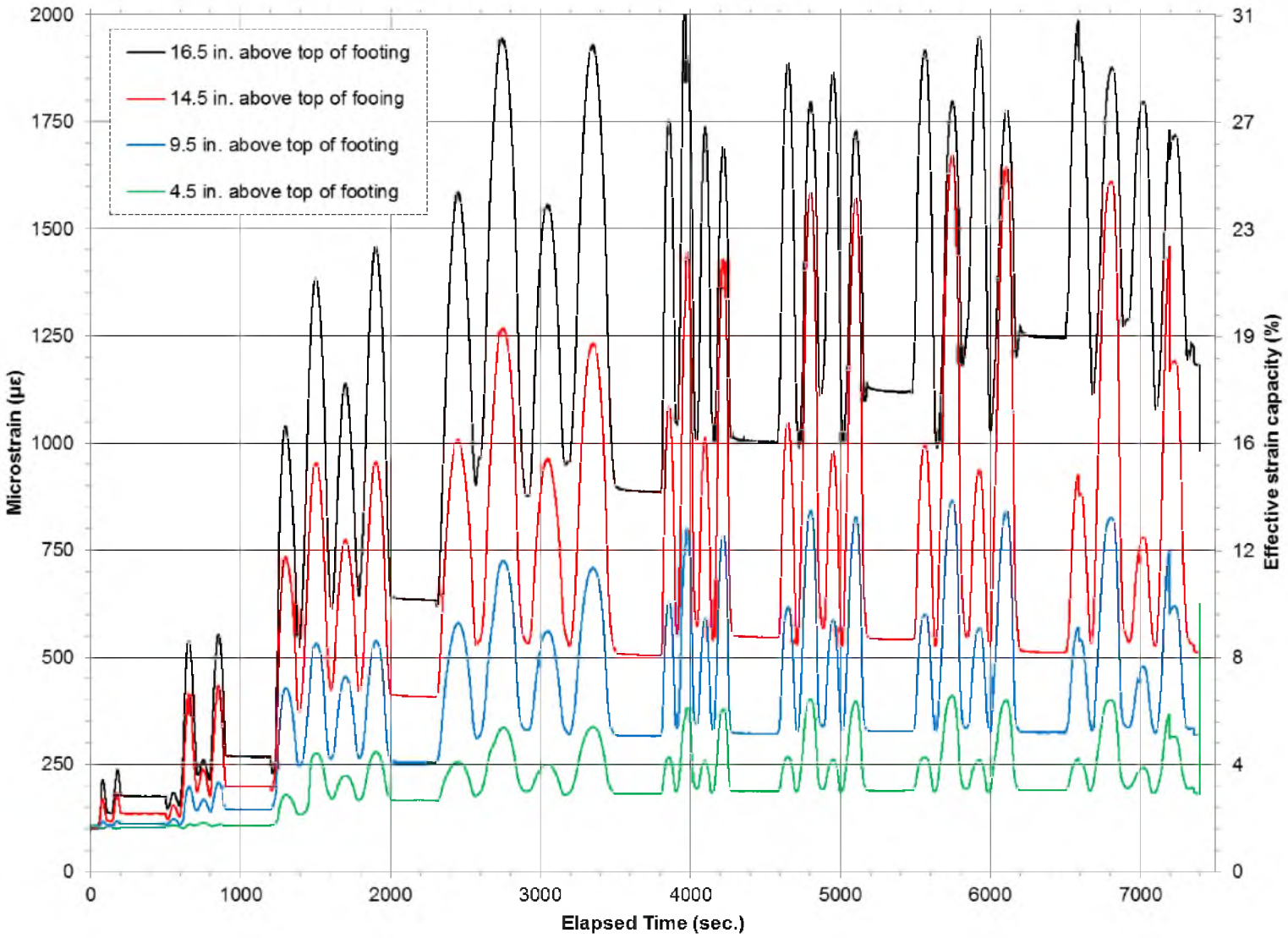

Figure 4.18 – NMB-2 Repair wrap strain gauge data averaged by height

present up to the first cycle of the 4-in. displacement step when the jacket developed the transverse crack. The cracking relieved the uneven distribution of directional strain.

The onset of transverse cracking can be seen from individual strain gauge data from the top band, shown in Figure 4.19. The top band east strain gauge is engaged in both of the displacement directions through the first cycle of the 4-in. displacement step when transverse cracking began. The onset of the transverse crack relieved the straining in both directions and the wrap began to act similar to the top band west strain gauge, shown in Figure 4.19(a).
At the pause between displacement steps, the wrap is experiencing residual strain from dilation of the repair concrete. It can be seen in both Figures 4.18 and 4.19 that there is a slight increase in residual strain at the completion of each displacement step. The largest increase in residual jacket strain is between the 1-in. and 2-in. displacement steps. This increase is due to the repair concrete cracking, which was observed as radial cracks during testing, shown in Figure 4.8(a). The radial cracks cause the repair concrete to dilate and increase the pressure on the CFRP wrap, thereby increasing the wrap strain.

4.4.2 NMB-3 Repair

The repair concrete used for NMB-3 Repair was expansive concrete; the average pre-tensioning in the CFRP jacket due to the repair concrete prior to testing was 1535 microstrain. This is a significant amount of pre-tensioning, accounting for nearly 24% of the jacket's effective strain capacity. No transverse cracking occurred during testing, which was likely due in part to the high pre-tensioning in the jacket. The pre-tensioning increases the tensile strength of the repair concrete and alleviates the need for the CFRP to be stressed in the longitudinal direction.

The maximum strain that the wrap developed occurred during the 4-in. displacement step, shown in Figure 4.20. The 4-in. displacement step was the last displacement step before one of the west longitudinal bars broke. The maximum lateral load was reached during the 3-in. displacement step. The maximum strain in the jacket during testing was 3695 microstrain at a location 1 in. below the top of the wrap on the west side of the repair. This maximum strain is an increase of 2160 microstrain from the pre-tensioning. The effective strain capacity of the jacket is 6440 microstrain, meaning the jacket reached 57% of its effective strain capacity.

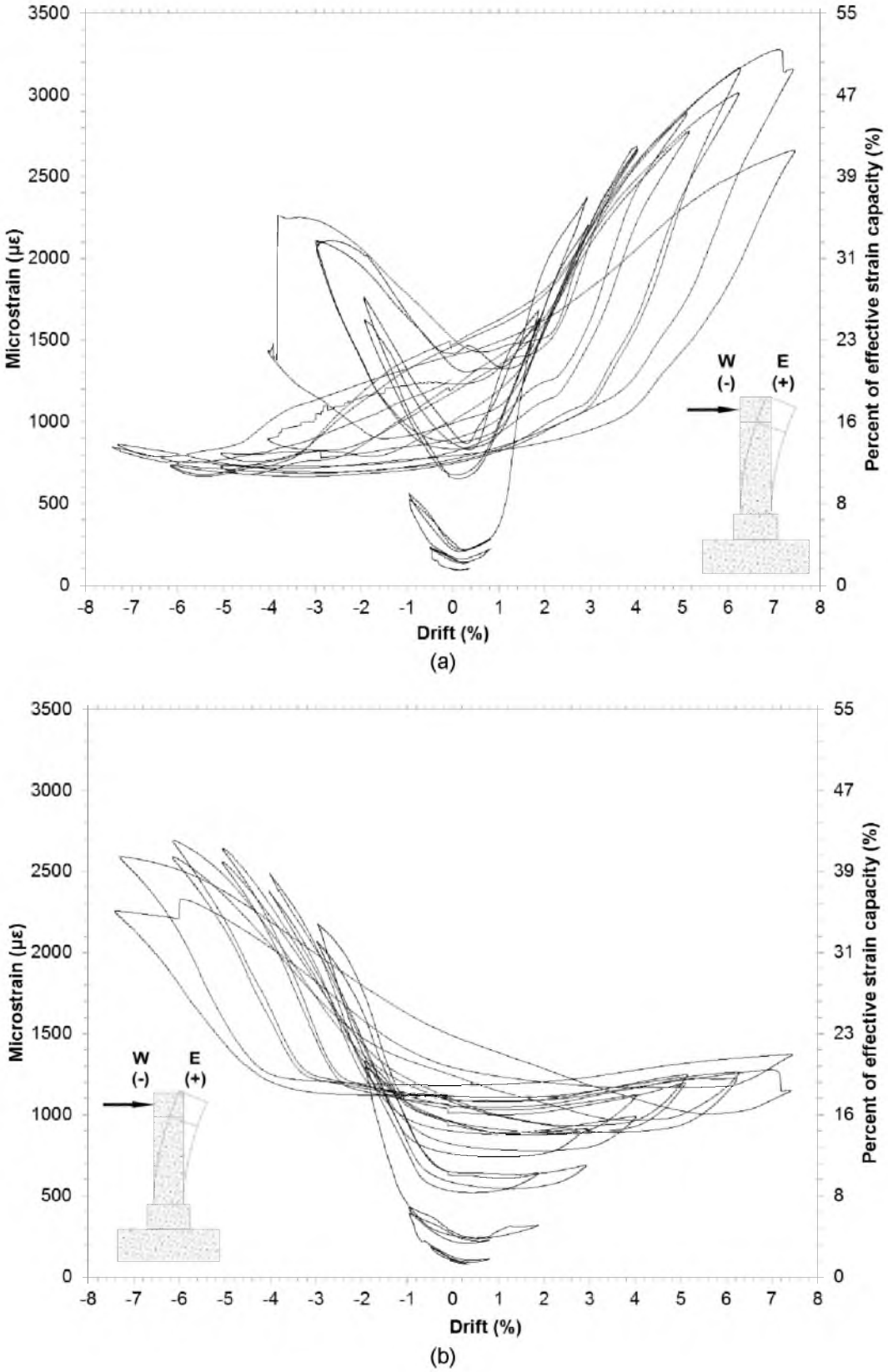

Figure 4.19 – NMB-2 Repair wrap strain gauge data from top band, 3 in. below the top of the repair: (a) East, (b) West

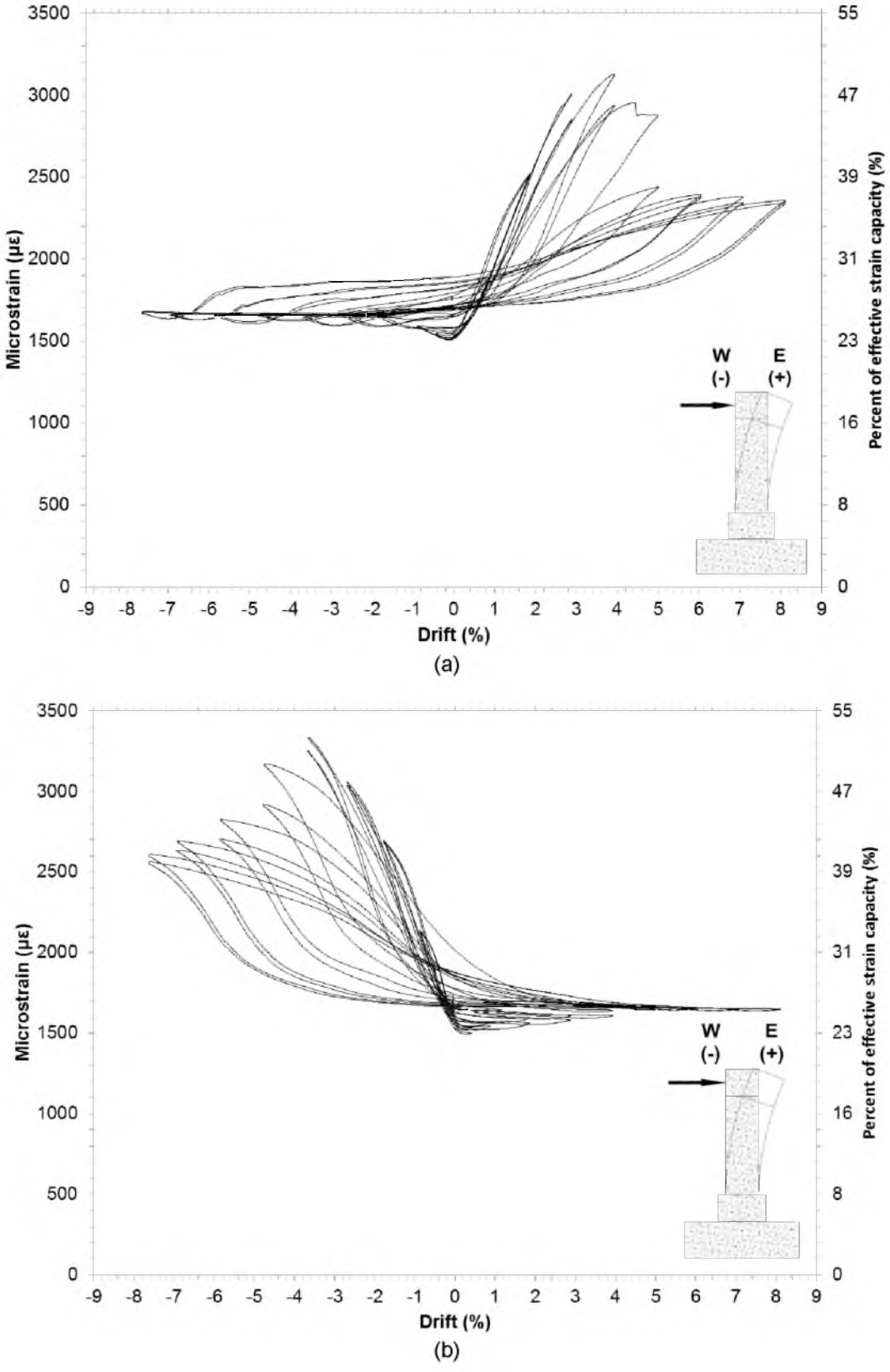

Figure 4.20 – NMB-3 Repair wrap strain gauge data from top band, 3 in. below the top of the repair: (a) East, (b) West

In Figure 4.21 the uneven distribution of strain vertically throughout the jacket is shown. The strain profile in Figure 4.21 is a plot of the strain gauge height above the footing versus the maximum strain that the gauge read during a displacement step. All of the points from a given displacement step are then connected with a dashed line due to the uncertainty in strain between points.

The strain that the jacket experiences, as a function of distance above the top of the footing, exponentially increases up to a height of 15 in. above the top of the footing. At 15 in. above the top of the footing there is a discontinuity in the strain profiles. The postinstalled headed bars extended to 15 in. above the top of the footing and are thought to be the reason for the discontinuity in the wrap strain profiles. The mechanisms that transfer tension to the CFRP wrap are the headed rebar and the column bearing on the expansive concrete and transferring tension to the wrap. The discontinuity in the strain profile signifies the contribution that the headed rebar plays in transferring tension to the wrap.

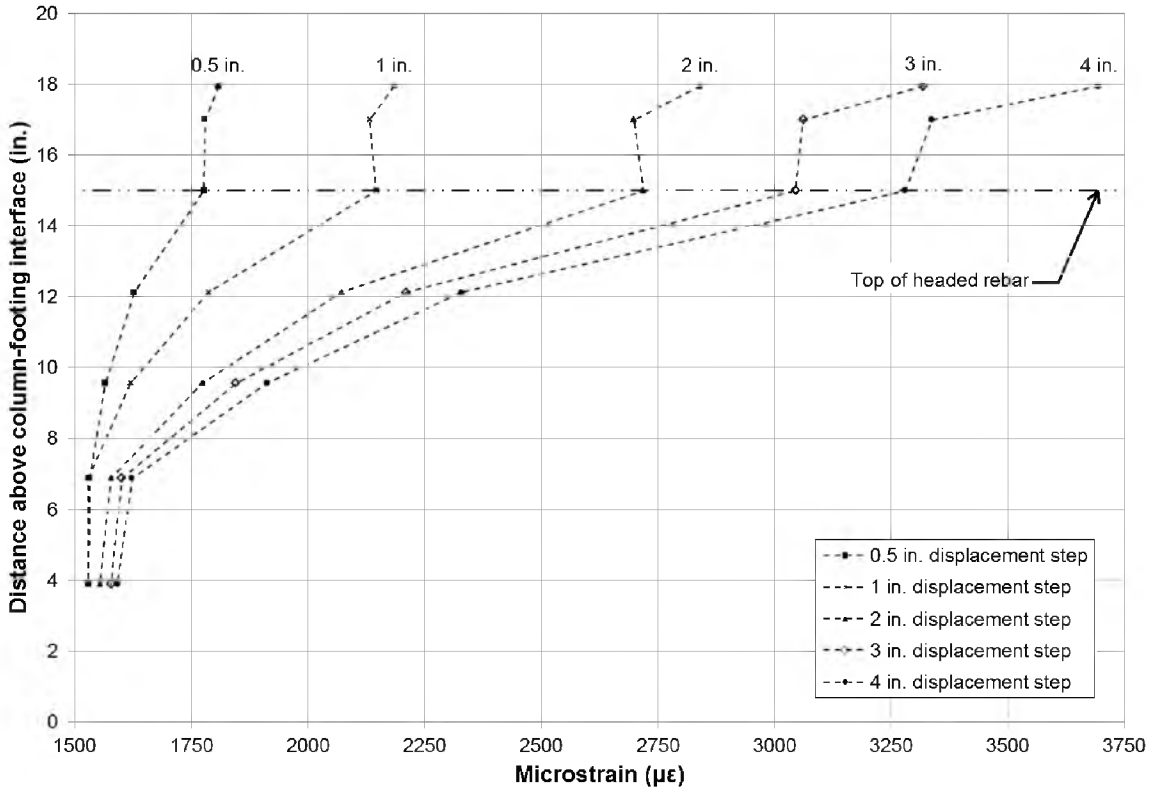

Figure 4.21 – NMB-2 Repair west face wrap strain profile up to 4-in. displacement step

The maximum strain that the wrap experiences at 3.875 in. above the top of the footing is 1601 microstrain. This is only a 66 microstrain increase from the pre-tensioning, an additional 1.02% of the effective strain capacity. The strain gauge located 6.875 in. above the top of the footing only experiences a 92 microstrain increase from the pre-tensioning, an additional 1.43% of the effective strain capacity. These numbers show the minimal strain that the wrap develops after pre-tensioning near the top of the footing.

4.4.3 Comparison of wrap performance

The behavior of the CFRP wrap used for NMB-2 Repair and NMB-3 Repair is directly related to the ultimate load that the system experiences. The CFRP jacket strain results for both tests can be found in Table 4.2 along with the averaged ultimate load achieved by the specimen. The average ultimate load is the average of the ultimate loads achieved during testing in the east and west directions. In Table 4.2, the maximum strain recorded in the CFRP jacket is listed for NMB-2 Repair and NMB-3 Repair from gauges located at 2 in. and 1 in. below the top of the repair, respectively. The maximum value of strain recorded while testing NMB-2 Repair was 87% of the maximum strain recorded in the CFRP jacket while testing NMB-3 Repair. This difference is nearly the same as the 86% difference in average ultimate loads. This indicates that the pre-tensioning does not significantly affect the ultimate strain that the wrap experiences; however, it does affect the increase in strain beyond pre-tensioning that the wrap develops. The pre-tensioning in MNB-2 Repair was only 7% of the pre-tensioning in NMB-3 Repair.

Although the pre-tensioning does not change the maximum strain within the jacket, the pre-tensioning may influence the likelihood of transverse cracking. NMB-3 Repair did not experience transverse cracking in the jacket even though the maximum strain values were larger. One of the main differences regarding the CFRP wrap for NMB-3 Repair was the larger pre-tensioning. This leads to the notion that the pre-tensioning may help to mitigate transverse cracking by increasing the tensile strength of the repair concrete. Additional tensile strength of the repair concrete mitigates cracking and alleviates the longitudinal stresses in the CFRP wrap. More research is needed to determine the optimal pre-tensioning for the repair.

Table 4.2 – CFRP jacket strains and comparison for NMB-2 Repair and NMB-3 Repair

		NMB-2 Repair	NMB-3 Repair	NMB-2 Repair/ NMB-3 Repair
Average ultimate load (kips)		44.6	52.1	86%
CFRP jacket strains (με)	Prestressing	105	1535	7%
	Maximum recorded	3200	3695	87%
	Maximum increase after prestressing	3095	2160	143%

4.5 Headed rebar performance

The performance of the headed rebar used for repairing NMB-2 Repair and NMB-3 Repair will be studied in this section. The differences between the performances of the headed rebar in the two tests will also be examined. The six no. 8 headed rebar provided sufficient flexural strength and tension transfer between the column and footing to successfully relocate the plastic hinge region to the top of the repair for both tests. The design and installation procedure used for the headed bars can be found in Chapter 3. The material properties of the headed rebar and epoxy used to anchor the headed rebar can be found in Section 4.1.

4.5.1 NMB-2 Repair

Two strain gauges were placed halfway up the free length of the headed rebar, correlating to 7.5 in. above the top of the footing, on the extreme east and west headed bars prior to testing. The data recorded during testing from these strain gauges is shown in Figure 4.22. The strain gauge on the east headed rebar went off scale during the 2-in. displacement step due to the high level of strain that the bar experienced.

The behavior of the headed rebar observed during testing seems to be influenced by the final damage state of NMB-2. The east longitudinal rebar in the column of NMB-2 fractured during testing, diminishing the flexural capacity of the specimen in that direction. The headed rebar replaced this lack of flexural capacity in both tension and compression creating a moment couple. The east headed rebar yielded in tension during the 1-in. displacement step reaching

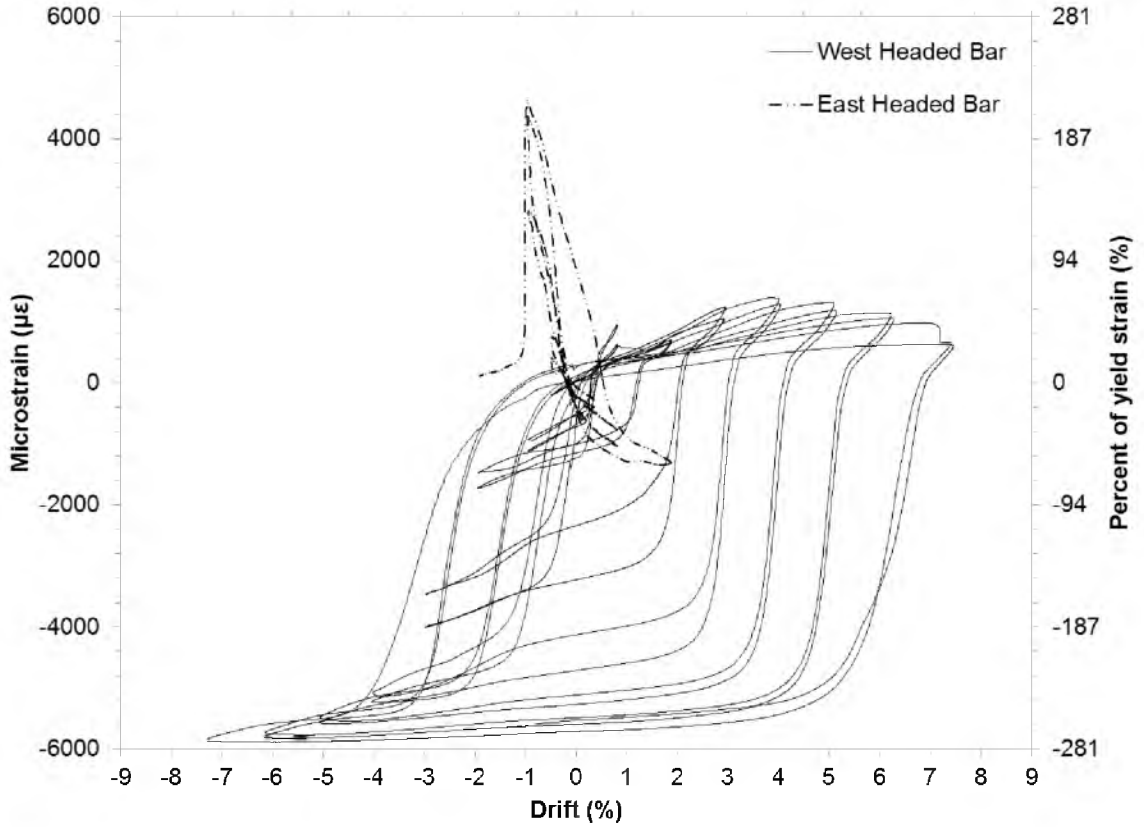

Figure 4.22 – NMB-2 Repair headed bar strain gauge data from 7.5 in. above the footing level

strains of over 1.9 times the yield strain during this displacement step. After the 1-in. displacement step the east strain gauge was lost. It is assumed that the east headed bar went well beyond 1.9 times the yield strain in subsequent displacement steps. The west headed rebar yielded in compression during the 3-in. displacement step, reaching compressive strains of nearly 2.8 times the yield strain during the 7-in. displacement step.

4.5.2 NMB-3 Repair

The strain gauge data from 7.125 in. above the top of the repair on the west extreme headed rebar and 6.5 in. above the top of the footing on the east extreme headed rebar are shown in Figure 4.23 versus both drift and lateral load. From Figure 4.23 it can be seen that the headed rebar at these two locations reached up to 50% of the yield strain during testing. When looking at the strain data plotted versus load it can be seen that the headed rebar acted linearly with a different stiffness in compression and tension. This linear relationship with load remains

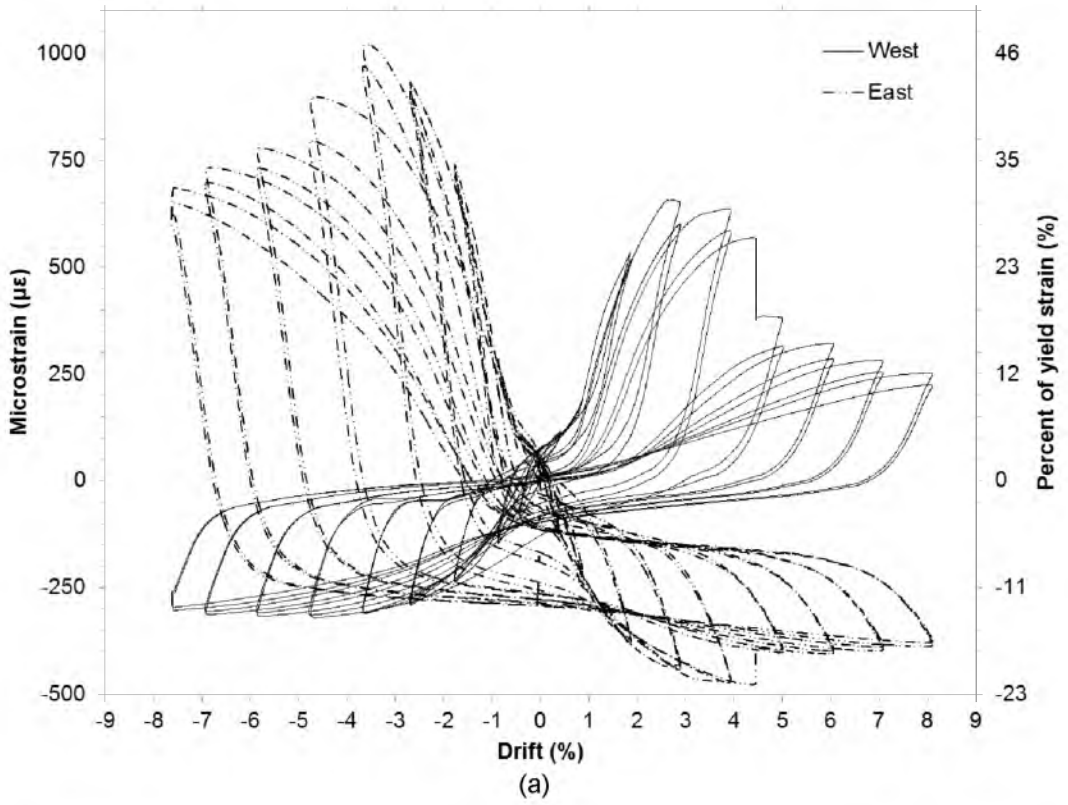

(a)

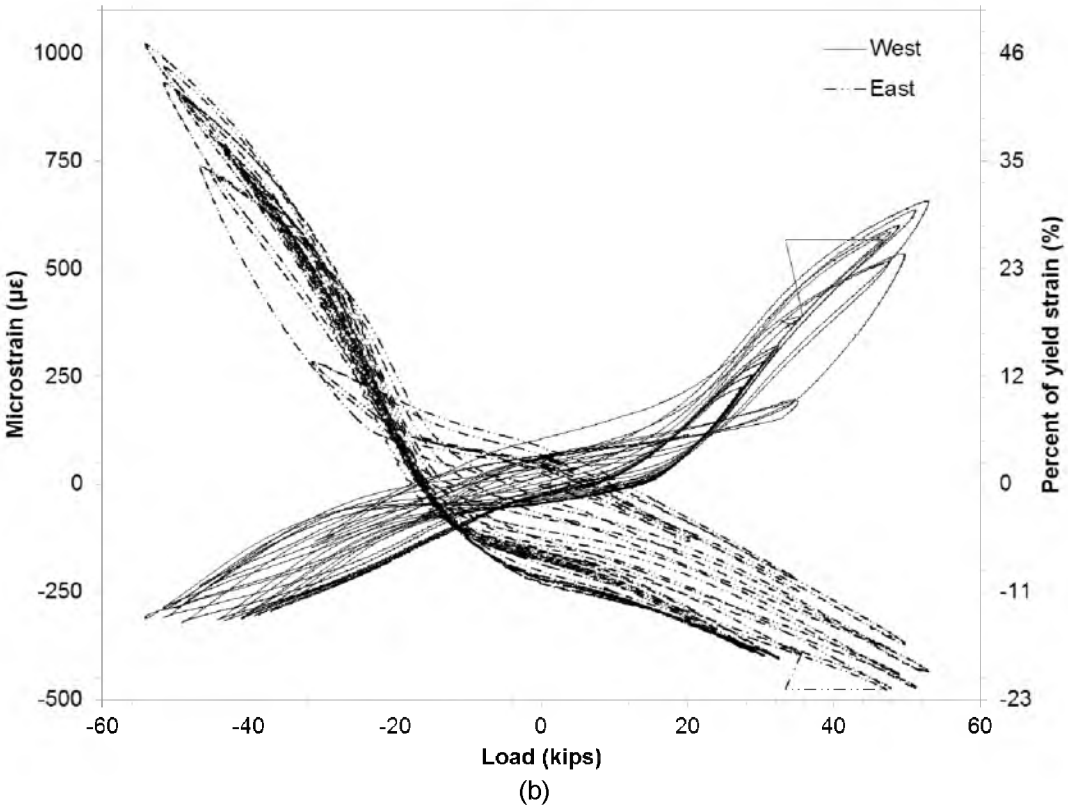

(b)

Figure 4.23 – NMB-3 Repair headed bar strain gauge data from west gauge 7.125 in. above the footing level and east gauge 6.5 in. above the footing level plotted versus: (a) Drift, (b) Load

constant throughout the test since the headed rebar remained elastic. The east headed rebar appears to have more strain than the west headed rebar, partially due to the gauge being located closer to the footing on the east rebar.

There were six strain gauges placed on the extreme west headed rebar located at 1 in, 4.25 in., 7.125 in., 8.375 in., 10.5 in., and 14.5 in. above the top of the footing. The maximum strain during the 0.5-in. through 4-in. displacement steps in tension and compression is plotted versus the distance from the top of the footing in Figure 4.24. These strain profiles show that the highest strains in the headed rebar occur at the repair-footing interface. This is reasonable since this is the location with the maximum development length and maximum moment demand. There is a large variation in the strain profiles for the displacement steps up to 2 in., which is due to the large difference in the maximum load during those displacement steps. The envelope curve of NMB-3 Repair, in Figure 4.11, shows that the maximum load starts to form a plateau at the 2-in. displacement step.

4.5.3 Comparison of headed rebar performance

Unlike the CFRP wrap performance, the headed rebar performance does not seem to follow a trend between NMB-2 Repair and NMB-3 Repair. Although NMB-3 Repair reached a higher ultimate load than NMB-2 Repair, the headed bars were strained much less in NMB-3 Repair. At the midheight of the headed bar length above the top of the footing, the maximum strains recorded in the NMB-2 Repair and NMB-3 Repair tests were 1.9 and 0.44 times the yield strain, respectively. Furthermore the maximum strain gauge reading, of 1.9 times the yield strain, for NMB-2 Repair occurred during the 1-in. displacement step and likely experienced much higher strains in subsequent displacement steps. However, it would be expected that NMB-3 Repair would experience somewhat less demand on the headed rebar due to the higher column and footing concrete strength and the higher repair concrete strength.

The extreme east longitudinal rebar was fractured in the as-built column during both the NMB-2 Repair and NMB-3 Repair tests. This deficiency in the as-built column can be clearly seen during the NMB-2 Repair test due to the large moment couple that the headed bars provide

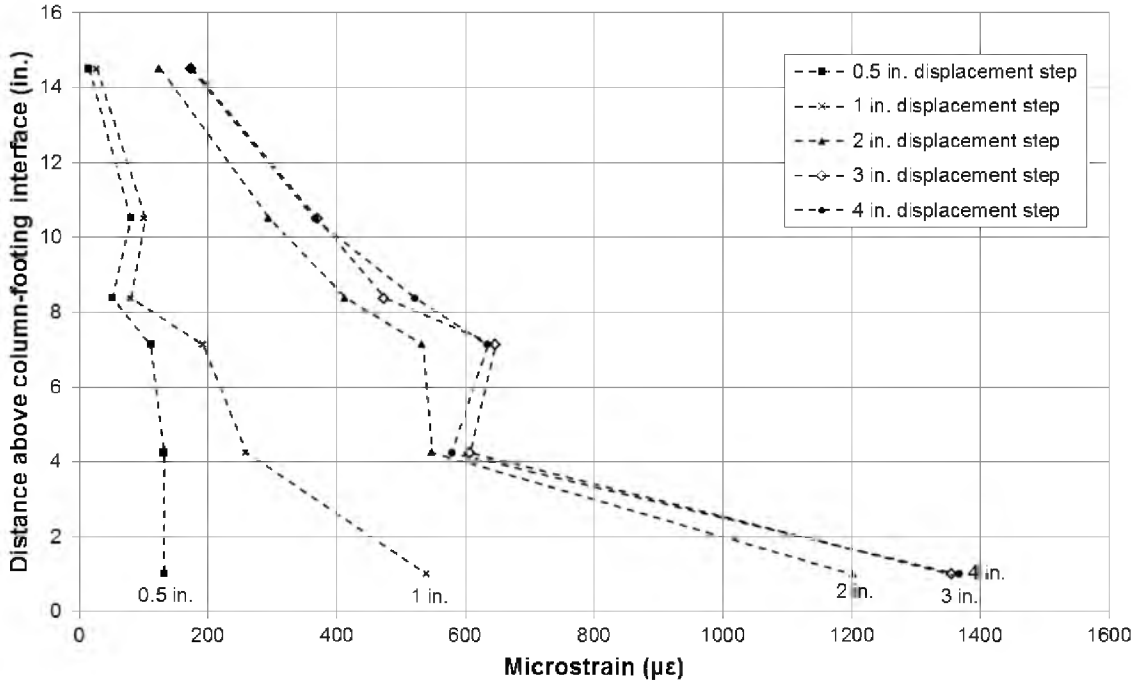

(a)

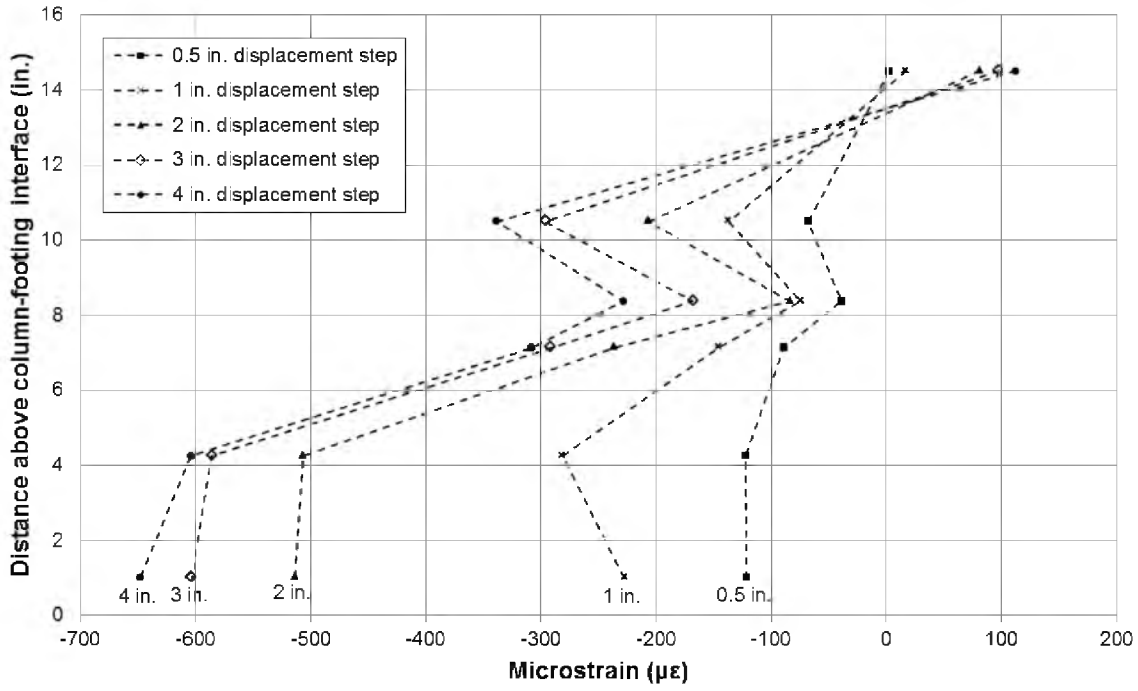

(b)

Figure 4.24 – NMB-3 Repair west headed rebar strain profile up to 4-in. displacement step: (a) Tension, (b) Compression

when the specimen is displaced to the west. However, the headed rebar shared the load symmetrically between the west and east sides during the NMB-3 Repair test.

The repair concrete, which had drastically different properties between NMB-2 Repair and NMB-3 Repair, may play a large role in the behavior of the headed rebar. The repair concrete in NMB-2 Repair was nonshrink, and in NMB-3 Repair the repair concrete was expansive. As mentioned previously, the increased pre-tensioning of the CFRP jacket for NMB-3 Repair increased the tensile strength of the repair concrete significantly. The amount of tension that is transferred to the headed bars would be significantly decreased when the repair concrete can take much of the tensile load. The pre-tensioning in NMB-3 Repair also increases the compressive strength of the repair concrete significantly, which reduces the demand on the headed rebar. The expansive repair concrete used for NMB-3 Repair is thought to be the main reason that the demand on the headed rebar during the NMB-3 Repair test was much less than during the NMB-2 Repair test.

4.6 Comparison of tests

To understand the performance of the repair tests, the results must be compared to the as-built tests. This is a comparison between the cyclic performance of a precast concrete column-to-footing assembly where the column is connected to the footing using GSS connections and the subsequent repair. Also, the results from the NMB-2 Repair and NMB-3 Repair tests must be compared to understand the advantages and disadvantages of the design decisions made between the two. This section will compare the results of NMB-2, NMB-2 Repair, NMB-3, and NMB-3 Repair in terms of the overall system performance, energy dissipation capacities, and stiffness degradation characteristics.

4.6.1 System performance

The system performance of all the tests in terms of lateral load capacity, displacement capacity, displacement ductility, and energy dissipation capacity is shown in Table 4.3. It can be seen that the repair tests had approximately 30% larger lateral load capacities than the as-built

Table 4.3 – Performance evaluation criteria comparison

Performance evaluation criterion		NMB-2	NMB-2 Repair	NMB-3	NMB-3 Repair	NMB-2 Repair / NMB-2 (%)	NMB-3 Repair / NMB-3 (%)	NMB-2 Repair / NMB-3 Repair (%)
Lateral load capacity (kips)	East	37.8	44.4	39.9	51.0	118	128	87
	West	-31.9	-45.6	-41.2	-53.6	143	130	85
	Average	34.3	44.6	40.6	52.1	130	128	86
Displacement capacity (in.)	East	6.61	6.68	7.83	4.41	101	56	151
	West	-6.00	-6.69	-7.33	-5.66	111	77	118
	Average	6.42	6.68	7.59	4.64	104	61	144
Displacement ductility	East	6.44	7.52	6.66	3.86	117	58	195
	West	5.39	4.15	6.90	3.88	77	56	107
	Average	6.10	5.95	6.79	3.66	98	54	162
Cumulative energy dissipation (kip-in.)	4 in. displacement step	573	654	301	696	114	231	94
	Total	1563	2240	2753	1114	143	40	201

tests. This increase in load capacity is thought to be due to two reasons. First, the moment arm for the repair tests is decreased by nearly 20% due to the height of the repair and therefore, a larger load is required to achieve a plastic hinge. Second, the repair tests occurred after the as-built tests and therefore, the concrete compressive strength of the as-built concrete was always larger.

The displacement capacity of NMB-2 Repair is slightly greater than the displacement capacity of NMB-2. This is an interesting trait because the repair should have a decreased displacement capacity due to the shortened column length. This truncated column means that for a given displacement the repair will have a larger rotational demand than the as-built. However, the as-built is a precast specimen using GSS as the connection and the displacement capacity may be adversely affected due to slip. The repair transforms the precast specimens into systems that perform more like monolithic assemblies in terms of curvature. NMB-3 Repair did not have

as much displacement capacity as NMB-3 due to the longitudinal rebar fracture occurring during the 5-in. displacement step. This fracture is thought to be an anomaly due to a flaw in the rebar from welding.

The averaged displacement ductility of NMB-2 Repair, 5.95, is nearly identical to the displacement ductility of NMB-2, which was 6.10. NMB-3 Repair did not achieve large displacement ductility values due to the longitudinal rebar fracture. However, from the NMB-2 Repair test it can be seen that the repair is capable of restoring the diminished load and displacement and displacement ductility capacities of the precast specimens, which have experienced large amounts of earthquake induced damage.

Another useful comparison is to superimpose the hysteretic responses of the as-built and repair tests, as shown in Figure 4.25. From Figure 4.25(a) it can be seen that the NMB-2 Repair hysteresis is at higher values of load for all displacements than the NMB-2 hysteresis. This is an indication that NMB-2 Repair is dissipating more energy at all displacement steps. The NMB-3 Repair hysteresis is very stiff during the cycles prior to the longitudinal rebar fracture, as shown by the difference from the NMB-3 hysteresis. After the bar fracture, the hysteretic response is highly degraded. This degradation is primarily when NMB-3 Repair is displaced to the east. The hysteretic loops of NMB-3 Repair in the west direction of testing never fall below the hysteretic response of NMB-3.

All four tests can be easily compared using the force-displacement response envelopes, shown in Figure 4.26. From Figure 4.26 it can be seen that the repaired specimens achieve higher load values for each displacement step than the as-built specimens. The only exception to this is NMB-3 Repair in the east direction of testing after the longitudinal rebar fractured. Also, it can be seen from Figure 4.26 that the initial stiffness of the repaired specimens is larger than the as-built tests, due to the smaller column length.

The curvature profiles up to the 4-in. displacement step from the NMB-2 Repair and NMB-3 Repair tests are shown in Figure 4.27. From this plot, the curvature below the top of the repair, prior to transverse cracking of the CFRP jacket in NMB-2 Repair, was larger during the NMB-3 Repair test. However, the curvature just above the repair was larger during the NMB-2

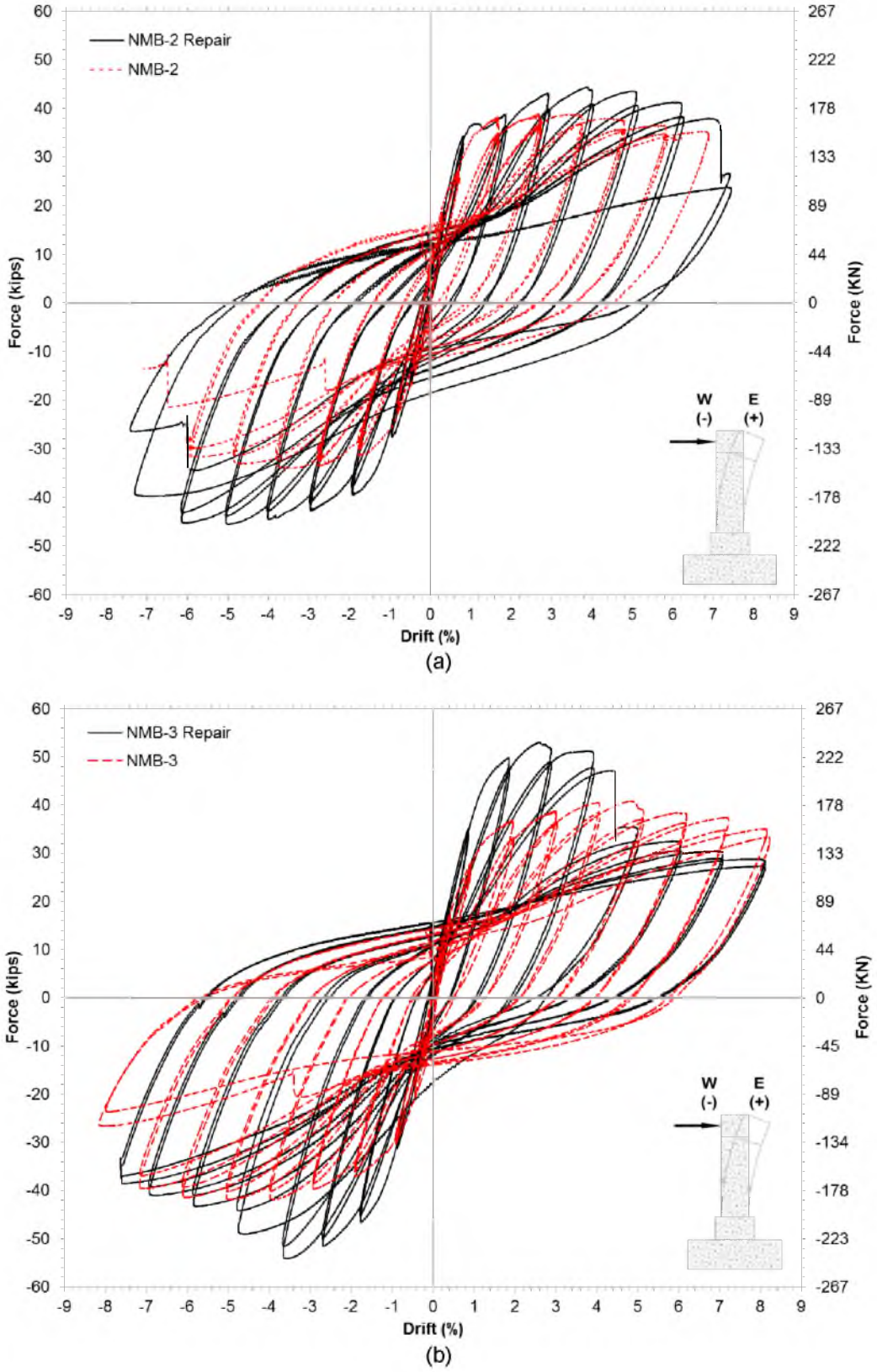

Figure 4.25 – Overlapping as-built and repair hysteresis: (a) NMB-2 and NMB-2 Repair, (b) NMB-3 and NMB-3 Repair

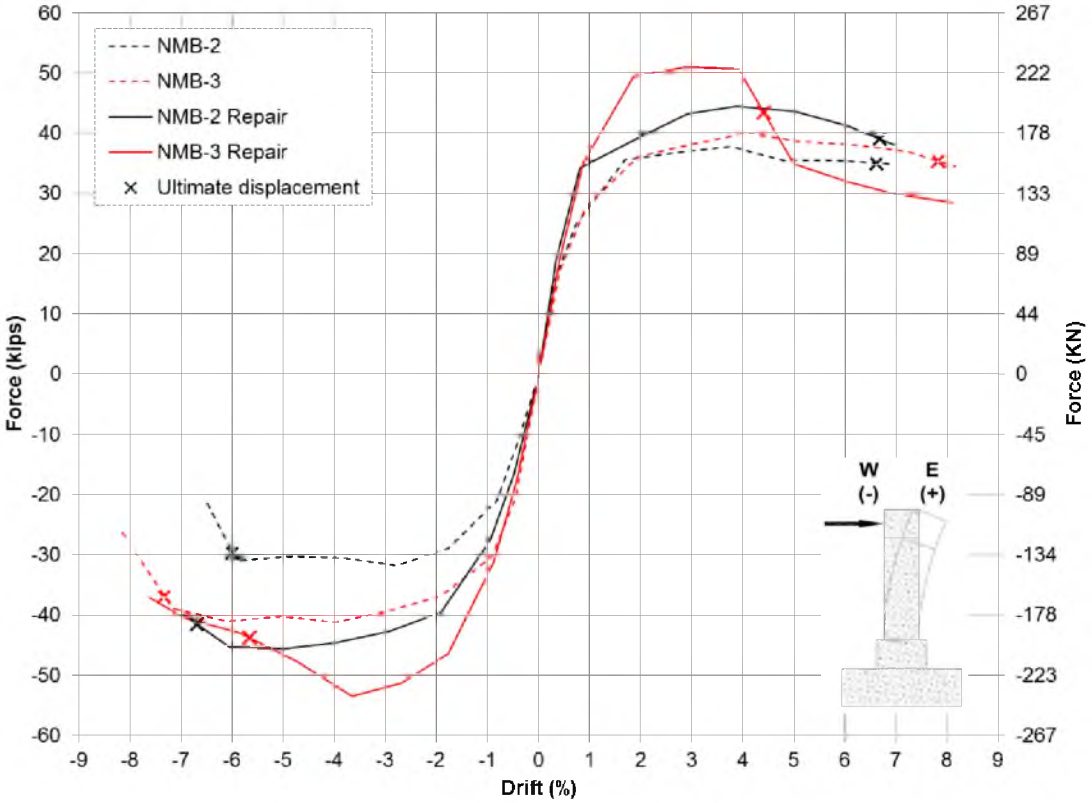

Figure 4.26 – As-built and repair testing response envelopes

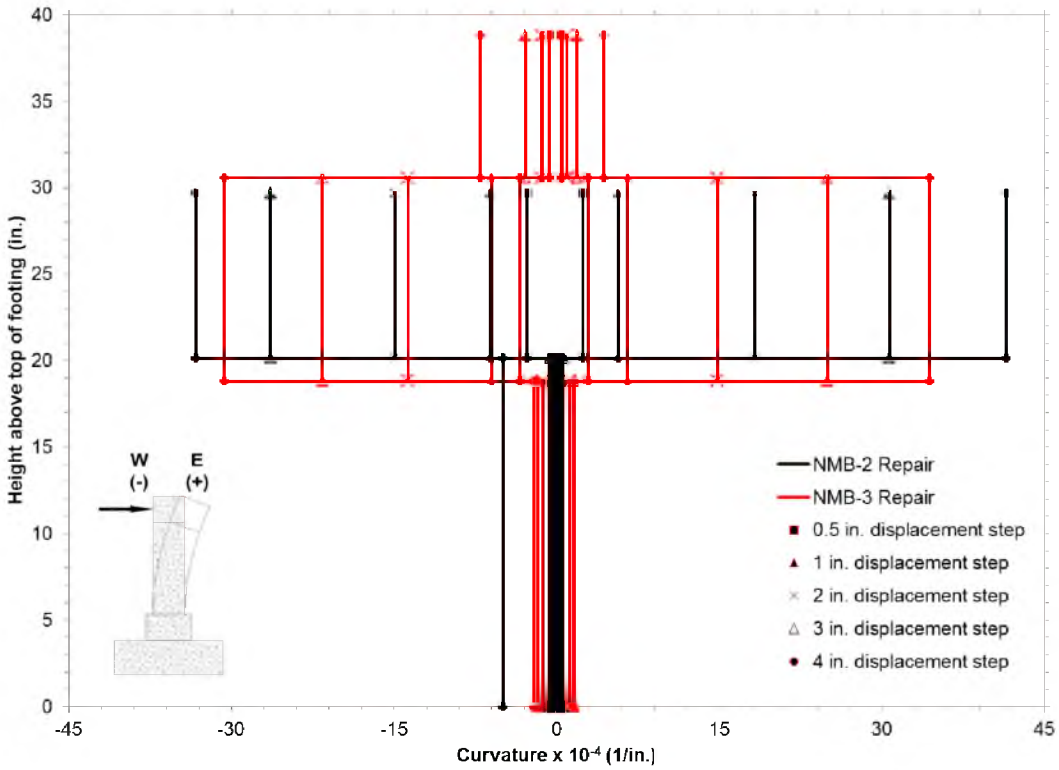

Figure 4.27 – Curvature profiles for NMB-2 Repair and NMB-3 Repair

Repair test than during the NMB-3 Repair test. The smaller curvature in NMB-3 Repair just above the repair indicates that curvature was spread to higher column sections. This curvature demand at higher sections was highlighted by the longitudinal rebar fracturing 10.5 in. above the top of the repair in NMB-3 Repair versus 3 in. above the top of the repair during NMB-2 Repair.

4.6.2 Energy dissipation capacity

The cumulative energy dissipation curves for NMB-2, NMB-2 Repair, NMB-3, and NMB-3 Repair is shown in Figure 4.28. The energy dissipation at the completion of each displacement step was calculated for each specimen and summed with previous displacement steps to obtain the cumulative energy dissipation values. The ultimate displacement of each specimen is marked by an X on the cumulative energy dissipation curve. When the ultimate displacement occurred between displacement steps, linear interpolation was used to obtain the total energy dissipation value, as listed in Table 4.3.

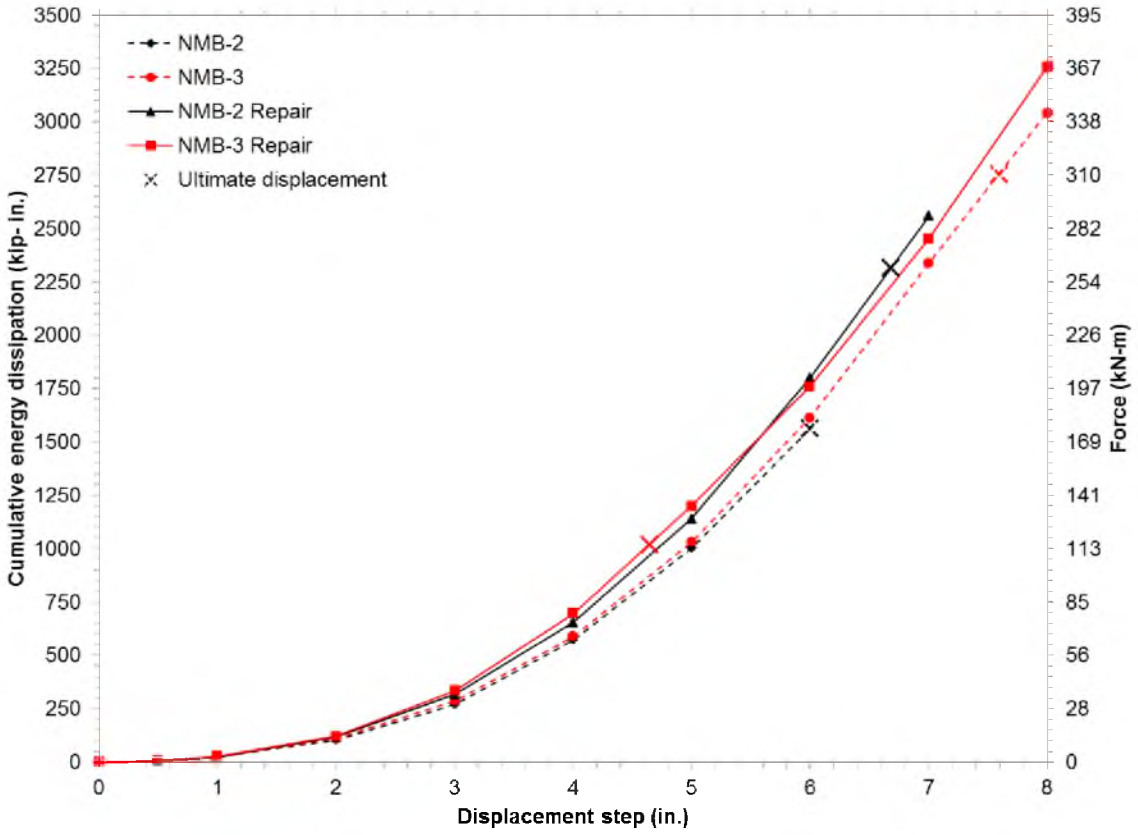

Figure 4.28 – Cumulative energy dissipation capacity of four tests

From Figure 4.28 it can be seen that both repairs dissipate more energy at each displacement step than the as-built specimens. NMB-2 Repair has a cumulative energy dissipation capacity equal to 143% of the cumulative energy dissipation capacity of NMB-2. Since the ultimate displacement of NMB-3 Repair is very low due to the premature longitudinal rebar fracture, the cumulative energy dissipation capacity of NMB-3 Repair is only 40% of the cumulative energy dissipation capacity of NMB-3. However, when the cumulative energy dissipation of all four tests is compared at the completion of the 4-in. displacement step, NMB-3 Repair dissipates the most energy. NMB-3 Repair dissipates 231% of the energy that NMB-3 had dissipated at the completion of the 4-in. displacement step.

4.6.3 Stiffness degradation

The stiffness degradation curves for NMB-2, NMB-2 Repair, NMB-3, and NMB-3 Repair are shown in Figure 4.29. To allow comparison between the as-built and repaired specimens the stiffness of each test has been normalized to the initial stiffness. The initial stiffness for each specimen, found in Table 4.4, is the stiffness during the 0.5-in. displacement step. It is known that the repaired specimens will have higher stiffness than the as-built specimens due to the shortened column length. Therefore, to provide a comparison of the stiffness degradation characteristics of all the tests, the normalization was made. The ultimate displacement of each specimen is marked by an X on the stiffness degradation curve.

From Figure 4.29 it can be seen that the repaired specimen's exhibit higher normalized stiffness at each displacement step compared to the as-built specimens, prior to the ultimate displacement. NMB-3 Repair has much less stiffness degradation, up to the 4-in. displacement step, than any of the other specimens. The stiffness of NMB-3 Repair degrades rapidly between the 4-in. and 5-in. displacement step due to the longitudinal rebar fracturing. After the 4-in. displacement step NMB-3 Repair's normalized stiffness is very close to the normalized stiffness of the other three specimens. NMB-2 Repair and NMB-2 demonstrate very similar stiffness degradation characteristics throughout all of the displacement steps prior to the ultimate displacement.

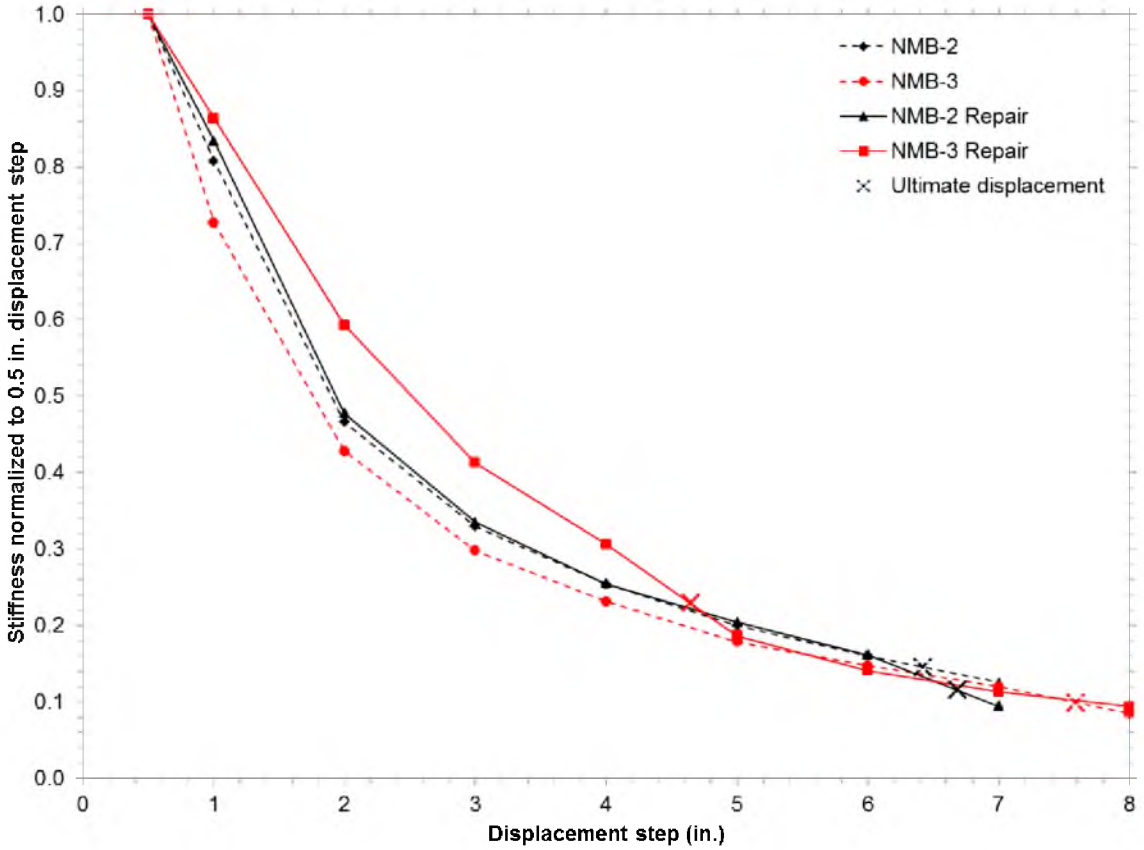

Figure 4.29 – Stiffness degradation of all four tests

Table 4.4 – Initial stiffness values

Test	Initial Stiffness (kip/in.)
NMB-2	40.8
NMB-2 Repair	42.9
NMB-3	44.4
NMB-3 Repair	45.3

4.6.4 Conclusions

The comparisons from Section 4.6 have shown that the repair procedure developed in this study is capable of restoring the capacities of cyclically damaged precast concrete bridge column-to-footing assemblies to levels equal to the undamaged performance in terms of lateral load capacity, displacement capacity, displacement ductility, and cumulative energy dissipation capacity. The damage state of the specimens prior to repair was severe, including longitudinal rebar fracture for both specimens. From these results it can be seen that the repair is capable of achieving the desired performance, which was to emulate the performance of the as-built specimen, making the repair an attractive alternative to replacing damaged bridges following an earthquake. However, to confirm the belief that NMB-3 Repair is an outlier due to embrittled longitudinal rebar prior to repair, more testing is needed.

CHAPTER 5

STRUT-AND-TIE MODELING

A Strut-and-Tie Model (STM) is an idealized truss model of a reinforced concrete member where compressive forces are carried through struts and tensile forces are carried through ties. Structural systems can be divided into two portions, B-regions where Bernoulli beam theory applies and D-regions where the internal stress-strain distribution defies beam theory. Disturbances in the internal stress-strain distribution, D-regions, come to an end roughly one member-depth away from a disturbance, as defined by Saint Venant's Principle. A disturbance is caused by a geometric discontinuity, such as an abrupt change in cross-section, or a static discontinuity, such as a point load. Therefore, any joint region within a structural system is defined as a D-region. The repair procedure developed in this study induces two geometric discontinuities: one at the repair-column interface and another at the repair-footing or repair-pier cap interfaces. These geometric discontinuities create additional D-regions in the system due to the abrupt changes in cross-section. STMs have been adopted as an appropriate method to model the force distributions in D-regions (*5*, *12)*.

Two STM procedures have been developed for the as-built and repaired specimens. The formulation of both STMs rely on the large amount of shear reinforcement provided in the as-built specimens, preventing shear failure for both the as-built and repaired specimens. Both of the STMs are based on a flexural failure mode as observed in testing for both the as-built and repaired specimens. A conventional STM has been developed, which predicts the ultimate load capacity of the assembly being modeled and associated member forces at ultimate lateral loading conditions. This model is referred to as the conventional model because it is the STM method outlined in ACI 318 (*5*) and is commonly used. Additionally, a nonlinear STM has been

developed, which predicts the system's force-displacement response envelope and takes into consideration the cyclic degradation of concrete. Both of the STM procedures were developed using standardized modeling parameters that can be applied to different reinforcement and geometrical layouts. Once the modeling parameters are established, the designer can use the models to design the repair components and predict the assembly's performance at the service and ultimate condition.

Four specimens are modeled in this Chapter, NMB-2 Repair and NMB-2, which are described in Chapters 2–4, as well as LEN-2 Repair and LEN-2. The details pertaining to LEN-2 Repair and LEN-2 are not covered in this document. Detailed descriptions, test results, and analysis for LEN-2 and LEN-2 Repair are the subjects of other studies (*2*, *34)*. LEN-2 is a column-to-pier cap specimen that is connected using a GSS manufactured by Lenton Interlock. The GSS cast in the pier cap of LEN-2 uses grout to secure the field dowel and threads to secure the bar cast into the concrete. The GSS are located in the pier cap, which is dimensioned 9 ft. long, 2 ft. wide, and 2 ft. tall. The geometry and reinforcement in the column is identical to NMB-2. LEN-2 was tested at the same lab and under the same loading protocol as NMB-2. LEN-2 Repair was repaired using the same methodology as NMB-2 Repair.

5.1 Strut-and-tie model layout

An infinite number of STM layouts are possible for a given structural system. The proper STM layout to use is one that effectively models the force transfer mechanism of the system. As a structural system progresses from service to ultimate loading conditions, the STM arrangement that accurately models the force transfer mechanism changes. However, it is not possible to change the arrangement of the model at intermediate steps when modeling. This issue is not a concern for the conventional STM. The objective of the conventional STM is to predict the performance at the ultimate limit state and therefore, a model that represents the force transfer mechanism at the ultimate limit state is the most accurate model. However, the objective of the nonlinear STM is to predict the structural performance of the system at all loading states up to the ultimate limit state. Following the different force transfer mechanisms of the system up to the

ultimate limit state would yield many STM layouts, which is not possible to model. Following the recommendations of previous research *(16),* a model that reflects the force transfer mechanism at the ultimate limit state was adopted for the nonlinear STM. This decision leads to the conventional and nonlinear STMs having the same geometrical layouts. A model reflecting a flexural failure at ultimate loading was adopted to match the performance of NMB-2, NMB-2 Repair, LEN-2 Repair, and LEN-2. Adjustments to the formulated STM layout, which models the laboratory loading, will have to be made to reflect the in-situ loading conditions.

The STM layout has been adapted from a previously developed conventional STM, which modeled a column-to-pier cap assembly and the subsequent repair *(34)*. It is critical that the conventional STM developed is statically determinate and both internally and externally stable. Determinacy makes the model independent of the truss member's geometrical and material properties, which are often difficult to obtain. An indeterminate truss is reliant upon the members modulus of elasticity, E, and the members cross-sectional area, A, to determine the axial loads of the truss members, assuming the system remains elastic. To achieve determinacy, the model must satisfy eq. 5.1:

$$b + r = 2j \tag{5.1}$$

where b is equal to the number of truss members, r is the number of reactions, and j is the number of joints.

The STM layout developed for NMB-2 Repair can be seen in Figure 5.1, where the generic model inputs are labeled symbolically. Figure 5.1 will be used to help explain the generic model layout parameters that were used to model all of the specimens in this chapter. These generic model layout parameters were developed to be easily adapted with other specimen configurations. It should be noted that the model in Figure 5.1 is statically determinate with 43 truss members, 3 reactions due to the simple supports at Q and W, and 23 joints. The model reflects the loading condition during testing where external loads were applied at joints A, B, U, and V. Joints A and B are the points of lateral and axial load application, respectively. Joints U

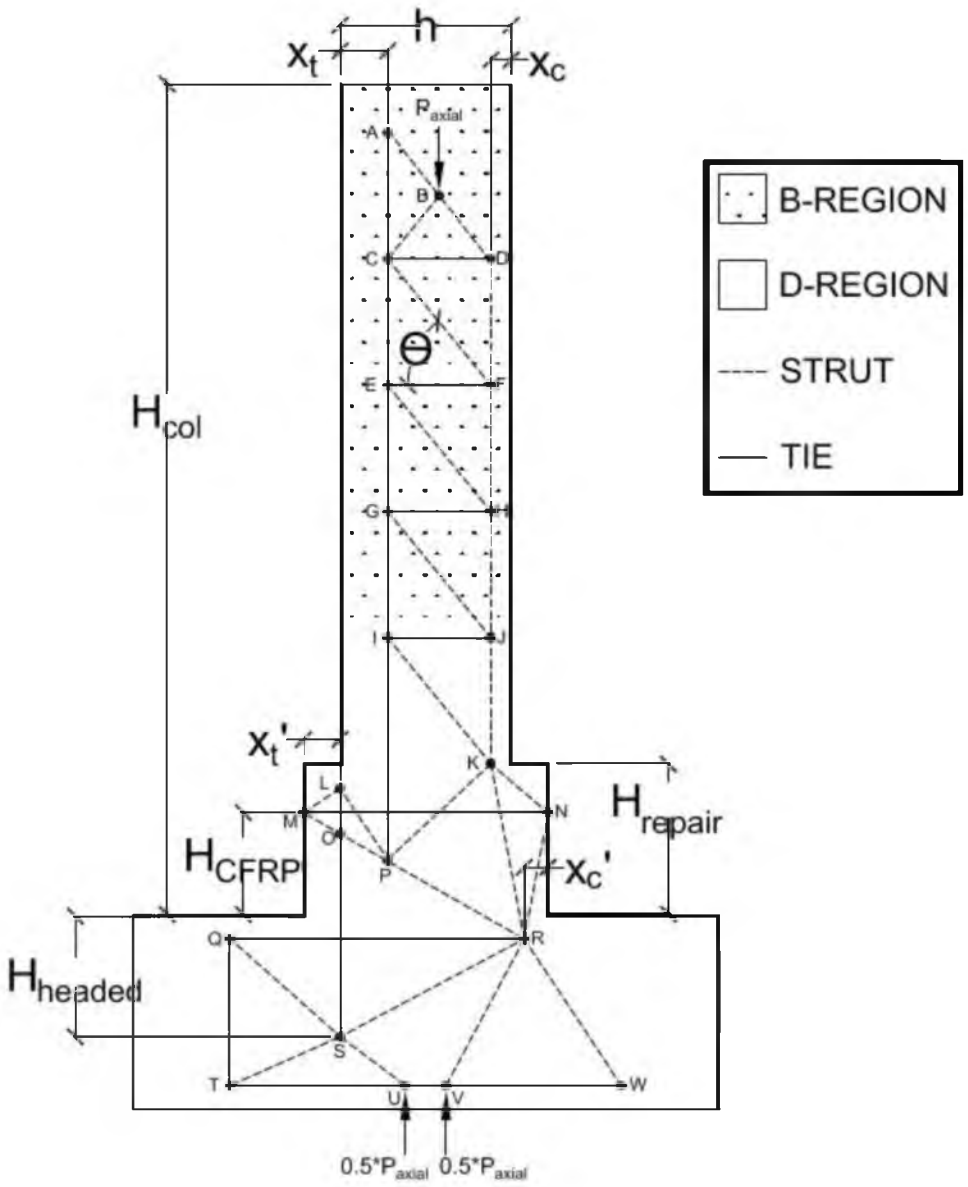

Figure 5.1 – STM layout

and V are the reactions due to the base plate at the bottom of the axial load application system. The distributed load that the base plate applies onto the footing was idealized as two point loads at joints U and V. The loads applied at joints U and V are each equal to half of the load applied at B.

The model formulation of the as-built column B-region is quite simple, with three design parameters. The angle, Θ, which is measured between the axes of the diagonal strut and transverse reinforcement. The tension force centroid at first yield, x_t, and compression force

centroid at first yield, x_c. The angle Θ is to remain constant between the axes of all the diagonal struts and transverse reinforcement ties. The recommended range of values for Θ is between 31°–59° *(16)*. For the given formulation the largest value of Θ that remained within the recommended values was used. To determine Θ, the integer number of equal length vertical cells, x, can be manipulated until a satisfactory Θ value is obtained from eq. 5.2:

$$\Phi = \tan^{-1}\left(\frac{H_{col} - H_{repair}}{x * (h - (x_c + x_t))}\right) \quad (5.2)$$

The correct value of x yields a Θ that is between 31°–59°. In Figure 5.1, x is equal to 5, meaning there are 5 equal vertical lengths between node A and K. H_{col} is the height of the column measured from the top of the footing to the point of lateral load application. H_{repair} is the height of the repair measured from the top of the footing to the top of the repair. For the as-built specimens H_{repair} is equal to zero. h is the width of the as-built column parallel to the direction of lateral loading.

The tension and compression force centroids at first yield, x_t and x_c respectively, are found from a sectional analysis of the as-built column. The first yield state is defined by the onset of the extreme tension steel yielding or the extreme concrete compression fiber reaching a strain value of 0.002 in./in. *(16)*. Once x_t and x_c are determined, the nodes on the compression face of the as-built column are located a distance x_c away from the edge of concrete, and the nodes on the tension face of the as-built column are located a distance x_t away from the edge of the column concrete in tension, as shown in Figure 5.1. The distance from the extreme concrete compression fiber to the neutral axis, c, at first yield should be recorded at this stage. Any reinforcement located within the tension zone at first yield, as shown in Figure 5.2, will contribute to the associated tie area.

Similarly, the tension and compression force centroids of the repair at first yield, x_t' and x_c' respectively, are found from a sectional analysis of the repair cross-section. The confined compressive strength of the concrete within the repair, f_{cc}', should be used due to the high

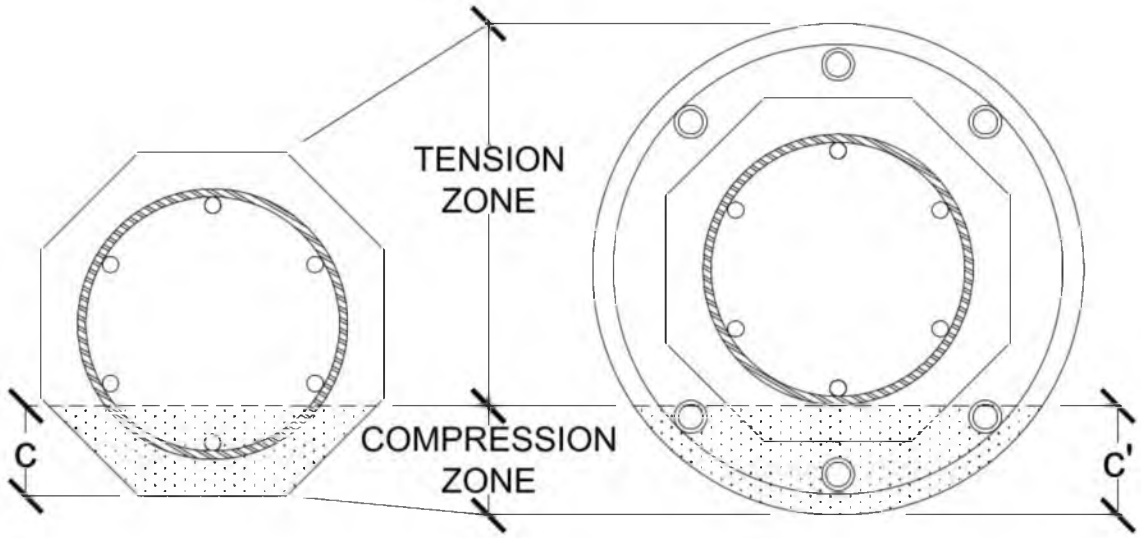

Figure 5.2 – Graphical representation of first yield state

confinement that the CFRP wrap provides. An accurate prediction of f_{cc}' can be determined from previous research *(35)* or can be conservatively taken as $1.5f_c$' (*6*). The contribution of the as-built column steel is neglected in the repair sectional analysis due to the damage state of the longitudinal steel. Once x_t' is determined, the nodes and corresponding ties that represent the contribution of the headed rebar (nodes L, O and S, in Figure 5.1) are located a distance x_t' away from the edge of repair. Any headed rebar located within the tension zone at first yield, as shown in Figure 5.2, will contribute to the headed rebar tie area.

The compression force centroid in the repair, x_c', is used to locate the node that transmits the compressive forces from the repair into the footing (node R in Figure 5.1). This node is located a distance x_c' away from the edge of the repair and at the height of the top longitudinal rebar tie in the footing. The distance from the extreme concrete compression fiber to the neutral axis, c', at first yield should be recorded at this stage. The height of the CFRP tie from the top of the footing, H_{CFRP}, was determined from the strain profiles recorded during the NMB-3 Repair test, as shown in Figure 4.20. The centroid of the tensile force for the 1-inch displacement step strain profile was used to determine H_{CFRP}. The 1-inch displacement step strain profile was used since first yield occurs between the 0.5-inch and 1-inch displacement steps. The H_{CFRP}

calculated from the strain profile was 12.5 in. above the top of the footing, correlating to 70% of H_{repair}.

The height that the headed rebar terminates below the top of the footing, H_{headed} in Figure 5.1, is equal to the embedment length of the headed rebar minus half of the epoxy anchorage development length. Anchorage of ties at half of the bond length has been used in previous studies *(36)*. The node at the top of the headed rebar is located at the location of the head. This is due to the drastically shortened development length of headed rebar *(15)*.

The tie representing the longitudinal as-built column rebar was terminated above the GSS interface because the STM developed is for an as-built condition in which longitudinal rebar fracture occurred. The rule for anchoring the reinforcement half way up the development length of the tie does not apply to the longitudinal rebar in the as-built column due to the high clamping forces the CFRP wrap provide. The logical place for termination of the as-built column longitudinal rebar tie is at the intersection of the longitudinal rebar and the strut that connects the headed rebar to x_c' (node P in Figure 5.1). This location provides anchorage for the longitudinal column rebar from struts developed in the headed rebar, CFRP wrap, and as-built column. This strong anchorage matches test data from NMB-2 Repair where the as-built column longitudinal rebar fractured 21.5 in., 50% of the design development length, above the fracture location from the NMB-2 test. This short development length implies that there was significant clamping force on the longitudinal rebar, which is represented in the STM by the anchorage struts.

All of the ties in the STM layout must correlate to the actual reinforcement arrangement, which consists of transverse and longitudinal steel. There is no tensile capacity in the concrete at the ultimate limit state. Also, longitudinal ties in the footing should be located at the centroid of the rebar for positive and negative moment steel.

An axial load, P_{axial}, is applied to the model that replicates the axial load applied during testing. During testing, P_{axial} was applied through an actuator resting on the top of the column. This actuator pushed against a steel beam, which transferred P_{axial} to the footing or pier cap through high strength rods. To replicate this loading scenario, P_{axial} is applied downward at node B on Figure 5.1, and the reactions are applied at nodes U and V upward, as shown in Figure 5.1.

Each node U and V is loaded with half of P_{axial} in the upward direction and replicates the bearing plate, which transferred the load to the footing or pier cap. More detailed schematics and pictures of the axial load apparatus can be found in Chapter 2.

5.2 Conventional strut-and-tie model

The conventional STM developed is a general design procedure used to predict the ultimate load capacity of a column-to-footing or column-to-pier cap assembly. The conventional STM developed is a determinate truss model that does not rely on the geometrical or material properties of the members. Thus, modeling can be carried out by hand or with any structural analysis package capable of analyzing a truss.

5.2.1 Allowable design forces

The design procedures adopted by ACI (*5*) were used for the formulation of the conventional STM. The allowable concrete stress of a strut, f_{ce}, is given by eq. 5.3:

$$f_{ce} = 0.85 * \beta_s * f_c' \tag{5.3}$$

where β_s is equal to 0.75 for bottle shaped struts with adiquate transverse reinforcement. The allowable concrete stress on the face of a nodal zone, f_{ce}, is given by eq. 5.4:

$$f_{ce} = 0.85 * \beta_n * f_c' \tag{5.4}$$

where, β_n is equal to 1.0 for nodes not anchoring any ties, 0.80 for nodes anchoring one tie, or 0.60 for nodes anchoring two or more ties. From the allowable stresses given in eqs. 5.3 and 5.4, the minimum required area of a strut, $A_{cs,\ min}$, can be found in eq. 5.5:

$$A_{cs,min} = \frac{F_u}{\min(0.85 * \beta_s * f_c', 0.85 * \beta_n * f_c')} \tag{5.5}$$

where F_u is the force the strut develops in the model. $A_{cs,\ min}$ must then be checked against the minimum available area, A_{cs}, for the strut along its length. If A_{cs} is less than $A_{cs,\ min}$, the strut has crushed, and the model cannot resist any more load. The A_{cs} available in the cylindrical repair section is a portion of an ellipse. In lieu of determining the area of an elliptical segment, a circular sector of equal width can be used and the simplification will always yield a smaller A_{cs}.

The nominal strength of a mild steel rebar tie, F_{nt}, in a nonprestressed member is given by eq. 5.6:

$$F_{nt} = A_{ts} * f_y \tag{5.6}$$

where A_{ts} is the cross-sectional area of steel of all the reinforcement that is in the tension zone at first yield, which represents the tie, as seen in Figure 5.2. f_y is the nominal yield strength of the reinforcement. This indicates that a tie yielding is considered failure.

The nominal strength of the CFRP tie, F_{nt}, is given by eq. 5.7:

$$F_{nt} = A_{ts} * f_{fd} \tag{5.7}$$

where A_{ts} is the cross-sectional area of the CFRP jacket, calculated by multiplying H_{repair} times the thickness of the CFRP jacket. The thickness of the CFRP jacket is calculated by multiplying the CFRP thickness per layer times the number of layers used for the repair. f_{fd} is the effective stress level in the CFRP jacket at failure, which can be determined from eq. 5.8:

$$f_{fd} = E_f * \kappa_\varepsilon * \varepsilon_{fu} \tag{5.8}$$

Equation 5.8 must be less than $0.004E_f$. κ_ε is the CFRP strain efficiency factor, which has been determined experimentally, and accounts for the multiaxial state of stress acting on the jacket and strain concentrations. It is recommended that κ_ε be taken as a value between 0.57–0.61 *(33)*. Conservatively, κ_ε has been taken as 0.57 for this study. If the force in the CFRP tie,

F_u, is larger than F_{nt}, the CFRP wrap will rupture. The minimum lateral load at which a strut crushes, the mild steel yields, or the CFRP wrap ruptures is defined ultimate load capacity of the system.

5.2.2 NMB-2 Repair model

All of the layout recommendations given in Section 5.1 were followed for NMB-2 Repair. The material properties recorded on the day of test were used in the model. The layout parameters and design inputs can be found in Table 5.1. All of the STM dimensions can be seen in Figure 5.3. Due to the semi-expansive nature of the concrete placed within the repair, an accurate compressive strength, f_c', on the day of testing could not be obtained. It was determined, from concrete hammer tests, that the f_c' of the repair concrete was approximately equal to the f_c' of the as-built concrete. Due to the uncertainty of f_c' for the repair concrete, a conservative value of $1.5f_c'$ was used for f_{cc}'. The axial load applied to the model was equal to 86.80 kips, which was the recorded value of axial load at the beginning of testing.

From these model inputs it was determined that the maximum lateral load the model could withstand was 42.55 kips. The maximum lateral load NMB-2 Repair developed during testing was 45.46 kips. Therefore, the model predicted the ultimate lateral load capacity to be 93.6% of the actual ultimate load achieved in the test. The model reached the ultimate load when simultaneous yielding of the headed rebar ties LO and OS occurred, as seen in Figure 5.3. This ultimate condition replicates the behavior observed during testing where yielding of the extreme east headed rebar occurred during the 1-inch displacement step. The modeling results can be found numerically for the struts and ties in Tables 5.2 and 5.3, respectively.

The required width of each strut was determined from eq. 5.5 for $A_{cs,min}$, which takes into account the material properties as well as strut and nodal strength along the strut. A_{cs} was then determined for each end of the struts and checked against $A_{cs,min}$. A graphical representation of $A_{cs,min}$, at a load that causes strut JK to crush, can be seen in Figure 5.4. The width required to develop $A_{cs,min}$ at this load is shaded in grey. None of the struts crushed in this model, but strut JK, which is the longitudinal strut at the column-repair interface, was at 88.6% of the struts

Table 5.1 – Modeling parameters used for NMB-2 Repair STM

Model input	Location/ member	Value
P_{axial}	Global	86.8 kips
x_c	As-built column	2.5 in.
x_t	As-built column	5.8 in.
x_c'	Repair	2.9 in.
x_t'	Repair	4.5 in.
h_{CFRP}	Repair	12.5 in.
h_{headed}	Footing	15.0 in.
Θ	As-built column	50.7 deg.
f_c'	As-built	6.43 ksi
f_{cc}'	Repair	9.65 ksi
f_y	As-built long.	68 ksi
f_y	As-built trans.	63 ksi
f_y	Headed rebar	62 ksi
f_u	CFRP wrap	101 ksi

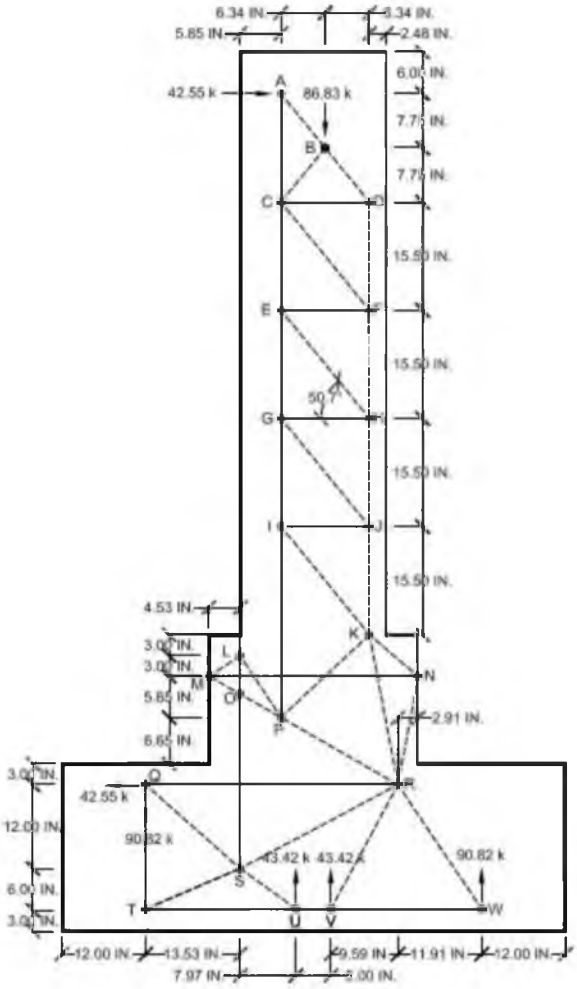

Figure 5.3 – NMB-2 Repair STM dimensions, loading, and reactions

Table 5.2 – NMB-2 Repair conventional STM strut results

Member	Location	F_u (kips)		β_n	$A_{cs,\,min}$ (in.^{2})	$A_{cs} > A_{cs,\,min}$
AB	Column	67.20	@A	0.8	16.39	OK
			@B	1.0		
BC	Column	56.09	@B	1.0	17.10	OK
			@C	0.6		
BD	Column	123.29	@B	1.0	30.08	OK
			@D	0.8		
CF	Column	67.20	@C	0.6	20.49	OK
			@F	0.8		
DF	Column	95.43	@D	0.8	23.28	OK
			@F	0.8		
EH	Column	67.20	@E	0.6	20.49	OK
			@H	0.8		
FH	Column	147.44	@F	0.8	35.97	OK
			@H	0.8		
GJ	Column	67.20	@G	0.6	20.49	OK
			@J	0.8		
HJ	Column	199.45	@H	0.8	48.66	OK
			@J	0.8		
IK	Column	67.20	@I	0.6	20.49	OK
			@K	1.0		
JK	Column	251.47	@J	0.8	61.35	OK
			@K	1.0		
KN	Repair	165.78	@K	1.0	26.96	OK
			@N	0.8		
KP	Repair	139.58	@K	1.0	22.70	OK
			@P	0.8		
KR	Repair/ Footing	101.79	@K	1.0	24.83	OK
			@R	0.8		
LM	Repair	80.43	@L	0.8	13.08	OK
			@M	0.8		
LP	Repair	122.04	@L	0.8	19.85	OK
			@P	0.8		
MO	Repair	90.53	@M	0.8	18.40	OK
			@O	0.6		
NR	Repair/ Footing	110.04	@N	0.8	26.84	OK
			@R	0.8		
OP	Repair	90.69	@O	0.6	18.44	OK
			@P	0.8		
PR	Repair/ Footing	50.75	@P	0.8	12.38	OK
			@R	0.8		
QS	Footing	200.11	@Q	0.6	61.02	OK
			@S	0.8		
RS	Footing	211.43	@R	0.8	51.58	OK
			@S	0.8		
RV	Footing	49.19	@R	0.8	15.00	OK
			@V	0.6		
RW	Footing	108.90	@R	0.8	26.57	OK
			@W	0.8		
ST	Footing	103.52	@S	0.8	31.57	OK
			@T	0.6		
SU	Footing	72.80	@S	0.8	22.20	OK
			@U	0.6		

Table 5.3 - NMB-2 Repair conventional STM tie results

Member	Material	F_u (kips)	F_{nt} (kips)	F_u / F_{nt} (%)	F_{nt} > F_u
AC	As-built long. rebar	52.01	268.60	19	OK
CD	As-built trans. rebar	78.07	156.24	50	OK
CE	As-built long. rebar	60.61	268.60	23	OK
EF	As-built trans. rebar	42.55	156.24	27	OK
EG	As-built long. rebar	112.62	268.60	42	OK
GH	As-built trans. rebar	42.55	156.24	27	OK
GI	As-built long. rebar	164.64	268.60	61	OK
IJ	As-built trans. rebar	42.55	156.24	27	OK
IP	As-built long. rebar	216.65	268.60	81	OK
LO	Headed rebar	146.37	146.94	100	YIELD
MN	CFRP wrap	145.94	195.08	75	OK
OS	Headed rebar	146.69	146.94	100	YIELD
QR	As-built long. rebar	192.26	429.76	45	OK
QT	As-built trans. rebar	41.96	99.20	42	OK
TU	As-built long. rebar	94.63	322.32	29	OK
UV	As-built long. rebar	36.96	322.32	11	OK
VW	As-built long. rebar	60.09	322.32	19	OK

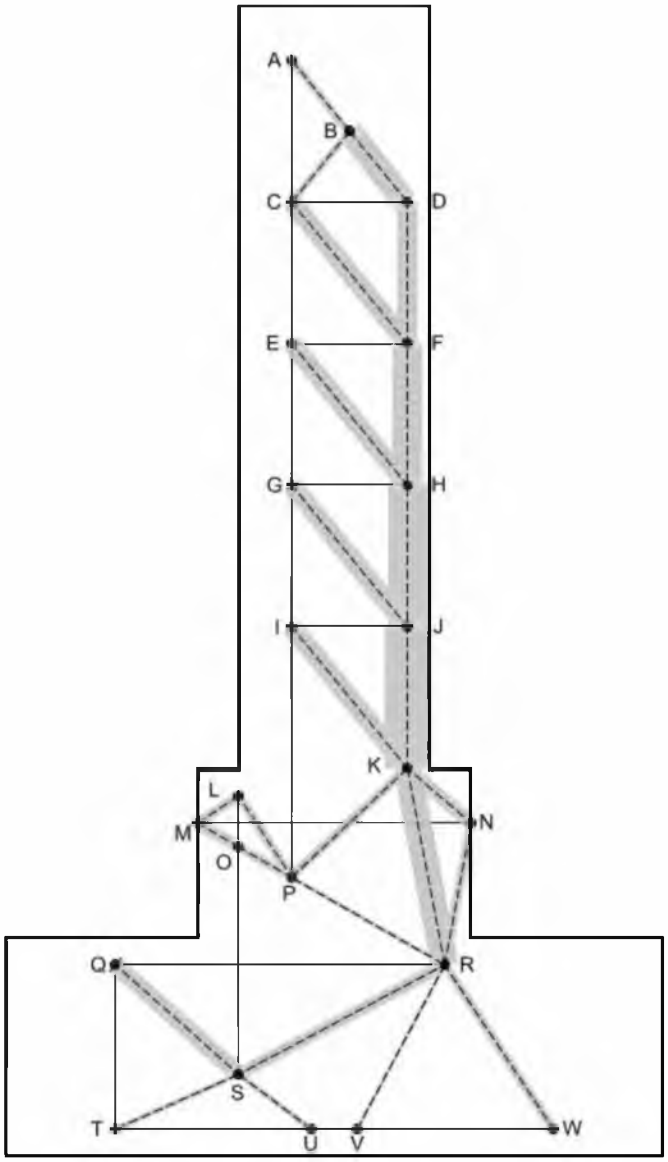

Figure 5.4 – Graphical representation of $A_{cs,min}$ for NMB-2 Repair at a fictitious load crushing JK

capacity. It should be noted that nodes M and N were moved 1.5 in. into the repair concrete to establish the maximum allowable strut areas for KN, LM, MO, and NR. Nodes M and N are located on the exterior of the repair concrete since they represent the CFRP wrap. If the nodes were not relocated, the previously mentioned struts would have allowable areas equal to zero. Due to the vast amount of confinement the wrap provides to the concrete struts located within the wrap, the relocation of the nodes was deemed acceptable. The node relocation of M and N was only done to calculate A_{cs}.

The tie forces were checked against the available strength of each tie using the area of reinforcement the tie represents and the associated material properties. It can be seen in Table 5.3 that only the headed rebar yield. Tie IP, which represents the longitudinal rebar in the column, is stressed to 81% of the tie's yield capacity.

5.2.3 NMB-2 model

All of the layout recommendations given in Section 5.1 were followed for NMB-2. The material properties recorded on the day of the test were used in the model. The layout parameters and design inputs can be found in Table 5.4. All of the STM dimensions are shown in Figure 5.5. The axial load applied to the model was equal to 94.14 kips, which was the recorded value of the axial load at the beginning of the test.

From these model inputs it was determined that the maximum lateral load the model could withstand was 33.69 kips. The maximum lateral load NMB-2 developed during testing was 38.80 kips. Therefore, the model predicted the ultimate lateral load capacity to be 86.8% of the actual ultimate load achieved. The model reached the ultimate load when the column longitudinal strut LN crushed, shown in Figure 5.5. This ultimate load condition for the model replicates the observed behavior of NMB-2 during testing where the ultimate load capacity was reached when concrete was crushed in the column core. The column longitudinal rebar tie KO reached 82% of its yield capacity at the failure load. The modeling results can be found numerically for the struts and ties in Tables 5.5 and 5.6, respectively.

Table 5.4 – Modeling parameters used for NMB-2 STM

Model input	Location/ member	Value
P_{axial}	Global	94.1 kips
x_c	As-built column	2.7 in.
x_t	As-built column	5.8 in.
Θ	As-built column	52.8 deg.
f_c'	As-built	5.45 ksi
f_y	As-built long.	68 ksi
f_y	As-built trans.	63 ksi

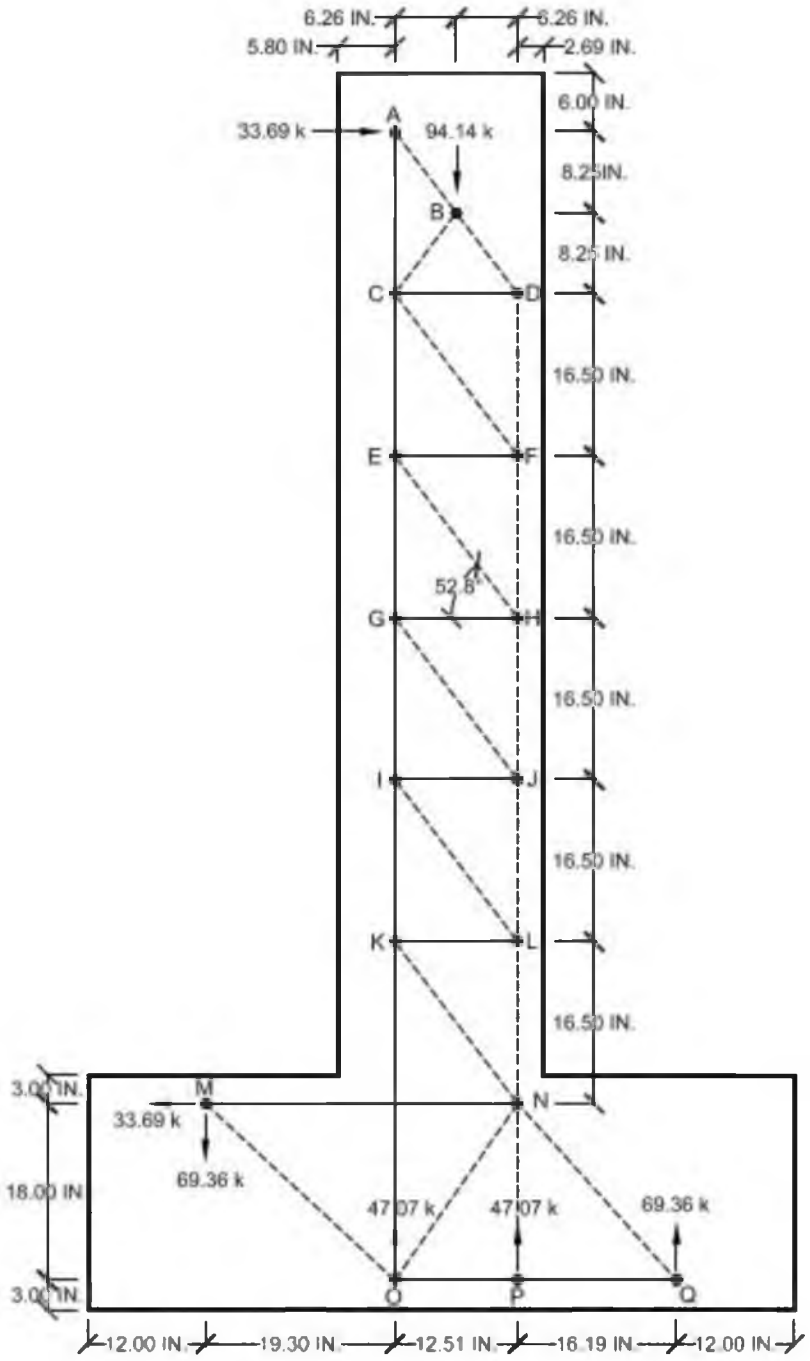

Figure 5.5 – NMB-2 STM dimensions, loading, and reactions

Table 5.5 – NMB-2 conventional STM strut results

Member	Location	F_u (kips)		β_n	$A_{cs,\,min}$ (in.^{2})	$A_{cs} > A_{cs,\,min}$
AB	Column	56.14	@A	0.8	13.70	OK
			@B	1.0		
BC	Column	60.04	@B	1.0	18.31	OK
			@C	0.6		
BD	Column	114.65	@B	1.0	27.97	OK
			@D	0.8		
CF	Column	55.76	@C	0.6	17.00	OK
			@F	0.8		
DF	Column	91.02	@D	0.8	22.20	OK
			@F	0.8		
EH	Column	55.76	@E	0.6	17.00	OK
			@H	0.8		
FH	Column	135.45	@F	0.8	33.04	OK
			@H	0.8		
GJ	Column	55.76	@G	0.6	17.00	OK
			@J	0.8		
HJ	Column	179.89	@H	0.8	43.88	OK
			@J	0.8		
IL	Column	55.76	@I	0.6	17.00	OK
			@L	0.8		
JL	Column	224.32	@J	0.8	54.72	CRUSH
			@L	0.8		
KN	Column/ Footing	55.76	@K	0.6	11.34	OK
			@N	0.8		
LN	Column/ Footing	268.76	@L	0.8	43.71	OK
			@N	0.8		
MO	Footing	101.69	@M	0.8	31.01	OK
			@O	0.6		
NO	Footing	239.62	@N	0.8	48.71	OK
			@O	0.6		
NP	Footing	47.07	@N	0.8	9.57	OK
			@P	0.6		
NQ	Footing	93.29	@N	0.8	15.17	OK
			@Q	0.8		

Table 5.6 - NMB-2 Repair conventional STM tie results

Member	Material	F_u (kips)	F_{nt} (kips)	F_u / F_{nt} (%)	F_{nt} > F_u
AC	As-built long. rebar	44.90	268.60	17	OK
CD	As-built trans. rebar	69.72	166.32	42	OK
CE	As-built long. rebar	41.31	268.60	15	OK
EF	As-built trans. rebar	33.69	166.32	20	OK
EG	As-built long. rebar	85.75	268.60	32	OK
GH	As-built trans. rebar	33.69	166.32	20	OK
GI	As-built long. rebar	130.18	268.60	48	OK
IJ	As-built trans. rebar	33.69	166.32	20	OK
IK	As-built long. rebar	174.62	268.60	65	OK
KL	As-built trans. rebar	33.69	166.32	20	OK
KO	As-built long. rebar	219.05	268.60	82	OK
MN	As-built long. rebar	108.06	429.76	25	OK
OP	As-built long. rebar	62.38	322.32	19	OK
PQ	As-built long. rebar	62.38	322.32	19	OK

5.2.4 LEN-2 Repair model

All of the layout recommendations given in Section 5.1 were followed for LEN-2 Repair. The material properties recorded on the day of the test were used in the model. The layout parameters and design inputs can be found in Table 5.7. All of the STM dimensions can be seen in Figure 5.6. Due to the semi-expansive nature of the concrete placed within the repair, an accurate concrete compressive strength, f_c', on the day of testing was not obtained. It was determined, from concrete hammer tests, that the f_c' of the repair concrete was approximately

Table 5.7 – Modeling parameters used for LEN-2 Repair STM

Model input	Location/ member	Value
P_{axial}	Global	105 kips
x_c	As-built column	2.7 in.
x_t	As-built column	5.7 in.
x_c'	Repair	3.1 in.
x_t'	Repair	4.5 in.
h_{CFRP}	Repair	12.5 in.
h_{headed}	Footing	15.0 in.
Θ	As-built column	50.8 deg.
f_c'	As-built	6.00 ksi
f_{cc}'	Repair	9.00 ksi
f_y	As-built long.	68 ksi
f_y	As-built trans.	63 ksi
f_y	Headed rebar	62 ksi
f_u	CFRP wrap	101 ksi

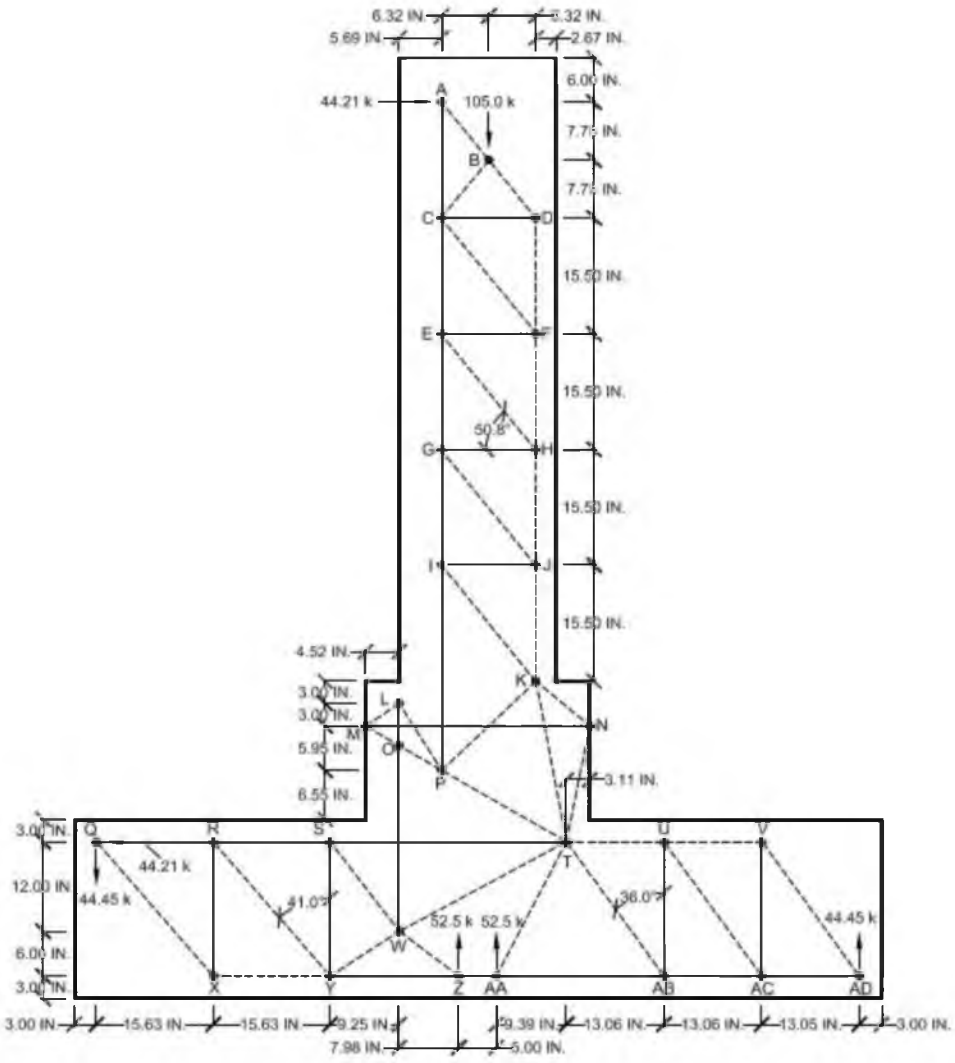

Figure 5.6 – LEN-2 Repair STM dimensions, loading, and reactions

equal to the f_c' of the as-built concrete. Due to the uncertainty of f_c' for the repair concrete, a conservative value of $1.5f_c$' was used for f_{cc}'. The axial load applied to the model was equal to 105.0 kips, which was the recorded value of axial load at the beginning of the test.

From these model inputs it was determined that the maximum lateral load the model could withstand was 44.21 kips. The maximum lateral load LEN-2 Repair developed during testing was 40.46 kips. Therefore, the model predicted the ultimate lateral load capacity to be 109.3% of the actual ultimate load achieved. This STM overpredicted the load capacity of the specimen more than any other model. This is likely due to the initial condition of LEN-2 Repair prior to cyclic testing. LEN-2 Repair was tested monotonically to a drift of 6.93% in the east direction prior to the cyclic testing. This pushover damaged the concrete and steel making the specimen behave in a nonsymmetrical manner when tested cyclically and degrading the LEN-2 Repaired specimen cyclic performance.

The model reached the ultimate load when the headed rebar ties LO and OW, as seen in Figure 5.6, yielded simultaneously. The modeling results can be found numerically for the struts and ties in Tables 5.8 and 5.9, respectively. It can be seen in Table 5.9 that tie IP, which represents the longitudinal rebar in the column, is stressed to 81% of its capacity, and the CFRP wrap represented by tie MN was stressed to 72% of its effective capacity. The longitudinal column strut at the column-repair interface was at 85.8% of its capacity at failure. The same procedure used for NMB-2 Repair was used to calculate A_{cs} for struts KN, LM, MO, and NT.

5.2.5 LEN-2 model

All of the layout recommendations given in Section 5.1 were followed for LEN-2. The material properties recorded on the day of test were used in the model. The layout parameters and design inputs can be found in Table 5.10. All of the STM dimensions can be seen in Figure 5.7. The axial load applied to the model was equal to 104.0 kips, which was the recorded value of axial load on the day of testing.

From these model inputs it was determined that the maximum lateral load the model could withstand was 36.71 kips. The maximum lateral load LEN-2 developed during testing was

Table 5.8 – LEN-2 Repair conventional STM strut results

Member	Location	F_u (kips)		β_n	$A_{cs,\,min}$ (in.^{2})	$A_{cs} > A_{cs,\,min}$
AB	Column	69.95	@A	0.8	17.06	OK
			@B	1.0		
BC	Column	67.74	@B	1.0	20.66	OK
			@C	0.6		
BD	Column	137.70	@B	1.0	33.59	OK
			@D	0.8		
CF	Column	69.95	@C	0.6	21.33	OK
			@F	0.8		
DF	Column	106.71	@D	0.8	26.03	OK
			@F	0.8		
EH	Column	69.95	@E	0.6	21.33	OK
			@H	0.8		
FH	Column	160.93	@F	0.8	39.26	OK
			@H	0.8		
GJ	Column	69.95	@G	0.6	21.33	OK
			@J	0.8		
HJ	Column	215.14	@H	0.8	52.48	OK
			@J	0.8		
IK	Column	69.95	@I	0.6	21.33	OK
			@K	1.0		
JK	Column	269.35	@J	0.8	65.71	OK
			@K	1.0		
KN	Repair	156.33	@K	1.0	25.42	OK
			@N	0.8		
KP	Repair	137.59	@K	1.0	22.38	OK
			@P	0.8		
KT	Repair/ Pier cap	130.99	@K	1.0	31.96	OK
			@T	0.8		
LM	Repair	73.50	@L	0.8	11.95	OK
			@M	0.8		
LP	Repair	122.22	@L	0.8	19.88	OK
			@P	0.8		
MO	Repair	86.32	@M	0.8	17.55	OK
			@O	0.6		
NT	Repair/ Pier cap	102.32	@N	0.8	24.96	OK
			@T	0.8		
OP	Repair	86.46	@O	0.6	17.58	OK
			@P	0.8		
PT	Repair/ Pier cap	46.12	@P	0.8	11.25	OK
			@T	0.8		
QX	Pier cap	58.87	@Q	0.8	14.36	OK
			@X	0.8		
RY	Pier cap	58.87	@R	0.6	17.95	OK
			@Y	0.6		
SW	Pier cap	233.28	@S	0.6	71.14	OK
			@W	0.8		
TU	Pier cap	64.45	@T	0.8	15.72	OK
			@U	0.8		
TW	Pier cap	327.86	@T	0.8	79.98	OK
			@W	0.8		
TAA	Pier cap	59.21	@T	0.8	18.06	OK
			@AA	0.6		
TAB	Pier cap	54.90	@T	0.8	16.74	OK
			@AB	0.6		
UV	Pier cap	32.23	@U	0.8	7.86	OK
			@V	0.8		
UAC	Pier cap	54.90	@U	0.8	16.74	OK
			@AC	0.6		
VAD	Pier cap	54.90	@V	0.8	13.39	OK
			@AD	0.8		
WY	Pier cap	257.84	@W	0.8	78.63	OK
			@Y	0.6		
WZ	Pier cap	87.36	@W	0.8	26.64	OK
			@Z	0.6		
XY	Pier cap	38.60	@X	0.8	11.77	OK
			@Y	0.6		

Table 5.9 – LEN-2 Repair conventional STM tie results

Member	Material	F_u (kips)	F_{nt} (kips)	F_u / F_{nt} (%)	F_{nt} > F_u
AC	As-built long. rebar	54.21	268.60	20	OK
CD	As-built trans. rebar	87.02	156.24	56	OK
CE	As-built long. rebar	55.93	268.60	21	OK
EF	As-built trans. rebar	44.21	156.24	28	OK
EG	As-built long. rebar	110.14	268.60	41	OK
GH	As-built trans. rebar	44.21	156.24	28	OK
GI	As-built long. rebar	164.35	268.60	61	OK
IJ	As-built trans. rebar	44.21	156.24	28	OK
IP	As-built long. rebar	218.57	268.60	81	OK
LO	Headed rebar	146.66	146.94	100	YIELD
MN	CFRP wrap	140.02	195.08	72	OK
OW	Headed rebar	146.93	146.94	100	YIELD
QR	As-built long. rebar	82.81	429.76	19	OK
RS	As-built long. rebar	121.41	429.76	28	OK
RX	As-built trans. rebar	44.45	262.58	17	OK
ST	As-built long. rebar	263.83	429.76	61	OK
SY	As-built trans. rebar	184.76	262.58	70	OK
UAB	As-built trans. rebar	44.45	219.41	20	OK
VAC	As-built trans. rebar	44.45	219.41	20	OK
YZ	As-built long. rebar	139.12	429.76	32	OK
ZAA	As-built long. rebar	69.29	429.76	16	OK
AAAB	As-built long. rebar	96.68	429.76	22	OK
ABAC	As-built long. rebar	64.45	429.76	15	OK
ACAD	As-built long. rebar	32.23	429.76	7	OK

Table 5.10 – Modeling parameters used for LEN-2 Repair STM

Model input	Location/ member	Value
P_{axial}	Global	104 kips
x_c	As-built column	2.7 in.
x_t	As-built column	5.7 in.
Θ	As-built column	52.5 deg.
f_c'	As-built	6.00 ksi
f_y	As-built long.	68 ksi
f_y	As-built trans.	63 ksi

36.32 kips. Therefore, the model predicted the ultimate lateral load capacity to be 101.1% of the actual ultimate load achieved. This slight overprediction is likely due to the failure mode of LEN-2 during the test. The specimen failed due to a combined flexure/grout pull out failure. The conventional STM models LEN-2 as monolithic and this precast connection failure is not accurately captured within the model. The model reached the ultimate load when the column longitudinal strut LP crushed. The column longitudinal rebar tie KU reached 88% of its yield capacity at the predicted ultimate load. The modeling results can be found numerically for the struts and ties in Tables 5.11 and 5.12 respectively.

5.3 Nonlinear strut-and-tie model

The change that is made from the conventional STM to the nonlinear STM is going from a model that appropriately simplifies the force-transfer mechanism to a model that predicts both the force-transfer, the sequence of yielding of ties and crushing of struts, and the deflection of a reinforced concrete system. The additional parameters required in establishing a nonlinear STM from a conventional STM are the member areas and the material properties. The most accurate model a designer could produce would be one that could encompass all of the reinforcement and concrete, use the actual stress-strain material properties, and subject the model to typical seismic ground motions. This type of modeling is very detailed, requiring a significant investment of time, and produces challenges in even the most current Finite Element Models (FEM). The goal of the current nonlinear STM is to establish a model that provides the designer with many of the output

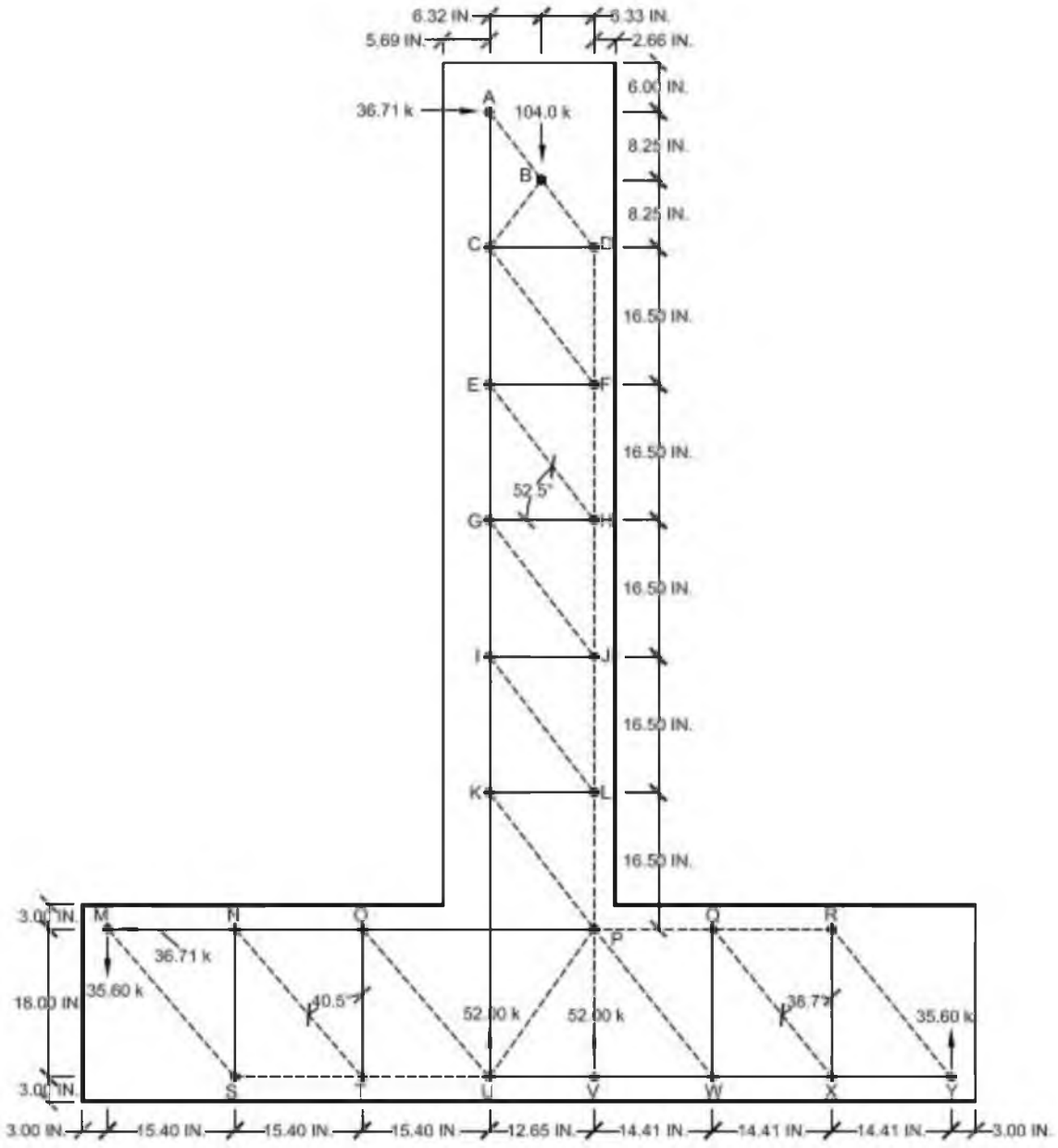

Figure 5.7 – LEN-2 STM dimensions, loading, and reactions

Table 5.11 – LEN-2 conventional STM strut results

Member	Location	F_u (kips)	β_n		$A_{cs,\,min}$ (in.^{2})	$A_{cs} > A_{cs,\,min}$
AB	Column	60.37	@A @B	0.8 1.0	15.78	OK
BC	Column	65.60	@B @C	1.0 0.6	21.44	OK
BD	Column	125.84	@B @D	1.0 0.8	32.90	OK
CF	Column	60.34	@C @F	0.6 0.8	19.72	OK
DF	Column	99.84	@D @F	0.8 0.8	26.10	OK
EH	Column	60.34	@E @H	0.6 0.8	19.72	OK
FH	Column	147.72	@F @H	0.8 0.8	38.62	OK
GJ	Column	60.34	@G @J	0.6 0.8	19.72	OK
HJ	Column	195.61	@H @J	0.8 0.8	51.14	OK
IL	Column	60.34	@I @L	0.6 0.8	19.72	OK
JL	Column	243.49	@J @L	0.8 0.8	63.66	OK
KP	Column/ Pier cap	60.34	@K @P	0.6 0.6	19.72	OK
LP	Column/ Pier cap	291.37	@L @P	0.8 0.8	76.18	CRUSH
MS	Pier cap	46.85	@M @S	0.8 0.8	12.25	OK
NT	Pier cap	46.85	@N @T	0.6 0.8	15.31	OK
OU	Pier cap	46.85	@O @U	0.6 0.6	15.31	OK
PQ	Pier cap	57.00	@P @Q	0.6 0.8	18.63	OK
PU	Pier cap	307.59	@P @U	0.6 0.6	100.52	OK
PV	Pier cap	52.00	@P @V	0.6 0.6	16.99	OK
PW	Pier cap	45.60	@P @W	0.6 0.6	14.90	OK
QR	Pier cap	28.50	@Q @R	0.8 0.8	7.45	OK
QX	Pier cap	45.60	@Q @X	0.8 0.6	14.90	OK
RY	Pier cap	45.60	@R @Y	0.8 0.8	11.92	OK
ST	Pier cap	30.46	@S @T	0.8 0.8	7.96	OK
TU	Pier cap	60.91	@T @U	0.8 0.6	19.91	OK

Table 5.12 – LEN-2 conventional STM tie results

Member	Material	F_u (kips)	F_{nt} (kips)	F_u / F_{nt} (%)	F_{nt} > F_u
AC	As-built long. rebar	47.92	268.60	18	OK
CD	As-built trans. rebar	76.61	166.32	46	OK
CE	As-built long. rebar	43.72	268.60	16	OK
EF	As-built trans. rebar	36.71	166.32	22	OK
EG	As-built long. rebar	91.61	268.60	34	OK
GH	As-built trans. rebar	36.71	166.32	22	OK
GI	As-built long. rebar	139.49	268.60	52	OK
IJ	As-built trans. rebar	36.71	166.32	22	OK
IK	As-built long. rebar	187.37	268.60	70	OK
KL	As-built trans. rebar	36.71	166.32	22	OK
KU	As-built long. rebar	235.25	268.60	88	OK
MN	As-built long. rebar	67.17	429.76	16	OK
NO	As-built long. rebar	97.62	429.76	23	OK
NS	As-built trans. rebar	35.60	352.80	10	OK
OP	As-built long. rebar	128.08	429.76	30	OK
OT	As-built trans. rebar	35.60	352.80	10	OK
QW	As-built trans. rebar	35.60	352.80	10	OK
RX	As-built trans. rebar	35.60	352.80	10	OK
UV	As-built long. rebar	85.49	429.76	20	OK
VW	As-built long. rebar	85.49	429.76	20	OK
WX	As-built long. rebar	57.00	429.76	13	OK
XY	As-built long. rebar	28.50	429.76	7	OK

that would be achieved with a FEM but in a much more time efficient manner.

The nonlinear STM developed is a general design procedure used to predict the nonlinear force-displacement response envelope for assemblies subjected to cyclic load reversals. To accurately predict the cyclic force-displacement response envelope from the monotonic nonlinear STM developed, material properties which take into consideration cyclic degradation have been adopted. The model can then be used as a design aid when selecting the proper reinforcement at service and at ultimate conditions. The nonlinear STM was run using a nonlinear static analysis option in the computer package SAP2000. Any truss members that were subjected to stresses that went beyond the elastic stress limit were assigned as two-joint multilinear elastic link elements. By definition, all members in an STM are loaded uniaxialy since it is a truss model. The elastic deflection of any given truss member, Δ_A, is given by eq. 5.9:

$$\Delta_A = \frac{F_u * L}{E * A} \tag{5.9}$$

where F_u is the axial force the member is subjected to from the given loading in the model. L, E, and A are the length, modulus of elasticity, and cross-sectional area for a given truss member, respectively. Therefore, the displacement of the system modeled by the STM is a product of all of the member's uniaxial deflections. The member material properties input into the model replace the modulus of elasticity in eq. 5.7 when the members become nonlinear. The link elements used to model the members in the nonlinear range require a multilinear force-displacement curve as the input. This input may be easily obtained from L, A, and the idealized multilinear material properties.

5.3.1 Member areas

STMs by nature are made up of discrete truss members that are not allowed to overlap. The designer's goal in the nonlinear STM is to model the concrete strut areas as large as possible without overlapping struts or nodes to accurately portray the rigidity provided by the

concrete. This design approach produces a model that is nearly solid concrete in compression zones and comes very close to a model which can represent all of the materials in 3D space.

The strut areas in the model should be made as large as possible without overlapping struts and while maintaining strut lengths in-between the nodes, even if this length is infinitesimally small. This process must be done graphically for all members, except for diagonal concrete struts in B-regions. The area of the diagonal struts in B-regions, A_{dc}, can be found by multiplying the perpendicular distance between the strut members by an effective web width. For rectangular members, such as the footing and pier cap, the effective width is equal to the width of the member. For columns that are circular, the effective width can be taken as 0.8h, where h is the diameter of the column. Although the columns that are being modeled are octagonal, an effective width of 0.8h was taken, conservatively. Therefore, the area of diagonal concrete struts located in the as-built column can be found with eq. 5.10:

$$A_{dc} = 2 * 0.8h * \sin \square * (h - (x_c + x_t)) \quad (5.10)$$

The rest of the strut areas should be found by maximizing the strut widths in 2D space. Once the maximum possible strut widths are established in a 2D plane parallel to the lateral load application, the strut areas can be found with the associate geometry of the system. If the strut area changes along the length of a member, the minimum area between nodes should be used along the entire length.

The ties used in the model can be classified as longitudinal ties and transverse ties. The longitudinal reinforcement ties in the as-built column have an area that is equal to the area of the longitudinal reinforcement located in the tension zone at first yield, as seen in Figure 5.2. The longitudinal reinforcement ties representing the headed rebar have an area that is equal to the area of the reinforcement located in the tension zone at first yield in the repair cross-section, as seen in Figure 5.2. In the case of the footing and pier cap there are two sets of longitudinal rebar ties, one that represents the positive moment steel and one that represents the negative moment

steel. The area of the CFRP wrap tie is the thickness of the wrap multiplied by the height of the repair.

The area used for steel transverse reinforcement ties, $A_{v,}$ takes into consideration the contribution of the transverse reinforcement strength, V_s, the shear strength provided by the concrete, V_c, and the shear strength provided by an externally applied axial load, V_p. If the transverse tie is located in the plastic hinge region, V_c should be neglected since the concrete capacity in this case is assumed as zero. A_v can be found from eqs 5.11 and 5.12 for transverse reinforcement ties located out of the plastic hinge region and in the plastic hinge region, respectively:

$$A_v = \frac{V_s + V_c + V_p}{f_{vy}} \tag{5.11}$$

$$A_v = \frac{V_s + V_p}{f_{vy}} \tag{5.12}$$

V_s, V_c, and V_p can be found using eqs. 5.13–5.16:

$$V_{s,spiral} = \frac{\pi * D'}{4s * \tan \square} * f_{vy} * A_{vs} \tag{5.13}$$

$$V_{s,stirrup} = \frac{d}{s * \tan \square} * f_{vy} * A_{vs} \tag{5.14}$$

$$V_c = \beta * \sqrt{f_c'} * A_{ve} \tag{5.15}$$

$$V_p = N * \left(\frac{h - 2 * x_c}{2 * (h_{col} - h_{repair})} \right) \tag{5.16}$$

where, $V_{s,\ spiral}$ and $V_{s,\ stirrup}$ are the values of V_s for spiral and stirrup transverse reinforcement,

respectively. f_{vy} is the yield strength of the transverse reinforcement. D' is the concrete core diameter measured center to center of spiral reinforcement. s is the pitch or spacing between transverse reinforcement. Θ is the angle measured between the axes of the diagonal strut and transverse reinforcement tie, as defined in Section 5.1. A_{vs} is the shear area of transverse reinforcement within one distance s. d is the member effective depth. β is a factor accounting for the tensile resistance of the concrete and is computed using the Modified Compression Field Theory *(37)*. A_{ve} is the effective shear area where $A_{ve} = 0.628\ A_g$ for circular cross-sections *(38)*. N is the externally applied axial load, where compression is positive and tension is negative. h is the overall width of the as-built column parallel to the direction of lateral loading, and for circular columns h is equal to the diameter of the column. x_c is the distance from the longitudinal strut in the column to the edge of concrete, as defined in Section 5.1.

5.3.2 Member material properties

Reinforced concrete members subjected to cyclic loading, simulating earthquake loading, experience material degradation in both the concrete and steel. Since the model is being subjected to a monotonic load and is simulating cyclic results, the effects of the material degradation must be taken into consideration in the material properties. The materials that are modeled in the nonlinear STMs are concrete, CFRP confined concrete, mild steel reinforcement, and the unidirectional CFRP wrap. All of the material properties have been simplified into linear or bilinear stress-strain relationships for use with the model, as shown in Figure 5.8.

Two material properties E_c and the effective strut strength, f_d, are required to model the concrete struts, located outside of the CFRP jacket. A typical value of E_c was adopted for all concrete struts and can be determined by eq. 5.17:

$$E_c = 57{,}000 * \sqrt{f_c'} \tag{5.17}$$

For longitudinal concrete struts located in the B-region, f_d was calculated from eq. 5.18:

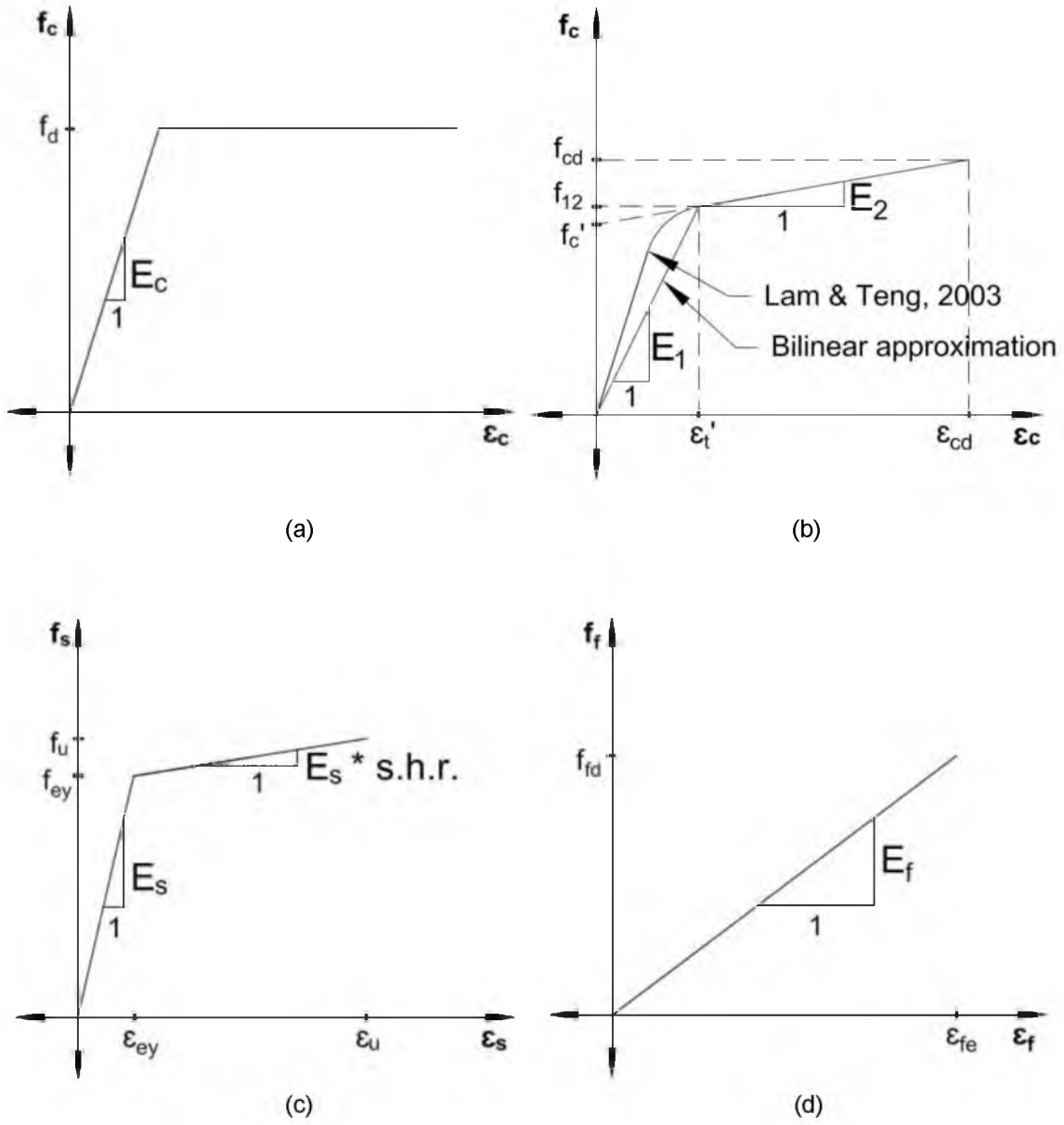

Figure 5.8 – Nonlinear STM material properties: (a) Concrete, (b) Confined concrete, (c) Mild steel, (d) CFRP

$$f_d = \frac{C_{c\,(max)}}{A_{cs}} \tag{5.18}$$

where $C_{c(max)}$ is the maximum flexural compression force the cross-section can develop. $C_{c(max)}$ is determined by a sectional analysis at which the extreme concrete compressive strain is at the maximum permissible compressive strain as determined from Mander's model *(39)*, $\varepsilon_{cu(max)}$, or the extreme fiber of the tensile steel reaches a strain of 15% *(18)*.

For concrete struts located in D-regions f_d is a parameter that is still being researched. It has been proposed that the predicted stress trajectory at the strut location prism, fan-shaped or bottle-shaped, influences f_d. Also, the given reinforcement and multiaxial state of stress play large roles in the determination of f_d. For the current study, previous values of f_d established in the literature were adopted *(18)* and are summarized in Table 5.13.

Generally, a value of $0.85f_c'$ was given to diagonal concrete struts located in B-regions. A value of $0.51f_c'$ was assigned to diagonal concrete struts in potential plastic hinge regions, diagonal struts adjacent to the column-footing joint, and longitudinal concrete struts. This value is assigned with the understanding that these struts are very well confined by extensive steel shear reinforcement. $0.68f_c'$ was assigned to all other diagonal concrete struts in D-regions.

A bilinear stress-strain relationship is used for CFRP confined concrete, which is based on a model developed by Lam and Teng *(40)*, as shown in Figure 5.8 (b). The model developed by Lam and Teng for CFRP confined concrete has been adopted by ACI 440, and the governing equations are shown in eqs. 5.19 and 5.20 *(33)*:

$$f_c = E_c * \varepsilon_c - \frac{(E_c - E_2)^2}{4 * f_c'} * \varepsilon_c^2 \quad \text{for } 0 \le \varepsilon_c \le \varepsilon_t' \tag{5.19}$$

$$f_c = f_c' + E_2 * \varepsilon_c \quad for\ \varepsilon_t' \le \varepsilon_c \le \varepsilon_{ccu} \tag{5.20}$$

where the strain hardening modulus, E_2, ε_t', and the ultimate compressive strain in CFRP confined concrete, $\varepsilon_{ccu,}$ are defined in eqs. 5.21–5.23, respectively:

Table 5.13 – D-region effective strut strength values

Effective strut strength, f_d	Strut description
$0.85f_c'$	This value can be used where a prism stress trajectory is anticipated, such as the diagonal concrete struts in the as-built column
$0.68f_c'$	This value is advised for regions of fan-shaped stress trajectories and in regions where minor cracking is expected
$0.51f_c'$	This value is apropriate for concrete struts neighboring steel where ε_s is less than 1%
$0.34f_c'$	This value is the maximum stress for bottle-shaped stress trajectories and for struts neigboring steel where ε_s is grater than 2%

$$E_2 = \frac{f_{cc}' - f_c'}{\varepsilon_{ccu}} \tag{5.21}$$

$$\varepsilon_t' = \frac{2 * f_c'}{E_c - E_2} \tag{5.22}$$

$$\varepsilon_{ccu} = \varepsilon_c' * \left[1.50 + \frac{12 * \kappa_b * f_l}{f_c'} * \left(\frac{\varepsilon_{fe}}{\varepsilon_c'}\right)^{0.45}\right] \tag{5.23}$$

where ε_{ccu} shall not be greater than 1.0%, ε_c' can be taken as 0.002, and κ_b is an FRP efficiency factor, which can be taken as 1.00 for circular cross-sections. Once E_2 and ε_t' are established, ε_{cd} can be found by from eq. 5.24:

$$\varepsilon_{cd} = \frac{f_{cd} - f_c'}{E_2} \tag{5.24}$$

where the effective strut strength of CFRP confined struts, f_{cd}, is obtained from Table 5.4 with one modification. The modification is that f_d was calculated with the unconfined compressive strength

of the concrete, f_c', and f_{cd} should be calculated with the confined compressive strength of the concrete, f_{cc}'. A conservative value of f_{cc}' was used equal to $1.5f_c'$ (*6*), but other expressions could be used that are available in the literature *(35)*. An f_d value of $0.68f_{cc}'$ was used for all of the CFRP confined concrete struts due to the semi-expansive concrete and extensive confinement.

To simplify Lam and Teng's model into a bilinear relationship, eq. 5.19 was approximated as linear by connecting the origin to the intersection of eqs. 5.19 and 5.20 at ε_t'. A new initial modulus is assigned to the confined concrete, E_1, and can be found by eq. 5.25:

$$E_1 = \frac{f_c'}{\varepsilon_t'} + E_2 \tag{5.25}$$

The stress at which E_1 and E_2 intersect is designated f_{12}. If f_{12} is greater than f_{cd}, then the confined concrete stress-strain properties become linear, making E_2 irrelevant. This was the case for both NMB-2 Repair and LEN-2 Repair, indicating the conservatism of this approach. If f_{12} is less than f_{cd}, f_{12} and f_{cd} should be linearly connected following a slope of E_2.

Three material properties are required to model the reinforcing steel ties in the nonlinear STM, the elastic modulus of steel, E_s, the effective yield strength of the steel, f_{ey}, and the strain hardening ratio, s.h.r. A typical E_s value for steel of 29,000 ksi was assumed for all reinforcing steel ties. f_{ey} is dependent upon the reinforcement arrangement, location, and the properties of the cross-section at first yield that the given tie represents. The general formula for obtaining f_{ey} for longitudinal rebar ties is given in eq. 5.26:

$$f_{ey} = \frac{T}{A_{rt}} \tag{5.26}$$

where T is the total tensile force in the reinforcing steel at first yield, and A_{rt} is the area of reinforcement in the tension zone at first yield; see Figure 5.2. The reason f_{ey} has been established is to represent the large strain gradient in reinforcing steel that can occur in column cross-sections due to the longitudinal rebar having varying moment arms. Procedures for

determining the f_{ey} of circular and rectangular columns reinforced with many peripheral rebar have been developed *(18)*. For a typical rectangular ductile footing or pier cap with the longitudinal reinforcement residing in a top and bottom layer, the total flexural force at first yield is very close to the total yield strength of the reinforcement. Therefore, it is safe to assume that f_{ey} is equal to the measured yield strength of the reinforcement in these locations. For longitudinal ties located in D-regions, which did not originate from a B-region, f_{ey} is equal to the measured yield strength of the reinforcement. Transverse reinforcement ties are not subjected to large strain gradients and therefore, f_{ey} is equal to the measured yield strength of the transverse reinforcement.

Following the recommendations of previous research *(18),* s.h.r.'s of 5.0% and 2.5% were adopted for longitudinal reinforcement. For reinforcement ties with large strain gradients, where eq. 5.26 yielded a f_{ey} value less than f_y, a s.h.r. of 5.0% should be used to model the fact that when f_{ey} is reached, not all of the reinforcement has yielded. The high s.h.r. helps model the fact that first yield occurs long before all of the longitudinal rebar have yielded. Additionally, the longitudinal B-region s.h.r. should be increased to 5.0% if there is not a significant amount of transverse reinforcement *(18)*.

The modeling parameters required to develop the stress-strain relationship for the CFRP tie are the elastic modulus of CFRP, E_f, and the effective strain level in the CFRP jacket at failure, ε_{fe}, where ε_{fe} is defined in eq. 5.27 *(33)*:

$$\varepsilon_{fe} = \kappa_\varepsilon * \varepsilon_{fu} \tag{5.27}$$

ε_{fe} must be less than 0.4%. κ_ε is the CFRP strain efficiency factor, which has been determined experimentally, and accounts for the multiaxial state of stress acting on the jacket and strain concentrations. It is recommended that κ_ε be taken as a value between 0.57–0.61 *(33)*. Conservatively, κ_ε has been taken as 0.57 for this study.

The nonlinear STM has reached its maximum applied force when the concrete crushes or the reinforcement ruptures. Concrete crushing is defined as reaching a stress value of f_d, for the

concrete located outside of the CFRP wrap or the CFRP confined concrete reaching a stress value of f_{cd}. Reinforcement rupture occurs when the mild steel or CFRP reaches a stress value of f_u of f_{fd}, respectively.

5.3.3 Determination of ultimate displacement

When the nonlinear STM has reached the ultimate load due to a concrete strut crushing, it has not necessarily reached the ultimate displacement of the system. If the model reaches an ultimate load due to reinforcement rupturing, the model has reached the ultimate load and ultimate displacement simultaneously. If a nonlinear STM reaches an ultimate load due to a concrete strut crushing, the ultimate displacement can be determined by the following method.

To find the ultimate displacement of the system the displacement ductility, μ_Δ, is multiplied by the yield displacement, Δ_y. The equation used to determine μ_Δ is based on the curvature ductility of the member, which can be found from a sectional analysis. For the nonlinear STM model, μ_Δ is found from eq. 5.28 *(27)*:

$$\mu_\Delta = \frac{\Delta_u}{\Delta_y} = M_r + \frac{1}{C_\phi} * (\mu_\phi - 1) * 3\lambda_p * \left(1 - \frac{\lambda_p}{2C_\phi}\right) \tag{5.28}$$

where M_r is equal to the moment capacity ratio of the column, found from eq. 5.29:

$$M_r = \frac{M_u}{M_y} \tag{5.29}$$

M_u is the ultimate moment capacity of the system, and M_y is the yield moment of the system. Conservatively, an elasto-plastic assumption can be made where M_r is assumed to equal 1.0. C_ϕ is the column curvature coefficient and is equal to 1.0 or 0.5 for single and double curvature bending, respectively. μ_ϕ is the curvature ductility of the column as defined in eq. 5.30:

$$\mu_{\phi} = \frac{\phi_u}{\phi_y} \tag{5.30}$$

where the ultimate and yield curvatures of the column cross-section, ϕ_u and ϕ_u, are determined from a moment-curvature analysis of the column cross-section. Mander's model was used to model the stress-strain relationship of transversely reinforced concrete when determining ϕ_u and ϕ_u *(39)*. Also, a steel model that includes strain hardening was used to accurately portray the steel forces at high moments. The normalized plastic hinge length for monolithic type column, λ_p, can be determined from eq. 5.31:

$$\lambda_p = \frac{L_p}{L_c} = 0.12C_{\phi} + 0.014\alpha_s * \left(\frac{f_{ye} * d_{bl}}{L_c}\right) \tag{5.31}$$

where L_p is the length of the plastic hinge, and L_c is the length of the column from the top of the repair to the point of inflection. Equation 5.31 was only used for the repaired specimens that demonstrated monolithic type curvature and damage during testing. It is known that plastic hinge regions at precast concrete joints will not follow the plastic hinge behavior of a monolithic counterpart. Therefore, λ_p was determined experimentally for NMB-2 and LEN-2, which exhibited plastic hinge lengths of 14 in. and 13 in., respectively. α_s is the reinforcement bond-slip coefficient, which is equal to 1.0 since bond-slip in the plastic hinge region is possible, as recommended *(27)*. f_{ye} and d_{bl} are the expected yield strength of the reinforcement and the diameter of the longitudinal rebar, respectively.

It is recommended that Δ_y for a single curvature column be found by eq. 5.32:

$$\Delta_y = \frac{\phi_y * {L_c}^2}{3} \tag{5.32}$$

Once both μ_{Δ} and Δ_y are determined, Δ_u can be easily established by multiplying μ_{Δ} by Δ_y.

5.3.4 NMB-2 Repair model

The nonlinear STM for NMB-2 Repair uses the same layout as the conventional STM as shown in Figure 5.3. The member areas for the nonlinear STM ties are the same as the conventional STM. The member areas of the struts are modified. The maximum possible strut areas were used in the model to accurately portray the stiffness that the concrete provides. This process must be done graphically for the D-regions to make sure that the struts fall within the member geometry and that none of the struts or nodes overlap. A graphical representation of the strut widths can be seen in Figure 5.9. It should be noted that nodes M and N were moved 1.5 in. into the repair concrete to establish the maximum allowable strut areas for KN, LM, MO, and NR. Nodes M and N are located on the exterior of the repair concrete since they represent the CFRP wrap. If the nodes were not relocated, the previously mentioned struts would have allowable areas equal to zero. Due to the vast amount of confinement the wrap provides to the concrete struts located within the wrap, the relocation of the nodes was deemed acceptable.

The material properties are based on the recorded material values on the day of testing and follow the recommendations of Section 5.3.2. Many of the material properties used in the nonlinear STM are summarized in Table 5.14. The allowable compressive stress of concrete struts, f_d, is not included in Table 5.14 since this is a function of the strut location and adjacent reinforcement.

The nonlinear STM force displacement results are shown in Figure 5.10 plotted over the hysteresis recorded during testing. The nonlinear STM results can also be found in Tables 5.15 and 5.16 for the struts and ties, respectively. A summary of the events during the modeling can be found in Table 5.17.

The ultimate load that the nonlinear STM force-displacement envelope predicted was 37.56 kip. This load is 82% of the 45.56 kip ultimate load that the specimen reached during testing and 89% of the 42.09 kip ultimate load that the idealized average elasto-plastic response reached. The ultimate displacement that the nonlinear STM predicted, using eqs. 5.28 and 5.31 for the displacement ductility and normalized plastic hinge length, respectively, was 5.89 in. This predicted ultimate displacement is 81% of the ultimate displacement that NMB-2 Repair reached

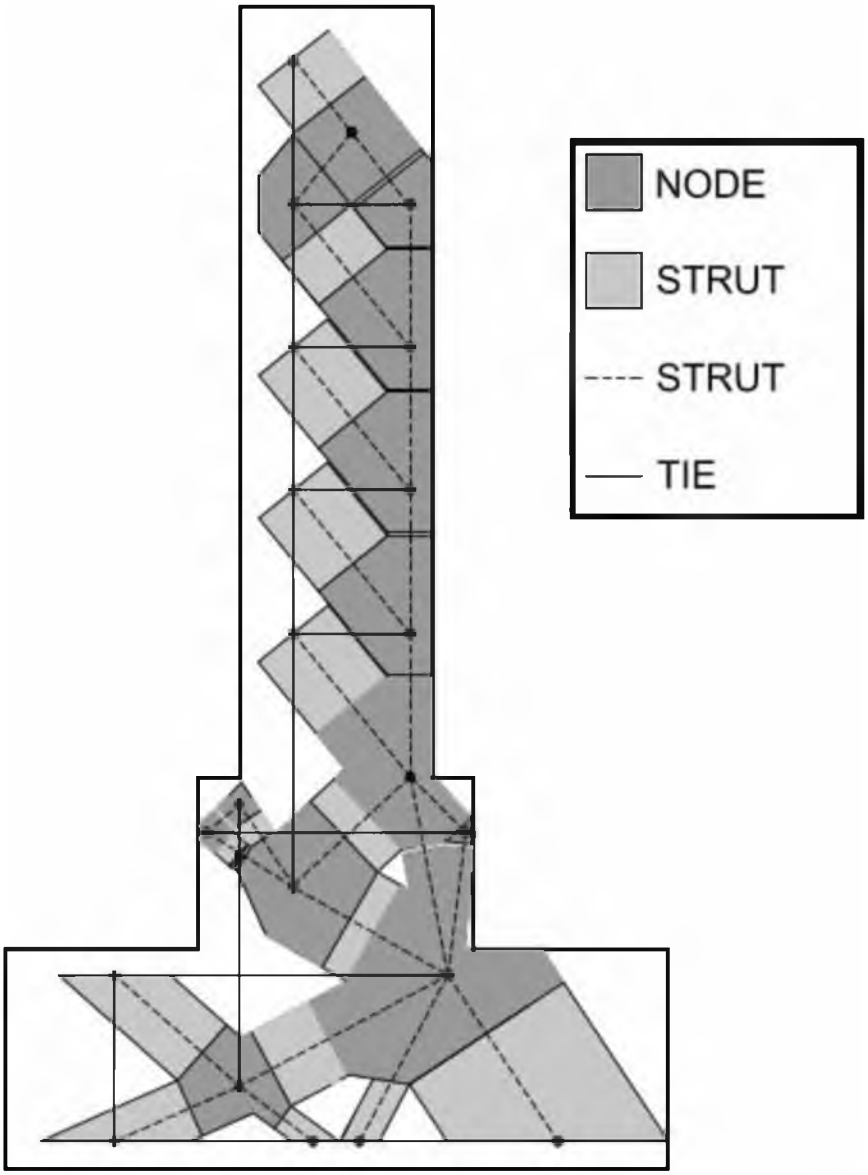

Figure 5.9 – Strut widths used to determine the member areas of NMB-2 Repair

Table 5.14 – Selected cyclic material properties used with NMB-2 Repair

Material input	Material	Value (ksi)
E_c	As-built concrete	4570
E_1	CFRP conf. conc.	2520
E_2	CFRP conf. conc.	469
f_{12}	CFRP conf. conc.	7.90
E_s	Reinforcing steel	29000
E_f	CFRP wrap	8990
f_{fd}	CFRP wrap	57.9

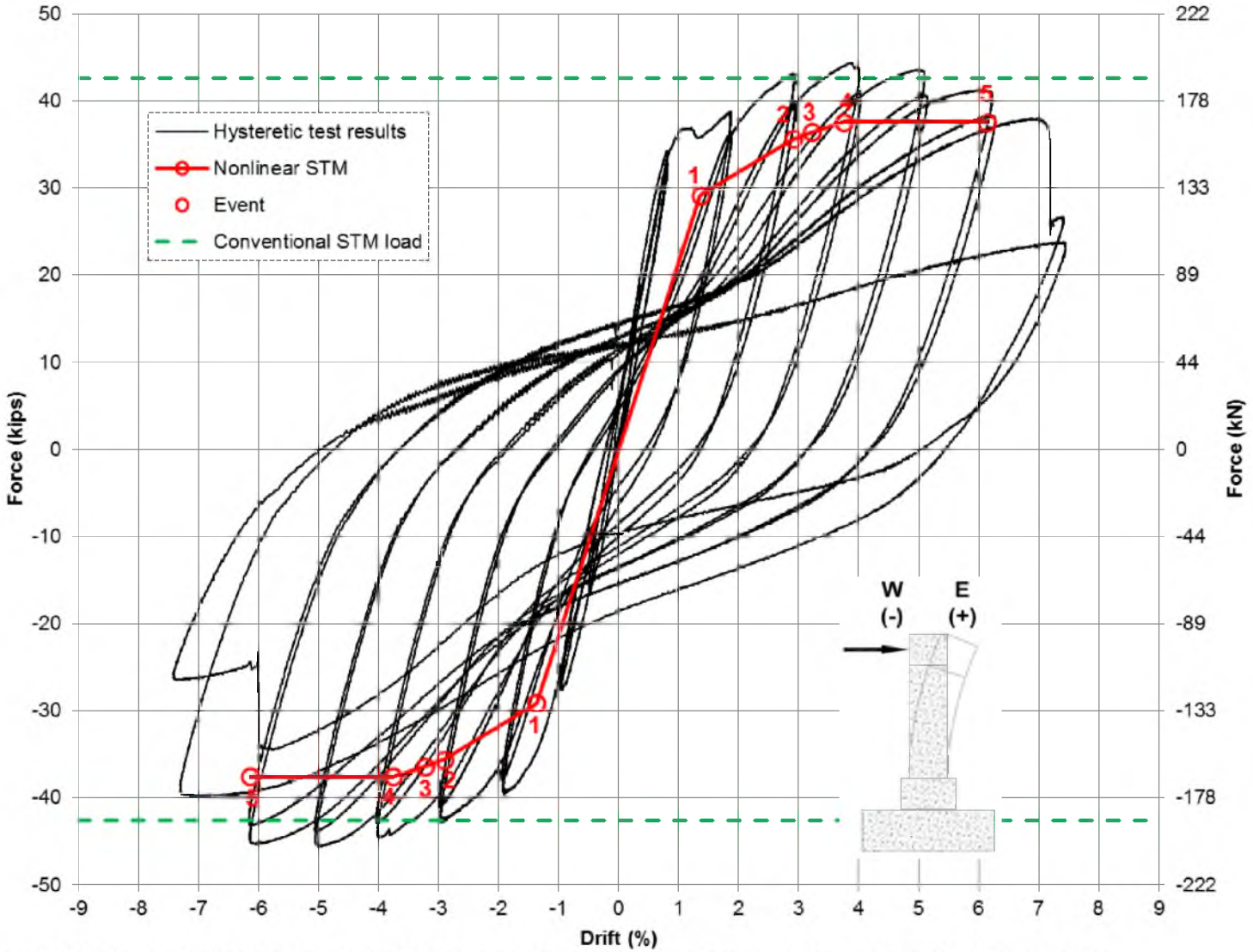

Figure 5.10 – NMB-2 Repair hysteresis, nonlinear STM force-displacement envelope, and conventional STM load results

Table 5.15 – NMB-2 Repair nonlinear STM tabular strut results

Member	Material	A ($in.^2$)	Effective strut strength		Event 1			Event 2			Event 3			Event 4		
			Eqn.	f_d or f_{cd} (ksi)	F_u (kips)	f_u (ksi)	f_u / f_d (%)	F_u (kips)	f_u (ksi)	f_u / f_d (%)	F_u (kips)	f_u (ksi)	f_u / f_d (%)	F_u (kips)	f_u (ksi)	f_u / f_d (%)
AB	Concrete	329	0.85 f_c'	5.47	46.0	0.1	2.6	56.3	0.2	3.1	57.5	0.2	3.2	59.3	0.2	3.3
BC	Concrete	329	0.85 f_c'	5.47	56.1	0.2	3.1	56.1	0.2	3.1	56.1	0.2	3.1	56.1	0.2	3.1
BD	Concrete	329	0.85 f_c'	5.47	102.1	0.3	5.7	112.4	0.3	6.2	113.6	0.3	6.3	115.4	0.4	6.4
CF	Concrete	329	0.85 f_c'	5.47	46.0	0.1	2.6	56.3	0.2	3.1	57.5	0.2	3.2	59.3	0.2	3.3
DF	Concrete	69	$C_{c(max)} / A_{cs}$	5.85	79.0	1.1	19.5	87.0	1.3	21.5	87.9	1.3	21.7	89.3	1.3	22.1
EH	Concrete	329	0.85 f_c'	5.47	46.0	0.1	2.6	56.3	0.2	3.1	57.5	0.2	3.2	59.3	0.2	3.3
FH	Concrete	69	$C_{c(max)} / A_{cs}$	5.85	114.6	1.7	28.3	130.5	1.9	32.2	132.4	1.9	32.7	135.2	2.0	33.4
GJ	Concrete	329	0.85 f_c'	5.47	46.0	0.1	2.6	56.3	0.2	3.1	57.5	0.2	3.2	59.3	0.2	3.3
HJ	Concrete	69	$C_{c(max)} / A_{cs}$	5.85	150.2	2.2	37.1	174.1	2.5	43.0	176.9	2.6	43.7	181.2	2.6	44.7
IK	Concrete	329	0.51 f_c'	3.28	46.0	0.1	4.3	56.3	0.2	5.2	57.5	0.2	5.3	59.3	0.2	5.5
JK	Concrete	69	0.51 f_c'	3.28	185.8	2.7	81.9	217.7	3.1	95.9	221.4	3.2	97.5	227.1	3.3	100.0
KN	CFRP conf. conc.	36	0.68 f_{oc}'	6.56	99.2	2.8	42.0	131.5	3.6	55.6	135.3	3.8	57.3	141.0	3.9	59.7
KP	CFRP conf. conc.	308	0.68 f_{oc}'	6.56	88.0	0.3	4.4	113.0	0.4	5.6	116.0	0.4	5.7	120.4	0.4	6.0
KR	CFRP conf. conc.	107	0.68 f_{oc}'	6.56	98.3	0.9	14.1	100.0	0.9	14.3	100.2	0.9	14.3	100.5	0.9	14.4
LM	CFRP conf. conc.	36	0.68 f_{oc}'	6.56	48.1	1.3	20.4	63.8	1.8	27.0	65.7	1.8	27.8	68.4	1.9	28.9
LP	CFRP conf. conc.	70	0.68 f_{oc}'	6.56	73.0	1.0	15.8	96.8	1.4	20.9	99.6	1.4	21.6	103.8	1.5	22.5
MO	CFRP conf. conc.	36	0.68 f_{oc}'	6.56	54.2	1.5	22.9	71.8	2.0	30.4	73.9	2.1	31.3	77.0	2.1	32.6
NR	CFRP conf. conc.	36	0.68 f_{oc}'	6.56	65.9	1.8	27.9	87.3	2.4	36.9	89.8	2.5	38.0	93.6	2.6	39.6
OP	CFRP conf. conc.	70	0.68 f_{oc}'	6.56	54.3	0.8	11.7	71.9	1.0	15.6	74.0	1.1	16.0	77.1	1.1	16.7
PR	CFRP conf. conc.	346	0.68 f_{oc}'	6.56	26.6	0.1	1.2	38.3	0.1	1.7	39.7	0.1	1.7	41.8	0.1	1.8
QS	Concrete	289	0.68 f_c'	4.37	146.2	0.5	11.6	172.3	0.6	13.6	175.4	0.6	13.9	180.0	0.6	14.2
RS	Concrete	326	0.51 f_c'	3.28	145.0	0.4	13.6	177.2	0.5	16.6	181.0	0.6	16.9	186.7	0.6	17.5
RV	Concrete	135	0.51 f_c'	3.28	49.2	0.4	11.1	49.2	0.4	11.1	49.2	0.4	11.1	49.2	0.4	11.1
RW	Concrete	721	0.51 f_c'	3.28	75.7	0.1	3.2	91.8	0.1	3.9	93.7	0.1	4.0	96.6	0.1	4.1
ST	Concrete	236	0.68 f_c'	4.37	83.5	0.4	8.1	93.2	0.4	9.0	94.4	0.4	9.1	96.1	0.4	9.3
SU	Concrete	262	0.68 f_c'	4.37	72.2	0.3	6.3	72.2	0.3	6.3	72.2	0.3	6.3	72.2	0.3	6.3

Table 5.16 - NMB-2 Repair nonlinear STM tabular tie results

Member	Material	A ($in.^2$)	Effective yield strength		Event 1			Event 2			Event 3			Event 4		
			Eqn.	f_{ey} or f_{fd} (ksi)	F_u (kips)	f_u (ksi)	f_u / f_{ey} (%)	F_u (kips)	f_u (ksi)	f_u / f_{ey} (%)	F_u (kips)	f_u (ksi)	f_u / f_{ey} (%)	F_u (kips)	f_u (ksi)	f_u / f_{ey} (%)
AC	As-built long. rebar	3.95	T / A_{rt}	34.1	35.6	9.0	26.4	43.6	11.0	32.4	44.5	11.3	33.1	45.9	11.6	34.1
CD	As-built trans. rebar	2.63	f_y	63.0	64.6	24.6	39.0	71.2	27.1	42.9	71.9	27.3	43.4	73.1	27.8	44.1
CE	As-built long. rebar	3.95	T / A_{rt}	34.1	27.8	7.0	20.7	43.7	11.1	32.5	45.6	11.5	33.9	48.4	12.3	36.0
EF	As-built trans. rebar	2.63	f_y	63.0	29.1	11.1	17.6	35.6	13.6	21.5	36.4	13.8	22.0	37.6	14.3	22.7
EG	As-built long. rebar	3.95	T / A_{rt}	34.1	63.4	16.1	47.1	87.3	22.1	64.8	90.1	22.8	66.9	94.3	23.9	70.1
GH	As-built trans. rebar	2.63	f_y	63.0	29.1	11.1	17.6	35.6	13.6	21.5	36.4	13.8	22.0	37.6	14.3	22.7
GI	As-built long. rebar	3.95	T / A_{rt}	34.1	99.0	25.1	73.5	130.9	33.1	97.2	134.6	34.1	100.0	140.2	35.5	104.2
IJ	As-built trans. rebar	1.93	f_y	63.0	29.1	15.1	24.0	35.6	18.5	29.3	36.4	18.9	29.9	37.6	19.5	30.9
IP	As-built long. rebar	3.95	T / A_{rt}	34.1	134.6	34.1	100.0	174.4	44.2	129.6	179.1	45.3	133.0	186.2	47.1	138.3
LO	Headed rebar	2.37	T / A_{rt}	49.1	87.8	37.0	75.5	116.4	49.1	100.0	119.8	50.5	102.9	124.8	52.7	107.2
MN	CFRP wrap	3.40	$E_f * \kappa_\varepsilon * \varepsilon_{fu}$	57.3	87.4	25.7	44.8	115.8	34.1	59.4	119.1	35.0	61.1	124.2	36.5	63.7
OS	Headed rebar	2.37	T / A_{rt}	49.1	87.6	37.0	75.3	116.1	49.0	99.8	119.5	50.4	102.7	124.5	52.5	107.0
QR	As-built long. rebar	4.74	f_y	68.0	138.5	29.2	43.0	164.6	34.7	51.1	167.7	35.4	52.0	172.3	36.3	53.4
QT	As-built trans. rebar	13.9	f_y	63.0	33.8	2.4	3.9	37.8	2.7	4.3	38.2	2.7	4.4	38.9	2.8	4.4
TU	As-built long. rebar	6.32	f_y	68.0	76.3	12.1	17.8	85.2	13.5	19.8	86.3	13.6	20.1	87.8	13.9	20.4
UV	As-built long. rebar	6.32	f_y	68.0	18.6	3.0	4.3	27.5	4.4	6.4	28.6	4.5	6.7	30.2	4.8	7.0
VW	As-built long. rebar	6.32	f_y	68.0	41.8	6.6	9.7	50.7	8.0	11.8	51.7	8.2	12.0	53.3	8.4	12.4

Table 5.17 – NMB-2 Repair nonlinear STM events

Event	1	2	3	4	5
Description	Longitudinal column tie yields (IP)	Headed rebar tie yields (LO & OS)	Longitudinal column tie yields (GI)	Longitudinal column strut crushes (JK)	Ultimate displacement is reached
Force (kip)	29	36	36	38	38
Displacement (in.)	1.3	2.8	3.1	3.6	5.9

during testing. The ultimate displacement of the specimen during testing is defined as the displacement in which a 20% decline in lateral load carrying capacity is reached.

Four ties yielded while running the nonlinear STM of NMB-2 Repair. Chronologically the ties that yielded were the longitudinal rebar tie in the column at the repair-column interface (IP), the headed rebar ties (LO and OS), and the longitudinal rebar tie in the column above IP (GI). The fourth event, and the point that the maximum lateral load was reached, was when the longitudinal concrete strut at the column-repair interface (JK) crushed. This performance matches the observed performance during testing in terms of members that yielded and the chronological order that they yielded in. Also, when the concrete strut crushes in the model, event 4, the displacement approximately lines up with the displacement in which the specimen reached its ultimate load carrying capacity. The deflected shape of the model matches the behavior of the test results, as seen in Figure 5.11. The footing and repair remain relatively stationary while the column deflects in both the model and the test results.

The initial stiffness of the force-displacement envelope is slightly less than that of the testing data. Since the nonlinear STM is used to predict the degraded performance of a specimen due to cyclic loading the last displacement during the 1-inch displacement step was used to compare the initial stiffness. The models initial stiffness is 22.2 k/in., which is 75% of the recorded test results.

5.3.5 NMB-2 model

The nonlinear STM for NMB-2 uses the same layout as the conventional STM as shown in Figure 5.5. The tie areas for the nonlinear STM are the same as in the conventional STM, but

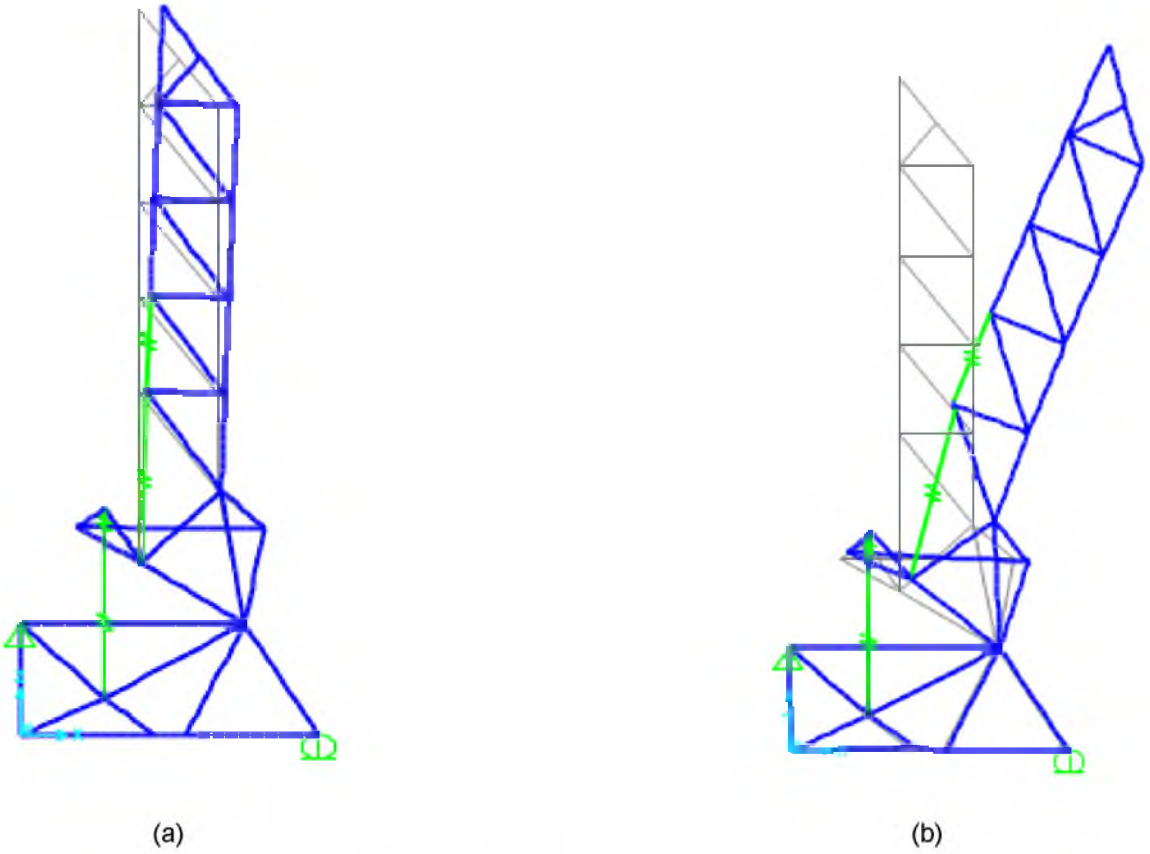

(a) (b)

Figure 5.11 – NMB-2 Repair nonlinear STM deflected shape at event 4: (a) 1x scale factor, (b) 10x scale factor

the member areas of the struts are modified. The maximum possible strut areas were used and were determined graphically. The strut widths used in the model are shown in Figure 5.12. The material properties used in the model are the recorded material values on the day of testing. Pertinent material properties can be found in Table 5.4.

The nonlinear STM force-displacement results can be seen in Figure 5.13 plotted over the hysteresis recorded during testing. The nonlinear STM results can also be found in Tables 5.18 and 5.19 for the struts and ties respectively. A summary of the events during the modeling can be found in Table 5.20. The ultimate load that the nonlinear STM force-displacement envelope predicted was 25.56 kips. This load is 66% of the 38.83 kip ultimate load that the specimen reached during testing and 79% of the 32.37 kip ultimate load that the idealized average elasto-plastic response reached. The ultimate displacement that the nonlinear STM

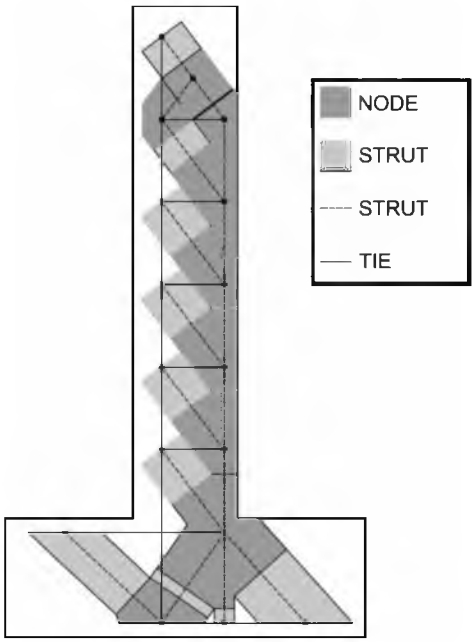

Figure 5.12 – Strut widths used to determine the member areas of NMB-

predicted, using a plastic hinge length of 14 in. and eq. 5.28 for the displacement ductility, was 6.81 in. This predicted ultimate displacement is 115% of the ultimate displacement that NMB-2 reached during testing, where the ultimate displacement of the specimen during testing is defined as the displacement in which a 20% decline in lateral load carrying capacity is reached.

One tie yielded while running the nonlinear STM of NMB-2, which was the longitudinal rebar tie in the column at the column-footing joint (KO). The second event, and the point that the maximum lateral load was reached, was when the longitudinal concrete strut at the column-footing interface (LN) crushed. This performance matches the observed performance during testing where the longitudinal rebar in the column yielded early on. Also, when the concrete strut crushes in the model, event 2, the drift is within 1% of the drift in which the specimen reached its ultimate load carrying capacity.

The initial stiffness of the force-displacement envelope is slightly less than that of the test data. Since the nonlinear STM is used to predict the degraded performance of a specimen due to cyclic loading, the last displacement during the 1-inch displacement step was used to compare the initial stiffness. The model's initial stiffness is 29.6 k/in., which is 113% of the recorded test results.

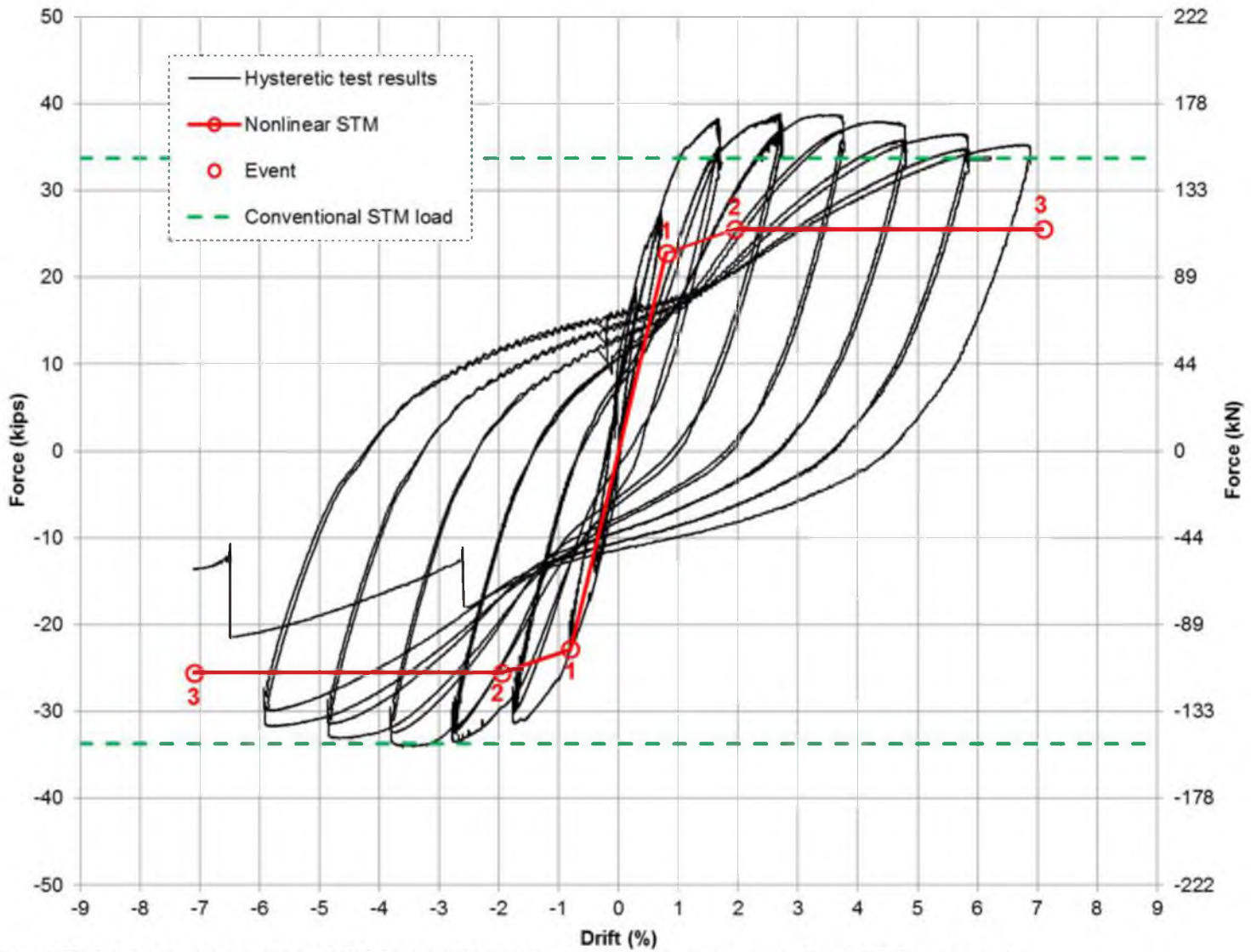

Figure 5.13 – NMB-2 hysteresis, nonlinear STM force-displacement envelope, and conventional STM load result

Table 5.18 – NMB-2 nonlinear STM tabular strut results

Member	Material	A ($in.^2$)	Effective strut strength		Event 1			Event 2		
			Eqn.	f_d or f_{cd} (ksi)	F_u (kips)	f_u (ksi)	f_u / f_d (%)	F_u (kips)	f_u (ksi)	f_u / f_d (%)
AB	Concrete	335	0.85 f_c'	4.71	38.0	0.1	2.4	42.6	0.1	2.7
BC	Concrete	335	0.85 f_c'	4.71	59.9	0.2	3.8	59.9	0.2	3.8
BD	Concrete	335	0.85 f_c'	4.71	96.6	0.3	6.1	101.1	0.3	6.4
CF	Concrete	335	0.85 f_c'	4.71	37.7	0.1	2.4	42.3	0.1	2.7
DF	Concrete	77	$C_{c(max)} / A_{cs}$	5.18	76.7	1.0	19.1	80.3	1.0	20.0
EH	Concrete	335	0.85 f_c'	4.71	37.7	0.1	2.4	42.3	0.1	2.7
FH	Concrete	77	$C_{c(max)} / A_{cs}$	5.18	106.7	1.4	26.6	114.0	1.5	28.4
GJ	Concrete	335	0.85 f_c'	4.71	37.7	0.1	2.4	42.3	0.1	2.7
HJ	Concrete	77	$C_{c(max)} / A_{cs}$	5.18	136.8	1.8	34.1	147.7	1.9	36.9
IL	Concrete	335	0.85 f_c'	4.71	37.7	0.1	2.4	42.3	0.1	2.7
JL	Concrete	77	$C_{c(max)} / A_{cs}$	5.18	166.9	2.2	41.6	181.4	2.3	45.3
KN	Concrete	335	0.51 f_c'	2.83	37.7	0.1	4.0	42.3	0.1	4.5
LN	Concrete	77	0.51 f_c'	2.83	196.9	2.5	90.1	215.1	2.8	98.4
MO	Concrete	360	0.68 f_c'	3.77	68.8	0.2	5.1	77.1	0.2	5.7
NO	Concrete	504	0.51 f_c'	2.83	162.0	0.3	11.4	181.7	0.4	12.8
NP	Concrete	144	0.51 f_c'	2.83	47.1	0.3	11.6	47.1	0.3	11.6
NQ	Concrete	504	0.51 f_c'	2.83	63.1	0.1	4.4	70.7	0.1	5.0

Table 5.19 - NMB-2 nonlinear STM tabular tie results

Member	Material	A ($in.^2$)	Effective yield strength		Event 1			Event 2		
			Eqn.	f_{ey} (ksi)	F_u (kips)	f_u (ksi)	f_u / f_{ey} (%)	F_u (kips)	f_u (ksi)	f_u / f_{ey} (%)
AC	As-built long. rebar	3.95	T / A_{rt}	33.7	30.4	7.7	22.9	34.1	8.6	25.6
CD	As-built trans. rebar	2.42	f_y	63.0	58.7	24.3	38.5	61.5	25.4	40.3
CE	As-built long. rebar	3.95	T / A_{rt}	33.7	12.6	3.2	9.5	19.9	5.0	14.9
EF	As-built trans. rebar	2.42	f_y	63.0	22.8	9.4	15.0	25.6	10.6	16.8
EG	As-built long. rebar	3.95	T / A_{rt}	33.7	42.7	10.8	32.1	53.6	13.6	40.3
GH	As-built trans. rebar	2.42	f_y	63.0	22.8	9.4	15.0	25.6	10.6	16.8
GI	As-built long. rebar	3.95	T / A_{rt}	33.7	72.7	18.4	54.7	87.3	22.1	65.7
IJ	As-built trans. rebar	2.42	f_y	63.0	22.8	9.4	15.0	25.6	10.6	16.8
IK	As-built long. rebar	3.95	T / A_{rt}	33.7	102.8	26.0	77.3	121.0	30.6	91.0
KL	As-built trans. rebar	1.77	f_y	63.0	22.8	12.9	20.4	25.6	14.4	22.9
KO	As-built long. rebar	3.95	T / A_{rt}	33.7	132.9	33.6	100.0	154.7	39.2	116.4
MN	As-built long. rebar	6.32	f_y	68.0	73.1	11.6	17.0	81.9	13.0	19.1
OP	As-built long. rebar	4.74	f_y	68.0	42.2	8.9	13.1	47.3	10.0	14.7
PQ	As-built long. rebar	4.74	f_y	68.0	42.2	8.9	13.1	47.3	10.0	14.7

Table 5.20 – NMB-2 nonlinear STM events

Event	1	2	3
Description	Longitudinal column tie yields (KO)	Longitudinal column strut crushes (LN)	Ultimate displacement is reached
Force (kip)	23	26	26
Displacement (in.)	0.77	1.9	6.8

5.3.6 LEN-2 Repair model

The nonlinear STM for LEN-2 Repair uses the same layout as the conventional STM as shown in Figure 5.6. The member areas for the nonlinear STM ties are the same as the conventional STM, but the member areas of the struts are modified. The maximum possible strut areas were used and were determined graphically. The strut widths used in the nonlinear STM can be seen in Figure 5.14. It should be noted that nodes M and N were moved 1.5 in. into the repair concrete to establish the maximum allowable strut areas for KN, LM, MO, and NR. Nodes M and N are located on the exterior of the repair concrete since they represent the CFRP wrap. If the nodes were not relocated, the previously mentioned struts would have zero allowable areas. Due to the vast amount of confinement the wrap provides to the concrete struts located within the wrap the relocation of the nodes was deemed acceptable.

The material properties are obtained from the recorded material values on the day of testing and follow the recommendations of Section 5.3.2. Many of the material properties used in the nonlinear STM are summarized in Table 5.21. The allowable compressive stress of concrete struts, f_d, is not included in Table 5.21 since it is a function of the strut location and adjacent reinforcement.

The nonlinear STM force-displacement results are shown in Figure 5.15 plotted over the hysteresis and pushover recorded during testing. It should be noted that LEN-2 Repair was tested monotonically in the east direction before it was tested cyclically. This monotonic pushover displacement to 7% drift degraded the strength of the specimen severely in the east direction. The nonlinear STM results can also be found in Tables 5.22 and 5.23 for the struts and ties, respectively. A summary of the events during the modeling can be found in Table 5.24.

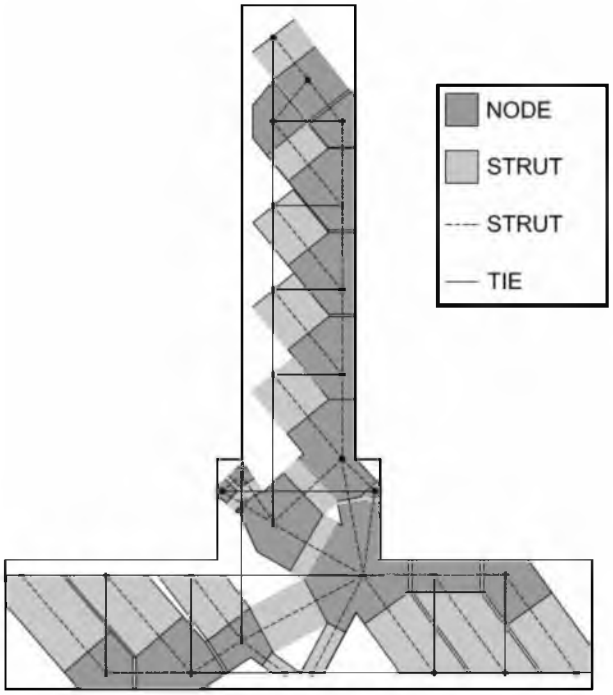

Figure 5.14 – Strut widths used to determine the member areas of LEN-2 Repair

Table 5.21 – Selected cyclic material properties used with LEN-2 Repair

Material input	Material	Value (ksi)
E_c	As-built concrete	4420
E_1	CFRP conf. conc.	2420
E_2	CFRP conf. conc.	420
f_{12}	CFRP conf. conc.	7.26
E_s	Reinforcing steel	29000
E_f	CFRP wrap	8990
f_{fd}	CFRP wrap	57.9

The ultimate load that the nonlinear STM force-displacement envelope predicted was 37.07 kips. This load is 79% of the 46.88 kip ultimate load that the specimen reached during the monotonic pushover and 93% of the 40.06 kip ultimate load that the specimen reached when tested cyclically. The ultimate displacement that the nonlinear STM force-displacement predicted, using eqs. 5.28 and 5.31 for the displacement ductility and normalized plastic hinge length respectively, was 5.74 in. This predicted ultimate displacement is 85% of the ultimate displacement that LEN-2 Repair reached during the cyclic test.

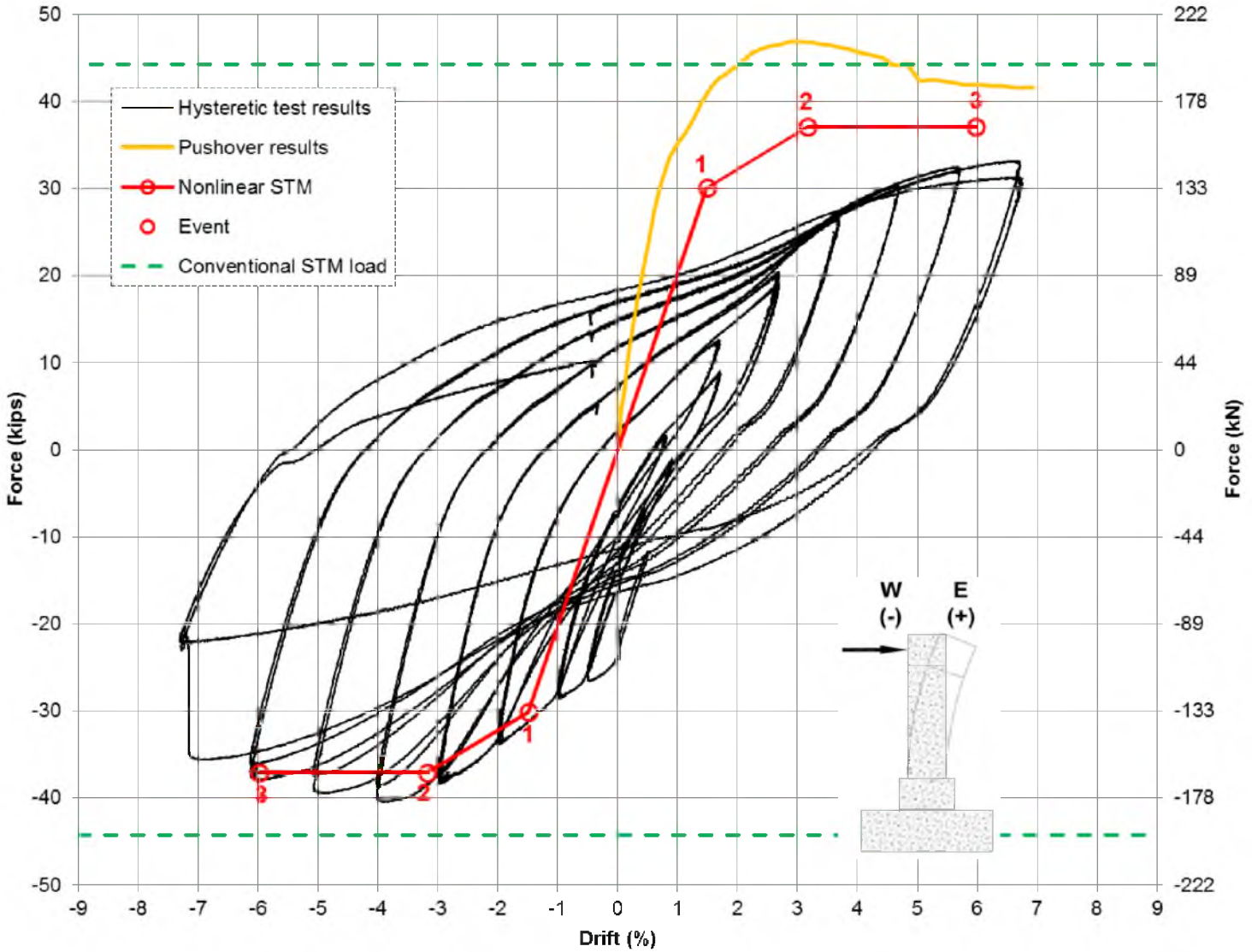

Figure 5.15 – LEN-2 Repair hysteresis, nonlinear STM force-displacement envelope, and conventional STM load result

Table 5.22 – LEN-2 Repair nonlinear STM tabular strut results

Member	Material	A ($in.^2$)	Effective strut strength		Event 1			Event 2		
			Eqn.	f_d or f_{cd} (ksi)	F_u (kips)	f_u (ksi)	f_u / f_d (%)	F_u (kips)	f_u (ksi)	f_u / f_d (%)
AB	Concrete	329	0.85 f_c'	5.10	47.7	0.1	2.8	58.7	0.2	3.5
BC	Concrete	329	0.85 f_c'	5.10	67.7	0.2	4.0	67.7	0.2	4.0
BD	Concrete	329	0.85 f_c'	5.10	115.4	0.4	6.9	126.4	0.4	7.5
CF	Concrete	329	0.85 f_c'	5.10	47.7	0.1	2.8	58.7	0.2	3.5
DF	Concrete	77	$C_{c(max)} / A_{cs}$	5.23	89.4	1.2	22.3	98.0	1.3	24.5
EH	Concrete	329	0.85 f_c'	5.10	47.7	0.1	2.8	58.7	0.2	3.5
FH	Concrete	77	$C_{c(max)} / A_{cs}$	5.23	126.4	1.7	31.6	143.4	1.9	35.8
GJ	Concrete	329	0.85 f_c'	5.10	47.7	0.1	2.8	58.7	0.2	3.5
HJ	Concrete	77	$C_{c(max)} / A_{cs}$	5.23	163.3	2.1	40.8	188.9	2.5	47.2
IK	Concrete	329	0.51 f_c'	3.06	47.7	0.1	4.7	58.7	0.2	5.8
JK	Concrete	77	0.51 f_c'	3.06	200.3	2.6	85.5	234.3	3.1	100.0
KN	CFRP conf. conc.	36	0.68 f_{cc}'	6.12	90.0	2.5	40.8	122.7	3.4	55.6
KP	CFRP conf. conc.	308	0.68 f_{cc}'	6.12	85.0	0.3	4.5	110.9	0.4	5.9
KT	CFRP conf. conc.	107	0.68 f_{cc}'	6.12	123.2	1.2	18.9	127.0	1.2	19.5
LM	CFRP conf. conc.	36	0.68 f_{cc}'	6.12	45.2	1.3	20.5	61.6	1.7	27.9
LP	CFRP conf. conc.	70	0.68 f_{cc}'	6.12	70.4	1.0	16.3	95.9	1.4	22.2
MO	CFRP conf. conc.	36	0.68 f_{cc}'	6.12	49.7	1.4	22.5	67.8	1.9	30.7
NT	CFRP conf. conc.	36	0.68 f_{cc}'	6.12	58.9	1.6	26.7	80.3	2.2	36.4
OP	CFRP conf. conc.	70	0.68 f_{cc}'	6.12	49.8	0.7	11.5	67.9	1.0	15.7
PT	CFRP conf. conc.	346	0.68 f_{cc}'	6.12	21.7	0.1	1.0	33.8	0.1	1.6
QX	Concrete	274	0.68 f_c'	4.08	40.8	0.1	3.7	49.7	0.2	4.5
RY	Concrete	274	0.68 f_c'	4.08	40.8	0.1	3.7	49.7	0.2	4.5
SW	Concrete	235	0.68 f_c'	4.08	172.3	0.7	18.0	202.3	0.9	21.1
TU	Concrete	144	0.51 f_c'	3.06	44.6	0.3	10.1	54.4	0.4	12.3
TW	Concrete	216	0.51 f_c'	3.06	224.9	1.0	34.0	275.7	1.3	41.7
TAA	Concrete	90	0.51 f_c'	3.06	59.2	0.7	21.5	59.2	0.7	21.5
TAB	Concrete	242	0.51 f_c'	3.06	38.0	0.2	5.1	46.3	0.2	6.2
UV	Concrete	144	0.51 f_c'	3.06	22.3	0.2	5.1	27.2	0.2	6.2
UAC	Concrete	242	0.68 f_c'	4.08	38.0	0.2	3.8	46.3	0.2	4.7
VAD	Concrete	242	0.68 f_c'	4.08	38.0	0.2	3.8	46.3	0.2	4.7
WY	Concrete	168	0.68 f_c'	4.08	194.1	1.2	28.3	225.5	1.3	32.9
WZ	Concrete	72	0.68 f_c'	4.08	87.4	1.2	29.7	87.4	1.2	29.7
XY	Concrete	144	0.51 f_c'	3.06	26.7	0.2	6.1	32.6	0.2	7.4

Table 5.23 - LEN-2 Repair nonlinear STM tabular tie results

Member	Material	A ($in.^2$)	Effective yield strength		Event 1			Event 2		
			Eqn.	f_{ey} or f_{fd} (ksi)	F_u (kips)	f_u (ksi)	f_u / f_{ey} (%)	F_u (kips)	f_u (ksi)	f_u / f_{ey} (%)
AC	As-built long. rebar	3.95	T / A_{rt}	33.5	36.9	9.4	27.9	45.5	11.5	34.4
CD	As-built trans. rebar	2.66	f_y	63.0	72.9	27.4	43.5	79.9	30.0	47.7
CE	As-built long. rebar	3.95	T / A_{rt}	33.5	21.4	5.4	16.2	38.4	9.7	29.0
EF	As-built trans. rebar	2.66	f_y	63.0	30.1	11.3	18.0	37.1	13.9	22.1
EG	As-built long. rebar	3.95	T / A_{rt}	33.5	58.3	14.8	44.1	83.9	21.2	63.4
GH	As-built trans. rebar	2.66	f_y	63.0	30.1	11.3	18.0	37.1	13.9	22.1
GI	As-built long. rebar	3.95	T / A_{rt}	33.5	95.3	24.1	72.1	129.3	32.7	97.8
IJ	As-built trans. rebar	1.97	f_y	63.0	30.1	15.3	24.3	37.1	18.8	29.9
IP	As-built long. rebar	3.95	T / A_{rt}	33.5	132.2	33.5	100.0	174.8	44.3	132.2
LO	Headed rebar	2.37	T / A_{rt}	48.9	84.5	35.6	72.9	115.1	48.6	99.4
MN	CFRP wrap	3.40	$E_f * \kappa_\varepsilon * \varepsilon_{fu}$	57.3	80.6	23.7	41.4	109.9	32.3	56.4
OW	Headed rebar	2.37	T / A_{rt}	48.9	84.6	35.7	73.0	115.3	48.7	99.5
QR	As-built long. rebar	6.32	f_y	68.0	56.9	9.0	13.2	69.7	11.0	16.2
RS	As-built long. rebar	6.32	f_y	68.0	83.6	13.2	19.5	102.2	16.2	23.8
RX	As-built trans. rebar	6.29	f_y	63.0	30.8	4.9	7.8	37.5	6.0	9.5
ST	As-built long. rebar	6.32	f_y	68.0	188.8	29.9	43.9	225.8	35.7	52.5
SY	As-built trans. rebar	6.29	f_y	63.0	136.4	21.7	34.4	160.3	25.5	40.4
UAB	As-built trans. rebar	5.61	f_y	63.0	30.8	5.5	8.7	37.5	6.7	10.6
VAC	As-built trans. rebar	5.61	f_y	63.0	30.8	5.5	8.7	37.5	6.7	10.6
YZ	As-built long. rebar	6.32	f_y	68.0	109.4	17.3	25.5	124.1	19.6	28.9
ZAA	As-built long. rebar	6.32	f_y	68.0	39.6	6.3	9.2	54.2	8.6	12.6
AAAB	As-built long. rebar	6.32	f_y	68.0	67.0	10.6	15.6	81.6	12.9	19.0
ABAC	As-built long. rebar	6.32	f_y	68.0	44.6	7.1	10.4	54.4	8.6	12.7
ACAD	As-built long. rebar	6.32	f_y	68.0	22.3	3.5	5.2	27.2	4.3	6.3

Table 5.24 – LEN-2 Repair nonlinear STM events

Event	1	2	3
Description	Longitudinal column tie yields (lP)	Longitudinal cloumn strut crushes (JK)	Ultimate displacement is reached
Force (kip)	30	37	37
Displacement (in.)	1.4	3.0	5.7

One tie yielded while running the nonlinear STM of LEN-2 Repair, which was the longitudinal column rebar tie at the repair-column interface (lP). The second event, and the point that the maximum lateral load was reached, was when the longitudinal concrete strut at the column-repair interface (JK) crushed. It can be seen in Figure 5.15 that the nonlinear STM results match the cyclic performance of LEN-2 Repair very closely, and the conventional STM results match the monotonic load capacity very closely. This comparison shows the applicability of the two types of STMs. The nonlinear STM is designed to match the cyclic performance of a system. This is achieved by entering allowable material stresses that reflect the cyclic degradation that occurs within materials when cyclically loaded. The conventional STM is modeled using monotonic material properties. This input is why the ultimate load of the conventional STM matches the pushover results very closely.

5.3.7 LEN-2 model

The nonlinear STM for LEN-2 uses the same layout as the conventional STM as shown in Figure 5.7. The member areas for the nonlinear STM ties are the same as the conventional STM but the member areas of the struts are modified. The maximum possible strut areas were used and were determined graphically. The strut widths used in the model can be seen in Figure 5.16. The material properties used in the model are the recorded material values on the day of testing. Pertinent material properties can be found in Table 5.10.

The nonlinear STM force-displacement results can be seen in Figure 5.17 plotted over the hysteresis results recorded during testing. It should be noted that the hysteretic response of LEN-2 is affected by the bond slip, which the GSS demonstrated during testing. This

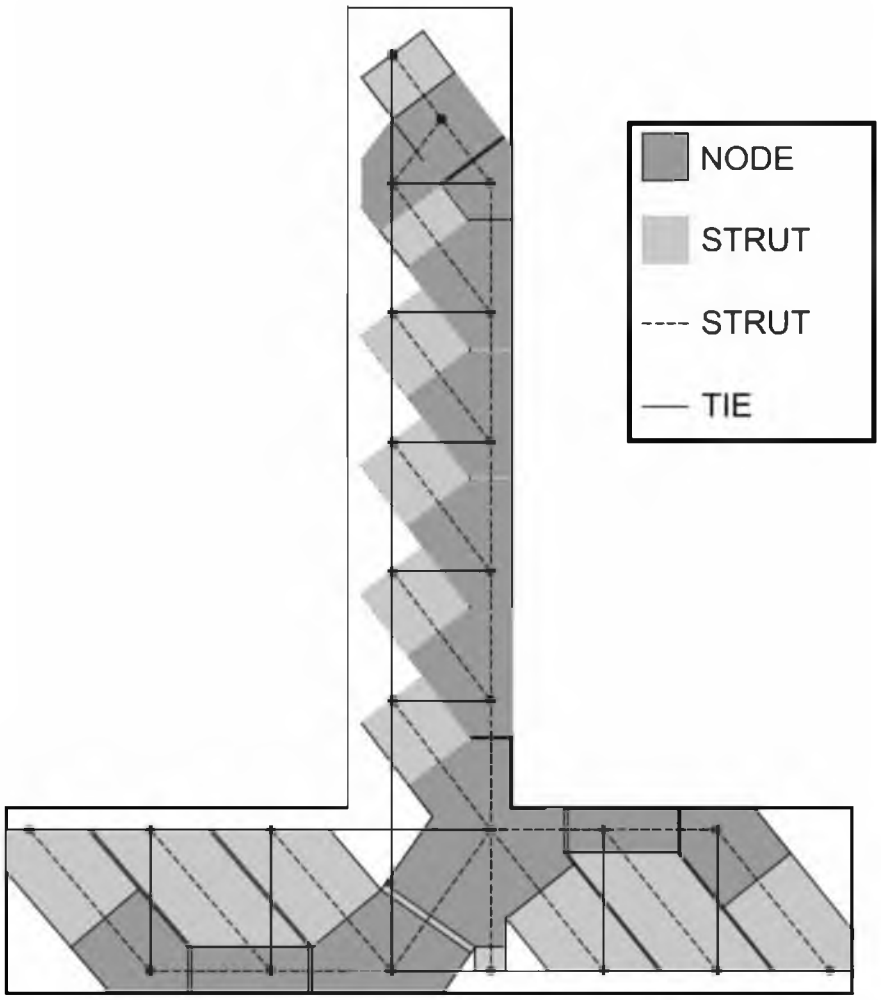

Figure 5.16 – Strut widths used to determine the member areas of LEN-2

characteristic pinches the hysteresis and leads to less desirable performance when compared to NMB-2. The nonlinear STM results can also be found in Tables 5.25 and 5.26 for the struts and ties, respectively. A summary of the events during the modeling can be found in Table 5.27.

The ultimate load that the nonlinear STM force-displacement envelope predicted was 27.78 kips. This load is 78% of the 35.68 kip ultimate load that the specimen reached during testing and 83% of the 33.29 kip ultimate load that the idealized average elasto-plastic response reached. The ultimate displacement that the nonlinear STM force-displacement predicted, using a plastic hinge length of 13 in. and eq. 5.28 for the displacement ductility, was 6.22 in. This predicted ultimate displacement is 96% of the ultimate displacement that LEN-2 reached during testing.

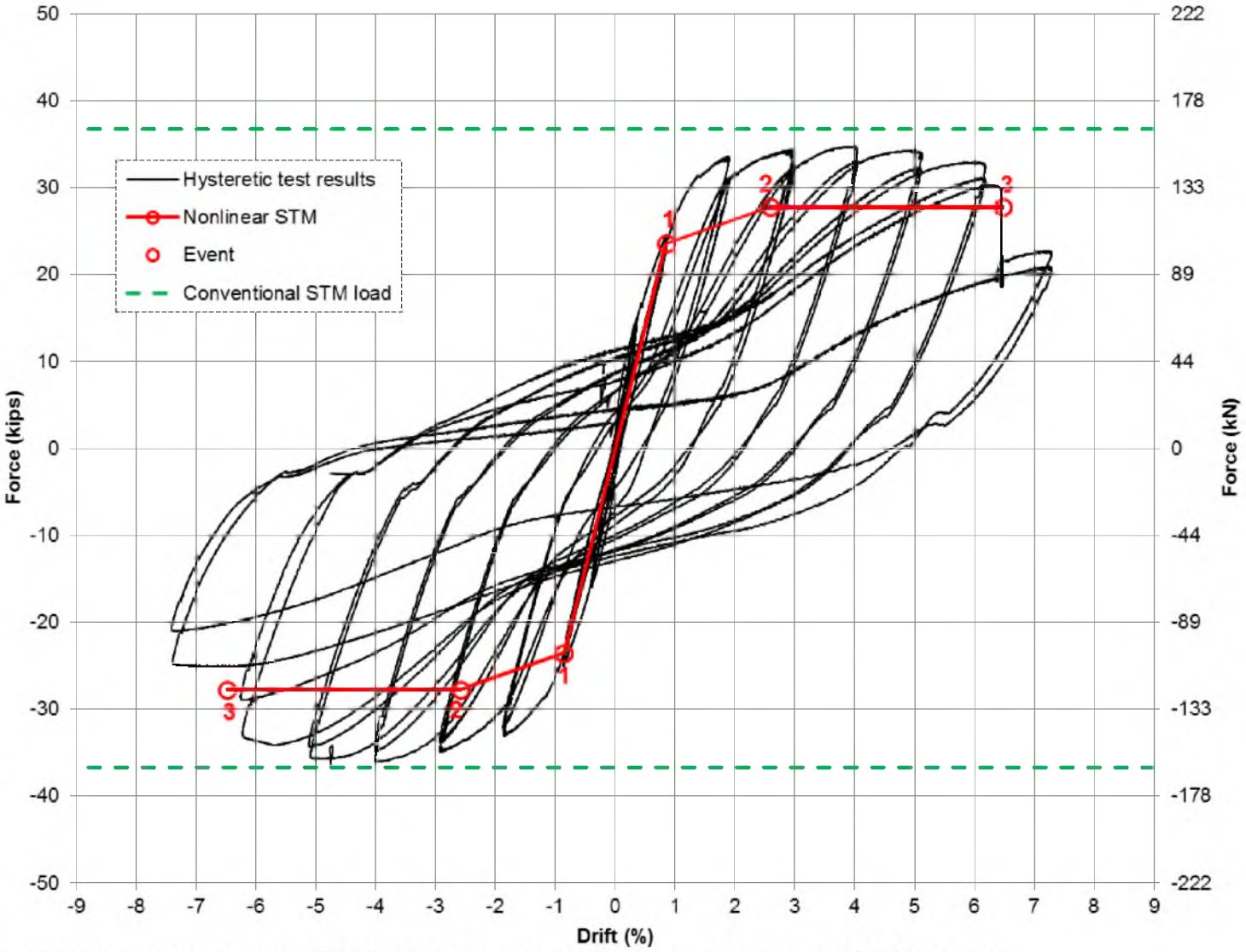

Figure 5.17 – LEN-2 hysteresis, nonlinear STM force-displacement envelope, and conventional STM load result

Table 5.25 – LEN-2 nonlinear STM tabular strut results

Member	Material	A ($in.^2$)	Effective strut strength		Event 1			Event 2		
			Eqn.	f_d or f_{cd} (ksi)	F_u (kips)	f_u (ksi)	f_u / f_d (%)	F_u (kips)	f_u (ksi)	f_u / f_d (%)
AB	Concrete	337	0.85 f_c'	5.10	38.7	0.1	2.3	45.7	0.1	2.7
BC	Concrete	337	0.85 f_c'	5.10	65.6	0.2	3.8	65.6	0.2	3.8
BD	Concrete	337	0.85 f_c'	5.10	104.2	0.3	6.1	111.2	0.3	6.5
CF	Concrete	337	0.85 f_c'	5.10	38.7	0.1	2.2	45.7	0.1	2.7
DF	Concrete	76	$C_{c(max)} / A_{cs}$	5.26	82.7	1.1	20.6	88.2	1.2	22.0
EH	Concrete	337	0.85 f_c'	5.10	38.7	0.1	2.2	45.7	0.1	2.7
FH	Concrete	76	$C_{c(max)} / A_{cs}$	5.26	113.4	1.5	28.3	124.4	1.6	31.1
GJ	Concrete	337	0.85 f_c'	5.10	38.7	0.1	2.2	45.7	0.1	2.7
HJ	Concrete	76	$C_{c(max)} / A_{cs}$	5.26	144.1	1.9	36.0	160.7	2.1	40.1
IL	Concrete	337	0.85 f_c'	5.10	38.7	0.1	2.2	45.7	0.1	2.7
JL	Concrete	76	$C_{c(max)} / A_{cs}$	5.26	174.8	2.3	43.6	196.9	2.6	49.2
KP	Concrete	337	0.51 f_c'	3.06	38.7	0.1	3.7	45.7	0.1	4.4
LP	Concrete	76	0.51 f_c'	3.06	205.5	2.7	88.1	233.1	3.1	100.0
MS	Concrete	274	0.68 f_c'	4.08	30.0	0.1	2.7	35.5	0.1	3.2
NT	Concrete	274	0.68 f_c'	4.08	30.0	0.1	2.7	35.5	0.1	3.2
OU	Concrete	274	0.68 f_c'	4.08	30.0	0.1	2.7	35.5	0.1	3.2
PQ	Concrete	144	0.51 f_c'	3.06	36.5	0.3	8.3	43.1	0.3	9.8
PU	Concrete	336	0.51 f_c'	3.06	197.2	0.6	19.2	232.8	0.7	22.6
PV	Concrete	48	0.51 f_c'	3.06	52.0	1.1	35.4	52.0	1.1	35.4
PW	Concrete	264	0.51 f_c'	3.06	29.2	0.1	3.6	34.5	0.1	4.3
QR	Concrete	144	0.51 f_c'	3.06	18.3	0.1	4.1	21.6	0.1	4.9
QX	Concrete	264	0.68 f_c'	4.08	29.2	0.1	2.7	34.5	0.1	3.2
RY	Concrete	264	0.68 f_c'	4.08	29.2	0.1	2.7	34.5	0.1	3.2
ST	Concrete	144	0.51 f_c'	3.06	19.5	0.1	4.4	23.0	0.2	5.2
TU	Concrete	144	0.51 f_c'	3.06	39.1	0.3	8.9	46.1	0.3	10.5

One tie yielded while running the nonlinear STM of LEN-2, which was the longitudinal rebar tie in the column at the column-pier cap joint (KU). The second event, and the point that the maximum lateral load was reached, was when the longitudinal concrete strut at the column-pier cap interface (LP) crushed. This performance matches the observed performance during testing where the longitudinal rebar in the column yielded during small displacements.

The initial stiffness of the force-displacement envelope is very close to that of the test data. Since the nonlinear STM is used to predict the degraded performance of a specimen due to

Table 5.26 - LEN-2 nonlinear STM tabular tie results

Member	Material	A ($in.^2$)	Effective yield strength		Event 1			Event 2		
			Eqn.	f_{ey} (ksi)	F_u (kips)	f_u (ksi)	f_u / f_{ey} (%)	F_u (kips)	f_u (ksi)	f_u / f_{ey} (%)
AC	As-built long. rebar	3.95	T / A_{rt}	33.5	30.7	7.8	23.2	36.3	9.2	27.4
CD	As-built trans. rebar	2.49	f_y	63.0	63.4	25.5	40.4	67.7	27.2	43.1
CE	As-built long. rebar	3.95	T / A_{rt}	33.5	9.4	2.4	7.1	20.4	5.2	15.4
EF	As-built trans. rebar	2.49	f_y	63.0	23.5	9.5	15.0	27.8	11.2	17.7
EG	As-built long. rebar	3.95	T / A_{rt}	33.5	40.1	10.1	30.3	56.7	14.3	42.8
GH	As-built trans. rebar	2.49	f_y	63.0	23.5	9.5	15.0	27.8	11.2	17.7
GI	As-built long. rebar	3.95	T / A_{rt}	33.5	70.8	17.9	53.5	92.9	23.5	70.3
IJ	As-built trans. rebar	2.49	f_y	63.0	23.5	9.5	15.0	27.8	11.2	17.7
IK	As-built long. rebar	3.95	T / A_{rt}	33.5	101.5	25.7	76.7	129.1	32.7	97.7
KL	As-built trans. rebar	1.81	f_y	63.0	23.5	13.0	20.6	27.8	15.3	24.4
KU	As-built long. rebar	3.95	T / A_{rt}	33.5	132.2	33.5	100.0	165.4	41.9	125.1
MN	As-built long. rebar	6.32	f_y	68.0	43.1	6.8	10.0	50.8	8.0	11.8
NO	As-built long. rebar	6.32	f_y	68.0	62.6	9.9	14.6	73.9	11.7	17.2
NS	As-built trans. rebar	6.23	f_y	63.0	22.8	3.7	5.8	26.9	4.3	6.9
OP	As-built long. rebar	6.32	f_y	68.0	82.1	13.0	19.1	96.9	15.3	22.6
OT	As-built trans. rebar	6.23	f_y	63.0	22.8	3.7	5.8	26.9	4.3	6.9
QW	As-built trans. rebar	5.97	f_y	63.0	22.8	3.8	6.1	26.9	4.5	7.2
RX	As-built trans. rebar	5.97	f_y	63.0	22.8	3.8	6.1	26.9	4.5	7.2
UV	As-built long. rebar	6.32	f_y	68.0	54.8	8.7	12.8	64.7	10.2	15.1
VW	As-built long. rebar	6.32	f_y	68.0	54.8	8.7	12.8	64.7	10.2	15.1
WX	As-built long. rebar	6.32	f_y	68.0	36.5	5.8	8.5	43.1	6.8	10.0
XY	As-built long. rebar	6.32	f_y	68.0	18.3	2.9	4.3	21.6	3.4	5.0

Table 5.27 – LEN-2 nonlinear STM events

Event	1	2	3
Description	Longitudinal column tie yields (KU)	Longitudinal column strut crushes (LP)	Ultimate displacement is reached
Force (kip)	24	28	28
Displacement (in.)	0.82	2.5	6.2

cyclic loading, the last displacement during the 1-in. displacement step was used to compare the initial stiffness. The models initial stiffness is 28.87 k/in., which is 99% of the recorded test results.

5.4 Parametric study of strut-and-tie model material design values

The modeling procedures developed are intended to be used by designers who do not have the exact material properties of the concrete, steel, or CFRP that they are modeling. Two design procedures for material properties are examined in this study for both the conventional and nonlinear STMs. First, nominal material properties are modeled. Nominal material properties imply that grade 60 steel is input with a yield strength on 60 ksi and concrete ordered from the batch plant as 6 ksi is input into the model as 6 ksi. The other design procedure modeled is expected material properties. This is a design procedure used by designers performing capacity based design in which underprediction of the material strength is unconservative. Therefore, this design procedure is referred to as the seismic design material properties. To examine the outcomes of using the differing design property procedure for both the conventional and nonlinear STMs, NMB-2 Repair has been remodeled using nominal and seismic design material properties.

Many suggested values exist for expected material properties for both rebar and concrete. The seismic design value for the yield strength of steel used in this study is $1.25f_y$ (*5*), where f_y is the specified or nominal yield strength of the steel. The seismic design value for the compressive strength of concrete used in this study is $1.1f_c'$, where f_c' is the specified 28-day compressive strength. For the CFRP wrap the nominal design values were taken as the

manufacturer's recommended design values, and the seismic design values were taken as the manufacturer's expected material properties *(41)*.

5.4.1 Conventional strut-and-tie model

All of the layout parameters are based upon the material properties of the specimen that is being modeled. Therefore, to model the different material properties NMB-2 Repair has a different layout for each design procedure. The layout parameters and design inputs can be found in Table 5.28.

The three models using differing material properties were run until a failure load was reached. The results of the models can be found in Table 5.29. The ultimate loads achieved were 93%, 79%, and 94% of the ultimate load reached during testing for the day of test, nominal and seismic design material properties, respectively. Both the day of test and seismic design models reached failure due to yielding of the headed rebar. The nominal design model failed due to crushing on the longitudinal concrete strut at the column-repair interface.

Table 5.28 – Modeling parameters used for differing material properties for NMB-2 Repair

Model input	Location/ member	Material Properties		
		Day of Test	Seismic Design	Nominal
P_{axial}	Global	86.8 kips	86.8 kips	86.8 kips
x_c	As-built column	2.5 in.	2.4 in.	2.2 in.
x_t	As-built column	5.8 in.	5.9 in.	6.3 in.
x_c'	Repair	2.9 in.	2.8 in.	2.3 in.
x_t'	Repair	4.5 in.	4.5 in.	5.2 in.
h_{CFRP}	Repair	12.5 in.	12.5 in.	12.5 in.
h_{headed}	Footing	15.0 in.	15.0 in.	15.0 in.
Θ	As-built column	50.7 deg.	50.7 deg.	50.9 deg.
f_c'	As-built	6.43 ksi	6.60 ksi	6.00 ksi
f_{cc}'	Repair	9.65 ksi	9.90 ksi	9.00 ksi
f_y	As-built long.	68 ksi	75 ksi	60 ksi
f_y	As-built trans.	63 ksi	75 ksi	60 ksi
f_y	Headed rebar	62 ksi	75 ksi	60 ksi
t_f	CFRP ply thickness	0.047 in.	0.04 in.	0.04 in.
f_u	CFRP wrap	101 ksi	123 ksi	104 ksi

Table 5.29 – Conventional STM results using differing material properties for NMB-2 Repair

Material properties used	Conventional STM load (kips)	Normalized to the tested ultimate load capacity (%)
Day of test	42.55	93
Nominal	35.85	79
Seismic design	42.8	94

From the results it can be seen that both design philosophies provide conservative estimates of the ultimate load capacity of NMB-2 Repair. From this analysis it appears that the seismic design material properties more accurately predict the specimen's performance than the nominal design properties. This result is expected since the seismic design material properties are closer to the tested values. However, the conventional STM does not always provide conservative results for cyclic load capacity, as seen by the results of LEN-2 Repair and LEN-2. Caution should be used when designing with the conventional STM since it does not account for cyclic degradation of materials as the nonlinear cyclic STM does; see Table 5.13.

5.4.2 Nonlinear strut-and-tie model

The nonlinear STM of NMB-2 Repair was run for the two different material strength design procedures and compared to the results obtained using the material properties from the day of testing. The same layout parameters were used for the nonlinear STM as the conventional STM and can be found in Table 5.28. Additional material values were input into the nonlinear model following the recommendations of Section 5.3.2 and are summarized in Table 5.30. The results from the three simulations can be found in Table 5.31 and seen in Figure 5.18.
All of the models underpredicted the ultimate load capacity of the specimen. When compared to the ultimate load of the idealized elasto-plastic response of NMB-2 Repair the day of test, nominal, and seismic design ultimate load capacities were 89%, 64%, and 92% of the peak elasto-plastic load, respectively. The ultimate displacement capacities of the three simulations were 88%, 83%, and 91% of the tested ultimate load capacity for the day of test, nominal, and seismic design simulations respectively. There was one event when running the nonlinear STM using nominal design values, which was crushing of the longitudinal concrete strut at the column-

Table 5.30 - Selected cyclic material properties used for NMB-2 Repair design procedures

Material input	Material	Material Properties (ksi)		
		Day of Test	Seismic Design	Nominal
E_c	As-built concrete	4571	4631	4415
E_1	CFRP conf. conc.	2520	2552	2411
E_2	CFRP conf. conc.	469	473	407
f_{12}	CFRP conf. conc.	7.90	8.10	7.22
E_s	Reinforcing steel	29000	29000	29000
E_f	CFRP wrap	8990	10200	9450
f_{fd}	CFRP wrap	57.9	69.8	52.8
ε_u (%)	CFRP tensile elongation	1.13%	1.12%	0.98%

Table 5.31 – Results from NMB-2 Repair parametric study

Model		Ultimate load					Ultimate displacement		
		Model (kips)	Test max (kips)	Test elasto-plastic (kips)	Model/Test (%)	Model/Test E.P. (%)	Model (in.)	Test (in.)	Model/Test (%)
NMB-2 Repair	Day of test	37.56	45.56	42.09	82	89	5.89	6.68	88
	Nominal	26.92			59	64	5.53		83
	Seismic design	38.85			85	92	6.11		91

repair interface (JK). There were two events when running the nonlinear STM using seismic design values, which was yielding of the longitudinal column rebar tie at the repair-column interface (IP), followed by crushing of the longitudinal concrete strut at the column-repair interface (JK). The progression of events that the seismic design model underwent replicates the observed behavior of NMB-2 Repair during testing better than the nominal design model. Yielding of the column rebar occurred far before the ultimate load was achieved from crushing of the column concrete.

From these results it can be seen that the nonlinear STM underpredicts the test results in terms of load capacity and ultimate displacement for both design procedures. The nominal design model predicts 64% of the tested ultimate load, and the seismic design model predicts 92% of the tested ultimate load. Unlike the conventional STM, the nonlinear STM underpredicted the ultimate load capacity for all of the tests modeled. Therefore, the most realistic design values should be used when implementing the nonlinear STM, close to the seismic design material properties used in this study.

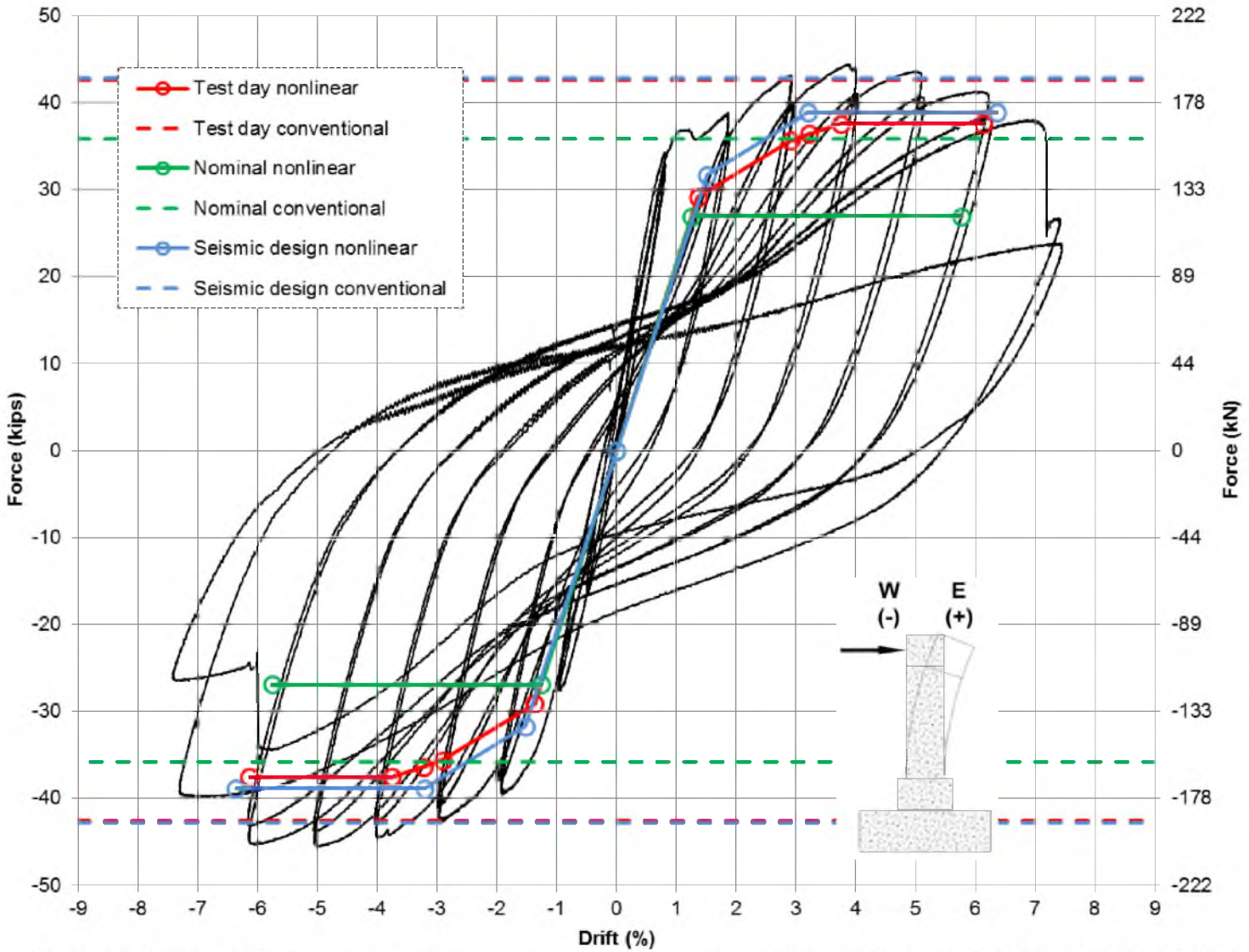

Figure 5.18 – Nonlinear STM force-displacement response envelopes and conventional STM results for NMB-2 Repair parametric study

5.5 Comparison of strut-and-tie model results to test data

To validate the applicability of both the conventional STM and nonlinear STM models, various aspects of the models were compared to the recorded test results. The system as a whole was examined in terms of global displacement and load capacity. Individual repair components including the headed rebar and CFRP wrap were examined in detail to assess the applicability of the STM procedure for designing the repair components.

5.5.1 System results

The conventional STM predicts the ultimate load capacity of the assembly being modeled. These results are compared to both the ultimate load achieved during testing and the ultimate load of the idealized elasto-plastic response, as found in Table 5.32. The nonlinear STM produces a force-displacement response envelope of the assembly being modeled. The results of the nonlinear STM in terms of ultimate load capacity, ultimate displacement capacity, displacement ductility, and initial stiffness can all be compared to the test results, as summarized in Table 5.33. The ultimate load capacity is compared to both the ultimate load achieved during testing and the ultimate load of the idealized elasto-plastic response. The initial stiffness is compared to the initial stiffness of the idealized elasto-plastic response curve.

All of the nonlinear STM and conventional STM results are plotted with the response envelope of the specimen being modeled as well as the idealized elasto-plastic response, in Figures 5.19–5.22. The response envelopes are the averaged response envelopes from both directions of testing, and the idealized elasto-plastic responses are obtained from the averaged response envelopes plotted. A description of the procedure used for creating the elasto-plastic responses is given in Section 3.4.3. The displacement ductility from testing is obtained from the average envelope idealized elasto-plastic response curves. It should be noted that an accurate response envelope cannot be obtained for LEN-2 Repair due to the existing damage at the start of the cyclic testing from the monotonic pushover test. Due to this fact, an idealized elasto-plastic response cannot be generated. However, the STM results are plotted with the monotonic

Table 5.32 – Conventional STM results

Model		Model ultimate load (kips)	Test ultimate load (kips)	Test elasto-plastic load (kips)	Model/Test (%)	Model/Test E.P. (%)
NMB-2 Repair	Day of test	42.55	45.56	42.09	93	101
	Nominal	35.85			79	85
	Seismic design	42.80			94	102
NMB-2		33.69	38.83	32.37	87	104
LEN-2 Rep		44.21	40.46	-	109	-
LEN-2		36.71	36.32	33.29	101	110

Table 5.33 – Nonlinear STM results

Model		Ultimate load					Ultimate displacement			Displacement ductility			Initial stiffness		
		Model (kips)	Test max (kips)	Test elasto-plastic (kips)	Model/Test (%)	Model/Test E.P. (%)	Model (in.)	Test (in.)	Model/Test (%)	Model	Test	Model/Test (%)	Model (kip/in.)	Test elasto-plastic (kip/in.)	Model/Test (%)
NMB-2 Repair	Day of test	37.56	45.56	42.09	82	89	5.89	6.68	88	4.49	5.95	75	22.21	37.47	59
	Nominal	26.92			59	64	5.53		83	4.58		77	22.27		59
	Seismic design	38.85			85	92	6.11		91	4.19		70	21.77		58
NMB-2		25.56	38.83	32.37	66	79	6.81	5.45	125	8.84	5.62	157	29.58	33.38	89
LEN-2 Rep (cyclic)		37.07	40.46	-	92	-	5.74	6.83	84	4.00	-	-	21.03	-	-
LEN-2		27.78	36.32	33.29	76	83	6.22	6.50	96	7.62	5.84	130	28.87	29.92	96

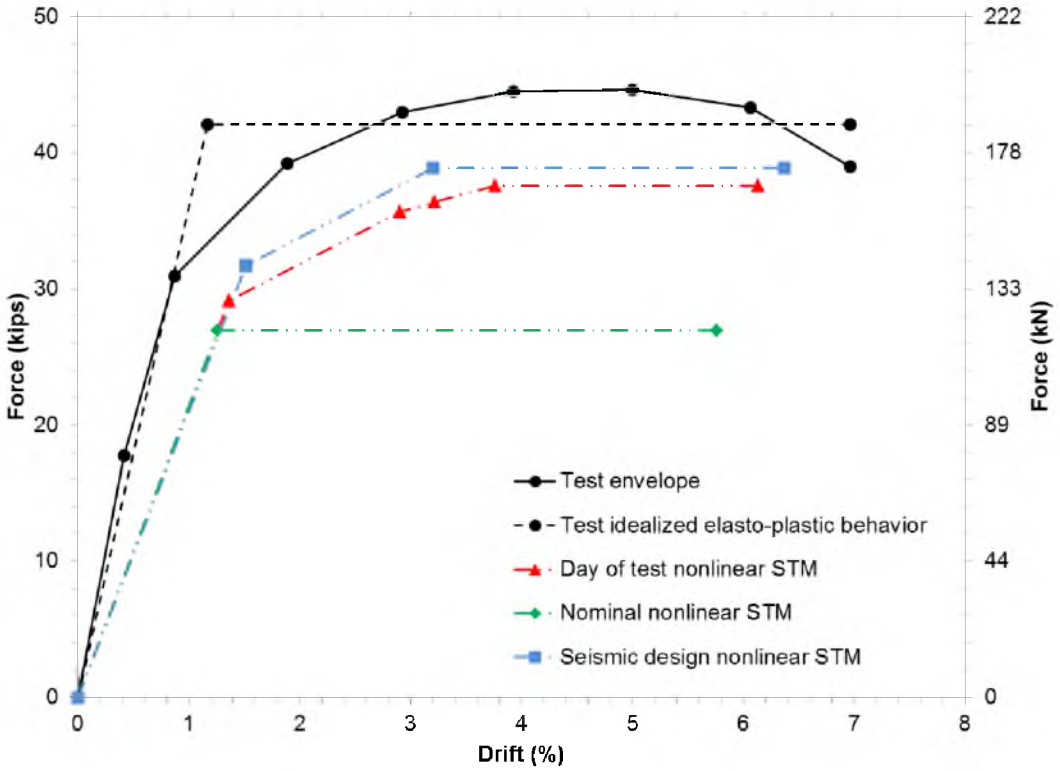

Figure 5.19 – NMB-2 Repair test envelope, elasto-plastic response, and modeling results

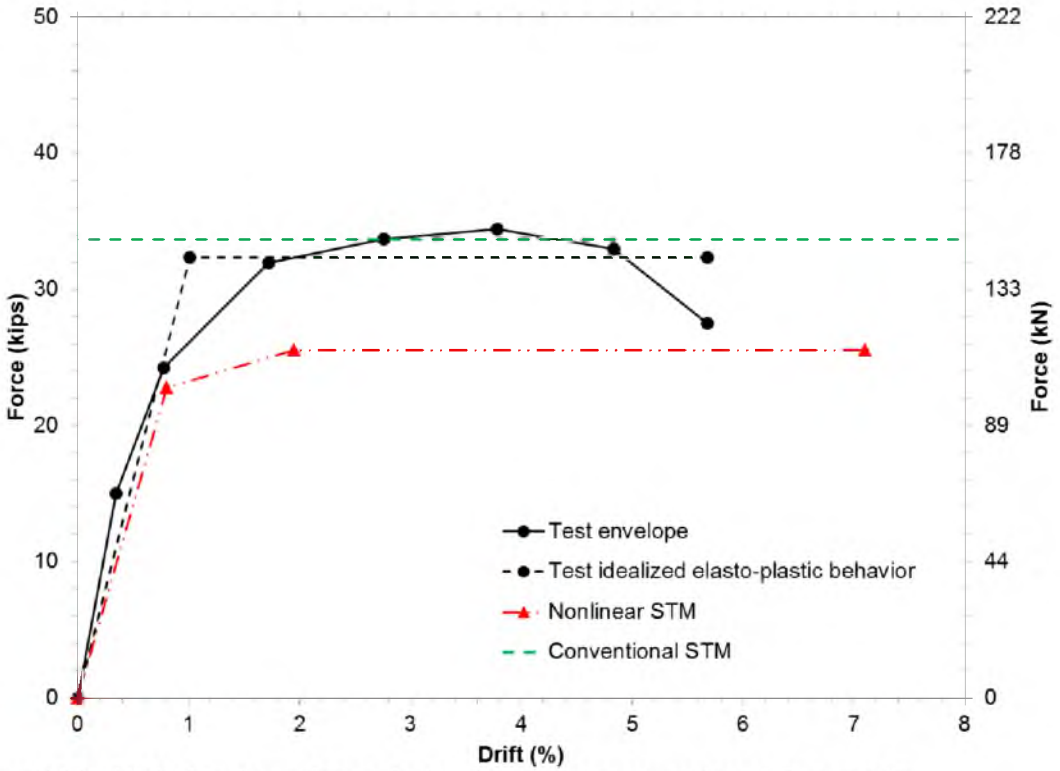

Figure 5.20 - NMB-2 test envelope, elasto-plastic response, and modeling results

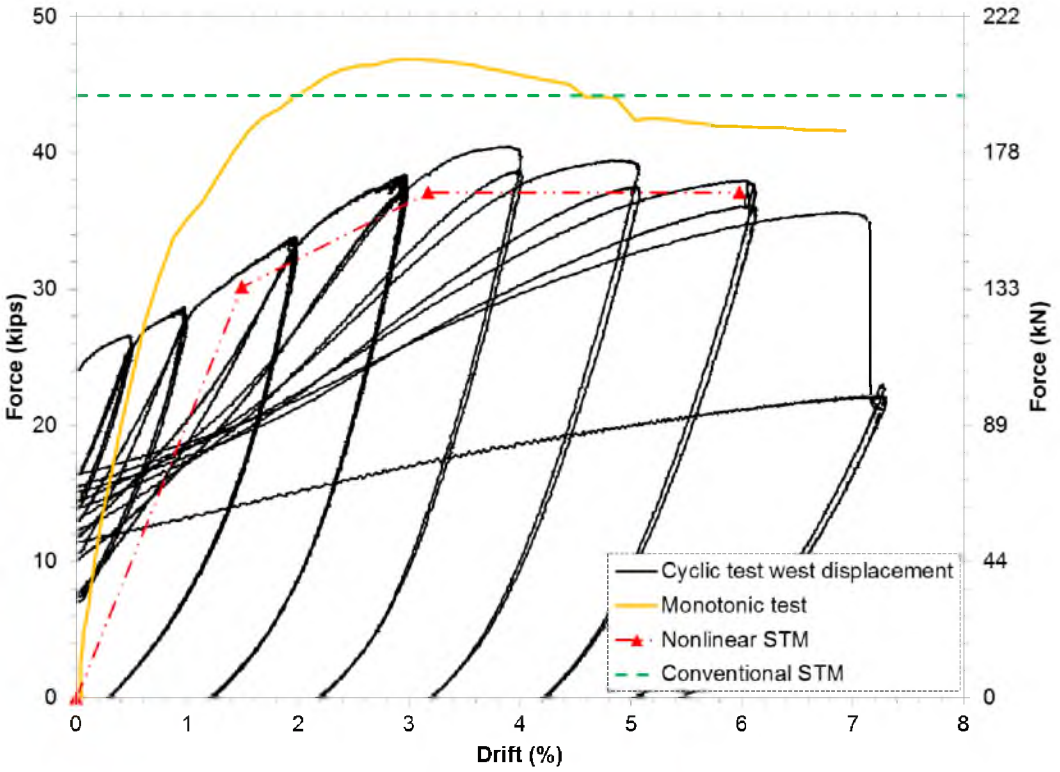

Figure 5.21 - LEN-2 Repair strong side hysteresis, monotonic pushover, and modeling results

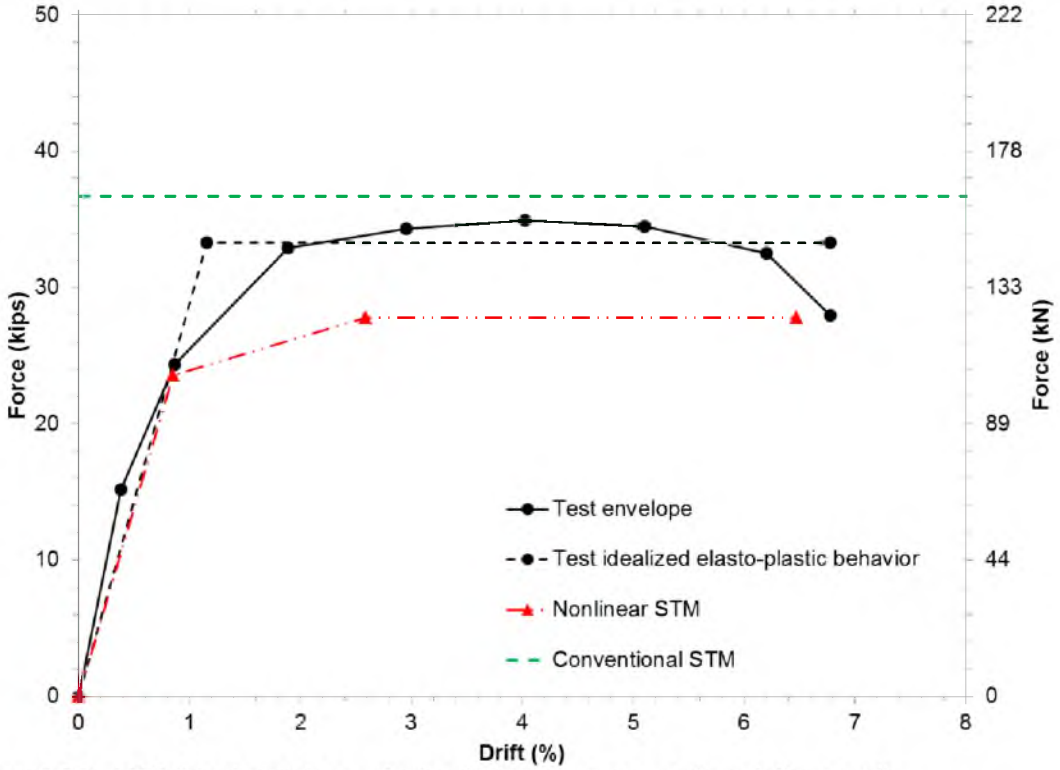

Figure 5.22 - LEN-2 test envelope, elasto-plastic response, and modeling results

pushover results and the less damaged side of the hysteresis. The less damaged side of the hysteresis is plotted in the third quadrant in previous hysteretic response plots of LEN-2 Repair.

All of the conventional STMs using day of test material properties fall within 13% of the ultimate load capacity of the specimen being modeled. The NMB models underpredict the ultimate load capacity by up to 13%. The LEN models overpredict the load capacity by up to 9%. When the models using day of test material properties are compared to the elasto-plastic ultimate load capacities of the specimens, all of the models overpredict the load, but fall within 10% of the load capacity. Both of these comparisons indicate that the conventional STM is a very good method for predicting the ultimate load capacity of the specimens. However, both NMB-2 Repair and LEN-2 Repair reach an ultimate load due to the headed rebar tie yielding. This would lead the designer to believe that there would be substantial overstrength capacity left within the system at the predicted ultimate load. However, we know this is not the case since the conventional STM actually overpredicted the ultimate load capacity of LEN-2 Repair. The conventional STM is not intended for the analysis of lateral force resisting elements. The results of the STMs and test in this study show that the conventional STM predicts the cyclic load capacity of these specimens with acceptable accuracy, but is unconservative in terms of overpredicting the ultimate load and predicting yielding rather that failure.

All of the nonlinear STMs using day of test material properties predict the ultimate load capacity of the specimens within 44% of the recorded value when testing. The nonlinear models capture the load capacity of the repaired specimens within 18%. The reason that the models more accurately predict the load capacity of the repaired specimens is likely due to the highly degraded materials that are present in the repaired specimens. The material properties entered into the model are for cyclically degraded concrete, which is likely very conservative for the as-built specimens.

The nonlinear STM predicts the ultimate displacement of the repaired and as-built specimens within 16% and 25%, respectively. For the as-built specimens the 25% overprediction of ultimate displacement capacity is likely due to the unknown plastic hinge length for the as-built specimens. For NMB-2 the assumed plastic hinge length was 14 in., determined from test

observations, but a more detailed investigation of curvatures and strain is needed to refine this estimate.

For each nonlinear STM the displacement ductility predicted by the model was calculated by dividing the ultimate displacement by the first yield displacement. For NMB-2 Repair the displacement ductility predicted by the nonlinear STM was less than the displacement ductility achieved during testing. For the as-built specimens the displacement ductility predicted by the nonlinear STM overpredicted the value by as much as 57%.

The nonlinear STMs predicted the initial stiffness of the as-built specimens within 11% and 4% for NMB-2 and LEN-2, respectively. For the repaired specimens the model underpredicted the initial stiffness by 41% for NMB-2 Repair. Due to the complex nature of the repair it can be seen that the nonlinear model does not accurately predict the initial stiffness.

5.5.2 CFRP results

For both NMB-2 Repair and LEN-2 Repair the STM results overpredict the force in the CFRP wrap. When looking at the forces in the wrap it is useful to look at the forces as a percentage of the effective CFRP jacket strength, which takes into consideration the CFRP efficiency factor. Table 5.34 summarizes the maximum strain recorded in the jacket while testing compared to the maximum forces in the jacket predicted using the conventional and nonlinear STMs. These values are summarized in Table 5.34 as a percent of the effective jacket strength. The top band strain values from testing are used to compare since the top band experienced the highest strain during testing. The monotonic pushover strain values are used to compare with LEN-2 Repair. It can be seen that the nonlinear and conventional STMs overpredict the force in the jacket by up to 19.6% and 35.3%, respectively. Both models overpredict the loads in the CFRP jacket and could be used conservatively for design. Due to the sudden and catastrophic nature of CFRP jacket failure, conservatism should be built into the design of the CFRP jacket. The highest recorded value of strain from testing at each displacement step and the strain associated with the nonlinear STM results for the wrap can be found in Figures 5.23 and 5.24 for NMB-2 Repair and LEN-2 Repair, respectively. From the force generated in the CFRP wrap at

Table 5.34 – Test and nonlinear STM CFRP wrap

	Percent of effective CFRP jacket strength		
	Maximum strain gage test results	Maximum nonlinear STM results	Maximum traditional STM results
NMB-2 Repair	50.8	63.7	74.8
LEN-2 Repair	36.5	56.1	71.8

different displacement steps in the nonlinear STM, the strain was calculated by converting the tie force to a stress and dividing the stress by the CFRP tensile modulus.

5.5.3 Headed rebar results

The headed rebar yielded during the simulations using both the nonlinear and conventional STMs for NMB-2 Repair. This yielding prediction matches the observed results during testing where the headed rebar yielded during the 1-in. displacement step. Unfortunately, the strain gauges were lost during testing at higher displacement values and the ultimate strains achieved during testing are unknown. Due to the high level of strain during the 1-in. displacement step, it is believed that much higher levels of strain were reached during testing. The nonlinear STM does predict the yielding of the headed rebar, but underpredicts the magnitude of strain in the case of NMB-2 Repair. No reliable strain gauge data was recorded for LEN-2 Repair.

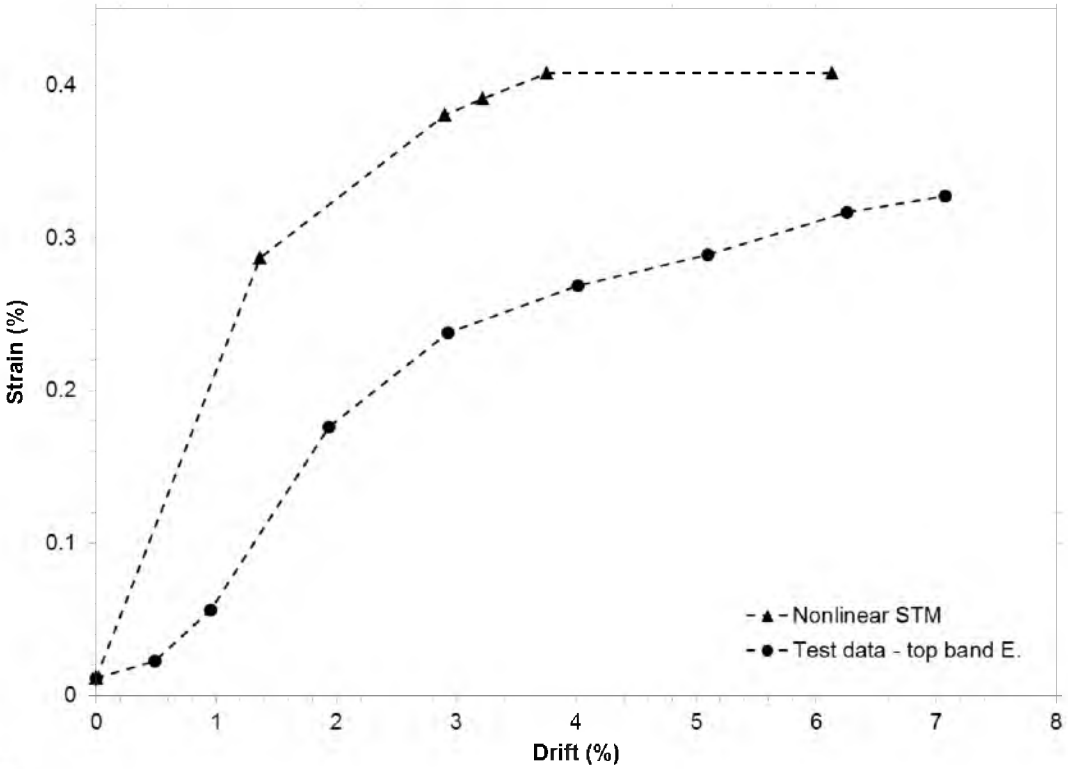

Figure 5.23 – NMB-2 Repair CFRP wrap strain gauge data and nonlinear STM output

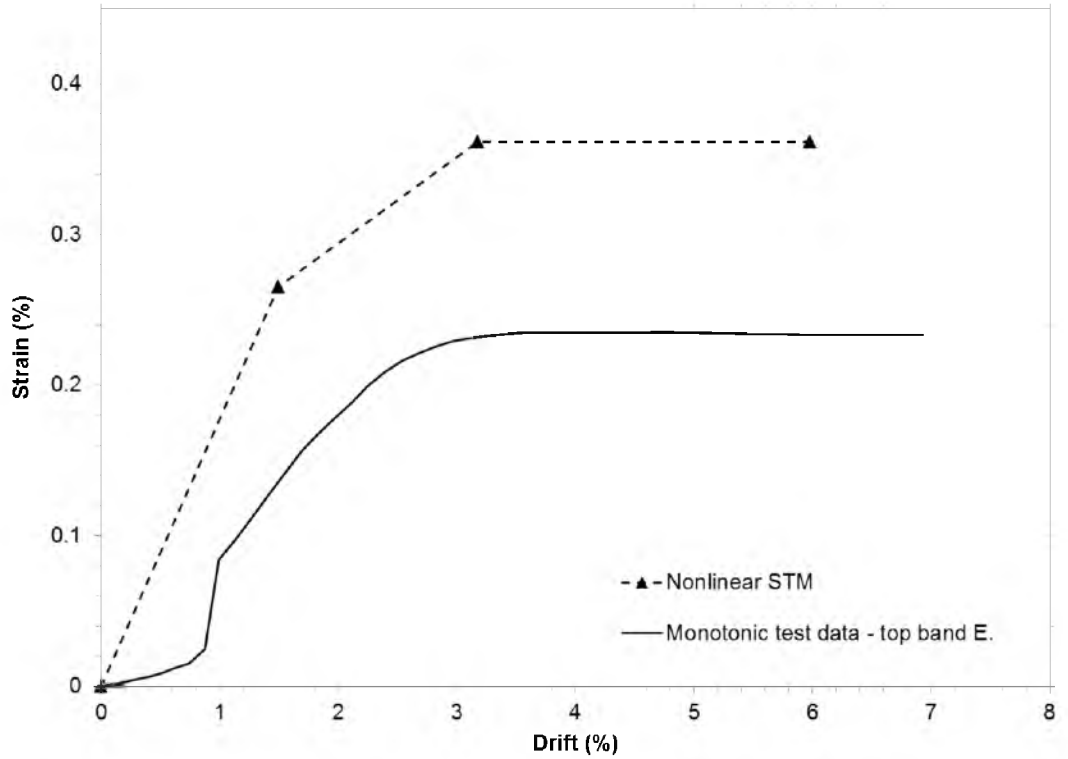

Figure 5.24 – LEN-2 Repair CFRP wrap strain gauge data and nonlinear STM output

CHAPTER 6

CONCLUSIONS

A repair method has been developed and tested on precast column-to-footing bridge assemblies connected using GSS, which have been damaged by an earthquake. The repair method has been tested on two cyclically damaged specimens; both specimens had fractured longitudinal rebar at the time of repair. The performance of the specimens has been successfully restored in terms of load, displacement, and energy dissipation capacities. The repair procedure provides an attractive alternative to the high cost and user interruption that bridge replacement poses after an earthquake. The repair procedure is rapid, cost effective, corrosion resistant, easily constructible, and uses readily available materials. Future applications of the repair method may be expanded to all types of column plastic hinges in bridges or building for precast or monolithic construction. However, necessary shear reinforcement is required to achieve satisfactory performance. In columns that lack the surplus of shear reinforcement required for the repair method, the use of externally bonded shear reinforcement should be investigated.

The lateral load capacity of both repaired specimens was larger than that of the as-built specimens. NMB-2 Repair had 130% of the average lateral load capacity of NMB-2, and NMB-3 Repair had 128% of the average lateral load capacity of NMB-3. NMB-2 Repair had a higher displacement capacity than NMB-2 and had 98% of the displacement ductility, achieving an average displacement ductility of 5.95. NMB-2 Repair also dissipated 43% more cumulative energy than NMB-2 at the ultimate displacement. NMB-3 Repair only achieved an average displacement ductility of 3.66 due to a column longitudinal rebar fracturing prematurely during the 5-in. displacement step. The early rebar fracture during the NMB-3 Repair test is believed to be due to welding of a threaded rod to the longitudinal bar. The embrittlement of the bar was shown

by the fracture surface of the bar being flat and the location of the fracture not matching any of the other tests. From the results of NMB-2 Repair, it can be seen that the repair procedure is capable of restoring all critical performance criteria of an earthquake damaged column.

Generalized STM modeling procedures have been developed to aid in the design of as-built and repaired, column-to-footing, and column-to-pier cap assemblies. Two STM methods have been used; the conventional STM and nonlinear STM. The conventional STM follows the design guidelines within ACI 318, which does not take into account the degrading cyclic strength of the model elements and predicts the ultimate load capacity of the assembly being modeled but not the displacement. The nonlinear STM produces a force-displacement response envelope for the assembly, using effective member strengths, which take into consideration the cyclic degradation of the materials. When compared to the test results it can be seen that the conventional STM can overpredict the ultimate load capacity of the assembly being modeled. The conventional STM should be used to predict the monotonic strength of an assembly, and the nonlinear STM should be used to predict the cyclic force-displacement envelope. This difference in the models is best observed for LEN-2 Repair, which was tested both monotonically and cyclically.

In addition to overpredicting the ultimate strength of half the specimens that were modeled, the conventional STM vastly overpredicts the yield strength of the specimens, which is defined as failure in the conventional STM. Yielding of rebar ties was the failure mode of both repair models. This failure mode could lead a designer to believe the actual specimen would have much more overstrength. However, this is not the case since the conventional STM overpredicted the ultimate load capacity of LEN-2 Repair, which the model predicted as yielding of the headed rebar ties. Both the overprediction of the ultimate load capacity and the overprediction of the yield strength of the specimens show the unconservative nature of the conventional STM. This should be expected when the conventional STM is used to model lateral force resisting elements.

The nonlinear STM predicts the force-displacement response envelopes of the cyclically damaged assemblies, which can be used to predict the ultimate load capacity, displacement

capacity, yield displacement, displacement ductility, and stiffness at varying displacements. The nonlinear STM predicted the ultimate load capacities of the repaired column-to-footing and repaired column-to-pier cap assemblies to be 82% and 92% of the tested capacities, respectively. The nonlinear STM also predicted the ultimate displacement of the repaired column-to-footing and repaired column-to-pier cap assemblies to be 88% and 84% of the tested capacities respectively. When modeling the two as-built specimens, the nonlinear STM results, in terms of ultimate load capacity, were slightly more conservative and underpredicted the ultimate load by as much as 44%. However, the nonlinear STM seems to be a reasonable estimate of the force-displacement characteristics for the as-built and repaired column-to footing and column-to-pier cap assemblies.

6.1 Repair design recommendations

The design and procedure outlined in Chapter 3 was followed for NMB-2 Repair and NMB-3 Repair, which successfully relocated the plastic hinge regions of the specimens. Throughout the research process a few design improvements were recognized and should be considered for future applications.

The thickness of the CFRP wrap should be larger than that calculated in Chapter 3 by an appropriate margin of safety. The shear strength and confinement that the wrap provides is paramount to the performance of the repair. To ensure proper performance from the CFRP wrap, all available methods to mitigate transverse CFRP cracking should be taken. This includes decreasing the cover of the headed rebar, which was 3 in. in this study. Also, additional means of providing longitudinal strength to the CFRP wrap should be investigated. In previous tests that have implemented this repair procedure on column-to-pier cap assemblies *(34)*, the CFRP jacket has ruptured. The rupturing of the CFRP jacket was thought to be due to brittle repair concrete, high strength as-built concrete, high effective strength of the longitudinal rebar in the column, minor damage during the as-built test above the height of the repair, and the early onset of transverse CFRP cracking. This test demonstrated some of the factors that can rapidly increase the demand on the jacket.

The amount of expansion in the repair concrete highly influences the behavior of the repaired section. NMB-2 Repair was designed with Komponent as 13% of the cementitious materials, whereas NMB-3 was designed with 41% Komponent. The 41% Komponent mix design provided 14.6 times as much pre-tensioning of the CFRP jacket prior to testing than the 13% Komponent mix design. The large amount of pre-tensioning provided in NMB-3 Repair did not pose any problems, in fact it seemed to help the performance, but this was a short-term study where the repaired column was tested 20 days after casting the repair concrete. It is believed that the repair concrete used for NMB-3 Repair would have expanded much more with time, decreasing the remaining strain capacity of the jacket. Further research should be conducted to optimize the repair concrete mix design

6.2 Recommendations for further research

Further research should be conducted for the repair procedure as well as the STM modeling procedures. More tests need to be conducted on precast GSS specimens of varying geometries incorporating the repair, following the design recommendations provided in Section 6.1. It is also believed that the repair procedure would work well for column plastic hinges in monolithic type bridge or building applications, but further research is needed to verify this. Optimization of the repair concrete mix design would offer significant benefits to the repair process. This includes the amount of expansion, the strength, and the workability of the concrete for construction. Improvements to the CRFP wrap should be researched. This includes methods to mitigate transverse cracking; including longitudinally oriented CFRP sheets, prefabricated CFRP wraps, and decreasing headed rebar cover. The rapid application of the repair procedure could be refined where bridge reopening times could be estimated. Rapid curing of the CFRP wrap would need to be investigated. Also, repair concrete that has high early strength could be used.

Many avenues exist for further research into STMs; some of the major topics are mentioned here. An improved material force-displacement input for the longitudinal rebar in the column should be investigated for the nonlinear STM. Due to the extremely large strain gradient

that exists in the column longitudinal bars and their importance to the model a more accurate input is needed. The current input used in this study was a bilinear curve that followed the steel modulus up to the effective yield point and then followed a strain hardening ratio (s.h.r.) after the effective yield, as recommended in previous research *(18)*. The effective yield is the point at which the extreme longitudinal rebar yields. However, since the tie represents five longitudinal bars with highly varying distances to the neutral axis, the stiffness beyond yield is dramatically underpredicted by the s.h.r. An improvement to the force-displacement input would be to obtain it from a sectional analysis, using a confined concrete model for the concrete in the column core and an accurate tension steel model for the longitudinal bars in tension. This requires incremental levels of concrete strain to be used, and the corresponding force in the longitudinal rebar would need to be recorded. Once a satisfactory number of points were recorded from the sectional analysis, the improved force-displacement input for the longitudinal rebar in the column could be generated. This process could improve the input for any longitudinal tie that represents multiple steel bars with varying moment arms.

Another aspect of the nonlinear STM that could use some refinement is the effective strength of the CFRP confined concrete struts. This effective strength would need to be determined from cyclic tests on CFRP confined concrete. The CFRP confined concrete model used for the repair concrete struts and the allowable effective stress that was assigned to these struts made the effective strength less than the unconfined concrete strength. This is a highly conservative approach. Although the CFRP confined concrete struts did not control any of the loads in this study, it still needs to be refined.

The last research recommendation for the nonlinear STM would be to refine the plastic hinge length of the precast GSS specimens. This improvement would help to better predict the last point of the nonlinear STM output for the as-built specimens. Also, including concrete ties in the model could improve results by increasing the initial stiffness.

REFERENCES

(*1*) California Department of Transportation. *Seismic design criteria*; Division of Engineering Services, Sacramento, CA. 2010.

(*2*) Ameli, M.J. Seismic Design of Grouted Splice Sleeve Connections for Bridge Piers used in Accelerated Bridge Construction. Ph.D. Dissertation, University of Utah, Salt Lake City, UT, to be submitted for publication (2015).

(*3*) Haber, Z.; Saiidi, M.; Sanders, D. *Precast Column-Footing Connections for Accelerated Bridge Construction in Seismic Zones*; Final Report No. CA13-2290; Nevada, 2013.

(*4*) Belleri A.; Riva, P. Seismic Performance and Retrofit of Precast Concrete Grouted Sleeve Connections. *PCI J.* **2012**, *57*, 97–109.

(*5*) American Concrete Institute. ACI 318-11 Building Code Requirements for Structural Concrete; Farmington Hills, MI, 2011.

(*6*) Seible, F.; Priestley, M.J.; Hegemier, G. Seismic Retrofit of RC Columns with Continuous Carbon Fiber Jackets. *J. Compos. Constr.* **1997**, *1*, 52–62.

(*7*) Pantelides, C.P.; Gergely, I.; Reaveley, L.D.; Volnyy, V.A. Retrofit of R/C Bridge Pier with C CFRP Advanced Composites. *J. Struct. Eng.*, **1999**, *125*, 1094–1099.

(*8*) Chai, Y.; Priestley, M.J.; Seible, F. Seismic Retrofit of Circular Bridge Columns for Enhanced Flexural Performance. *ACI Structural J.* **1991**, *88*, 572–584.

(*9*) Lehman, D.; Gookin, S.; Nacamuli, A.; Moehle, J. Repair of Earthquake-Damaged Bridge Columns. *ACI Structural J.* **2001**, *98*, 233–242.

(*10*) Hose, Y.D; Seible, F; Priestley, M.J. Strategic Relocation of Plastic Hinges in Bridge Columns, SSPR 97–05.

(*11*) Rutledge, S.; Kowalsky, M.;Seracino, R.; Nau, N. *Repair of Damaged Circular Reinforced Concrete Columns by Plastic Hinge Relocation*, Proceedings of the 15 WCEE, Lisbo, 2012.

(*12*) American Association of State Highway and Transportation Officials (AASHTO). AASHTO LRFD Bridge Design Specifications. AASHTO: Washington, DC 2012.

(*13*) Saenz N.; Pantelides, C.P.; Reaveley, L.D. Strut-and-tie model for shear friction of concrete with fiber-reinforced polymer composites. *ACI Structural J.* **2004**, *101*, 863–871.

(*14*) Park S.; Aboutaha R.S. Strut-and-tie method for CFRP strengthened deep beams. *J. Structural Eng.* **2009**, *135*, 632–643.

(*15*) Hong, S.G.; Chun, S.C.; Lee, S.H.; Oh, B. Strut and Tie Model for Development of Headed Bars in Exterior Beam Column Joint. *ACI Structural J.* **2007**, *104*, 590–600.

(*16*) To, N.H.T.; Ingham, J.M.; Sriharan, S. Strut-and-tie computer modelling of reinforced concrete bridge joint systems. *J. Earthquake Eng.* **2003**, *7*, 463–493.

(*17*) To, N.H.T.; Ingham, J.M.; Sriharan, S. Strut-and-tie computer modelling of reinforced concrete bridge portal frames. *Bulletin of the New Zealand Society for Earthquake Eng.* **2002**, 165–189.

(*18*) To, N.H.T.; Ingham, J.M.; Sriharan, S. Monotonic nonlinear strut-and-tie computer models. *Bulletin of the New Zealand Society for Earthquake Eng.* **2001**, 169–190.

(19) Park, H.; Eom, T. Truss model for nonlinear analysis of RC members subject to cyclic loading. *J. Structural Eng.* **2007**, *133*, 1351–1363.

(20) To, N.H.T.; Sriharan, S.; Ingham, J.M. Strut-and-tie nonlinear cyclic analysis of concrete frames. *J. Structural Eng.* **2009**, *135*, 1259–1268.

(*21*) American Association of State Highway and Transportation Officials (AASHTO). AASHTO Guide Specifications for LRFD Seismic Bridge Design. AASHTO: Washington, DC 2011.

(*22*) American Concrete Institute. ACI 374.2-13 Guide for Testing Reinforced Concrete Structural Elements under Slowly Applied Simulated Seismic Loads; Farmington Hills, MI, 2013.

(*23*) Hilti Corporation. Technical application document: Hilti HIT-RE 500-SD; Champs sur Marne, France, 2010.

(*24*) Mortazavi, A.A.; Pilakoutas, K.; Sang Son, K. RC column strengthening by lateral pre-tensioning of FRP. *Constr. and Build. Mater.* **2003**, *17*, 491–497.

(*25*) Zihan, Y.; Pantelides, C.P.; Reaveley L.D. Fiber-reinforced polymer jacketed and shape-modified compression members: I-Experimental behavior. *ACI Structural J*. **2006**, *103*, 885–893.

(*26*) Priestley, M.J.N.; Seible, F. Design of seismic retrofit measures for concrete and masonry structures. *Constr. and Building Materials* **1995**, *5*, 365–377.

(*27*) Pantelides, C.P.; Moran, D.A. Design of FRP jackets for plastic hinge confinement of RC columns. *J. Compos. Constr*. **2013**, *17*, 881–898.

(*28*) ASTM Standard A370, 2012, “Methods for Testing Steel Reinforcing Bars,” ASTM International, West Conshocken, PA, 2012, DOI 10.1520/C0109_C0109M, www.astm.org.

(*29*) ASTM Standard D3039, 2008, “Standard Test Method for Tensile Properties of Polymer Matrix Composite Materials,” ASTM International, West Conshocken, PA, 2008, DOI 10.1520/D3039_D3039M-08, www.astm.org.

(*30*) ASTM Standard C39, 2012, “Standard Test Method for Compressive Strength of Cylindrical Concrete Specimens,” ASTM International, West Conshocken, PA, 2012, DOI 10.1520/C0039_C0039M-12A, www.astm.org

(*31*) ASTM Standard A109, 2012, "Standard Test Method for Compressive Strength of Hydraulic Cement Mortars (Using 2-in. Cube Specimens," ASTM International, West Conshocken, PA, 2012, DOI 10.1520/A0307-12, www.astm.org.

(*32*) CTS Cement Manufacturing Corporation. KSC concrete technical guide; Cypress, CA, 2013.

(*33*) American Concrete Institute. ACI 440.2R-08 Guide for the Design and Construction of Externally Bonded FRP Systems for Strengthening Concrete Structures; Farmington Hills, MI, 2008.

(*34*) Parks, J.E. Seismic rehabilitation of column to pier cap accelerated bridge construction connections and acoustic emission monitoring assessment. Masters Thesis, University of Utah, Salt Lake City, Utah, 2012

(*35*) Moran, D.; Pantelides, C. Elliptical and Circular FRP-Confined Concrete Sections: A Mohr-Coulomb Analytical Model. *Int. J. Solids and Struct*. **2012**, *49*, 881–898.

(*36*) Xiao, Y.; Priestley, M.J.; Seible, F. Seismic Assessment and Retrofit of Bridge Column Footing. *ACI Structural J.* **1996**, *93*, 79–94.

(*37*) Collins, M.P.; Mitchell, D.; Adebar, P.; Vecchio, F.J. A General Shear Design Method. *ACI Structural J.* **1996**, *93*, 36–45.

(*38*) Priestley, M.J.N.; Seible, F.; Calvi, G.M. Seismic Design and Retrofit of Bridges; John Wiley & Sons, Inc.: New York, 1996.

(*39*) Mander, J.B.; Priestley, M.J.N.; Park, R. Theoretical Stress-Strain Model for Confined Concrete. *J. Structural Division* **1988**, *114*, 1804–1826.

(*40*) Lam, L.; Teng, J.G. Design-Oriented Stress-Strain Model for FRP-Confined Concrete. *Constr. and Build. Mater.* **2003**, *17*, 471–489.

(*41*) Sika Corporation. Product data sheet: SikaWrap Hex 103C; Lyndhurst, NJ, 2011.